Universidade de Aveiro
2017

Departamento de Engenharia de Materiais e Cerãmica

Javier Macías Montiel

$SrVO_3$-based anode materials for hydrocarbon-fueled solid oxide fuel cells

Materiais de ânodo a base de $SrVO_3$ para pilhas de combustivel de óxido sólido alimentadas por hidrocarbonetos

Universidade de Aveiro Departamento de Engenharia de Materiais e Cerãmica
2017

Javier Macías Montiel

$SrVO_3$-based anode materials for hydrocarbon-fueled solid oxide fuel cells

Materiais de ânodo a base de $SrVO_3$ para pilhas de combustivel de óxido sólido alimentadas por hidrocarbonetos

Dissertação apresentada à Universidade de Aveiro para cumprimento dos requisitos necessários à obtenção do grau de Doutor em Ciencia e Engenharia de Materiais, realizada sob a orientação científica do Doutor Jorge Ribeiro Frade, Professor Catedrático do Departamento de Engenharia de Materiais e Ceramica da Universidade de Aveiro e do Doutor Aleksey Yaremchenko, Investigador Principal do Departamento de Engenharia de Materais e Ceramica da Universidade de Aveiro.

Apoio financeiro da FCT e do FSE no âmbito do III Quadro Comunitário de Apoio.

A mis Padres,

Sin vosotros no hubiera sido posible.

o júri

Presidente

Doutor José Carlos Esteves Duarte Pedro , Professor Catedrático, Universidade de Aveiro

Doutor Enrique Rodriguez Castellón, Professor Catedrático, Facultade de Ciências, Universidade de Málaga

Doutor Albano Augusto Cavaleiro Rodrigues de Carvalho, Professor Catedrático, Facultade de Ciências e Tecnologia, Universidade de Coimbra

Doutor Fernando Manuel Bico Marques, Professor Catedrático, Universidade de Aveiro

Doutor Aleksey Yaremchenko, Equiparado a Investigador Principal, Universidade de Aveiro. (Coorientador)

Doutor João Carlos de Castro Abrantes, Professor Adjunto, Escola Superior de Tecnologia e Gestão, Instituto Politécnico de Viana do Castelo

agradecimentos

I would like to express my gratitude to my supervisors, Prof. Frade and Dr Yaremchenko for their assistance, useful recommendations and for their infinite patience to my faults and my poor English on my early stage.

I am particularly thankful to all my colleagues from the University of Aveiro, especially to Sonia, Nuno, Ines e Ana for always being there when I needed them. Also I would like to express many thanks to Dr. Holtapells, Dr. Sudireddy and Dr. Veltzé for their assitance during my stage in DTU (Denmark), and those people who made from Denmark (in winter) a warm place for me, especially to my italinas brothers: Filippo and Simon.

Financial support from Fundaçao para a Ciencia e Tecnologia (grant SFRH/BD/91675/2012) is gratefully acknowledged.

A Migue y Rafa por su amistad y su apoyo en mis peores momentos, a aquellos con los que empecé esta locura, Beloki, Natoly y Jose. A mis niñas Laura, Jessy y Paloma por cada aventura inolvidable.

Finalmente a vosotros, Papa, Mama y Nuria sin vosotros, sin vuestro apoyo y sin vuestro cariño incondicional nada de esto lo hubiera conseguido. Os quiero.

palavras-chave

Vanadato de estroncio, ânode, quimica de defeitos, stabilidade, conductividade

resumo

Este trabalho foi focado na avaliação de perovskites à base de SrVO3 como potenciais materiais de ânodo para pilhas de combustível de óxido sólido alimentadas por hidrocarbonetos ou eletrocatalisadores para outros procesos de conversão. A principal motivação resulta da tolerância ao enxofre de materiais à base de óxidos de vanádio, a inibição da deposição de carbono em eletrocatalisadores óxidos em comparação com eletrocatalisadores metálicos, a estabilidade de $SrVO_3$ em condições redutoras impostas pelos combustíveis, e a sua elevada condutividade elétrica quando comparada com outras perovskites propostas para a conversão de hidrocarbonetos. No entanto, a síntese e processamento de $SrVO_3$ monofásico requerem condições redutoras devido à elevada instabilidade em condições oxidantes. Os limites da tolerância redox também levantam dúvidas sobre a capacidade para funcionar em condições de elevada conversão de combustível e a tolerância a interrupções das condições de operação (temperaturas intermedias ou relativamente elevadas e atmosferas reductoras), para manutençao ou mesmo por paragem inesperada de funcionamento.

Assim, o objetivo principal foi desenvolver materiais baseados em $SrVO_3$ com tolerância a condições relativamente inertes ou atmosferas oxidantes, sem perda excesiva de conductividade elétrica e outras propriedades relevantes para o uso como elétrodos em pilhas de combustivel ou eletrocatalisadores. Para além disto, foi também considerado o desenvolvimento de materiais alternativos a base de $SrVO_3$ com uma maior flexibilidade para o processamento de electrodos ou eletrocatalisadores em contato com eletrólitos.

Os resultados experimentais confirmaram que as fases secundarias mais comuns são o pirovanadato ($Sr_2V_2O_7$) promovido em condições oxidantes, e /ou ortovanadato ($Sr_3V_2O_8$), que é mais provável numa combinação de condições de oxidação e elevada razão de atividades Sr:V. Neste sentido, as propiedades de transporte, a estabilidade relativa e outras propiedades relevantes (por exemplo expansão termoquímica) foram estudadas em detalhe no capítulo III, e comparados com as correspondentes características da perovskite $SrVO_3$.

Mudanças na composição das perovskites baseadas em $SrVO_3$ e os correspondentes impactos na estabilidade redox, metaestabilidade, química de defeitos, propriedades de transporte, expansão termoquímica, entre outras propriedades, foram estudadas nos capítulos IV e V. O desenho destas composições foi guiado por análise termodinâmica dos impactos da razão de atividades Sr:V e das condições redox, em combinação com os efeitos previstos com base na variação do fator de tolerância em função da composição de $(Sr_{1-x}A_x)(V_{1-y}B_y)O_{3+\delta}$ com substituições parciais em ambos posições da perovskite; A = La, Y e B = Nb.

Previsões termodinâmicas e o fator de tolerância foram igualmente usados como orientações para conceber composições e condições redox necessárias para obter uma única fase de $Sr(V,Ti)O_3$ e materiais constituidos por duas fases, uma com dopajem de Ti na perovskite SrVO3 e outra com dopajem de V na perovskite $SrTiO_3$, conforme descrito no capitulo VI. Este capitulo inclui um estudo detalhado das condições de processamento para *design* flexível das fases constituintes de materiais no sistema Sr-V-Ti-O, e também sobre o impacto em propriedades relevantes, designadamente estabilidade, propriedades de transporte, expansão termoquímica e respostas transientes a ciclos térmicos ou redox.

Os estudos relatados maioritariamente no capítulo VI, em conjunto com orientações obtidas nos capítulos IV e V, forneceram informações essenciais para a preparação de células simétricas e a realização de ensaios eletroquímicos preliminares, relatados no capitulo VII; isto inclui; i) a reatividade entre materiais à base de $SrVO_3$ e eletrólitos sólidos (YSZ e CGO), ii) a deposição de elétrodos sobre electrólito YSZ com ou sem camada tampão de CGO, e um estudo eletroquímico preliminar. Variações na resistência de polarização evidenciaram as diferenças entre elétrodos monofásicos ($SrV_{1-x}Ti_xO_3$) e difásicos, o papel de camadas tampão de CGO, e o impacto fundamental de efeitos microestruturais relacionáveis com o processamento.

keywords

Strontium vanadate, defect chemistry, stability, conductivity, anode

abstract

This work was focused on the assessment of $SrVO_3$-based perovskites as prospective anodes for hydrocarbon-fueled solid oxide fuel cells or electrocatalysts for other fuel conversion processes. The main motivation was the known sulfur tolerance of vanadium-based oxide compounds, their inhibition of carbon deposition, when compared to metallic electrolacalysts, the stability of $SrVO_3$ under very reducing conditions imposed by fuels, and its high electrical conductivity when compared with alternative perovskite materials proposed for conversion of hydrocarbons. Yet, processing conditions require reducing conditions for synthesis and firing of single-phase $SrVO_3$, due to the limited tolerance to oxidizing conditions. Limited redox tolerance also raises doubts about its ability to operate under conditions of high fuel conversion, and to allow discontinuous operation and interruption of operating conditions (intermediate or relatively high temperatures and reducing atmospheres) for maintenance or due to unexpected shutdown.

Thus, the main objective was to develop $SrVO_3$-based materials with extended tolerance to relatively inert or oxidizing atmospheres, without excessive penalty for electrical conductivity and other relevant properties, seeking applicability as fuel electrodes or electrocatalysts. One also considered the development of alternative $SrVO_3$-based materials with greater flexibility for processing as electrodes or electrocatalysts in contact with SOFC electrolytes.

Relations between the stability of $SrVO_3$-based materials and redox conditions imposed by fuels are overviewed in Chapter I, based on relevant literature, and then re-examined by thermodynamic analysis of gradual fuel conversion and corresponding materials stability ranges (Chapter II). This also emphasizes the impact of Sr:V activity ratio on stability of the $SrVO_3$-based perovskite phase, and provides guidelines to prevent onset of unwanted secondary phases by composition changes.

Experimental evidence confirmed that the most common secondary phases are the pyrovanadate $Sr_2V_2O_7$, promoted by oxidizing conditions, and/or the orthovanadate $Sr_3V_2O_8$, which is most likely by a combination of oxidizing conditions and high Sr:V activity ratio. Thus, their inferior transport properties, relative stability, and other relevant properties (e.g. thermochemical expansion) were studied in detail in Chapter III, and compared with corresponding properties of the $SrVO_3$ perovskite.

Composition changes and corresponding impact on redox stability and metastability, defect chemistry, transport properties, thermochemical expansion and other relevant properties of $SrVO_3$-based perovskites were studied in Chapters IV and V. The design of these compositions was guided by thermodynamic analysis of the impact of Sr:V activity ratio and redox conditions on stability, combined with guidelines provided by the dependence of tolerance factor of $(Sr_{1-x}A_x)(V_{1-y}B_y)O_{3+\delta}$ compositions on partial substitutions in both sites, i.e., A = La, Y and B = Nb.

Thermodynamic predictions and the tolerance factor were also guidelines to design compositions and redox conditions required to obtain single phase $Sr(V,Ti)O_{3-\delta}$ materials and corresponding 2-phase materials with separate Ti-doped $SrVO_3$ and V-doped $SrTiO_3$ phases, as described in Chapter VI. This chapter includes a detailed study of processing conditions for flexible phase design, and also the relevant impact on stability, transport properties, thermochemical expansion, and transient responses to thermal or redox cycling.

Those detailed studies reported mainly in Chapter VI, combined with guidelines from Chapters IV and V, provided the required information for the preparation of half cells and preliminary electrochemical tests, reported in Chapter VII; this includes: i) reactivity between $SrVO_3$-based materials and solid electrolytes (YSZ and CGO), ii) deposition of electrodes onto YSZ electrolyte, with or without CGO buffer layer, and preliminary electrochemical screening. Effects on polarization resistance emphasize significant differences between single-phase $Sr(V,Ti)O_{3-\delta}$ and 2-phase $SrVO_3$-$SrTiO_3$ electrodes, demonstrate the role of CGO buffer layers, and suggest major impact of microstructural effects, ascribed to processing.

Table of contents

List of figures ………………………………………………………………………. V

List of tables ……………………………………………………………………... XIII

List of symbols …………………………………………………………………... XV

List of abbreviations ……………………………………………………………. XVII

Chapter 1: Introduction …………………………………………………………… 1

1.1 Global warming and energy conversion technologies ………………………. 1

1.2 Fuel Cells ………………………………………………………………………. 4

1.2.1 Open cell voltage and fuel cell efficiency ……………………………………. 6

1.2.2 Type of fuel cells: differences and advantages/disadvantages ………………. 7

1.3 Solid Oxide Fuel Cells ……………………………………………………………. 9

1.3.1 State of the art materials …………………………………………………….... 10

1.3.1.1 Electrolyte …..………………………………………………………………. 10

1.3.1.2 Interconnects ….…………………………………………………………….. 11

1.3.1.3 Sealant materials ……..……………………………………………………… 11

1.3.1.4 Electrodes ……………………………………………………………………… 12

1.3.1.4.1 Cathode …………………………………………………………… 12

1.4 Anodes for Solid Oxide Fuel Cells ………………………………………………. 13

1.4.1 Ni-based cermets: advantages and problems …………………………………. 13

1.4.1.1 Behavior in hydrocarbons-based fuels ……………………………… 13

1.4.1.1.1 Carbon deposition…………………………………………. 14

1.4.1.1.2 Sulfur poisoning …………………………………………… 14

1.4.2 Ceramic anodes ………………………………………………………………….. 16

1.4.2.1 Rutile-type structure ………………………………………………… 18

1.4.2.2 Fluorite-type structure ……………………………………………….. 18

1.4.2.3 Pyrochlores-type structure ……………………………………………19

1.4.2.4 Tungsten bronce type structure ……………………………………… 19

1.4.2.5 Perovskite - type structure …………………………………………… 20

1.4.2.5.1 Chromite …………………………………………………. 21

1.4.2.5.2 Titanate ………………………………………………… 21

1.4.2.5.3 Mixed perovskite compositions ………………………….. 21

1.4.2.6 Double perovskite- type structure ……………………………….. 22

1.5 SrVO$_3$- based materials ……………………………………………………... 24

Chapter 2: Methodology ………………………………………………………… 27

2.1 Experimental procedure ……………………………………………..…… 27

2.1.1 Synthesis and ceramic processing …………………………………………….. 27

2.1.2 X-ray diffraction ………………………………………………………………….. 30

2.1.3 Microstructural characterization ……………………………………………….. 30

2.1.4 Thermal analysis ……………………………………………………………….. 31

2.1.4.1 Thermogravimetric analysis ………………………………………….. 31

2.1.4.2 Dilatometry ……………………………………………………………… 31

2.1.5 Electrical conductivity …………………………………………………… 31

2.1.6 Electrochemical studies ………………………………………………………… 33

2.1.6.1 Electrode preparation ………………………………………………. 33

2.1.6.1.1 Paint-brushing method ……………………………………… 33

2.1.6.1.2 Screen printing ……………………………………..…….. 33

2.1.6.2 Ni-CGO infiltration …………………………………………………… 36

2.1.6.3 Electrochemical Impedance Spectroscopy (EIS) ……………………36

2.6.1.3.1 EIS experimental instrumentation ……………………………41

2.2 Thermodynamics calculations.…………………………………………………42

2.2.1 Thermodynamic analysis of methane conversion and carbon deposition ……… 42

2.2.2 Thermodynamic analysis of $SrVO_3$ based fuel electrodes ……………………… 45

Chapter 3: Redox transition in strontium vanadates ……………………………… 51

3.1 Crystal structure and microstructures of as-prepared materials …………….. 51

3.2 Thermal expansion ………………………………………………………………. 54

3.3 Electrical conductivity ……………………………………………………….. 56

3.4 Redox transition ……………………………………………………………….. 59

3.4.1 Reduction of strontium orthovanadate ……………………………………….. 59

3.4.2 Reduction of strontium pyrovanadate ……………………………………………60

3.4.3 Oxidation of perovskite-type strontium vanadate ………………………………..63

3.5 Final remarks and conclusions ……………………………………………….. 67

Chapter 4: Effect of niobium substitution ………………………………………. 69

4.1 Phase composition, structure and microstructure …………………………….. 69

4.2 Thermochemical expansion under reducing conditions …………………….....71

4.3 Electrical conductivity under reducing conditions ……………………………. 73

4.4 Defect chemistry guidelines ……………………………………………………… 75

4.5 Stability boundary of perovskite phase …………………………………………. 79

4.6 Oxidative decomposition in air and under inert atmosphere ………………….. 81

4.7 Conclusions ………………………………………………………………………. 86

Chapter 5: Perovskite-type $Sr_{1-x}Ln_xV_{1-y}Nb_yO_{3-\delta}$ system: Impact of donor type co-substitutions……………………………………………………………..…………. 89

5.1 Phase composition, structure and microstructure ……………………………… 91

5.2 Electrical conductivity and defect chemistry …………………………………… 92

5.3 Stability limits of perovskite phase ……………………………………………… 97

5.4 Metastability under inert atmosphere ……………………………………………102

5.5 Thermomechanical compatibility with solid electrolytes ………………………. 107

5.6 Conclusions ………………………………………………………………………. 108

Chapter 6: $SrVO_3$-$SrTiO_3$ solid solutions …………………………………………… 111

6.1 Sr(V,Ti)O_3 series prepared under reducing conditions ……………...................111

6.1.1 Phase composition, structure and microstructure …………………………………111

6.1.2 Thermochemical expansion under reducing conditions …………………………..113

6.1.3 Electrical conductivity ……………………………….…………………………114

6.1.4 Stability of perovskite phase ……………………….…………………………….. 115

6.2 Sr(V,Ti)O_3 series prepared under oxidizing conditions ……………………...... 121

6.2.1 Phase composition, structure and microstructure …….………………………….. 122

6.2.2 Thermal expansion …………………………….………………………………… 124

6.2.3 Electrical conductivity and redox behavior …….……………………………….. 125

6.3 Conclusions ………………………………………………………………………. 128

Chapter 7: Preliminary screening of electrode performance …...….……………….… 129

7.1 Chemical compatibility between electrodes and electrolytes ………………..…. 129

7.2 Electrodes prepared by screen printing ……………………………………….…… 130

7.2.1 Microstructural characterization …………………….………………………….…… 130

7.2.2 Electrochemical test of screen-printed electrodes..……………………………….. 133

7.3 Electrode layers prepared by brush painting ……...……………………………. 137

7.3.1 Microstructural characterization ……….…………………………………..….. 137

7.3.2 CGO buffer layer ……….………………………………………….…………...138

7.3.3 Electrochemical characterization of prepared electrodes …………..…………….. 138

7.4 Preliminary conclusions on electrode behavior …...…………………...…….. 140

Chapter 8: Final remarks and future work ………………… …………………….. 141

8.1 Main conclusions…………………………………………………………..…. 141

8.2 Future work ………………………..……………………………………………… 142

References ……………………………………………………………………..…… 145

List of figures

Fig.1.1 Evolution of world primary energy production (in million tone oil equivalent) and corresponding carbon dioxide emissions. Source: Statistics from International Energy Agency statistics (www.iea.org/statistics), edited by J.R.Frade and J.Macias…………………………………………………………………………….....2

Fig.1.2. Evolution of total primary energy consumption and main contributions of crude oil, coal and natural gas. Source: Statistics from International Energy Agency statistics (www.iea.org/statistics), edited by J.R.Frade and J.Macias.……..............................2

Fig.1.3 IEA statistics of % renewable energies in total primary energy supply in Europe in 2000 and 2013. Source: IEA statistics (http://energyatlas.iea.org) edited by J.R.Frade and .Macias)…………………………………………………………………………...3

Fig. 1.4 Principle of operation of a fuel cell (SOFC-type to be discussed below) (left); and stack cell design (right)………………………………………………………...4

Fig.1.5 Thermodynamic calculations of open cell voltages for the main types of fuels proposed for conversion in fuel cells…………………………………………………6

Fig. 1.6 Main type of fuel cells and ion diffusion within the electrolyte [fuelcells.org, 2015]……………………………………………………………………………..8

Fig.1.7 Ionic conductivity of candidate materials for SOFC electrolyte. (Data from Yamamoto et al. (1995) at 800 ºC are measured after aging at 1000 C for 1000 h) [Recent trends in Fuel Cell Science and Technology, 2007)]………………………….11

Fig. 1.8 Sulfur poisoning mechanism of an SOFC anode [Sazaki, 2011]……………..16

Fig 1.9. Type-structures for different promising SOFCs anodes: (A) Fluorite, (B) tungsten bronze, (C) pyrochlore, (D) perovskite and (E) rutile. [Reproduced from Sun, 2007] ……………………………………………………………………………...17

Fig. 1.10. The structure of (A) the perovskite $SrTiO_3$ and (B) the tungsten bronze $Sr_{0.6}Ti_{0.2}Nb_{0.8}O_3$ viewed down the [001] axis. [Slater, 1999]…………………………..20

Fig. 1.11. Process flow diagram of proposed system…………………………………25

Fig 2.1. Phase diagrams of $SrO-V_2O_5$ system [Krasnenko, 1983]…………………….27

Fig. 2.2. Scheme of synthesis for Ti-rich series under oxidizing conditions. (*)Different temperatures for each compositions are listed in table 2.2. ……………………………29

Fig. 2.3. Schematic representation (right) of 4-probe technique in comparison with (left) 2-point……………………………………………………………………….31

Fig. 2.4 Schematic representation of the cell for the conductivity measurements (left) and contacts between current and potential leads and sample (right)………………….32

Fig. 2.5 Schematic representation of symmetrical cells preparation and infiltration process……………………………………………………………………………....33

Fig. 2.6 Flow chart representing the manufacturing processes of cell preparation……34

Fig. 2.7 Screen printing photography (left) and schematic representation of screen printing process (right)……………………………………………………………………35

Fig 2.8. Typical process for the infiltration of metal salt nitrate solution into a pre-sintered electrode porous structure………………………………………………….36

Fig. 2.9 Non ohmic polarization curve showing AC potential input and current response. Supplied potential, V_1, results in current response i_1………………………………..37

Fig 2.10 An example Nyquist plot for a solid, oxygen ion conducting electrolyte with conducting electrodes. The equivalent circuit such as system is displayed above…….38

Fig. 2.11. Schematic representation in ideal Nyquist plot, of corresponding resistance to polarization (Rp) and ohmic resistance (Rs)………………………………………...40

Fig. 2.12 Impedance sample holder and gas inlet and outlet for measuring EIS under a reducing atmospheres…………………………………………………………..…41

Fig 2.13. Equilibrium gas composition and methane conversion as a function of oxygen partial pressure, at 1073 K for (A) H_2O:methane ratio 0.5 and (B) CO_2:methane ratio 0.5. Red dotted show zone with C-deposition………………………………………44

Fig 2.14 Thermodynamic consideration of carbon deposition in chemical equilibrium diagram of C-H-O system at 1173 K…………………………………………………...44

Fig 2.15 Stability limits of Ni/NiO (solid line) and predictions of conditions of methane combustion in the range 10-90% (shaded area), and carbon deposition. The upper dashed line indicates changes in effective oxygen partial pressure for 90% conversion with anodic overpotential $\eta = 0.2V$……………………………………………..…...45

Fig 2.16. Redox equilibria for the Sr-V-O system at 1073K, and corresponding H_2/H_2O equilibrium. Vertical lines show conditions for 1% H2O with η=-0.15V (left) and (90% H2O with η=0.1V (right)…………………………………………………………48

Fig 2.17. Redox equilibria for the Sr-V-O system at 1073K, and corresponding H_2/H_2O equilibrium. Vertical lines shows CO-rich conditions representative of CO_2 electrolysis (99% CO with η=-0.15V) and fuel cell conditions (90% CO_2 with η=0.1V (right)….50

Fig 3.1. XRD patterns of $SrVO_{3-\delta}$, (A) $Sr_2V_2O_7$ (B) and $Sr_3V_2O_8$ (C) as prepared…….52

Fig 3.2. *SEM* micrographs of as prepared fractured $SrVO_{3-\delta}$ (A), $Sr_2V_2O_7$ (B) and $Sr_3V_2O_8$ (C) ceramics…………………………………………………………………..53

Fig 3.3. XRD patterns of 2SrO:V_2O_5 mixture calcined in air at 853 K for 30 h………54

Fig. 3.4. Dilatometric curves of $SrVO_{3-\delta}$ ceramics in 10 % H_2-N_2 and $Sr_3V_2O_8$ ceramics in air. Inset shows variations of oxygen nonstoichiometry in $SrVO_{3-\delta}$ in 10 % H_2-N_2 atmosphere calculated from the thermogravimetric data……………………………55

Fig 3.5. Dilatometric curves of $Sr_2V_2O_7$ ceramics in air in two subsequent runs in different temperature ranges……………………………………………………………56

Fig.3.6. Electrical conductivity of $SrVO_{3-\delta}$ ceramics as function of temperature in 10% H_2 atmosphere (A) and as function of oxygen partial pressure at 973-1173 K (B).......57

Fig.3.7. Temperature dependence of electrical conductivity of $Sr_2V_2O_7$ and $Sr_3V_2O_8$ ceramics in air and ir Ar atmosphere ($p(O_2)$ ~5 x 10^{-5} atm)............................... 58

Fig.3.8. XRD pattern of $Sr_3V_2O_8$ reduced in 10%H_2 low at 1173 K for 25h (A); thermogravimetric curves of powdered $Sr_3V_2O_8$ on heating in 10% H_2 flow (B) and variation of electrical conductivity of $Sr_3V_2O_8$ ceramics with time at 1173 K upon reduction in 10%H_2 (C) 59

Fig.3.9. XRD pattern of $Sr_2V_2O_7$ reduced in 10% H_2 flow at 1173 K for 25 h (A) and variation of electrical conductivity of $Sr_2V_2O_7$ ceramic with time at 1173 K upon reduction in 10% H_2 flow (B). Dotted line corresponds to conductivity value of as-prepared $SrVO_{3-\delta}$ ceramics in 10% H_2 atmosphere at given temperature..............60

Fig 3.10. Thermogravimetric curves of powdered $Sr_2V_2O_7$ on heating in 10% H_2 flow (A) and relative weight change of powdered $Sr_2V_2O_7$ in one redox cycle at 1173 K (B). Average oxidation state of vanadium cations was calculated assuming that all V is in 5+ state after equilibration with air...61

Fig. 3.11. XRD patterns of powdered $Sr_2V_2O_7$ samples heated in 10% H_2-N_2 flow in TGA equipment to T_{max} at 2 K/min and then immediately cooled to room temperature at 10K/min 61

Fig 3.12. Image of bar-shaped $Sr_2V_2O_7$ ceramic samples illustrating irreversible length changes after redox treatments.. 63

Fig .3.13. Thermogravimetric curves of powdered $SrVO_{3-\delta}$ samples on heating in 10% H_2 flow (A) and isothermal treatment at 1173 K (B).......................................64

Fig 3.14. XRD patterns: after oxidation in air for 25 h at 1173 K and subsequent reduction in 10% H_2 flow at 1173 K for 25h (A) and $Sr_2V_2O_7$ obtained by oxidation of $SrVO_{3-\delta}$ on heating in air to 1273 K (B) . Marked reflections are indexed according to JCPDS PDF #79-8160 and 81-1844. 64

Fig. 3.15. Variation of electrical conductivity of $SrVO_{3-\delta}$ ceramic with time at 1173 K upon reduction in 10% H_2 or oxidation in air. Dotted line corresponds to conductivity value of as prepared $SrVO_{3-\delta}$ ceramics in 10% H_2 at given temperature.................65

Fig. 3.16. Dilatometric curves on heating and subsequent cooling of $SrVO_{3-\delta}$ ceramic in air and $Sr_2V_2O_7$ ceramics in 10% H_2 (A) and images of bar-shaped $SrVO_{3-\delta}$ ceramic sample illustrating irreversible length changes after consecutive redox treatments (B). Each treatment included heating/cooling (5K/min) in a given atmosphere with annealing at 1273 K for 1 h..66

Fig.3.17 XRD patterns of $SrVO_{3-\delta}$ samples: after annealing in flowing Ar atmosphere with $p(O_2)$ = 5 x 10^{-5} atm at 1173 K for 20h (A); after annealing in flowing Ar atmosphere with $p(O_2)$ = 10^{-4} atm at 1173 K for 35 h (B). Marked reflections are indexed according to JCPDS PDF # 81-1844 ($Sr_3V_2O_8$), 79-8160 (SrV_6O_{11}) and 81-0837 ($Sr_2V_2O_7$)..67

Fig 4.1. XRD patterns of as-sintered $SrV_{1-x}Nb_xO_{3-\delta}$ ceramics…………………….. 69

Fig 4.2. SEM micrographs (A-C) and SEM micrograph with EDS element mapping (D) of fractured cross-sections of as-prepared $SrV_{1-x}Nb_xO_{3-\delta}$ ceramics…………………. 71

Fig 4.3. Dilatometric curves of $SrV_{1-x}Nb_xO_{3-\delta}$ ceramics (A) and thermogravimetric curves of powdered $SrV_{1-x}Nb_xO_{3-\delta}$ ceramics and the corresponding relative changes in oxygen deficiency with temperature (B) in 10% H_2-N_2 ………………………..…..72

Fig 4.4. Temperature dependence of electrical conductivity of $SrV_{1-x}Nb_xO_{3-\delta}$ ceramics in 10%H_2-N_2 atmosphere: (A) experimental values (σ), and (B) values corrected for porosity (ε) using the model for materials with homogeneous distribution of spherical pores $\sigma_0 = \sigma\ (1+0.5\varepsilon)/(1-\varepsilon)$. Inset shows the dependence of electrical conductivity on Nb content at 623 K……………………………………………………………………74

Fig 4.5. Oxygen partial pressure dependence of electrical conductivity of $SrV_{1-x}Nb_xO_{3-\delta}$ ceramics at 1173 K.…………………………………………………………………..….75

Fig 4.6. Simulated Kroger-Vink diagrams for $SrV_{0.90}Nb_{0.10}O_{3-\delta}$ computed for different values of the mass action constant of disproportionation reaction $k_d = 10^{-2}$ (thick lines) and 2×10^{-3} (thin lines). The limiting solutions for negligible disproportionation (and negligible concentration of pentavalent V^{5+}) are shown dashed. ……………………78

Fig 4.7. Simulated Kroger-Vink diagrams for $SrV_{0.80}Nb_{0.20}O_{3-\delta}$ (solid lines) and $SrVO_{3-\delta}$ (dashed lines) computed on assuming $k_d = 10^{-2}$…………………………………..…78

Fig 4.8. Determination of approximate stability limits of $SrV_{1-x}Nb_xO_{3-\delta}$ perovskites from *log* σ - *log* $p(O_2)$ dependencies (A), and approximate high-$p(O_2)$ stability boundary of perovskite phase for $Sr(V,Nb)O_{3-\delta}$ system at 1173 K (B). Dotted horizontal line in (B) marks the phase boundary between V_2O_3 and V_3O_5 at this temperature [Okinaka, 1971]……………………………………………………………………..….79

Fig 4.9. XRD patterns of $SrV_{1-x}Nb_xO_{3-\delta}$ ceramics after phase stability boundary determination (see Fig.4.8A). Marked reflections are indexed according to JCPDS PDF # 81-1844…………………………………………………………………………80

Fig 4.10. Predictions of tolerance factor of $SrV_{1-x}Nb_xO_{3-\delta}$ and its dependence on redox changes based on defect concentrations (Eq.(4.11)). Solid lines were computed on assuming negligible disproportionation ($k_d \approx 0$), and dotted lines were computed for $k_d \approx 0.04$………………………………………………………………………… 81

Fig 4.11. Relaxation of electrical conductivity of $SrV_{0.80}Nb_{0.20}O_{3-\delta}$ ceramics in (A) 10%$H_2 \rightarrow$air$\rightarrow$10%H_2 and (B) 10%$H_2 \rightarrow$air$\rightarrow$10%H_2 redox cycles at 1173 K……….82

Fig 4.12. XRD patterns of $SrV_{0.80}Nb_{0.20}O_{3-\delta}$ samples after redox cycling at 1173 K. Patterns (A) and (C) were obtained after conductivity relaxation studies, performed with bulk ceramic samples (Fig.4.11), and pattern (B) was obtained after thermogravimetric studies of crushed samples (see Fig.4.14)…………………………………………..…83

Fig 4.13. (A-C) SEM micrographs of fractured cross-section of $SrV_{0.80}Nb_{0.20}O_{3-\delta}$ ceramic samples after conductivity relaxation measurements in $10\%H_2 \rightarrow air \rightarrow 10\%H_2$ redox cycle at 1173 K, and (D) EDS elemental mapping corresponding to micrograph (C). …………………………………………………………………………….…84

Fig 4.14. Relative weight change of powdered $SrV_{0.80}Nb_{0.20}O_{3-\delta}$ sample in $10\%H_2 \rightarrow air \rightarrow 10\%H_2$ redox cycle at 1173 K…………………………………………85

Fig 4.15. Lattice parameter values obtained for the as-prepared $SrV_{1-x}Nb_xO_{3-\delta}$ samples (circles) and for the corresponding residual Nb-lean perovskites $SrV_{1-x+y}Nb_{x-y}O_{3-\delta}$ after exposing powdered samples to the reducing → inert → reducing cycle (diamonds) or reducing → oxidizing → reducing cycle (square). Dotted lines show the expected changes in composition……………………………………………………………..85

Fig 4.16. XRD patterns of powdered $SrV_{1-x}Nb_xO_{3-\delta}$ ceramic samples after thermal treatment in Ar flow at 1173 K for 20 h………………………………………………86

Fig 5.1. Calculated Goldschmidt tolerance factors for $Sr_{1-x}Ln_xV_{1-y}Nb_yO_3$: (A) Ln = La and (B) Ln = Y. ……………………………………………………………………….. 89

Fig.5.2. SEM micrographs of fractured as-prepared $Sr_{1-x}Y_xV_{1-y}Nb_yO_{3-\delta}$ ceramics…..92

Fig 5.3. Electrical conductivity of $Sr_{1-x}Ln_xV_{1-y}Nb_yO_{3-\delta}$ ceramics as function of temperature in $10\%H_2$-N_2 atmosphere **(A)** and as function of oxygen partial pressure at 1173 K **(B)**……………………………………………...…………………..…..93

Fig 5.4. Relative changes of oxygen nonstoichiometry in $Sr_{1-x}Ln_xV_{1-y}Nb_yO_{3-\delta}$ ceramics under $10\%H_2$-N_2 atmosphere (cooling, 2°C/min)……………………………………..94

Fig. 5.5. Simulated Kröger-Vink diagrams of $SrVO_{3-\delta}$, $Sr_{0.8}Ln_{0.2}VO_{3-\delta}$ and $Sr_{0.8}Ln_{0.2}V_{0.90}Nb_{0.10}O_{3-\delta}$. ……………………………………………………………96

Fig 5.6. Simulated Kröger-Vink diagrams of $Sr_{0.8}Ln_{0.2}VO_{3-\delta}$ computed for different values of the equilibrium constant K_{red}…………………………………………………96

Fig 5.7. Relative weight gain on oxidation of powdered $Sr_{0.8}Ln_{0.2}V_{1-y}Nb_yO_{3-\delta}$ ceramic samples in one heating/cooling cycle in air…………………………………………....97

Fig 5.8. XRD patterns of $Sr_{1-x}Ln_xV_{1-y}Nb_yO_{3-\delta}$ oxidized in air in one heating/cooling cycle (2°C/min, T_{max} = 1000°C). Most intense reflections of $LaVO_4$ (JCPDS PDF # 75-3158), YVO_4 (JCPDS PDF # 82-1968) and unidentified phase(s) are marked with symbols. Unmarked intense reflections belong to $Sr_2V_2O_7$ phase (JCPDS PDF # 81-0737)………………………………………………………………………...…98

Fig 5.9. Relative length change of $Sr_{0.8}Ln_{0.2}V_{1-y}Nb_yO_{3-\delta}$ ceramic samples on oxidation in one heating/cooling cycle (3°C/min) in air…………………………………….…99

Fig 5.10. Determination of approximate phase stability limits of $Sr_{0.8}La_{0.2}V_{1-y}Nb_yO_{3-\delta}$ perovskites at 900°C from the *log* σ *- log p(*O_2*)* dependencies……………………100

Fig 5.11. Approximate high-p(O_2) stability limits of perovskite phase. Cubic perovskite phase exists below the stability boundary; perovskite phase decomposition occurs at oxygen partial pressures above the stability limit. The data on $SrV_{1-y}Nb_yO_{3-\delta}$ (from previous chapter) are shown for comparison………………………………………101

Fig 5.12. Relaxation of electrical conductivity of $Sr_{0.8}La_{0.2}V_{1-y}Nb_yO_{3-\delta}$ ceramics in one 10% $H_2 \rightarrow Ar \rightarrow 10\%H_2$ redox cycle at 900°C……………………………………103

Fig 5.13. SEM micrographs of fractured $Sr_{0.8}La_{0.2}V_{0.90}Nb_{0.10}O_{3-\delta}$ ceramics: (A) as-prepared and (B) after conductivity relaxation studies in one 10% $H_2 \rightarrow Ar \rightarrow 10\%H_2$ redox cycle at 900°C…………………………………………………….…103

Fig 5.14. XRD patterns of powdered $Sr_{0.8}Ln_{0.2}V_{1-y}Nb_yO_{3-d}$ ceramics: (A-B) after conductivity relaxation studies in one 10% $H_2 \rightarrow Ar \rightarrow 10\%H_2$ redox cycle at 900°C; (C-E) after thermal treatment in Ar flow at 900°C for 20 h (C-D) and 60 h (E). Phase impurities: triangles – $Sr_3V_2O_8$ (JCPDS PDF # 81-1844); circles – YVO_4 (JCPDS PDF # 82-1968); diamonds – $Sr_2V_2O_7$ (JCPDS PDF # 81-0737)…………………………104

Fig 5.15. Relative changes of oxygen content in powdered $Sr_{0.8}La_{0.2}VO_{3-\delta}$ sample in one $10\%H_2 \rightarrow Ar \rightarrow 10\%H_2$ cycle at 900°C……………………………………………104

Fig 5.16. Relative changes of oxygen content in powdered $Sr_{0.8}Ln_{0.2}V_{1-y}Nb_yO_{3-\delta}$ samples on heating and subsequent cooling in argon flow……………………………………105

Fig 5.17. Comparison of the lattice parameters of perovskite-type $Sr_{0.8}Ln_{0.2}V_{1-y}Nb_yO_{3-\delta}$: as-prepared (closed symbols) and after heating-cooling cycle (T_{max} = 1200°C) in argon flow (open symbols)…………………………………………………………..……106

Fig 5.18. Dilatometric curves of $Sr_{0.8}Ln_{0.2}V_{1-y}Nb_yO_{3-\delta}$ ceramics on heating (solid lines) and subsequent cooling (dotted lines) in argon flow. The curves are shifted with respect to each along Y axis for clarity……………………………………………………106

Fig 5.19. Dilatometric curves of (A) $Sr_{1-x}La_xV_{1-y}Nb_yO_{3-\delta}$ and (B) $Sr_{1-x}Y_xV_{1-y}Nb_yO_{3-\delta}$ ceramics in $10\%H_2$-N_2 atmosphere…………………………………………………..108

Fig 6.1. Lattice parameter values obtained for the as prepared $SrV_{1-y}Ti_yO_{3-\delta}$ samples.112

Fig 6.2 SEM micrographs of fractured cross-sections for (A) $SrV_{0.70}Ti_{0.30}O_{3-\delta}$ and (B) $SrV_{0.50}Ti_{0.50}O_{3-\delta}$ ceramics……………………………………………………...…113

Fig 6.3. Dilatometric curves (A) and average thermal expansion coefficient (1150-950ºC) (B) of $SrV_{1-x}Ti_xO_{3-\delta}$ ceramics in 10% H_2-N_2 atmosphere. CGO, LSGM and 8YSZ TEC values are represented for comparison…………………………………..…114

Fig 6.4. Relative changes in oxygen deficiency with temperature of powdered $SrV_{1-x}Ti_xO_{3-\delta}$ ceramics in 10% H_2-N_2 atmosphere……………………………………………114

Fig 6.5. Electrical conductivity of $SrV_{1-x}Ti_xO_{3-\delta}$ ceramics as function of temperature 10% H_2-N_2 atmosphere (A) and as function of oxygen partial pressure at 1173 K (B)……………………….……………………………………………………….115

Fig 6.6. Thermogravimetric curves (A), dilatometric curves (B) and XRD pattern (C) of oxidizing powdered $SrV_{1-x}Ti_xO_{3-\delta}$ ceramics……………………………………………116

Fig 6.7. Determination of approximate stability limits of $SrV_{1-x}Ti_xO_{3-\delta}$ perovskites from log s – log p(O_2) dependencies (A) and corresponding XRD patterns after phase stability boundary determination (B). Marked reflection are indexed according to JCPDS #81-1844 ………………………………………………………………………..117

Fig 6.8. XRD pattern of powdered $SrV_{1-x}Ti_xO_{3-\delta}$ ceramics after thermal treatment in Ar flow at 900ºC for 20 h…………………………………………………………….. 118

Fig 6.9. Relaxation of electrical conductivity in both reducing/air/reducing and reducing/inert reducing redox cycling at 900ºC (A) and relative weight change in the powdered $SrV_{0.50}Ti_{0.50}O_{3-\delta}$ (B)…………………………………………………………..119

Fig 6.10. XRD patterns of $SrV_{0.50}Ti_{0.50}O_{3-\delta}$ samples after redox cycling at 900ºC….120

Fig 6.11. SEM micrographs of the fractured cross-section of $SrV_{0.50}Ti_{0.50}O_{3-\delta}$ ceramic samples as prepared (A), after redox cycling under inert conditions (B), after redox cycling in air (C), and EDS elemental mapping corresponding to micrograph (C) (D)……………………………………………………………………………….…121

Fig 6.12. XRD patterns of $SrV_{1-x}Ti_xO_3$ samples sintered in air. Phase impurities ($Sr_3V_2O_8$ JCPDS PDF #81-1844)…………………………………………………..122

Fig 6.13. SEM micrographs (A) single phase $SrV_{0.30}Ti_{0.70}O_{3-\delta}$ (B-C) multiphase $SrV_{0.30}Ti_{0.70}O_{3-\delta}$ and (D) EDS element mapping of micrograph C. (Ti: Green; V: Blue)………………………………………………………………………………..123

Fig 6.14. Dilatometric curves of $SrV_{0.30}Ti_{0.7}O_3$ single phase ceramics sintered in air and measure in both, oxidizing and reducing atmosphere. Inset table of Average thermal expansion coefficient (TECS) at range of temperature between 100-1000 º C……..124

Fig 6.15. Temperature dependence of electrical conductivity of $SrV_{1-x}Ti_xO_3$ ceramics in air of (A) single phase and (B) multiphase compositions……………………………125

Fig 6.16. Variation of electrical conductivity of $SrV_{1-x}Ti_xO_3$ ceramics with time at 1173 K upon reduction in 10% H_2-N_2………………………………………………………125

Fig 6.17. (A) XRD patterns of multi-phase $SrV_{0.3}Ti_{0.70}O_3$ ceramics before and after reduction (see fig 6.16). Marked reflections are indexed according to JCPDS PDF #81-1844 and (B-C) SEM and EDS of ceramics samples after measured of relaxation conductivity…………………………………………………………………………...127

Fig 6.18. Relative changes in the oxygen content in powdered $SrV_{0.30}Ti_{0.70}O_3$ samples on heating and measure agains time………………………………………………… 127

Fig 7.1. XRD patterns for reactivity test for a 50:50 wt % mix of $Sr_{1-x}Ln_xV_{1-y}Ti_yO_{3-\delta}$ and 8YSZ powders intimately ground after annealing at 1473 K in 10%H_2-N_2…………130

Fig 7.2. XRD patterns for reactivity test for a 50:50 wt % mix of $Sr_{1-x}Ln_xV_{1-y}Ti_yO_{3-\delta}$ and CGO powders intimately ground after annealing at 1473 K in 10%H_2-N_2………… 131

Fig 7.3. SEM micrographs of selected anode layers applied by screen printing onto 8YSZ electrolyte (A,B,C and D) corresponding to $SrV_{0.50}Ti_{0.50}O_3$_red at 1423,1473, 1523 and 1573 K respectively under reducing conditions (E and F) to $SrV_{0.30}Ti_{0.70}O_3$_MP at 1423 and 1473 K sintered in air and (G) SEM/EDS of composition corresponding to micrographs E………………………………………. 132

Fig 7.4. (A) Impedance spectra of $SrV_{0.50}Ti_{0.50}O_3$-red backbone without infiltration and measured against temperature in 3% H_2O – H_2 and (B) calculated Ea using Arrhenius equation……………………………………………………………………………… 133

Fig 7.5. (A) Impedance spectra of Ni-CGO infiltrate on $SrV_{0.50}Ti_{0.50}O_3$-red backbone and measured against temperature in 3% H_2O – H_2 and (B) calculated Ea using Arrhenius equation…………………………………………………………………... 134

Fig 7.6. Impedance spectra of $SrV_{0.30}Ti_{0.70}O_3$_MP backbones sintered at 1373 and 1398 K and measured at 1123 K in 3% H_2O-H_2... 135

Fig 7.7. (A) Impedance spectra of Ni-CGO infiltrate on $SrV_{0.30}Ti_{0.70}O_3$-MP backbone and measured against temperature in 3% H_2O – H_2 and (B) calculated Ea using Arrhenius equation…………………………………………………………………... 135

Fig 7.8. (A) Impedance spectra of Ni-CGO infiltrate on $SrV_{0.30}Ti_{0.70}O_3$-MP backbone measured at different time, and (B) calculated Rp from figure (A)……………..….. 136

Fig 7.9. SEM micrographs of selected anode electrodes by brush pinting onto 8YSZ electrolyte: (A) SLV:8YSZ 50% wt at 1523 K (B) $SLV_{CGOlayer}$:CGO 50% wt at 1523 K (C) $SLV_{CGOlayer}$:CGO 50% wt at 1473 K and (D) $SLV_{CGOlayer}$:CGO 50% wt at 1423 K with Ni infiltration……………………………………………………………….…137

List of tables

Table 1.1 Main type of fuel cells ………………………………………………………..8

Table 1.2 Conductivity and electrochemical properties of selected conducting oxides as SOFC anodes (table modified from Jiang, 2004) ……………………………………..22

Table 2.1 Starting reagents, synthesis technique and processing conditions for synthesized compositions under reducing conditions.…………………………………28

Table 2.2 Annealed temperature for single phase $SrV_{1-x}Ti_xO_3$ synthesized under oxidizing conditions. ……………………………………………………………………..29

Table 2.3 Ink preparation for subsequent screen printing ……………………………..34

Table 2.4 Screen printing parameters used for electrode preparation …………………35

Table 2.5 Summary of capacitance values and their corresponding physical process. [Irvine, 1990] ……………………………………………………………………………..39

Table 2.6 Formulations of 2-phase boundaries and relation between activites remaining coefficients to ensure conservation of every chemical element ………………………46

Table 2.7 Thermodynamic predictions for interactions of solid phases in the system Sr-V-O with carbon dioxide …………………………………………………………....49

Table 3.1 Unit cell parameters…………………………………………………………51

Table 3.2 Density and average thermal expansion coefficients ………………………53

Table 3.3 Activation energy for electrical conductivity ………………………………58

Table 3.4 Phase compositions as result of thermal/redox treatments………………….68

Table 4.1 Propiertes of the as-prepared $SrV_{1-x}Nb_xO_{3-\delta}$ ceramics[a] ………………………70

Table 4.2 Average thermal expansion coefficients of $SrV_{1-x}Nb_xO_{3-\delta}$ ceramics in a 10% H_2-N_2 atmosphere and common solid electrolyte in air………………………………..73

Table 5.1 Literature data on solid solution formation ranges in pseudo-binary $Sr_{1-x}La_xVO_{3-\delta}$ system………………………………………………………………90

Table 5.2 Density and lattice parameters of as-prepared $Sr_{1-x}Ln_xV_{1-y}Nb_yO_{3-\delta}$ ceramics…………………………………………………………………………...91

Table 5.3 Dimensional changes of $Sr_{0.8}La_{0.2}V_{0.90}Nb_{0.10}O_{3-\delta}$ ceramics after dilatometric studies at different temeperature……………………………………………………99

Table 5.4 Average linear thermal expansion coefficients of $Sr_{1-x}Ln_xV_{1-y}Nb_yO_{3-\delta}$ ceramics in 10%H_2-N_2 atmosphere…………………………………………………………………107

Table 6.1 Density of as-prepared reduced $SrV_{1-y}Ti_yO_{3-\delta}$ ceramics………………….112

Table 6.2 Semi-quantification of $Sr_3V_2O_8$ phase after annealing in Ar……………...118

Table 6.3 Properties of the as-prepared $SrV_{1-x}Ti_xO_3$ ceramics sintered in air……….124

Table 7.1 R_{ohm} and Rp of electrode layer with and without Ni-CGO infiltrated $SrV_{0.50}Ti_{0.50}O_3$_red in 3% H_2O-H_2 ……………………………………………..……134

Table 7.2 Summarized of Rp for different electrodes measured in impedance spectroscopy. ………………………………………………………………….....…139

List of symbol

A - Area

A_0 – Pre – exponential factor for conductivity

C – Capacitance

C_B – Bulk capacitance

$C_{G.B}$ – Grain boundary capacitance

E_e – Equilibrium potential of the chemical reaction

F – Faraday Constant

I – Current

K – Equilibrium constant

K_d – Disproportionation constant

K_{red} – Reduction constant

L – Thickness / Length

M – Molar mass

m – Mass of a sample

n – Number of electrons

O^{2-} – Oxide ion

$p(O_2)$ – Oxygen partial pressure

R – Ideal gas constant

R_B – Bulk resistance

$R_{G.B}$ – Grain boundary resistance

r_A – Ionic radius of the A-site cation

r_B – Ionic radius of the B-site cation

r_O – Ionic radius of the oxyben cation

T – Temperature

t – Time

V – Voltage

V_O – Oxygen vacancy

Z – Impedance

$\Delta\delta$ – Oxygen nonstoichiometry

ΔG – Gibbs Free energy

ΔH – Standard enthalpy

μ – Chemical potential

σ – Conductivity

τ – Time constant

τ – Tolerance factor

ω – Frequency

List of abbreviations

a.c – Alternating current

AFC – Alkaline fuel cell

d.c – Direct current

CPE – Constant phase element

DSC – Differential scanning calorimetry

DTA – Differential thermal analysis

EDS – Energy-dispersive X-ray spectroscopy

Eq – Equation

PAFC – Phosphoric acid fuel cell

PCFC – Proton conducting fuel cell

PEMFC – Polymer electrolyte membrane fuel cell

SEM – Scanning electronic microscopy

SOFC – Solid oxide fuel cell

TC – Total conductivity

TEC – Thermal expansion coefficient

TGA – Thermogravimetry analysis

U.S – Unites States

XRD – X-ray diffraction

Prepared Materials

SLV – $Sr_{0.80}La_{0.20}O_{3-\delta}$

STV50_red – $SrV_{0.50}Ti_{0.50}O_{3-\delta}$ sintered in 10% H_2

STV30_Ox_MP – $SrV_{0.30}Ti_{0.70}O_3$ sintered in air, with multi-phase composition

STV30_Ox_P – $SrV_{0.30}Ti_{0.70}O_3$ sintered in air, with single-phase composition

1. Introduction

1.1 Global warming and energy conversion technologies

Greenhouse gases absorb and re-emit infrared radiation, thus regulating the heat balance within the surface-troposphere system [Intergovernmental Panel on Climate Change (IPCC) Fourth Assessment Report, 2007]. The main greenhouse contributions are related to combustion of fossil fuels (CO_2, NOx, VOCs). Other significant contributions also result from intensive activities such as agriculture (NOx), and industrial processes such as aluminum production (C_nF_{2n+2}), refrigeration (HFCs), etc. Thus, there is very little doubt that global warming is mainly due to the fast increase in CO_2 emissions after onset of the industrial area, well above the natural carbon dioxide level of the Earth's carbon cycle, i.e., natural circulation of carbon among the atmosphere, oceans, soil, plans, and animals, determined mainly by the ability of natural sinks, like forests, to remove it from the atmosphere [Advancing the Science of Climate Change, NRC, 2010]. Measurements of CO_2 from the Mauna Loa observatory show that concentrations have increased from about 313 ppm in 1960 to over 400 ppm in 2015 [www.esrl.noaa.gov/gmd/ccgg/trends/, 2015]. An increase in global temperature has direct consequences such as rise of sea levels, change of the amount and pattern of precipitations, decrease of glaciers. Other likely effects include increases in the intensity of extreme weather events, species extinctions and changes in agricultural yields.

International Energy Agency statistics Fig.1.1 show that CO_2 emissions are closely related to overall energy production, which is still mostly dependent on combustion of oil, carbon and natural gas (Fig.1.2). These are mostly derived from pre-historic fossils and projections predict decreasing availability in the next decades [Lewis, 2006]. Thus, sustainable development is closely linked with the ability of mankind to seek increasing use of renewable energy sources and to enhance efficiency to minimize the environmental impact of increasing energy demand. Schematic maps of different energy sources and conversion technologies have been identified shortly after the Rio Summit [Korobitsyn, 1995], emphasizing prospects for renewable energy sources and technologies. Still, the world energy statistics did not change significantly towards the goal of carbon neutral energy, even in Europe (Fig.1.3).

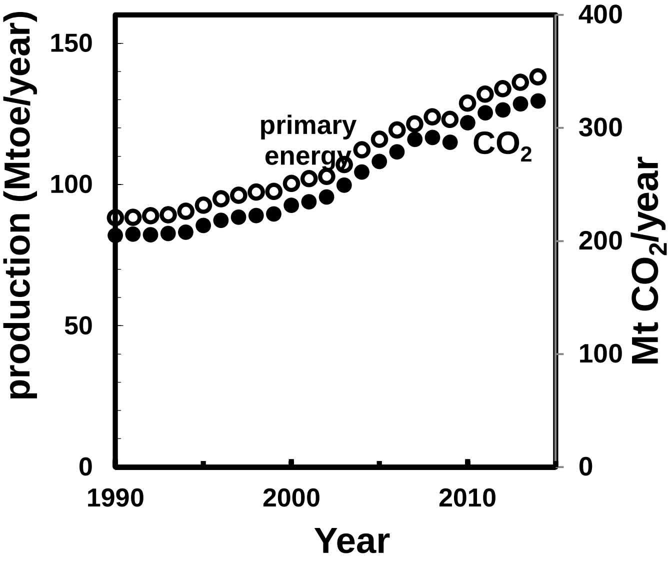

Fig.1.1 Evolution of world primary energy production (in million tone oil equivalent) and corresponding carbon dioxide emissions. Source: Statistics from International Energy Agency statistics (www.iea.org/statistics), edited by J.R. Frade and J. Macias.

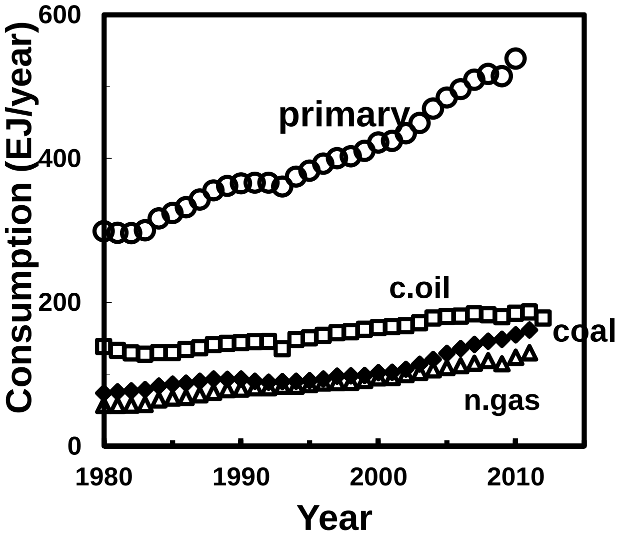

Fig.1.2. Evolution of total primary energy consumption and main contributions of crude oil, coal and natural gas. Source: Statistics from International Energy Agency statistics (www.iea.org/statistics), edited by J.R. Frade and J. Macias.

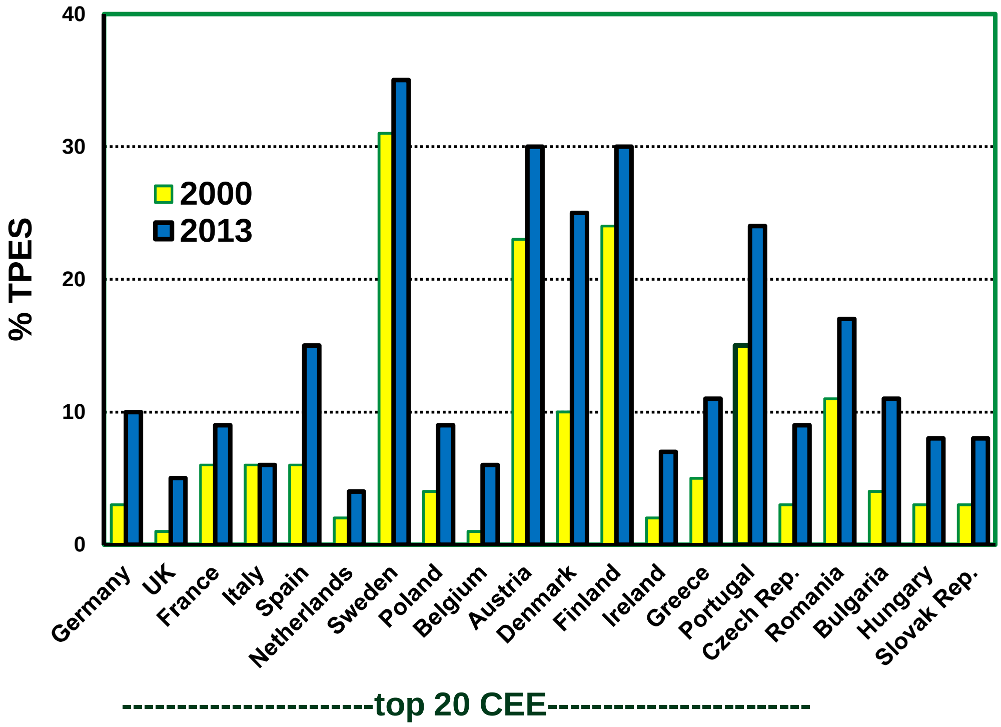

Fig.1.3 IEA statistics of % renewable energies in total primary energy supply in Europe in 2000 and 2013. Source: IEA statistics (http://energyatlas.iea.org), edited by J.R. Frade and J. Macias).

Several reasons may explain the limited contribution of renewable energies to total energy consumption; this includes the current status of energy consumptions of the industrial and mobility sectors, still mostly based on combustion of fossil fuels, and a variety of different limitations in classical renewable energy sources (e.g. hydroelectric), cost of some of the fastest growing technologies (e.g. wind mills for eolic generation) and/or insufficient efficiency (e.g. photovoltaic generation), ill-suited technologies to take full advantage of other renewable sources (biomass, biogas, geothermal,…), still mainly based on combustion, or a debatable advantage of other energy sources (e.g. biofuels from crops).

Additional difficulties in the slow progress towards carbon neutral societies are imposed by the variability and/or intermittency of renewable energies, and supply-demand gaps; this explains the current emphasis of technologies to enable energy storage and re-conversion, including reversible hydroelectric systems with up-hill pumping, reversible electrolyzer/fuel cell systems, rechargeable batteries, etc.

Thus, fossil fuels are very likely to remain the main contributions to total energy consumption in the next decades, and a major emphasis should be on conversion with enhanced efficiency and lower environmental impact (e.g. negligible NOx) combined with energy saving. Solid oxide fuel cells (SOFCs) have great potential for progress in this direction, as discussed below. In addition, SOFCs are best suited for conversion of renewable fuels such as biogas or syngas mixtures obtained by gasification of biomass, etc., when compared with other fuel cell types.

1.2 Fuel Cells

Fuel cells are amongst the most promising technologies for energy conversion and storage, with ability to attain very high efficiencies in co-generation (electricity, heat and possibly even chemicals), without Carnot efficiency limitations. A fuel cell is an electrochemical device that produces electricity by direct conversion of the chemical energy of a fuel. The electricity is generated through the reaction between the fuel (on the anode side) and air, pure O_2 or other suitable oxidant (on the cathode side), separated by an ion conducting electrolyte. Electrons between the anode and cathode flow through the external circuit producing electricity (DC) (Fig1.4 left). The function of the electrolyte is to conduct ions between the two electrodes. The reactants flow into the cell, and the reaction products flow out of it. Thus, fuel cells can operate virtually continuously as long as the necessary flows of fuel and oxidant are maintained; this is markedly different from conventional electrochemical cell batteries, which consume reactants in closed conditions, until these are exhausted, requiring subsequent recharging or disposal for recycling.

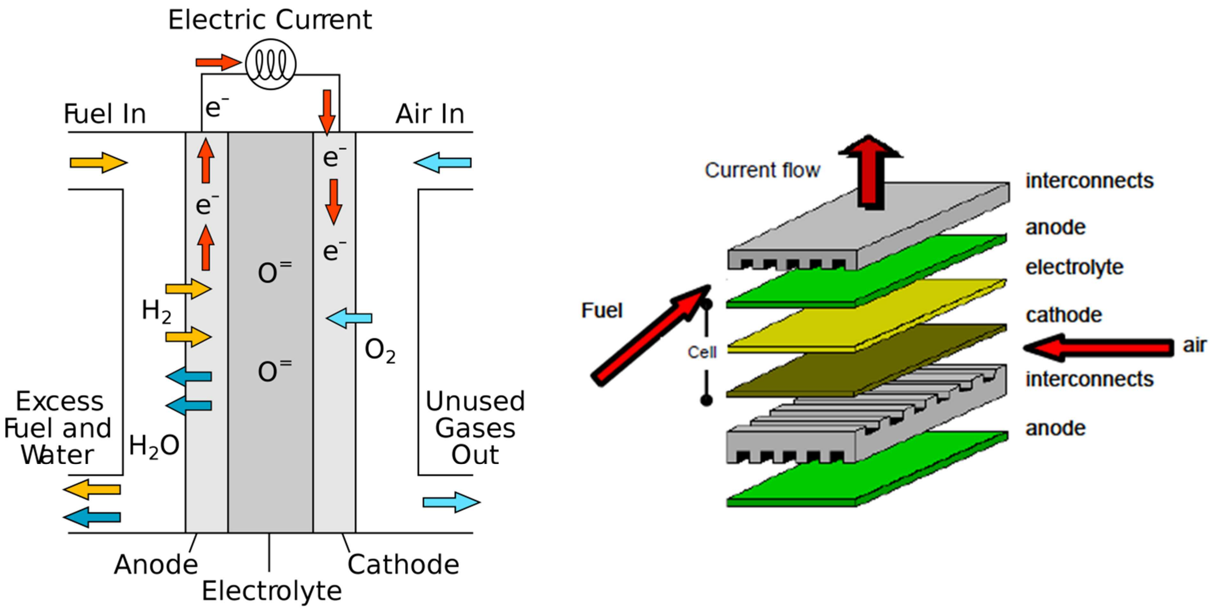
Electric Current
Fuel In
Air In
e⁻
e⁻
e⁻
e⁻
O⁼
O⁼
H₂
O₂
H₂O
Excess Fuel and Water
Unused Gases Out
Anode
Electrolyte
Cathode
Current flow
interconnects
anode
electrolyte
cathode
air
interconnects
anode
Fuel
Cell

Fig. 1.4 Principle of operation of a fuel cell (SOFC-type to be discussed below) **(left)**; and stack cell design **(right).** (Reproduced from Porras, 2010)

Most fuel cell products still rely on hydrogen as fuel and air, based on the ultimate goal of carbon-free energy generation. Still, much of the recent literature is now focused on different fuels, with emphasis on hydrocarbons and alcohols as fuels, though often requiring previous partial reforming to syngas. Proposals for electrochemical conversion of hydrocarbons are also based on the prospects for much higher efficiency and minimum emissions of greenhouse gases when compared to thermogeneration. The same applies to direct carbon fuel cells, which attracted significant interest in the last decade [Guer, 2013].

Other fuel cell concepts seek alternative vectors for energy storage and conversion, with emphasis on widely consumed synthetic chemicals such as ammonia [Alif, 2016]. Alternative oxidants such as chlorine and chlorine dioxide have also been proposed [Meibuhr, 2009]. Thus, expected advantages of fuel cells include:

- High efficiency in energy conversion.
- Carbon-free sub-products, such as water/steam when hydrogen is used as fuel, steam + N_2 for alternative ammonia-based fuel cells,
- Not noisy
- Fast response to variations of the energy demand
- Modular construction that facilitates changes in the energy demand.
- Location versatility, therefore, saving in energy losses by transport
- Flexibility in the type of fuel used: hydrogen, natural gas, methane, methanol ethanol, etc.
- Small production of pollutants (products of reaction are not pollutants in the case of hydrogen as a fuel).

A single unit cell usually generates less than 1 V in operating conditions. Thus, commercial applications require multi-cell stacks (Fig.1.4 right), with suitable interconnectors, to reach the required total voltage and power.

Fuel cells devices are composed of different parts with specific characteristics:

- Electrolyte: It is the fuel cell core, allowing ionic conduction between both electrodes, while preventing electronic short circuit, i.e., closing the electric circuit of the fuel cell, and also providing a physical barrier to separate the fuel and the oxidant.
- Electrodes: The reduction semi-reaction occurs at the cathode, consuming the electronic current generated at the anode and also generating anions (e.g. $O_2+4e^- \rightarrow 2O^{2-}$ in SOFCs) or consuming cations ($4H^++4e^- + O_2 \rightarrow 2H_2O$ in PEMFCs); this is coupled with the

oxidation semi-reaction, occurring at the anode ($2O^{2-}+2H_2 \rightarrow 2H_2O+4e^-$ in SOFCs or $2H_2O \rightarrow 4H^++4e^- + O_2$ in PEMFCs). Electrodes must be porous to minimize inhibition to gas phase transport and should maximize triple contacts (gas/electrode/electrolyte), as required for co-existence of the electroactive gas with electronic and ionic species. Enhanced electrochemical activity is also often promoted by mixed conduction.

- Interconnectors: It gives the connection in series between adjacent electrochemical cells, and works as a current collector.

1.2.1 Open cell voltage and fuel cell efficiency

The upper limit of the cell voltage occurs under open cell conditions (E^o), i.e., without current in the external circuit, and also assuming that internal leakage is negligible; this is related to the Gibbs free energy of overall reaction

$$E^o = -\Delta G/(nF), \qquad \text{Eq. 1.1}$$

n being the number of electrons transferred between the anodic and cathodic reactions and F the Faraday constant. For the simplest case of H_2-fueled solid oxide fuel cells the combination of cathodic reaction $O_2+4e^- \rightarrow 2O^{2-}$ and anodic reaction $2O^{2-}+2H_2 \rightarrow 2H_2O+4e^-$ yields the overall reaction $O_2+2H_2 \rightarrow 2H_2O$. Classical thermodynamics then yields the Gibbs free energy and the open cell voltage is readily obtained as $E^o=-\Delta G/(4F)$. Similar calculations are also shown in Fig.1.5, for other representative fuel cell concepts operating with different fuels.

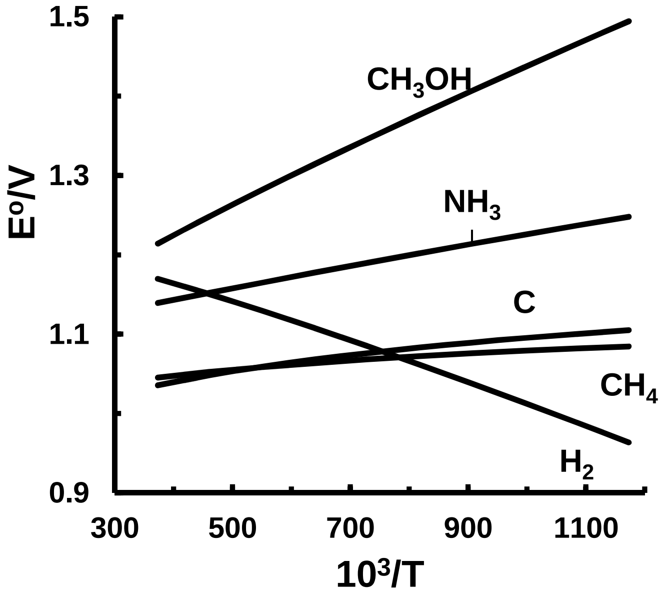

Fig.1.5 Thermodynamic calculations of open cell voltages for the main types of fuels proposed for conversion in fuel cells.

Though fuel cells are not limited by Carnot efficiency, the open cell voltage of H_2-fueled fuel cells decreases significantly with increasing temperature. This is imposed by the second law of thermodynamics [Castellano, 2012], due to negative entropy change, implying a relative decrease in open cell voltage given by the decrease in $\Delta G/\Delta H$ with increasing temperature.

Nevertheless, the main factors responsible for decrease in efficiency are related to ohmic losses due to insufficient conductivity and degradation of electrode performance by overpotential, mainly due to sluggish electroreduction of molecular oxygen, which becomes more serious with decreasing temperature, and exceeds largely the expected gain in $\Delta G/\Delta H$. Other negative effects on fuel cells tend to be more serious at higher temperatures, as found for microstructural ageing, mainly at Ni/YSZ cermet anodes, contamination by fuel impurities (sulfur), and reactivity or interdiffusion with other cell materials (e.g. contamination of cathodes by diffusion of chromium from interconnectors). Some of these degradation effects may also cause failure by cracking.

Most of these issues are even more serious if one considers fuel cell designs for alternative fuels such as natural gas, biogas, carbon, or NH_3, which impose much harsher conditions, completely reverting the gains in open cell voltage shown in Fig.1.5. In fact, these concepts are at much earlier stage of development, requiring much research and development to assess their real prospects.

1.2.2 Type of fuel cells: differences and advantages/disadvantages

Traditionally fuel cells have been classified depending mainly on the type of electrolyte and ionic carrier [Steele, 1993; Steele, 2001; Ormerod, 2003; Brandom, 2003], as shown schematically in Fig.1.6. Table 1.1 shows the main claimed advantages of these concepts. Still, those reports refer mainly to H_2-fuel cells, and failed to identify the main issues and challenges imposed by alternative fossil fuels or corresponding renewable biofuels.

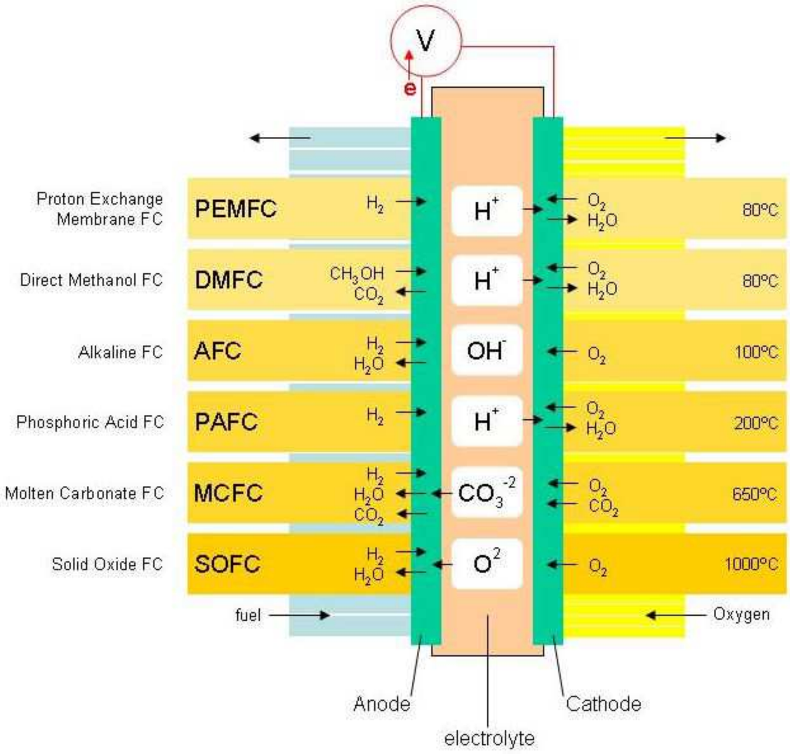
V
e
Proton Exchange Membrane FC
PEMFC
H_2
H^+
O_2
H_2O
80°C
Direct Methanol FC
DMFC
CH_3OH
CO_2
H^+
O_2
H_2O
80°C
Alkaline FC
AFC
H_2
H_2O
OH^-
O_2
100°C
Phosphoric Acid FC
PAFC
H_2
H^+
O_2
H_2O
200°C
Molten Carbonate FC
MCFC
H_2
H_2O
CO_2
CO_3^{-2}
O_2
CO_2
650°C
Solid Oxide FC
SOFC
H_2
H_2O
O^2
O_2
1000°C
fuel
Oxygen
Anode
electrolyte
Cathode

Fig. 1.6 Schematic representations of some of the main type of fuel cells with different ion conducting electrolytes [fuelcells.org, 2015]

Table 1.1
Main type of fuel cells

Type	Common Electrolyte	Operation temperature (K)	Electrical efficiency	Benefits	Disadvantages
Alkaline (AFC)	Aqueous alkaline solution of potassium hydroxide	363-373	60-70 %	Faster cathodic reaction in alkaline electrolyte. Increased efficiency	Affected by impurities
Solid oxide (SOFC)	Zirconium oxide doped with yttrium	873-1273	50-60%	Unexpensive electrocatalysts. Solid electrolyte	Corrosion because of high temperatures. Low lifetime
Polymeric membrane (PEMFC)	Wet solid polymer	333-373	40-60%	Solid electrolyte. Reduces corrosion. Fast start-up	Expensive catalysts. Affected by impurities using H_2 or other fuel

Phosphoric acid (PAFC)	Liquid phosphoric acid	448-473	36-42%	85% efficiency in heat and power cogeneration. It can use impure H_2	Pt catalyst. Low voltage and current. High weight and volume
Molten carbonates (MCFC)	Liquid lithium, sodium and potassium carbonates	873-1273	50-60%	Higher efficiency. Cheaper catalysts.	Corrosion at high temperatures. Low lifetime

Each fuel cell type has its own unique chemistry, and also different operating temperatures, catalysts, and electrolytes. Fuel cell operating characteristics determine its application – for example, lower temperature fuel cells are used to power passenger vehicles, while higher temperature fuel cells are used for stationary power generation.

Nowadays researchers continue to improve fuel cell technologies, examining different catalysts and electrolytes in order to improve performance and reduce costs. Other fuel cell types are also emerging at lab scale, such as microbial fuel cells.

1.3 Solid Oxide Fuel Cells

SOFCs are characterized by the use of a solid oxide electrolyte. The basic concept was proposed by Nernst et al. [Nernst, 1889; 1897; 1899] by the end of the nineteenth century. Still, considerable efforts are needed to advance in theory and experiment even more than 100 years later. The solid oxide electrolyte is a key ceramic component of SOFCs, acting as a conductor of oxide ions at temperatures in the range 873-1273 K. This ceramic electrolyte allows molecular oxygen to be reduced on the porous cathode surface by electrons, thus being converted into oxide ions, which are transported through the ceramic electrolyte, usually by a vacancy diffusion mechanism, towards the porous anode where oxide ions react with the fuel, giving electrons to an external circuit.

Due to their high operating temperatures, SOFCs do not require expensive catalysts and are less prone to degradation by carbon monoxide, when compared with other fuel cell types. However, vulnerability to carbon deposition and sulfur poisoning are still major limitations if one considers conversion of fossil fuels or renewable fuels such as biogas or biomass gasification products.

Nowadays, the standard SOFC materials are still yttria-stabilized zirconia electrolyte, cermet Ni-YSZ anode, and cathode based on lanthanum-strontium manganite (LSM). However, most up-to-date literature on SOFCs is dedicated to alternative materials (e.g.

mixed conducting cathodes) seeking operating conditions for longer durability (e.g. at intermediate temperatures) without undue effects on performance.

1.3.1 State of the art materials

1.3.1.1 Electrolyte

The electrolyte material must meet specific requirements such as:

- Ionic conductivity in the order of ≥ 0.1 S/cm, with wide electrolytic domain extending from oxidizing conditions to the very reducing conditions imposed by fuels.
- Chemical compatibility with other cell materials, allowing high temperature processing and long term exposition to working conditions, i.e. temperatures up to 1273 K and wide chemical gradients between air and fuels;
- Suitable thermochemical expansion to allow tolerance to thermal cycling and compatibility with other cell materials, on changing from high temperature firing to room temperature and to typical conditions of fuel cell operation;
- Sinterability to allow up to at least 97% density, without open porosity, to ensure gas tightness;
- Sufficient mechanical properties (tensile and bending strength, toughness), and ability to sustain significant strain without cracking.

Currently, most of the SOFC developers use yttria stabilized zirconia (YSZ). Alternative scandia-stabilized zirconia (ScSZ) have also been proposed [Yamamoto, 1995] to minimize the drop in ionic conductivity at intermediate temperatures (Fig.1.7). However, electrolytes manufactured with ScSZ also present higher costs and fast degradation [Mori, 2004; Muller, 2004]. Thus, up-to-date technologies rely mainly on lowering the electrolyte thickness to the range of 10-50 μm. Ceria-gadolinia- electrolytes also demonstrate high ionic conductivity at intermediate temperatures, but their applicability may be limited mainly due to partial reducibility of Ce^{+4} to Ce^{+3} in reducing atmospheres [Yahiro, 1989], causing onset of electronic conductivity with impact on open cell voltage and internal short circuiting, and also implying risks of excessive strain under air/fuel gradients [Atkinson, 1997]. Another alternative material proposed for intermediate-temperature solid oxide fuel cells (ITSOFC) is lanthanum gallate with simultaneous substitutions in A- and B-sites [Ishihara1994]. A comparison of the ionic conductivity of mentioned materials is illustrated in Fig 1.7. The applicability of other potential solid electrolytes [Kharton, 2004] is more debatable except possibly for $La_{10}Si_6O_{27}$-based apatite-type silicates [Yoshioka, 2014].

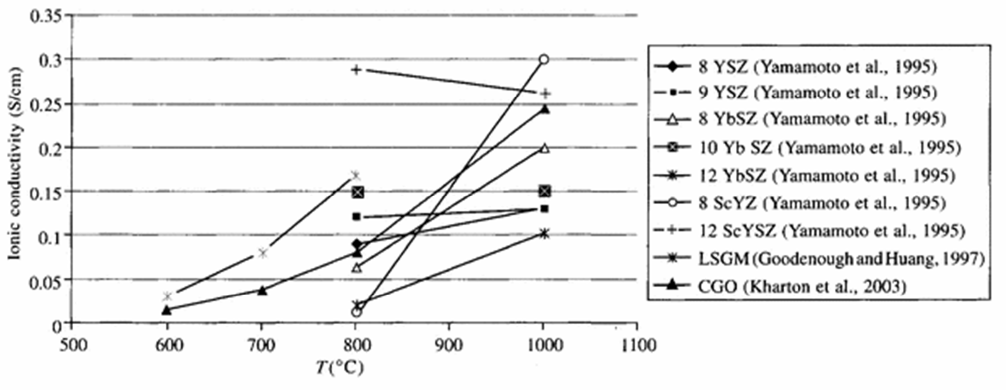

Fig 1.7 Ionic conductivity of candidate materials for SOFC electrolyte. (Data from Yamamoto et al. (1995) at 1073 K are measured after aging at 1273 K for 1000 h) [Recent trends in Fuel Cell Science and Technology, 2007)].

1.3.1.2 Interconnects

The materials for interconnects must satisfy a number of stringent requirements, while maintaining low cost (material and manufacturing). Lanthanum chromites with Sr-additions and oxidation-resistant alloys are commonly used, depending on operating temperatures. Chromites with a perovskite structure combine satisfactory conductivity, thermochemical compatibility with other cell materials, and excellent high temperature stability, as required for operating temperatures up to 1273 K [Sfeir, 2003; Liu, 2000; Mori, 1993]. There are, however, significant drawbacks and challenges ahead to improve the poor sinterability, to suppress chemical expansion under strongly reducing conditions, and to prevent undue contamination of other cell materials with chromium.

1.3.1.3 Sealant materials

Glass-ceramic [Lahl, 1999] and composite seals [Loehman, 2005] are most commonly proposed based on their ability to ensure sealing within acceptable leakage rates. Relevant characteristics include phase and dimensional stability, and low chemical reactivity with other cell materials. However, there are still limitations if one considers long-term operation due to slow corrosion effects, long-term devitrification or other phase changes, resulting in cracks under thermal cycles.

1.3.1.4 Electrodes.

Specific requirements for the anode and cathode may be found in relevant literature [Takeda, 1987; Minh, 1995; Atkinson 2004)]:

- Electrodes must be chemically and physically stable in operating conditions, i.e. reducing (anode) or oxidizing (cathode);
- Electrode materials should present sufficiently high electronic conductivity at working temperature (> 100 S cm^{-1}).
- Mixed electronic and ionic conductivity is also favorable for electrocatalytic activity;
- Electrodes must possess appropriate catalytic activity to facilitate electrooxidation of the fuel (anode) and electroreduction of the oxidant (cathode).
- Electrode materials should be chemically compatible with the electrolyte, to allow firing and long-term operation in fuel cell conditions.
- Their thermochemical expansion must be compatible with other cell components, allowing for changes from firing conditions to room temperature and to operating conditions, without differential strain and risks of fracture.
- Electrodes should be processed as highly porous layers to allow gas phase transport to and from electrochemically active sites, and should possess high specific area to maximize these sites.
- The anode layers must possess phase and microstructural stability under fuel cell operation.
- Anode materials intended for a specific fuel should be tolerable to certain levels of pollutants present in the fuel.

1.3.1.4.1 Cathodes

There is an enormous variety of cathode materials, especially with perovskite structure. However, lanthanum strontium manganite, $La_{1-x}Sr_xMnO_{3-\delta}$ (LSM) is most commonly used as cathodes for YSZ-based SOFCs, and lanthanum strontium cobalt ferrite, $La_{1-x}Sr_xFe_{1-y}Co_yO_{3-\delta}$ (LSCF) is mainly used in combination with CGO. LSM shows high thermal stability and compatibility with YSZ electrolyte [Kuo, 1990; Yokokawa, 1990] at SOFC operating conditions, and has an excellent microstructural stability, which explains its long-term performance stability [Wang, 2004; Jiang, 2005A; Jorgensen, 2000]. The electrocatalytic activity of LSM can also be substantially enhanced by infiltration with nanostructured catalysts [Jiang, 2005B/2005C]. Other relevant cathode materials with perovskite structure are $La_{0.7}Sr_{0.3}FeO_{3-\delta}$ (LSF) [Huang,1998], $Ba_{0.5}Sr_{0.5}Co_{0.8}Fe_{0.2}O_{3-\delta}$ (BSCF) [Shao,2004], and RP-type Ln_2NiO_4-based cathodes [Sun, 2008; Laguna-Bercero, 2014]. Less common perovskites (e.g. $SrMn_{0.6}Nb_{0.4}O_{3-\delta}$), and RP materials (e.g. $LaSr_2Mn_{1.6}Ni_{0.4}O_{7-d}$, $La_4Ni_{3-x}Cu_xO_{10-\delta}$, etc.) were proposed for apatite-type electrolytes [Yaremchenko, 2009]

1.4 Anodes for Solid Oxide Fuel Cells

1.4.1 Ni-based cermets: advantages and problems

Ni-based cermets have been chosen as SOFC anode materials [Spacil, 1970] because of the relatively low cost of Ni, good chemical stability, and excellent catalytic activity toward hydrogen oxidation. Their performance may even be enhanced by alloying, as reported for (Ni,M)/YSZ with M=Co,Fe,…[Ringuedé, 2002]. In a porous Ni-YSZ cermet anode, the Ni metal phase provides the required electronic conductivity and catalytic activity, whereas the YSZ ceramic phase lowers the coefficient of thermal expansion for the anode to match that of the electrolyte, prevents the Ni phase from coarsening, and offers a conduction path for oxide ions and thus may extend the active zones for anode reactions [Steele, 2000; Kuharuangrong, 2007]. However, pure nickel suffers from considerable mismatch in thermal expansion with YSZ, leading to poor binding to the electrolyte and significant coarsening, even when dispersed in Ni-YSZ cermets.

Ni is also an efficient catalyst for reforming of hydrocarbon fuels. However, nickel also catalyzes formation of carbon deposits when hydrocarbons are used as fuels, causing irreversible damage and degradation of anode performances [Matsuzaki, 2000; Chen, 2011; Muhammad, 2015; Tatsuya, 2002]. Furthermore, it has been reported [Dees, 1999; Aguilar, 2004] that Ni-YSZ composites are very sensitive to the sulfur poisoning even at very low concentrations, causing drastic degradation of anode performance. H_2S reacts with O_2 to release H_2O and S. This S then settles down on the active sites and at the SOFC operating temperatures; Ni_3S_2 may form by the reaction between Ni and S [Mingyang, 2007].

1.4.1.1 Behavior in hydrocarbons-based fuels

The convenience of using fossil fuels such as natural gas, kerosene or diesel reformate without additional purification may be critical for the commercialization of fuel cells [Sasaki, 2001; Mogensen, 2011]. Therefore, development of a viable technology requires alternative non-metallic anode materials with ability to prevent onset of carbon by hydrocarbon cracking, and highly tolerant to contaminants such as sulfur. Contaminants are present in fossil fuels or may even be deliberately added as odorant for safety reasons. For example, typical sulfur contents in natural gas are kept at a typical level of about 50 ppm. Sulphur contents in low grade fuels (e.g. biogas) are even much higher, often exceeding 1000 ppm.

Design of alternative anode materials for hydrocarbon-fueled SOFCs requires proper understanding of redox conditions imposed under fuel conversion, with clear identification of ranges which are most likely to induce carbon deposition. This analysis should also be extended to redox conditions which may yield oxidation of sulfur or its most common related compound (H_2S).

1.4.1.1.1 Carbon deposition

Though SOFCs with Ni-YSZ anode may yield power densities up to 1 W/cm^2 at 1073 K [Liu, 2003], their long-term stability is limited by different degradation mechanisms, including microstructural ageing, risks associated with redox cycling and, most commonly by carbon deposition. Many studies in the literature have been reported on carbon formation and deactivation of supported Ni steam reforming catalyst [Abudula, 1996; Liu, 2011; Zhang, 1994]. Carbon can be formed through the thermal cracking of hydrocarbons such as CH_4 (eq. (1.2)) or by the decomposition of CO (eq. (1.3)):

$$CH_4 \rightarrow C_S + 2H_2 \qquad \text{Eq. 1.2}$$

$$2CO \rightarrow C_S + 2CO_2 \qquad \text{Eq. 1.3}$$

Carbon deposition results in catalyst deactivation by covering the active sites which ultimately results in performance degradation; this is a complex process, and there are many factors that influence the likelihood of carbon formation. The nature of catalyst is very important as well, as found on comparing nickel with ruthenium [Sauvet, 2001; Caillot, 2007; Bebelis, 2006] or copper [Park, 2000; Gorte, 2002]. In addition, the mechanisms and morphology of carbon formation on Ni-YSZ cermets may involve dissolution-precipitation [Holstein, 1995] in which C atoms dissolve into the Ni grains, diffuse through them and then deposit at their outer surface. Dissolution of carbon in the Ni grains may also result in significant morphologic changes, causing cracks in the cells [He, 2007], eventually even leading to “metal dusting” in which Ni disintegrates to dust [Shri, 2014].

Thus, some strategies were developed to suppress the degradation rate (e.g. by adding 5-10 mol% TiO_2 to YSZ) [Skarmoutsos, 2000]. Another possible alternative is the use of Ni- and Cu-ceria fuel electrodes [Kim, 2002], or Gd-and Sm-doped ceria anodes where only minor coke precipitation was detected after operation in methane and steam [Yamamoto, 2000]. The Cu-Ni alloy has been proposed, combining the ability to hinder coke formation, promoted by copper, with the electrocatalytic activity of nickel and its higher melting point.

1.4.1.1.2 Sulfur poisoning

Another challenge for the commercialization of SOFCs is to use commercially available fossil fuels, natural gas being the most obvious choice of fossil fuel for SOFCs. It is widely available in relatively high grade quality (i.e. lower contents of contaminant), at least on comparing with alternative fossil fuels or biogas, with best prospects to meet conditions for sulfur tolerance or feasibility of purification [Samokhvalov,2011]. The mechanisms of methane conversion by reforming and partial or complete oxidation have also been widely studied in detail.

Different sulfur compounds are known to interact with the Ni-YSZ anode in such a manner that polarization losses become dominant because they block the fuel supply to the active sites or by blocking the migration of O^{2-} ions towards the TPBs [Li, 2010], thus increasing polarization resistance and causing irreversible degradation [Li, 2010; Kromp, 2012]. Several studies [Dees, 1999; Aguilar, 2004] have shown that even few ppm of H_2S can be detrimental to the Ni-YSZ anodes. The proposed mechanisms of degradation of Ni-YSZ anode by physical adsorption, sulfidation or chemisorption have been described. The mechanism involved in the sulfur poisoning of Ni-YSZ anode have been summarized by Sasaki et al [Sazaki, 2011], as depicted Fig 1.8, and described by the following reactions:

$$H_2S_{(g)} \leftrightarrow HS_{ads} + H_{(g/ads)} \leftrightarrow S_{ads} + H_{2(g/ads)} \qquad \text{Eq. 1.4}$$

$$2Ni + xH_2S \leftrightarrow xH_2 + Ni_2S_x \qquad \text{Eq. 1.5}$$

$$Ni + H_2S \leftrightarrow H_2 + NiS \qquad \text{Eq. 1.6}$$

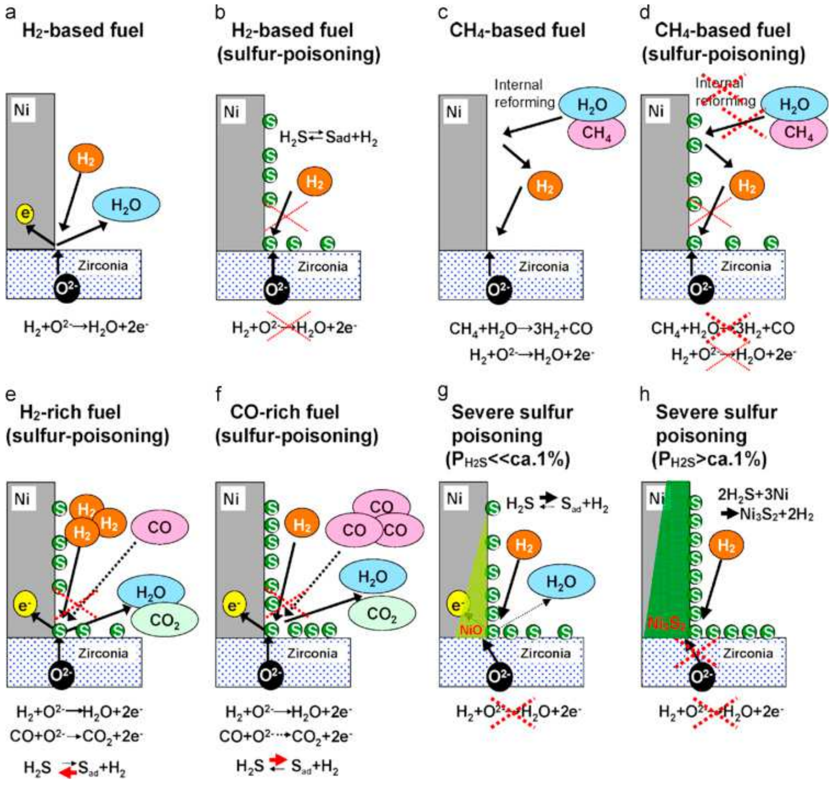
a
H2-based fuel
b
H2-based fuel
(sulfur-poisoning)
c
CH4-based fuel
d
CH4-based fuel
(sulfur-poisoning)
Ni
Zirconia
O2-
e
H2
H2O
H2S⇄Sad+H2
Internal
reforming
CH4
H2+O2-→H2O+2e-
CH4+H2O→3H2+CO
e
H2-rich fuel
(sulfur-poisoning)
f
CO-rich fuel
(sulfur-poisoning)
g
Severe sulfur
poisoning
(PH2S<<ca.1%)
h
Severe sulfur
poisoning
(PH2S>ca.1%)
CO
CO2
NiO
Ni3S2
2H2S+3Ni
→Ni3S2+2H2
CO+O2-→CO2+2e-
H2S⇄Sad+H2

Fig 1.8 Sulfur poisoning mechanism of an SOFC anode [Sazaki, 2011]

SO_2 is less adverse for Ni-YSZ anodes as compared to S, therefore, efforts have always been made to promote the oxidation of H_2S directly into SO_2 by the use of different techniques or by the applications of different materials.

1.4.2 Ceramic anodes

The limitations of Ni-YSZ and other cermet anodes have led to the development of oxide anode materials. Oxide anode materials are desirable to be mixed ionic and electronic conductors (MIECs) with high electronic conductivity and significant ionic conductivity. Then, the electrochemical oxidation is not confined to TBPs and extends to the whole oxide anode surfaces. Steele et al. [Steele, 1993] proposed several empirical criteria of oxide anodes for complete methane oxidation:

i) Good electronic conductivity at anode operating potentials. Probably n-type behavior preferable.

ii) Predominant anion lattice disorder to enhance oxygen diffusion coefficients

iii) High values for oxygen surface exchange kinetics

iv) Fabrication of porous adherent films with minimal processing problems

v) Compatibility with solid electrolyte.

Typical redox couples in SOFC anode materials are $Cr^{+3/+4}$, $Ti^{+3/+4}$, $Mn^{+3/+4}$, $Ce^{+3/+4}$, $Mo^{+5/+6}$, $V^{+3/+4}$, $Nb^{+3/+4}$, etc. The n-type conductivity is favorable because it is more likely to be retained under the reducing conditions imposed by fuels. Tested materials often possess the perovskite or fluorite structures, and less frequently pyrochlores, tungsten bronzes, etc. (Figure 1.9 and Table 1.2).

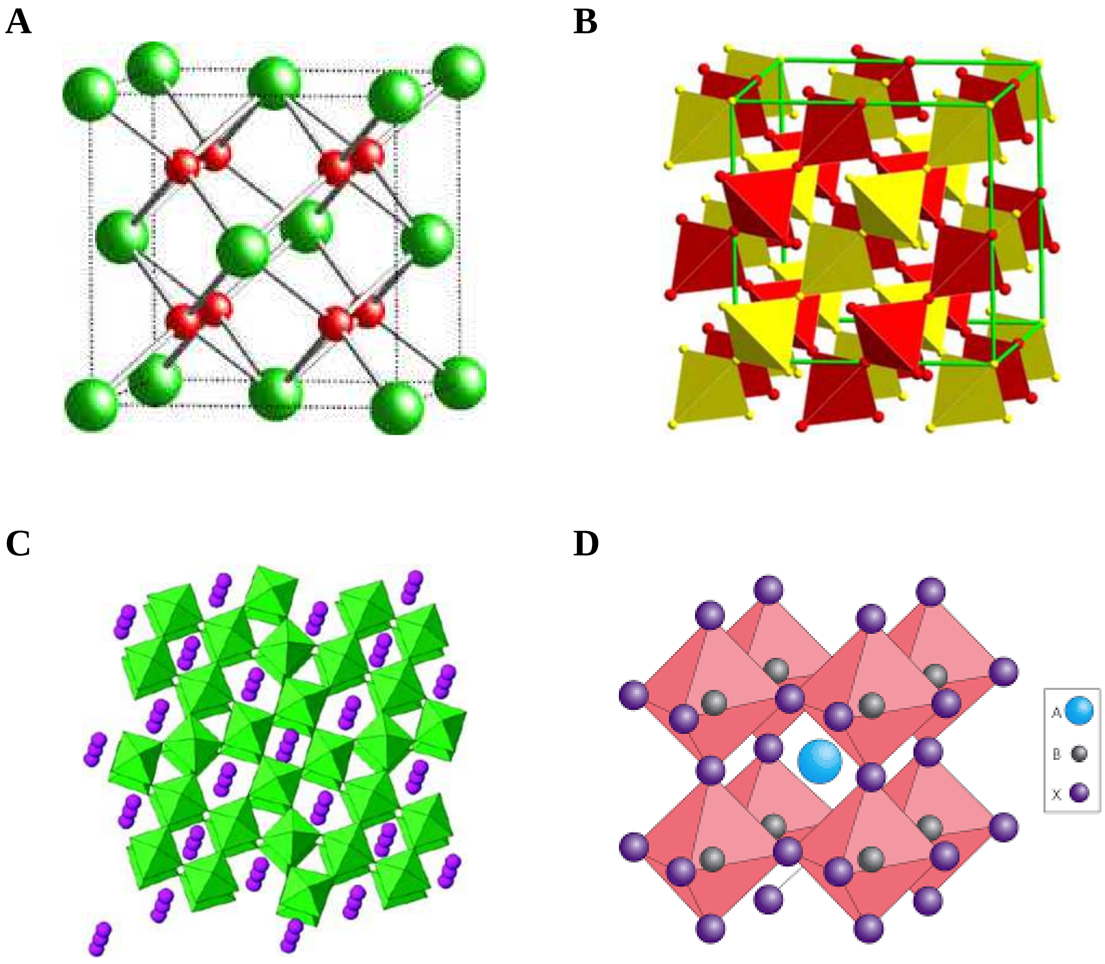

E

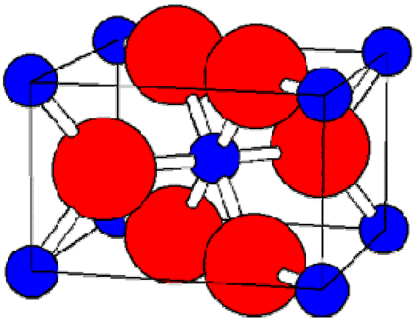

Fig 1.9. Type-structures for different promising SOFCs anodes: **(A)** Fluorite, **(B)** tungsten bronze, **(C)** pyrochlore, **(D)** perovskite and **(E)** rutile. [Reproduced from Sun, 2007]

1.4.2.1 Rutile-type structure

The rutile structure (TiO_2) and its impact on transport properties were described in detail in reference [Fergus, 2006]. It comprises a distorted hexagonal close packed anion arraying, and octahedral vacancy sites occupied by cations. Edge-sharing octahedra should facilitate electron transfer and electronic conductivity (Table 1.2), and oxygen vacancies might also be introduced into the rutile lattice. However, the mobility of vacancies in the rutile structure is much lower than in fluorite or perovskite structures; this has been ascribed to the required rotation of oxygen ion octahedra. Attempts to design rutile materials with enhanced properties were based on TiO_2-Nb_2O_5 solid solutions, reaching electronic conductivity up to ~10^2 S/cm at 1273 K. The incorporation of Cr_2O_3 into TiO_2-NbO_2 enhances redox stability but affects conductivity [Lashtabeg, 2009]. These materials also perform poorly as anodes materials for both in H_2 and CH_4 (Table 1.2).

1.4.2.2 Fluorite-type structure

Many SOFC developers tested doped ceria as anode materials for lower operating temperature. CeO_2 with trivalent lanthanides exhibit mixed ionic and electronic conductivity in a reducing atmosphere due to reduction of Ce^{+4} to Ce^{+3}, and this redox transition contributed to the excellent catalytic activity stemmed from the oxygen-vacancy formation and migration associated with reversible CeO_2-Ce_2O_3 transition [Sun,2008; Skorodumova, 2010]. The electronic conduction in ceria-based materials arises from the reduction of Ce^{+4} to Ce^{+3} and release of electrons at low oxygen partial pressure. Therefore, doped or undoped ceria is a MIEC at low pO_2 and high temperatures. Ceria-based anodes exhibit resistance to carbon deposition which permits the use of hydrocarbons as a fuel [Marina, 2002.].

Some authors also attempted to enhance the performance of Ni-YSZ cermets by inducing mixed conductivity. Since Zr^{+4} cannot be reduced to Zr^{+3} in contact with fuels, this approach was based on addition of transition metal oxides, such as TiO_2, MnO_x, Tb_4O_7, Nb_2O_5, and WO_3 [Huang ,1996]. However, the level of electronic conductivity remained low even under reducing atmosphere and its impact on SOFC anodes was inconclusive.

1.4.2.3 Pyrochlore-type structure

$A_2B_2O_7$ pyrochlores with A^{III}/B^{IV} and A^{II}/B^{V} cations also display versatile properties [Deng, 2008; Subramanian, 1983]. Their crystal structure can accommodate changes in oxygen stoichiometry and flexible cation combinations on both A and B sites, also allowing changes in structural stability and electrical properties to meet the requirements of SOFC anodes. Pyrochlores of generic compositions $Ln_{0.9}Ca_{0.1})_2Ti_2O_7$ (Ln= Gd, Y and Yb) are reported to exhibit good oxide ion conductivity at high temperatures [Kramer, 1995]. Under reducing conditions, $Gd_2(Ti_{1-x}Mo_x)_2O_7$ ($0.1< x < 0.7$) with Mo in +IV state exhibits high electronic conductivity (> 10 S/Cm), however, narrow stability range is observed in low partial pressures of oxygen at 1273 K [Porat, 1997]. This pyrochlore solid solution is only stable in a certain range of oxygen partial pressure and temperature. Mixed ionic-electronic conductivity may also be obtained for $Pr_2Zr_2O_{7-\delta}$ based materials with partial substitution of Mn and Ce in Zr sites. Unfortunately, most pyrochlore materials are either redox unstable or poorly conducting, and it seems difficult to find suitable mixed conducting anodes with this structure type.

1.4.2.4 Tungsten bronzes

Oxides with formula $A_2BM_5O_{15}$ (M = Nb, Ta, Mo, W and A or B = Ba, Na, etc.) show tetragonal tungsten bronze (TTB) or orthorhombic tungsten bronze (OTB) structure [Tournoux, 1992], described as a framework of MO_6 octahedra sharing summits, delimiting tunnels of pentagonal, square and triangular sections. The tetragonal tungsten bronze structure can be obtained from the perovskite by rotation of some of the MO_6 octahedra (Fig.1.10), and connection of short M-O bonds supplies a percolation path for charge transfer, which leads to high electronical conductivity.

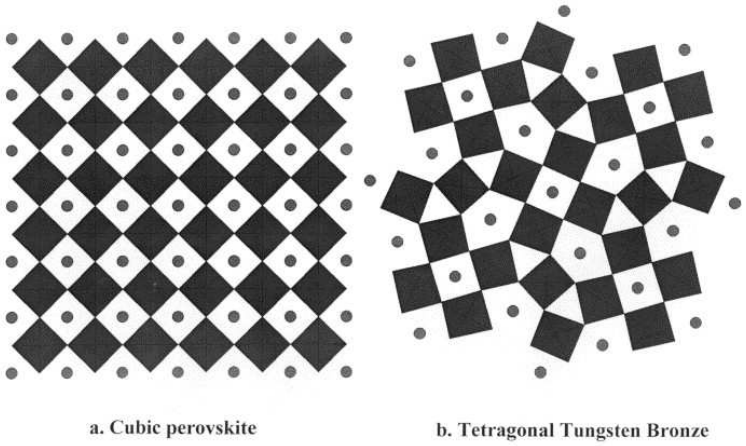

Fig. 1.10. The structure of **(A)** the perovskite $SrTiO_3$ and **(B)** the tungsten bronze $Sr_{0.6}Ti_{0.2}Nb_{0.8}O_3$ viewed down the [001] axis. [Slater, 1999]

Slater et al. [Slater, 1999] assessed the applicability of compositions $(Ba/Sr/Ca/La)_{0.6}M_xNb_{1-x}O_{3-\delta}$ (M = Mg, Ni, Mn, Cr, Fe, In, Ti, Sn) as anode materials for solid oxide fuel cells. However, these compounds showed poor oxygen exchange kinetics, possibly due to low oxide-ion conductivity or partial decomposition on long-term heat treatment at high temperature in reduction atmosphere. Still, other compositions such as $Ba_{0.6-x}A_xTi_{0.2}Nb_{0.8}O_3$ (A = Sr, Ca) may be processed in air and are stable also in reducing conditions, as required for potential anodes for SOFCs with ability to re-generate their transport properties by reduction in contact with the fuel. Kaiser et al. [Kaiser, 2000] also studied similar materials with this structure-type, finding relatively good properties for $Sr_{0.2}Ba_{0.4}Ti_{0.2}Nb_{0.8}O_3$ with electronic conductivity of about 10 S cm^{-1} at $p(O_2) \approx 10^{-20}$ atm at 1203 K.

1.4.2.5 Perovskite - type structure

The perovskite-type structure is also very flexible for changes in composition and high ability to accommodate oxygen vacancies, with impact on mixed transport properties, mainly with multivalent transition metal additives. This has been mainly demonstrated for oxidizing and inert conditions, as found mainly for ferrites and cobaltites. However, these are ill-suited for anodes materials because they undergo decomposition under reducing conditions. Still, some authors claimed similar prospects of mixed conducting perovskite also for reducing conditions in contact with fuels [Boukamp, 2003]. The best prospects for applicability as anode materials are for titanate or chromite perovskites, and mixed compositions with different combinations of Ti, Cr and Mn.

1.4.2.5.1 Chromites

(La,Sr)CrO_3 materials possess excellent stability and their thermal expansion coefficient can be adjusted as a function of Sr content to match the TEC of YSZ. However their poor sinterability complicates processing. In addition, the electrical conductivity was only about 20 S/cm in air, and decreased when exposed to reducing environments [Simner, 2000].

1.4.2.5.2 Titanates

$SrTiO_3$ is also very stable in wide ranges of redox conditions, and its thermal expansion is compatible with YSZ. This material may be tailored as a good n-type conductor under strongly reducing conditions, on adding a trivalent lanthanide (La^{3+}, Pr^{3+},…,Y^{3+}) as donor in A-site position or a pentavalent additive (Nb^{5+}, Ta^{5+}) in B position and firing at sufficiently high temperatures in reducing atmosphere. In fact, the conductivity is strongly dependent on the ability to sinter at very high temperatures under strongly reducing conditions, probably because reducibility involves defective structures and requires very sluggish cation rearrangements. For example, the electrical conductivity of $La_xSr_{1-x}TiO_3$ remains in the order of 10 S/cm under typical anode conditions if the initial sintering was performed in air, and only rises to about 100 S/cm after sintering in H_2 atmospheres at high temperature (>1773 K) [Marina, 2002]. The point defect chemistry is also complex, possibly involving partially frozen-in defects quenched on cooling from sintering conditions, and additional re-equilibration on changing the redox conditions at operating temperatures (<1273 K). $Sr_{1-1.5x}Y_xTiO_{3-\delta}$ compositions were also studied to minimize interdiffusion with YSZ, and the conductivity reached an optimum of 64 S/cm at 1073 K for $x = 0.08$ [Hui, 2002A]. However, the power density did not exceed 0.05 W/cm^2 in wet H_2 for a cell with this optimized $Sr_{0.88}Y_{0.08}TiO_{3-\delta}$ composition [Hui, 2002B].

1.4.2.5.3 Mixed perovskite compositions

The conductivity of mixed $La_{1-x}Sr_xCr_{1-y}Ti_yO_{3\pm\delta}$ (LSCT) was found orders of magnitude lower than 0.1 S/cm, i.e., much below the requirements of mixed conducting SOFC electrode materials. The polarization resistance (R_p) of LSCT, with Ti content in the range from 20% to 50% was also excessively high, even when the fuel was H_2 (>40 Ω cm^2 at 1123 K) [Pudmich, 2000]. $La_{1-x}Sr_xCr_{1-y}Mn_yO_{3\pm\delta}$ (LSCM) electrodes showed better electrochemical reaction kinetics, mainly for up to 50%Mn, possibly involving the $Mn^{+3/+4}$ redox couple. In this case, the electrode polarization dropped to 0.8 Ω cm^2 at 1173 K in wet CH_4 [Tao, 2003]. Furthermore, the electrode performance of LSCM can be improved via electrode engineering achieved by impregnation methods [Jian, 2006a; Jian, 2006b; Lu, 2007]. One of the main drawbacks of LSCM electrodes is their limited electronic conductivity, which remained below 30 S/cm in reducing environment [Jiang, 2008]. Thus, current collection may be a critical issue for fuel cells with LSCM anode.

1.4.2.6 Double perovskite-type structure

Double perovskite contain ordering of different B-site cations. The degree of cation ordering determines oxygen self-diffusion in double perovskites such as $GdBaCo_2O_{5+\delta}$ [Parfitt, 2011]. $Sr_2Mn_{0.8}Nb_{1.2}O_{6-\delta}$ had a total conductivity of 0.36 S/cm and exhibited p-type behavior in low pO_2 [Tao,2002]. Replacing Mn and Nb with Mg and Mo, $Sr_2Mg_{1-x}Mo_xO_{6-d}$ (SMMO) seemed to be a good material for hydrocarbon utilization with modest sulfur tolerance. The conductivity of SMMO reached 10 S/cm at 1073 K in H_2 and CH_4, and the system gave satisfactory anode performance in the same conditions, even allowing to be used under natural gas as a fuel, with negligible performance degradation up to 50 power cycles [Huang, 2006].

Table 1.2

Conductivity and electrochemical properties of selected conducting oxides as SOFC anodes (Table modified from Jiang, 2004). Temperature (K) is indicated in parentheses.

Composition	Electrical conductivity (S/cm)		Polarization resistance (Ω cm^2)		Reference
	reduced[a]	oxidized[b]	in hydrogen[c]	in methane[c]	
Rutiles					
NbO_2	~200 (1273)	-	-	-	(Reich, 2001)
$Nb_{1-x}Ti_xO_2$ (0<x<1)	~ 20 - 10^3 (1169)	-	>500 (1035)	> 1000 (1085)	
$Ti_{1-2x}Cr_xNb_xO_2$ (0<x<0.5)	>20 (1173)	(1.5-1.7) × 10^{-2} (1173)			(Lashtabeg, 2009)
$Ti_{0.93}Nb_{0.07}O_2$	>50 (673-1273)				(Michibata, 2011)
Fluorites					
$Ce_{0.9}Gd_{0.1}O_{2-\delta}$	0.70 (1073)	0.02-0.05 (1073)	-	-	(Reich, 2001)
$Ce_{0.8}Gd_{0.2}O_{2-\delta}$	0.60 (1073)	-	-	-	
$Ce_{0.6}Gd_{0.4}O_{1.8}$	-	-	0.39 (1273)	-	(Lashtabeg, 2009)
$Ce_{0.8}Sm_{0.2}O_{1.9}$	~0.125 (1073)	~0.05 (1073)	-	-	(Michibata, 2011)
CeO_2	-	1.31 x 10^{-6} (773)	-	-	
$Y_{0.20}Ti_{0.18}Zr_{0.62}O_{1.90}$	-	-	16.8 (932)	-	(Kelaidopoulou, 2001a)
	-	-	-	170 (932)	(Kelaidopoulou, 2001b)

Pyrochlores					
$Gd_2(Ti_{0.5}Mo_{0.5})_2O_7$	11 (1173)	0.02-0.05 (1073)	-	-	(Porat, 1997b)
$Gd_2(Ti_{0.3}Mo_{0.7})_2O_7$	~0.015 (1073)	~0.020 (1073)	-	-	(Porat, 1997a)
$Gd_2(Ti_{0.90}Mo_{0.1})_2O_7$	~0.06 (1173)	~0.03 (1173)	-	-	
$Gd_2Ti_{1.4}Mo_{0.6}O_7$	-	-	0.2 (1223)^d	-	(Zha, 2005)
$Pr_2Ce_{0.4}Zr_{1.6}O_{7\pm\delta}$	0.01 (1273)	3×10^{-4} (1273)	-	-	(Holtappels, 2000)
$Pr_2Zr_2O_{7\pm\delta}$	2×10^{-3} (1273)	6×10^{-5} (1273)	-	-	
Tungsten bronzes					
$Sr_{0.6}Ti_{0.2}Nb_{0.8}O_3$	2.5 (1203)	3×10^{-4} (1203)	-	-	(Slater, 1999a)
$Sr_{0.4}Ba_{0.2}Ti_{0.2}Nb_{0.8}O_3$	2.5 (1203)	2×10^{-4} (1203)	-	-	
$Sr_{0.2}Ba_{0.4}Ti_{0.2}Nb_{0.8}O_3$	3.2 (1203)	2×10^{-4} (1203)	-	-	
$Ba_{0.4}Ca_{0.2}Ti_{0.2}Nb_{0.8}O_3$	3.1 (1203)	2×10^{-4} (1203)	-	-	
$Ba_{0.6}Ti_{0.2}Nb_{0.8}O_3$	3.2 (1203)	1×10^{-4} (1203)	-	-	
$Ba_{0.6}Mn_{0.067}Nb_{0.933}O_3$	2.2 (1203)	4×10^{-4} (1203)	-	-	(Slater, 1999b)
$Ba_{0.6}Ni_{0.067}Nb_{0.933}O_3$	4.5 (1203)	5×10^{-4} (1203)	-	-	
$Ba_{0.6}Mg_{0.067}Nb_{0.933}O_3$	1.3 (1203)	8×10^{-5} (1203)	-	-	
$Ba_{0.6}Fe_{0.1}Nb_{0.9}O_3$	3.8 (1203)	1×10^{-2} (1203)	-	-	
$(Sr_{1-x}Ba_x)_{0.6}$ $Ti_{0.2}Nb_{0.8}O_{3-\delta}$	0.01-1 (1203)	~10^{-5} (1203)	~28 (1203)	-	(Kaiser, 2000)
Single-phase perovskite					
Chromites					
$La_{0.7}Ca_{0.32}CrO_{3-\delta}$	-	-	86 (1123)	-	(Primdahl,2001)
$La_{0.7}Mg_{0.3}CrO_{3-\delta}$	0.17 (1073)	3.35 (1073)	-	-	(Jiang, 2008)
$La_{0.75}Sr_{0.25}CrO_{3-\delta}$	7.07 (1073)	59.1 (1073)	-	-	
$La_{0.7}Ca_{0.3}CrO_{3-\delta}$	1.6 (1073)	50.1 (1073)	-	-	
$La_{0.7}Ba_{0.3}CrO_{3-\delta}$	-	2.69 (1073)	-	-	
$La_{0.8}Sr_{0.2}Cr_{0.97}V_{0.03}O_3$	-	-	-	28 (1123)	(Vernoux, 2000)
$La_{0.7}Sr_{0.3}Cr_{0.5}Ti_{0.5}O_{3-\delta}$	0.02 (1073)	-	-	-	(Pudmich,2000)
$La_{0.8}Sr_{0.2}Cr_{0.8}$ $Mn_{0.2}O_{3-\delta}$	-	-	51 (1123)	-	(Vernoux, 2001)
$La_{0.8}Sr_{0.2}Cr_{0.5}$ $Mn_{0.5}O_{3-\delta}$	1.3 (1173)	38 (1173)	0.26 (1173)	0.85 (1173)	(Tao, 2003)
$(La_{0.8}Sr_{0.2})_{0.9}Cr_{0.5}$ $Mn_{0.5}O_{3-\delta}$	-	-	0.18 (1173)	-	(Tao, 2005)
Titanates					
$La_{0.7}Ca_{0.3}TiO_3$	2.7 (1173)^d	-	-	-	(Pudmich,2000)
$La_{0.7}Ca_{0.3}Cr_{0.5}Ti_{0.5}O_3$	0.3 (1173)	-	-	-	
$La_{0.6}Sr_{0.4}TiO_3$	96 (1153)	-	-	-	(Neagu, 2010)
$La_{0.1}Sr_{0.9}TiO_3$	3 (1273)	1 (1273)	-	-	(Marina, 2002)
$SrTi_{0.97}Nb_{0.03}TiO_3$	-	-	700 (1073)	-	(Yashiro, 2001)
$SrTi_{1-x}Nb_xO_3$	9-28 (1073)	-	-	-	(Karczewsky,

$(0.01<x<0.08)$					2010)
$Sr_{0.895}Y_{0.07}TiO_3$	7-64 (1073)	-	-	-	(Vozdecky,2011)
$La_2Sr_4Ti_6O_{19-\delta}$	30 (1173)	8×10^{-4} (1173	2.97 (1173)	8.93 (1173)	(Canales-Vazquez, 2003)
$La_4Sr_8Ti_{11}$ $Mn_{0.5}Ga_{0.5}O_{38-\delta}$	0.5 (1173)	10^{-3} (1173)	0.2 (1173)	0.57 (1173)	(Ruiz-Morales, 2007)
Double perovskites					
$Sr_2Mn_{0.8}Nb_{1.2}O_6$	8×10^{-3} (1173)	0.36 (1173)	-	-	(Tao, 2002b)
$Sr_2Mn_{0.5}Nb_{0.5}O_6$	3.1×10^{-2} (1173)	1.23 (1173)	-	-	(Tao, 2002a)
$Sr_2Mg_{1-x}Mo_xO_{6-\delta}$	4-8 (1073)	-	-	-	(Huang, 2006b)
$Sr_2MgMoO_{6-\delta}$	-	-	0.41 (1173)	-	(Marrero-Lopez, 2010)
	0.19 (1073)	7.7×10^{-4} (1073)	-	-	(Marrero-Lopez, 2009)

[a] Testing in reducing atmosphere (forming gas)

[b] Testing in oxidizing atmosphere (air)

[c] Hydrogen and methane correspond to wet hydrogen and wet methane that are humidified at room temperatures

[d] 10 vol.% H_2S-H_2 fuels

1.5 $SrVO_3$- based materials.

Aguilar et al. [Aguilar, 2004A, 2004B, 2004C] found that lanthanum strontium vanadate (LSV) is tolerant to H_2S when used as a SOFC anode, with further evidence that this anode material is an active electrocatalyst for oxidation of H_2S. $La_xSr_yVO_3$ (LSV) has been utilized as a fuel cell anode in fuels with up to 10% H_2S, and performance of SOFCs utilizing LSV anodes showed no significant deterioration during 48 h, and may even show improved performance as H_2S concentration increased, in agreement with results by Mukundan et al. Still, power density was relatively low (≈140 mW/cm^2), comparing poorly with Ni-YSZ SOFC anodes fueled with H_2, and suggesting that the LSV anode preferentially oxidizes H_2S even in the presence of the H_2 [Mukundan, 2004]. Thus, those authors proposed an alternative concept based on the ability of the SLV anode to preferentially oxidize H_2S while leaving behind other fuel gases (H_2, CO, CH_4 etc.). LSV was considered an excellent choice to use H_2S also as a fuel to recover an additional contribution for electricity production, while simultaneously cleaning the remaining gases to be converted by conventional SOFCs after exhaust from the sulfur cleaning LSV SOFC unit. (Fig 1.11).

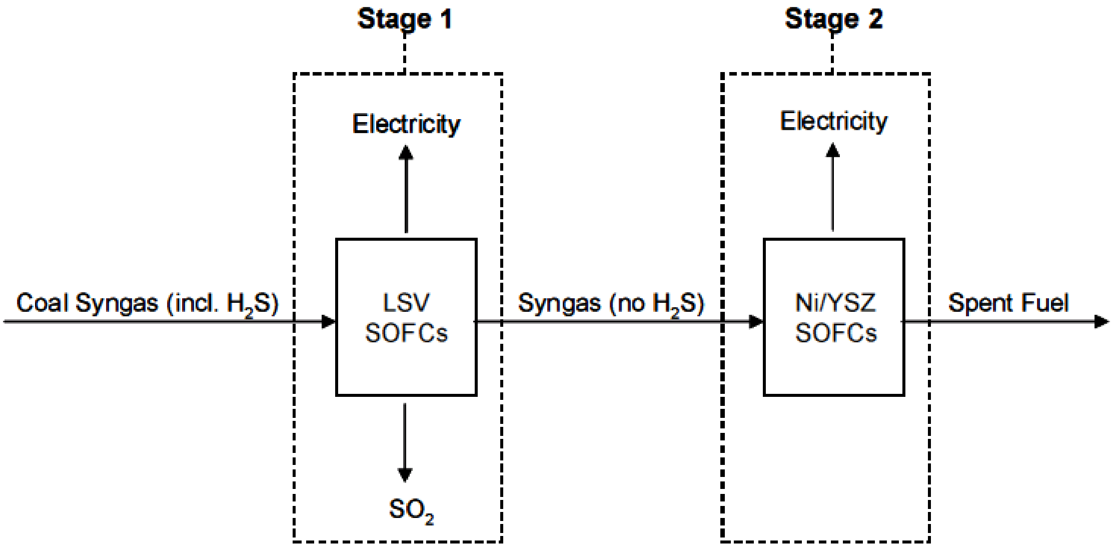
Stage 1
Stage 2
Electricity
Electricity
Coal Syngas (incl. H2S)
LSV SOFCs
Syngas (no H2S)
Ni/YSZ SOFCs
Spent Fuel
SO2

Fig.1.11. Process flow diagram of proposed system

In spite of attractive advantages of $SrVO_3$-based anodes, there are a number of drawbacks hindering their applications. Firstly, the perovskite lattice of $SrVO_3$ is stable only under reducing conditions ($p(O_2) < 10^{-17}$ atm at 1073 K) [Hui, 2001]. Under oxidizing conditions, it undergoes the transformation to V^{+5}-based compounds accompanied with large volume changes. Other drawback is related to the relatively high thermal expansion coefficient of $SrVO_3$, limiting the thermomechanical compatibility with common solid electrolytes [Maekawa, 2006]. Thus, the accurate compositional adjustment via doping is required in order to overcome these disadvantages.

2. Methodology

2.1 Experimental procedure

2.1.1 Synthesis and ceramic processing

Studied materials were prepared from stoichiometric mixtures of high purity starting materials through solid state reaction. The conditions of the materials processing as well as starting chemicals are listed in Table 2.1. Powders of $(ZrO_2)_{0.92}(Y_2O_3)_{0.08}$ (8YSZ) and $Ce_{0.8}Gd_{0.2}O_{2-\delta}$ (CGO) were supplied by Tosoh and Praxair, respectively.

In the case of, mixed components were pre-reacted in air at 773 K, 873 K and 973 K for 5 h at each temperature, with intermediate regrinding. After ball-milling with ethanol (Retsch centrifugal mill S1) and uniaxial compaction, $Sr_2V_2O_7$ and $Sr_3V_2O_8$ ceramic samples were sintered in air for 5 h at 1373 K and 1723 K, respectively.

The powders of $Sr_{1-x}Ln_xV_{1-y}Nb_yO_{3-\delta}$ (Ln = La and Y, x = 0 to 0.20 and y = 0 to 0.30) were prepared using chemicals shown in table 2.1, with prior calcination of niobium and rare-earth oxides in air to remove adsorbates. Weighed and mixed components were pre-reacted in air at 773 K and 873 K for 5 h. Subsequently, the mixtures were fired at 1173 K (3 × 5 h, with repeated regrinding) in flowing 10% H_2-N_2 atmosphere, and then subjected to high-energy milling (Retsch PM 100 planetary ball milling, 650 rpm, 3h, nylon containers with Tosoh tetragonal zirconia milling media) in order to promote homogenization. Then, the powders were compacted uniaxially at ~40 Mpa into disk-shaped samples and sintered at 1773 K in 10%H_2-N_2 atmosphere for 10 h.

The sintering temperatures were selected taking into account the latest available phase diagrams of SrO-V_2O_5 system. (Figure 2.1) [Krasnenko, 1983; Fotiev, 1985] and operational limits of available equipment for sintering under reducing conditions.

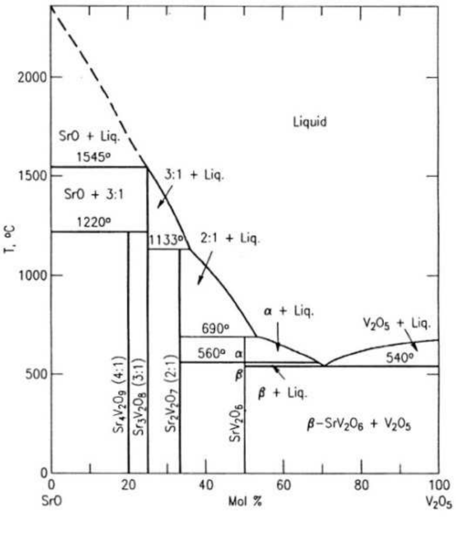

Fig 2.1. Phase diagram of SrO-V_2O_5 system [Krasnenko, 1983]

Table 2.1

Starting reagents and processing conditions for synthesized compositions under reducing conditions.

Composition	Starting component (supplier, purity)	Synthesis technique	Annealing temperatures, K	Sintering conditions (sintering temperature, dwell time and environment)
$Sr_2V_2O_7$	$SrCO_3$ (Sigma Aldrich, > 99.9%) V_2O_5 (Fluka, > 99%) Nb_2O_5 (Alfa Aesar, >99.%) Y_2O_3 (Hermann C.Starck) La_2O_3 (Sigma Aldrich, > 99.9%)	Solid state synthesis	773, 873, 973 (air)	1373 K, 5h, air
$Sr_3V_2O_8$			773,873,973 (air)	1723 K, 5h air
$SrVO_3$			773, 873 (air) 1173 (10%H_2-N_2)	1773 K, 10h (10%H_2-N_2)
$SrV_{1-x}Nb_xO_3$			773, 873 (air) 1173 (10%H_2-N_2)	1773 K, 10h (10%H_2-N_2)
$Sr_{1-x}La_xV_{1-y}Nb_yO_3$			773, 873 (air) 1173 (10%H_2-N_2)	1773 K, 10h (10%H_2-N_2)
$Sr_{1-x}Y_xV_{1-y}Nb_yO_3$			773, 873 (air) 1173 (10%H_2-N_2)	1773 K, 10h (10%H_2-N_2)
$SrV_{1-x}Ti_xO_3$	$SrCO_3$ (Sigma Aldrich, > 99.9%) V_2O_5 (Fluka, > 99%) TiO_2 (Sigma Aldrich, > 99.8%)	Solid state synthesis	773, 873 (air) 1273 (10%H_2-N_2)	1773 K, 10h (10%H_2-N_2)

Ceramic materials of $SrV_{1-x}Ti_xO_{3-\delta}$ series were prepared by solid state synthesis and sintered either in 10% H_2-N_2 atmosphere or in air. The processing of reduced materials followed the same route explained above for $Sr_{1-x}Ln_xV_{1-y}Nb_yO_{3-\delta}$ (Table 2.1) with preliminary calcination of TiO_2 at 1173 K.

Samples preparation under oxidizing conditions was limited to Ti-rich end of the series, with x = 0.7 to 0.9, and was done according to the scheme (Fig. 2.2).

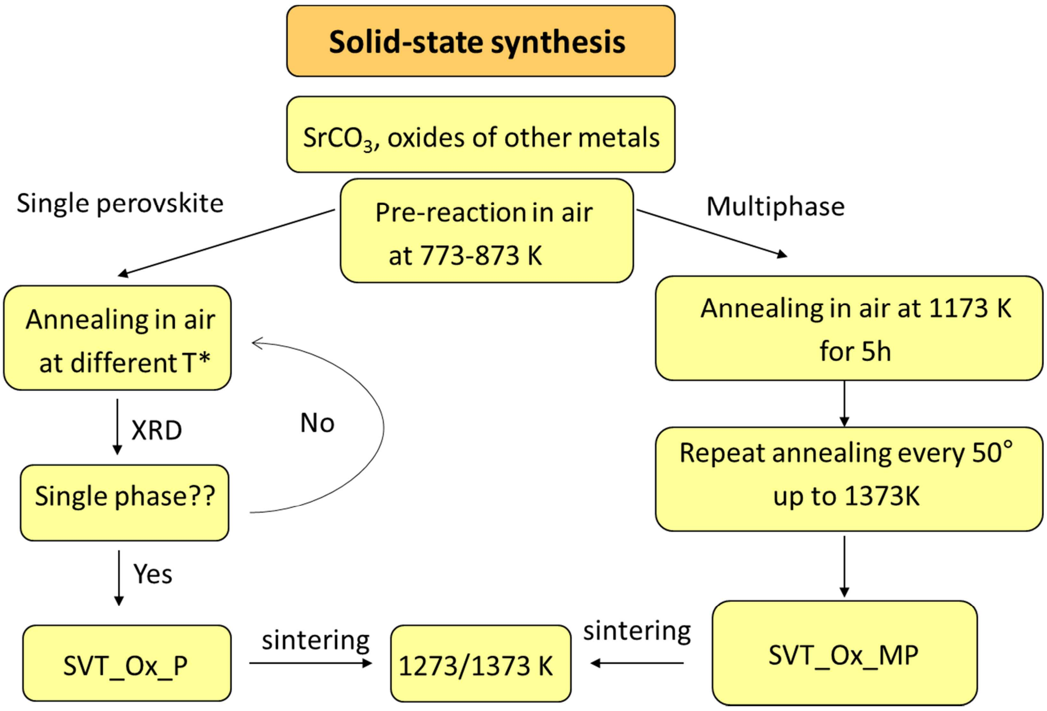
Solid-state synthesis
SrCO3, oxides of other metals
Pre-reaction in air at 773-873 K
Single perovskite
Multiphase
Annealing in air at different T*
XRD
No
Single phase??
Yes
Annealing in air at 1173 K for 5h
Repeat annealing every 50° up to 1373K
SVT_Ox_P
sintering
1273/1373 K
sintering
SVT_Ox_MP

Fig 2.2. Scheme of synthesis for Ti-rich $SrV_{1-x}Ti_xO_{3-\delta}$ series under oxidizing conditions. (*) Calcination temperatures for each composition are listed in Table 2.2.

Table 2.2

Calcination temperatures for single-phase oxidized $SrV_{1-x}Ti_xO_3$.

Composition	Sequence of calcination steps at different T (K); 5 hours per each step
$SrV_{0.9}Ti_{0.1}O_3$	773 / 873 / 1173 / 2x1373 / 1473 / milling / 1473 / 1503 / 2x1523
$SrV_{0.8}Ti_{0.2}O_3$	773 / 873 / 1173 / 2x1373 / 1473 / milling / 1473 / 1503 / 2x1523
$SrV_{0.7}Ti_{0.3}O_3$	773 / 873 / 2x1173 / 1223 / 1253 / 1273 / 2x1323 / 1353 / 3x1373 / 1423 / 1453 / 1473 / 1523 / 1573 / 1623 / 2x1653 / 1673 / 3x1693 / 1703 / 3x1713

2.1.2 X-ray diffraction

Phase analysis was performed by X-ray diffraction (XRD), on crushed powders, using a PANalytical X´pert PRO diffractometer (Cu K_{α} ; λ= 0.154178 nm, 20-80°, step 0.02° with exposition time of 1-5 seconds). For selected ceramic compositions, high-temperature XRD patterns were collected using the same equipment.

The JCPDS (International Centre for Diffraction Data) database was used for the phase identification. The crystal lattice parameters were calculated using Fullprof program [Rodriguez-Carvajal, 1993]. Theoretical density of ceramic materials was calculated as:

$$D_{theor} = \frac{N_U M}{N_A V} \qquad \text{Eq. 2.1}$$

where N_U- number of formula units per unit cell, M - molar weight, N_A- Avogadro constant, V- unit cell volume.

2.1.3 Microstructural characterization

For microstructural studies, the samples were glued to a holder using conductive carbon cement (Wetzlar). Then, a uniform carbon powder layer was sputtered over the samples (Emitech K950x turbo evaporator). Microstructural characterization was performed by scanning electron microscopy (SEM, Hitachi S-4100 and SU-70 instruments) coupled with energy dispersive spectroscopy (EDS, Rontec UHV and Bruker Quantax 400 detectors, respectively) for elemental analysis.

Average grain sizes were calculated from SEM images, using the image processing program ImageJ 1.37v software (Wayne Rasband, National Institutes of Health, USA).

To observe possible microstructural or compositional changes taking place in the electrode layers during the electrochemical tests, the solid electrolyte – electrode assemblies after the experiments were attached to the holder in a manner to keep the electrode layer on the top. Another approach involved breaking the cell across the electrode and electrolyte layers, perpendicular to the interface, and exposure of the fractured surfaces and the boundary between cell components to the microscopic studies, in order to examine the morphology of the electrode layer and detect possible interactions, cation interdiffusion, etc.

2.1.4 Thermal analysis

2.1.4.1 Thermogravimetric analysis

Thermogravimetric analysis (TGA) was carried out using a Setaram SetSys 16/18 instrument (sensitivity 0.4 μg, initial sample weight ~ 0.5 g) in a flow of air, Ar or 10% H_2-N_2 mixture, from 300 to 1273 K at a constant heating-cooling rate of 2-3° /min or isothermally as a function of time. Inert Al_2O_3 ceramic sample was used to record the baseline under identical conditions and correct the data for buoyancy effect.

2.1.4.2 Dilatometry

Dilatometric studies were performed using rectangular bar samples (~1.2 × 0.4 × 0.4 cm^3) in a vertical dilatometer Linseis L70 with a constant heating-cooling rate of 2-3° /min from 300 to 1273 K in different atmospheres. Calibration of the dilatometer was carried out on Al_2O_3 bar subjected to the same measurement procedure as the sample studied. The thermal expansion coefficients (TECs) were calculated from dilatometric curves via a least-square method.

2.1.5 Electrical conductivity

The total conductivity (TC) was studied as function of temperature and oxygen partial pressure under reducing conditions (H_2-H_2O-N_2 mixtures) by 4-probe DC technique (Yokogawa 7651 or Agilent E3640A DC power supply and Agilent 34460A multimeter) using bar-shaped ceramic samples. 4-probe measurement configuration eliminates the influence of the contact resistance (Figure 2.3). The potential is measured between probes which do not carry any current; thus, the measurement is independent of the contact resistances.

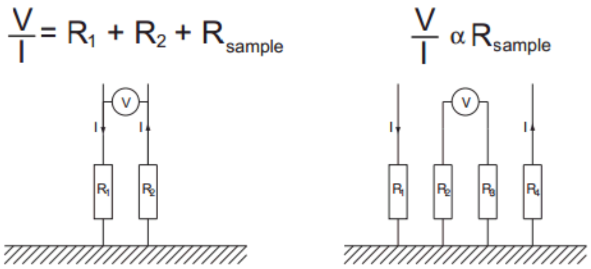
$\frac{V}{I} = R_1 + R_2 + R_{sample}$
$\frac{V}{I} \alpha R_{sample}$
V
I
R1
R2
V
I
R1
R2
R3
R4

Fig. 2.3. Schematic representation of 4-probe technique **(right)** in comparison with 2-point scheme **(left)**.

The temperature was varied from 473 K to 1273 K and was measured using S-type (Pt/Rh 90%/10% -Pt) thermocouples.

The isothermal measurements of total conductivity as function of oxygen partial pressure (10^{-19}-10^{-5} Pa) were performed at different temperatures (973,1073,1173 K) in an cell comprising electrochemical oxygen sensor.

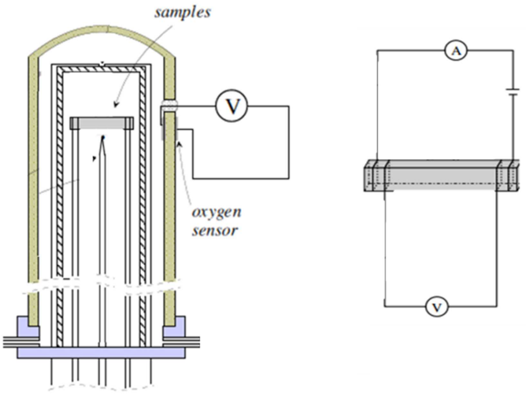

Fig 2.4 Schematic representation of the cell for the conductivity measurements **(left)** and contacts between current and potential leads and sample **(right)**.

Data points were obtained upon achievement of equilibrium between the samples and ambient. The conductivity relaxation time varied depending on oxygen pressure, temperature and sample composition.

The conductivity values were calculated from:

$$\sigma = \frac{L}{R\,S} \qquad \text{Eq. 2.2}$$

$$\sigma = \frac{I_1+I_2}{V_1+V_2} \cdot \frac{L}{S} \qquad \text{Eq. 2.3}$$

Where L- sample length; R- sample resistance; S- sample cross area; V_1,V_2, I_1 and I_2 voltage drop over the sample and current, for each of two opposite current directions. The activation energy was calculated using the standard Arrhenius equation (Eq. 2.4).

$$\sigma = \frac{A_0}{T}\exp\left(-\frac{E_a}{RT}\right) \qquad \text{Eq. 2.4}$$

For the samples with high resistivity, total conductivity was studied as function of temperature and oxygen partial pressure using 2-probe AC impedance spectroscopy (Agilent 4284A precision LCR meter). This technique was also used for the studies of conductivity relaxation on redox cycling between reducing and oxidizing atmospheres. In all cases, wires resistances were extracted from the measured resistance values.

2.1.6 Electrochemical studies

2.1.6.1 Electrode preparation

Electrochemical studies were performed using symmetrical cell configuration, with two identical electrodes applied onto opposite sides of disk-shaped solid electrolyte membrane. Two methods were used for application of electrode layers.

2.1.6.1.1 Brush-painting method

This simple procedure includes the preparation of a suspension of electrode material powder in α-terpineol followed by brush-painting of prepared ink onto the solid electrolyte substrate and subsequent firing under selected conditions (Fig 2.5).

Cell	Top view (both sides)	Cross section/ dimensions
Symmetrical (two electrodes)	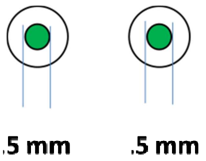	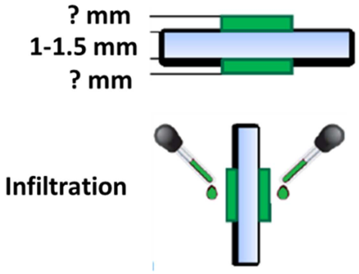

Fig 2.5 Schematic representation of symmetrical cells preparation and infiltration process.

2.1.6.1.2 Screen printing

Screen printing is a printing technique where a mesh is used to transfer ink onto a substrate, except in areas made impermeable to the ink by a blocking template. The manfacturing steps of cell preparation are shown in diagram in Figure 2.6.

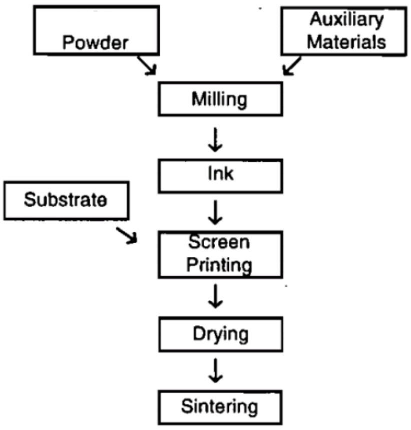

Fig. 2.6 Flow chart representing the manufacturing processes of cell preparation. [Mastrandea, 2004]

Two different electrode compositions, both based on vanadium-substituted strontium titanate, were employed for electrode fabrication by screen printing method. Materials and equipment used for ink fabrication are detailed in Table 2.3

Table 2.3

Preparation of inks for screen printing

Equipment or materials	Details	Amount /time
STV Powder*	Particle size: 1-3 μm	100 g
Solvent	Dowanol	20 g
Dispersant	DisperByk180	3 g
Binder	KS-10	5 g
Milling	PM container (Zirconia balls)	150 rpm / 15 min

*STV50_red and STV30_Ox_MP for two different inks

The preparation of electrode inks included the following steps:

1. Mixing STV powder with dispersant and Dowanol (dypropylenne glycol methyl eter) for 30 min using a ball-milling in PM container with 2×4 cm diameter zirconia balls at 150 rpm.
2. Addition of binder and continuous mixing in PM container for 15 min.
3. Homogenizing the resultant mixture using a triple roll mill.

The fraction of solid in the ink was 75 wt%.

DEK248 CERD screen printer was used for electrode preparation. The screen printing equipment and printing steps are schematically shown in Figure 2.7.

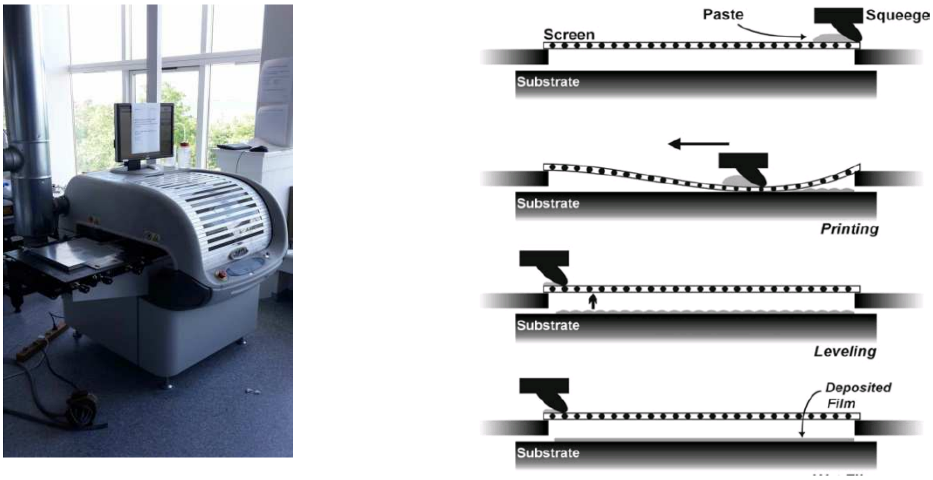

Fig. 2.7 Screen printing equipment **(left)** and schematic representation of screen printing process **(right)** [Solomon, 2007]

The main elements in screen printing are: the screen, which is the image carrier, the squeegee and the ink. The screen uses a porous mesh stretched tightly over a frame made of metal o some polymers. The ink is placed on top of the screen. The ink is then drawn across the screen using a squegee, applying pressure and thereby forcing the ink through the open areas of the screen, forming a film on the printing substrate. The conditions of screen printing parameters are summarised in Table 2.4

Table 2.4

Screen printing parameters used for electrode preparation

Parameter	Conditions
Print speed	0.06 m/seg
Squeegee type	Polyurethane
Squeegee load	7 Kg
Number of passes	2
Screen mesh type	225
Print gap	0.9 mm

The STV film (approx. 50μm in thickness) was screen printed on 8YSZ electrolyte slab (200 μm thickness, Kerafol), on both sides of the electrolyte, with a subsequent drying of the ink at 363 K for 20 min and firing at 1373/1398 K (STV30_air) and 1448 K (STV50) for 5 hour in air and 10% H_2 atmosphere, respectively.

2.1.6.2 Ni-CGO infiltration

Ni, CGO or a mixture of both were infiltrated into porous electrode layers for modification of electrochemical activity. The solutions for infiltration were prepared by dissolution of nickel nitrate $Ni(NO_3)_2$, ceria nitrate $Ce(NO_3)_3$ and gadolinium nitrate $Gd(NO_3)_3$ in water as a solvent with stirring.

A micro-pipette or a brush was used to deposit some drops of the solution on top of a sintered porous electrode layers. The solution was infiltrated into STV scaffold by capillary action. The sample was then fired at 900ºC for 2h to decompose the nitrate salts and to form Ni and CGO particles.

The loading of the infiltrated phase was estimated by measuring the weight differences before infiltration and after the heat treatment. The whole process was repeated up to three times to increase the loading of the metal phase. The typical infiltration process is demonstrated schematically in Figure 2.8

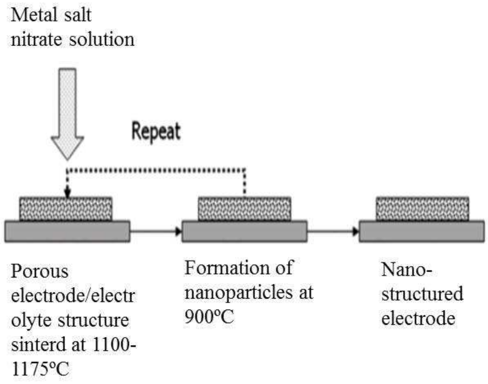
Metal salt
nitrate solution
Repeat
Porous electrode/electrolyte structure sinterd at 1100-1175ºC
Formation of nanoparticles at 900ºC
Nano-structured electrode

Fig 2.8. Typical process for the infiltration of metal salt nitrate solution into a pre-sintered electrode porous structure. [Jensen,2007]

2.1.6.3 Electrochemical Impedance Spectroscopy (EIS)

Electrochemical impedance spectroscopy is used to study the electrochemical performance of electrodes and electrolytes and can distinguish different processes occurring within the system. This technique has been extensively used in the study of SOFCs/SOECs systems, however a great care has to be taken when interpreting the results.

Impedance theory can be applied to systems which don´t obey Ohm´s law. Inducing a small alternating potential produces a small alternating current, the polarization curve can be described as pseudo linear if the perturbation is small, as depicted in the Figure 2.9.

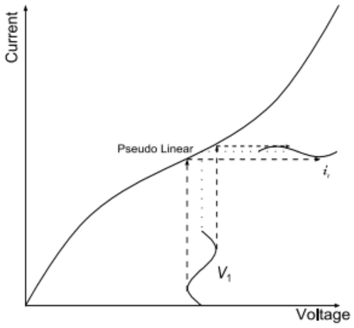

Fig. 2.9 Non ohmic polarization curve showing AC potential input and current response. Supplied potential, V_1, results in current response i_1.

When applying an alternating potential, V(ω), with amplitude V_0 and angular frequency ω (frequency f = ω/2π):

$$V(\omega) = V_0 e^{j\omega t} \qquad \text{Eq. 2.5}$$

where j = √-1 The resulting current I(ω) is:

$$I(\omega) = I_0 e^{(j\omega t+\varphi)} \qquad \text{Eq. 2.6}$$

where I_0 is the current amplitude and φ is the phase shift (φ = 0 for a purely resistive element and π/2 for a purely capacitive element).

Therefore, as impedance Z(ω) = V(ω)/I(ω) and expressing $|Z| = V_0/I_0$

$$Z = |Z|.e^{(-j\varphi)} \qquad \text{Eq. 2.7}$$

or

$$Z = |Z|.(\cos\varphi - j\sin\varphi) \qquad \text{Eq. 2.8}$$

Impedance is therefore a complex number and is often written as

$$Z = Z'-jZ'' \qquad \text{Eq. 2.9}$$

where:

$$Z' = |Z|\cos\varphi \qquad \text{Eq. 2.10}$$

$$Z'' = |Z|\sin\varphi \qquad \text{Eq. 2.11}$$

Impedance spectroscopy involves applying an alternating potential at range of frequencies, from MHz to mHz, recording the subsequent impedance, and representing the results as a Nyquist plot: imaginary impedance Z´´ against real impedance Z´, as illustrated in Fig. 2.10.

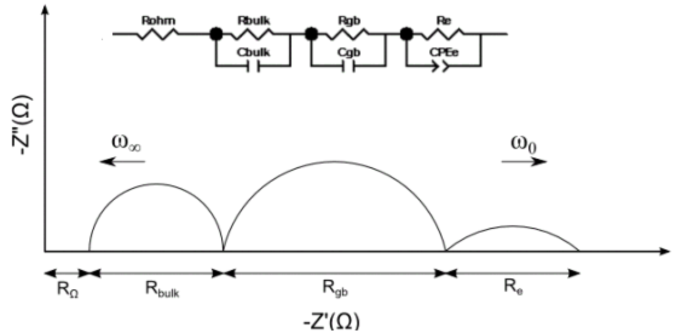

Fig 2.10 An example Nyquist plot for a solid, oxygen-ion conducting electrolyte with conducting electrodes. The equivalent circuit for such system is displayed above.

Characteristic arcs in the Nyquist plot represent responses from different processes of the system. The ability of this technique to separate these processes is due to fact that each process possesses a unique relaxation time, and the responses therefore occur at different frequencies.

Thus, each semicircle in the plot represents a different component of the system being studied. Semicircles produced at high frequencies are often attributed to the bulk of the electrolyte; medium-frequency semicircles are associated with the grain boundaries of the electrolyte, and semicircles at lower frequencies are attributed to electrode processes. However, analysis is often less simplistic as features in the plot can be caused by surface layer effects, interface effects, etc. [Irvine, 2010].

AC impedance data is analyzed employing equivalent circuits of resistors, capacitors, constant phase elements, etc., modelled to describe the system under study. The simplest equivalent circuit yielding a single semicircle is an RC circuit, with resistor (R) and capacitor (C) connected in parallel. The equivalent circuit of more than one semicircle is then the parallel RC circuit of each component connected in series. However, a number of different equivalent circuits may describe the same plot. Knowledge of the system is therefore required in order to select the circuit which best describes the processes occurring.

The resistance of the component can be found from the values corresponding to interception of semicircle with the real axis (Fig.2.10). The capacitance of the component may be determined using equation:

$$f_{\mathrm{max}}=\frac{\omega_0}{2\pi}=\frac{1}{2\pi RC} \qquad \text{Eq. 2.12}$$

where, for each component, f_{max} and ω_0 are the relaxation frequency and relaxation angular frequency which occur when Z´´ is maximum, R is the resistance and C the capacitance.

The dielectric relaxation time, or time constant τ is related to R, C and ω_0:

$$\tau = RC = \omega_0^{-1} \qquad \text{Eq. 2.13}$$

The capacitance of a particular Nyquist semicircle gives an indication of what the underlying process is. Irvine et al. [Irvine, 1990] related different capacitance values with different possible phenomena, as shown in Table 2.5.

Table 2.5

Summary of capacitance values and corresponding physical processes [Irvine, 1990]

Capacitance (F)	Phenomenon Responsible
10^{-12}	Grain bulk
10^{-11}	Minor, second phase
10^{-11}-10^{-8}	Grain boundary
10^{-10}-10^{-9}	Bulk ferroelectric
10^{-9}-10^{-7}	Surface layer
10^{-7}-10^{-5}	Oxygen transfer at sample-electrode interface
10^{-4}	Electrochemical reactions, charge transfer
10^{-4}-10^{-3}	Oxygen exchange on the electrode surface
10^{-3}	Electrochemical reactions on electrode
10^{-3}-10^{-2}	Oxygen diffusion through electrode, charge transfer at electrode surface
10^{-1}	Gas diffusion to electrode surface

The capacitance from a CPE (constant phase element) is calculated as:

$$C = (TR^{1-p})^{1/p} \qquad \text{Eq. 2.14}$$

Where T is the pseudo capacitance, R is the element´s resistance and p is a parameter related to the depression angle of the curve.

Resistivity and conductivity can be calculated from the resistance of each process. If the impedance technique is conducted over a range of temperature, an Arrhenius plot can be drawn. This is based on the Arrhenius equation (Eq. 2.4)

$$\sigma = \sigma_0 . e^{-E_a/R_g T} \qquad \text{Eq. 2.15}$$

Where E_a is the activation energy, T is the absolute temperature, R_g is the gas constant, σ_0 is a pre-exponential constant which derives from a number of constants such as the vibrating frequency of the moving ions [West, 1988], σ is the conductivity (calculated taking into account measured resistance, thickness and cross-sectional area of the cell).

Area specific resistance (ASR) is often used as a measure of electrode performance. The ASR of an electrode of a symmetrical cell is given by the following equation:

$$ASR = \frac{R_p A}{2} \qquad \text{Eq. 2.16}$$

Where R_p is the polarization resistance as worked out from the Nyquist plot, A is the surface area of the cell.

As with the conductivity, it is possible to find the activation energy using the resistance in the Arrhenius equation:

$$ASR = R_p . e^{E_a/R_g T} \qquad \text{Eq. 2.17}$$

Figure 2.11 shows an ideal Nyquist plot representation for an electrode, with both ohmic resistance and polarization resistance. However, one of the problems with real EIS spectra is associated with the overlapping between semi-circles which make it difficult to identify and to de-convolute the data into individual components.

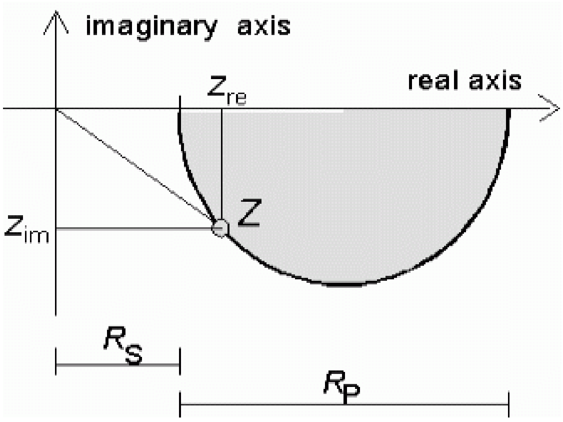

Fig. 2.11. Schematic representation in ideal Nyquist plot, of corresponding resistance to polarization (Rp) and ohmic resistance (Rs)

2.1.6.3.1 EIS experimental instrumentation

Electrochemical impedance spectroscopy measurements were performed using Solartron Analytical ModuLab frequency response analyser (FRA) over the frequency range 1 MHz- 0.01 Hz, over the temperature range 1023-1173 K in reducing atmosphere (3%H_2O-H_2) and Autolab PGSTAT302 instrumental with built-in FRA module (freqeuency range 10 mHz – 1 MHz) in the same temperature range in reducing atmosphere (3%H_2O-10%H_2-N_2). In both cases, Pt gauze was used a current collector. The pellets were mounted in a sample holder in two electrode configurations as described in Figure 2.12.

Electrical connections were made of platinum wires and platinum meshes as the symmetrical cell electrode current collectors. Measurements were taken in humid H_2 by flowing gas through a water bath at ambient temperature upstream of the sample holder.

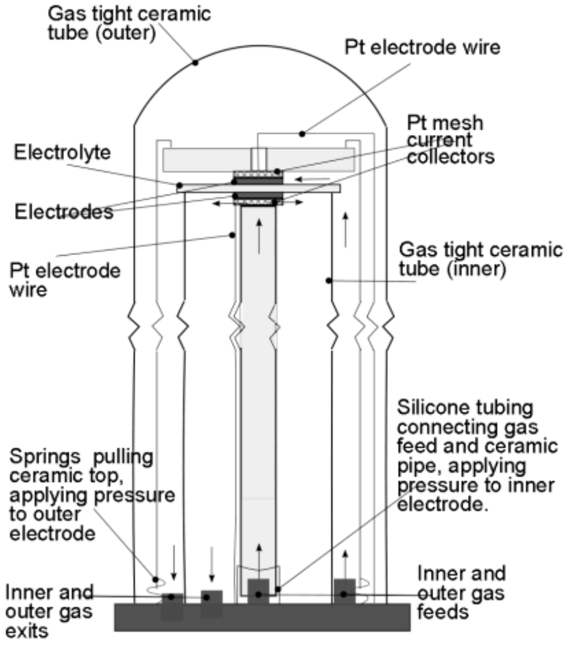
Gas tight ceramic tube (outer)
Pt electrode wire
Pt mesh current collectors
Electrolyte
Electrodes
Gas tight ceramic tube (inner)
Pt electrode wire
Silicone tubing connecting gas feed and ceramic pipe, applying pressure to inner electrode.
Springs pulling ceramic top, applying pressure to outer electrode
Inner and outer gas exits
Inner and outer gas feeds

Fig. 2.12 Impedance sample holder and gas inlet and outlet for measuring EIS under a reducing atmospheres.

2.2 Thermodynamic calculations

Thermodynamic calculations were employed to describe the conditions of fuel conversion and corresponding constraints imposed on the anode materials (i.e. Ni/YSZ cermets and $SrVO_3$-based anode materials). Thermodynamic predictions were also extended to redox conversion of sulphur-based species and their impacts on anode materials.

2.2.1 Thermodynamic analysis of methane conversion and carbon deposition

Methane is the main component of natural gas and biogas. It is thus a very important energy source and might be also converted to a variety of useful chemicals by pre-conversion to syngas, based on the following reaction:

$$CH_4 + \frac{1}{2}O_2 \leftrightarrow CO + 2H_2 \qquad \text{Eq. 2.18}$$

However, the equilibrium is unlikely to be attained easily, and one may need to resort to somewhat excessive oxygen partial pressure to attain high conversion of methane, thus running risk of further oxidation to water vapor and/or carbon dioxide:

$$CO + \frac{1}{2}O_2 \leftrightarrow CO_2 \qquad \text{Eq. 2.19}$$

$$H_2 + \frac{1}{2}O_2 \leftrightarrow H_2O \qquad \text{Eq. 2.20}$$

Under real conditions, one should also consider the risks of methane cracking, especially on contacting with metallic surfaces, (e.g. Ni).

$$CH_4 \leftrightarrow C + 2H_2 \qquad \text{Eq. 2.21}$$

One may, thus, estimate the changes in gas composition for this relatively complex system, as a function of temperature and oxygen partial pressure; this will provide guidelines for expected working conditions required to reach high methane conversion without the formation of unwanted products. Ideal conditions have been calculated by Frade et al. [Frade, 2004], relying on the mass action constants of the relevant previous reactions, combined with additional conditions for conservation of elements (C,O and H). A relevant solution for conditions when carbon deposition is prevented reduces to:

$$\frac{(1-pCH_4)^3}{pCH_4}=\frac{27}{4}K_1(pO_2)^{1/2}\left[1+K_2(pO_2)^{1/2}\right]x\left[1+K_3(pO_2)^{1/2}\right]^2 \qquad \text{Eq. 2.22}$$

where K_1, K_2 and K_3 are the mass actions constants of reactions 2.18, 2.19 and 2.20. The interdependence of pO_2 on $[CH_4]$ was then solved numerically, for given values of $p(CH_4)$ and to obtain the partial pressures of the remaining components of the gas mixture.

Similar calculations can be solved for different gas compositions and temperature obtaining predictions for conditions when carbon deposition takes place. Typical examples are shown in Figure 2.13, emphasizing gradual evolution from partial oxidation to complete oxidation as a function of oxidant:fuel ratio, for slightly humidified methane feed (H_2O:CH_4 = 0.5), as expected to promote steam reformation, or to simulate a biogas feed with CO_2:CH_4 = 0.5. Note that this degree of oxidation is still insufficient to prevent carbon deposition, marked by the shaded area. The theoretical calculations represented in the Figure 2.13 provide guidelines for the redox requirements of fuel electrodes.

A corresponding ternary C-O-H diagram is also included to emphasize that the minimum oxygen requirements to prevent carbon deposition decrease in the presence of hydrogen rich gas mixtures (Fig 2.14).

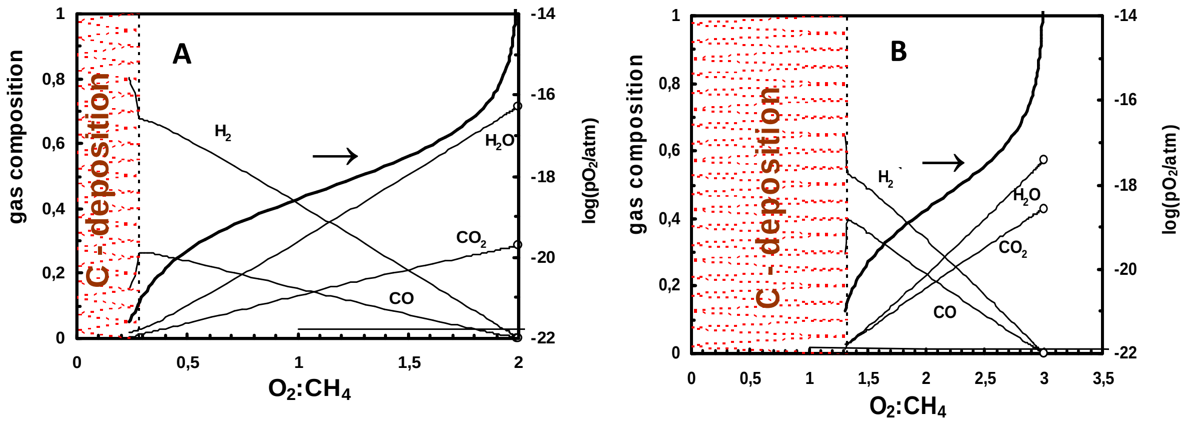

Fig 2.13. Equilibrium gas composition and methane conversion as a function of oxygen partial pressure at 1073 K for **(A)** H_2O:methane ratio 0.5 and **(B)** CO_2:methane ratio 0.5. Red dotted show zone with C-deposition.

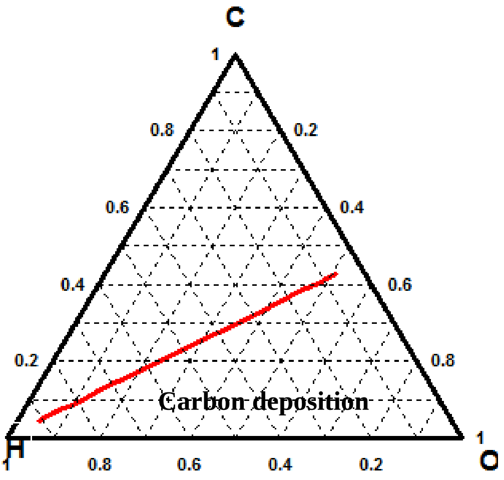

Fig 2.14 Thermodynamic consideration of carbon deposition in chemical equilibrium diagram of C-H-O system at 1173 K.

A representative case is illustrated in figure 2.15, which shows conditions imposed by methane conversion in the range 10-90%, and the stability limits of Ni (e.g Ni/NiO equilibrium). Indeed, these predictions may still be somewhat insufficient to establish precise stability requirements for fuel electrodes, as the effective electrochemical conditions also depend on kinetic limitations such as concentration gradients in the gas phase imposed by sluggish diffusion or overpotential contributions (η). The later impose differences between the effective oxygen partial pressure and the partial pressure in equilibrium with the partially converted fuel, as described by the Nernst equation:

$$\log\left(pO_{2,eff}\right)=\log\left(pO_{2,fuel}\right)+\frac{4F\eta}{2.303RT} \qquad \text{Eq. 2.23}$$

Thus, high fuel conversion combined with excessive overpontential may impose risks on Ni/YSZ anodes by the expansive oxidation of Ni to NiO.

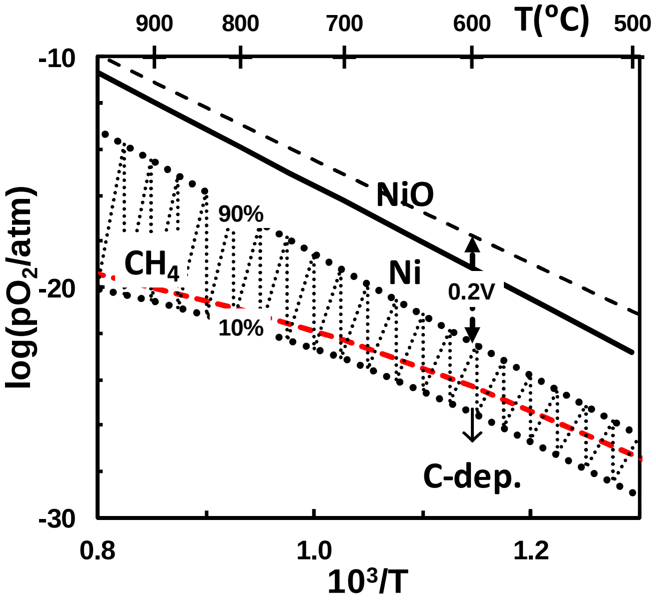

Fig 2.15 Stability limits of Ni/NiO (solid line) and predictions of conditions of methane combustion in the range 10-90% (shaded area), and carbon deposition. The upper dashed line indicates changes in effective oxygen partial pressure for 90% conversion with anodic overpotential $\eta = 0.2$V

2.2.2 Thermodynamic analysis of $SrVO_3$-based fuel electrodes

Thermodynamic analysis is also used as the basis to establish guidelines for redox stability limits of $SrVO_3$-based electrodes, and their tolerance to conditions imposed by redox pairs (H_2/H_2O, CO/CO_2) or more complex atmospheres upon conversion of CH_4 or other hydrocarbons. These thermodynamic analyses are also extended to assess sulphur tolerance, conditions for carbon deposition and interaction with carbon dioxide at intermediate temperatures.

Redox stability is assessed by chemical activity diagrams, as proposed by Yokokawa et al. [Yokokawa, 1991] for ternary A-B-O systems; this is expressed by plots of log (a_A/a_B) vs log(pO_2), as illustrated in Fig.2.16, which reproduces the chemical activity diagram reported for Sr-V-O. This diagram is calculated by formulating relevant reactions for 2-phase boundaries, using a suitable approach [Monteiro, 2009]. The method combines 3 types of phase equilibria, as described in detail for phase boundaries $SrVO_3/V_2O_3$, (eq.2.24) $SrVO_3/Sr_2V_2O_7$ (eq. 2.25) and $Sr_3V_2O_8$/ $SrVO_3$ (eq. 2.26).

$$SrVO_3 + V \Leftrightarrow Sr + V_2O_3 \qquad \log\left(\frac{a_{Sr}}{a_V}\right) = \log(k_1) \qquad \text{Eq.2.24}$$

$$4SrVO_3 + O_2 \Leftrightarrow 2Sr_2V_2O_7 \qquad \log(pO_2) = -\log(k_2) \qquad \text{Eq.2.25}$$

$$2Sr_3V_2O_8 + V \Leftrightarrow Sr + 5SrVO_3 + 0.5O_2 \qquad \log\left(\frac{a_{Sr}}{a_V}\right) = \log(k_3) - 0.5\log(pO_2) \qquad \text{Eq.2.26}$$

The $SrVO_3/Sr_2V_2O_7$ equilibrium maintains a constant Sr:V ratio and corresponds to a redox reaction. Equilibria between phases with different Sr:V ratio (e.g. $SrVO_3/V_2O_3$) is described by imposing unit stoichiometry coefficients for cation species (Sr and V), to yield the activity ratio a_{Sr}/a_V in the mass action constant, and then adjusting the remaining coefficients to ensure conservation of every chemical element; this includes participation of molecular O_2, when needed to account for redox changes, as for the $Sr_3V_2O_8/SrVO_3$ equilibrium. Equilibrium conditions for the remaining 2-phase boundaries are also shown in table 2.6.

Table 2.6

Formulations of 2-phase boundaries and relation between activites remaining coefficients to ensure conservation of every chemical element

Boundary	Reaction	Relation
$SrVO_3/V_2O_3$	$SrVO_3 + V \Leftrightarrow Sr + V_2O_3$	$\log\left(\frac{a_{Sr}}{a_V}\right) = \log(k_1)$
$SrVO_3/Sr_2V_2O_7$	$4SrVO_3 + O_2 \Leftrightarrow 2Sr_2V_2O_7$	$\log(pO_2) = -\log(k_2)$
$Sr_3V_2O_8/SrVO_3$	$2Sr_3V_2O_8 + V \Leftrightarrow Sr + 5SrVO_3 + 0.5O_2$	$\log\left(\frac{a_{Sr}}{a_V}\right) = \log(k_3) - 0.5\log(pO_2)$
V/VO	$2V + O_2 \Leftrightarrow 2VO$	$\log(pO_2) = -\log(k_4)$

V/SrO	$SrO \Leftrightarrow Sr + 0.5O_2$	$\log\left(\frac{a_{Sr}}{a_V}\right) = \log(k_5) - 0.5\log(pO_2)$
SrO/Sr$_2$VO$_4$	$3SrO + 0.5O_2 + V \Leftrightarrow Sr + Sr_2VO_4$	$\log\left(\frac{a_{Sr}}{a_V}\right) = \log(k_6) + 0.5\log(pO_2)$
VO/Sr$_2$VO$_4$	$0.5Sr_2VO_4 + V \Leftrightarrow Sr + 1.5VO + 0.25O_2$	$\log\left(\frac{a_{Sr}}{a_V}\right) = \log(k_7) - 0.25\log(pO_2)$
SrVO$_3$/Sr$_2$VO$_4$	$2Sr_2VO_4 + 0.5O_2 + V \Leftrightarrow Sr + 3SrVO_3$	$\log\left(\frac{a_{Sr}}{a_V}\right) = \log(k_8) + 0.5\log(pO_2)$
SrVO$_3$/VO	$SrVO_3 + V \Leftrightarrow Sr + 2VO + 0.5O_2$	$\log\left(\frac{a_{Sr}}{a_V}\right) = \log(k_9) - 0.5\log(pO_2)$
Sr$_3$V$_2$O$_8$/Sr$_2$VO$_4$	$5Sr_2VO_4 + 2O_2 + V \Leftrightarrow Sr + 3Sr_3V_2O_8$	$\log\left(\frac{a_{Sr}}{a_V}\right) = \log(k_{10}) + 2\log(pO_2)$
Sr$_3$V$_2$O$_8$/Sr$_2$V$_2$O$_7$	$2Sr_3V_2O_8 + 0.75O_2 + V \Leftrightarrow Sr + 2.5Sr_2V_2O$	$\log\left(\frac{a_{Sr}}{a_V}\right) = \log(k_{11}) + 0.75\log(pO_2)$
SrV$_2$O$_8$/Sr$_2$V$_2$O$_7$	$1.5Sr_2V_2O_7 + 0.75O_2 + V \Leftrightarrow Sr + 2SrV_2O_6$	$\log\left(\frac{a_{Sr}}{a_V}\right) = \log(k_{12}) + 0.75\log(pO_2)$
V$_2$O$_3$/Sr$_2$V$_2$O$_7$	$0.5Sr_2V_2O_7 + V \Leftrightarrow Sr + V_2O_3 + 0.25O_2$	$\log\left(\frac{a_{Sr}}{a_V}\right) = \log(k_{13}) - 0.25\log\left(pO_2\right)$
V$_2$O$_4$/SrV$_2$O$_6$	$SrV_2O_6 + V \Leftrightarrow Sr + 1.5V_2O_4$	$\log\left(\frac{a_{Sr}}{a_V}\right) = \log(k_{14})$
V$_2$O$_5$/SrV$_2$O$_6$	$SrV_2O_6 + 0.75O_2 + V \Leftrightarrow Sr + 1.5V_2O_5$	$\log\left(\frac{a_{Sr}}{a_V}\right) = \log(k_{15}) + 0.75\log(pO_2)$

Figure 2.16 shows the redox limits for $SrVO_3$ as well as secondary phases found by synthesis in oxidizing conditions, or by redox cycling ($Sr_2V_2O_7$ and $Sr_3V_2O_8$). Typical conditions for H_2O/H_2 equilibrium are also shown from very dry to very wet hydrogen. Representative limiting conditions are shown for steam electrolysis for 1% H_2O with cathodic overpotential η - 0.15 V, and fuel cell mode for 90% conversion with anodic overpotential η - 0.1V. Other phases (Sr_2VO_4 or SrV_2O_6 and vanadium oxides are not expected by maintaining the stoichiometric ratio Sr:V = 1:1). Thus, strategies to upgrade the redox stability of $SrVO_3$-based fuel electrodes are focused on enhancing the redox tolerance towards more oxidizing conditions and anodic polarization.

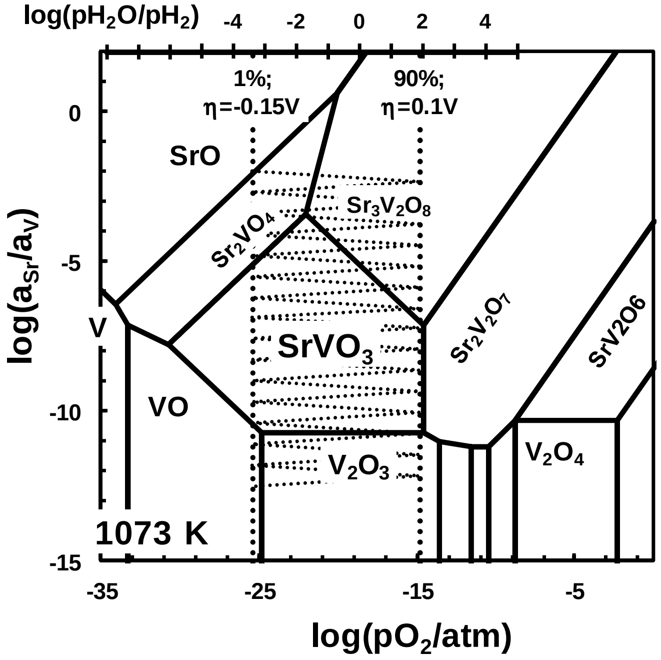

Fig 2.16. Redox equilibria for the Sr-V-O system at 1073K, and corresponding H_2/H_2O equilibrium. Vertical lines show conditions for 1% H_2O with η=-0.15V (left) and (90% H_2O with η=0.1V (right).

Thermodynamic analysis also provides guidelines for interaction of the relevant solid phases in the Sr-V-O diagram with fuel conversion gases, namely CO/CO_2, yielding unwanted phases ($SrCO_3$). The relevant relations were derived by analogy with those described to analyze the redox tolerance as indicated in Table 2.7, and representative predictions are shown in Figure 2.17.

Table 2.7
Thermodynamic predictions for interactions of solid phases in the system Sr-V-O with carbon dioxide

Boundary	Reaction	relation
	$CO_2 \Leftrightarrow CO + 0.5O_2$	$\log(pCO_2) = -\log\left[1 + k(pO_2)^{-1/2}\right]$
SrO/SrCO$_3$	$SrO + CO_2 \Leftrightarrow SrCO_3$	$\log(pCO_2) = \log(k)$
Sr$_2$VO$_4$/SrCO$_3$	$3SrCO_3 + 0.5O_2 + V \Leftrightarrow$ $Sr + Sr_2VO_4 + 3CO_2$	$\log\left(\frac{a_{Sr}}{a_V}\right) = \log(k) + 0.5\log(pO_2) - 3\log(pCO_2)$
SrVO$_3$/SrCO$_3$	$2SrCO_3 + 0.5O_2 + V \Leftrightarrow$ $Sr + SrVO_3 + 2CO_2$	$\log\left(\frac{a_{Sr}}{a_V}\right) = \log(k) + 0.5\log(pO_2) - 2\log(pCO_2)$
Sr$_3$V$_2$O$_8$/SrCO$_3$	$2.5SrCO_3 + 0.75O_2 + V \Leftrightarrow$ $Sr + 0.5Sr_3V_2O_8 + 2.5CO_2$	$\log\left(\frac{a_{Sr}}{a_V}\right) = \log(k) + 0.75\log(pO_2) - 2.5\log(pCO_2)$
Sr$_2$V$_2$O$_7$/SrCO$_3$	$2SrCO_3 + 0.75O_2 + V \Leftrightarrow$ $Sr + 0.5Sr_2V_2O_7 + 2CO_2$	$\log\left(\frac{a_{Sr}}{a_V}\right) = \log(k) + 0.75\log(pO_2) - 2\log(pCO_2)$
SrV$_2$O$_6$/SrCO$_3$	$1.5SrCO_3 + 0.75O_2 + V \Leftrightarrow$ $Sr + 0.5SrV_2O_6 + 1.5CO_2$	$\log\left(\frac{a_{Sr}}{a_V}\right) = \log(k) + 0.75\log(pO_2) - 1.5\log(pCO_2)$

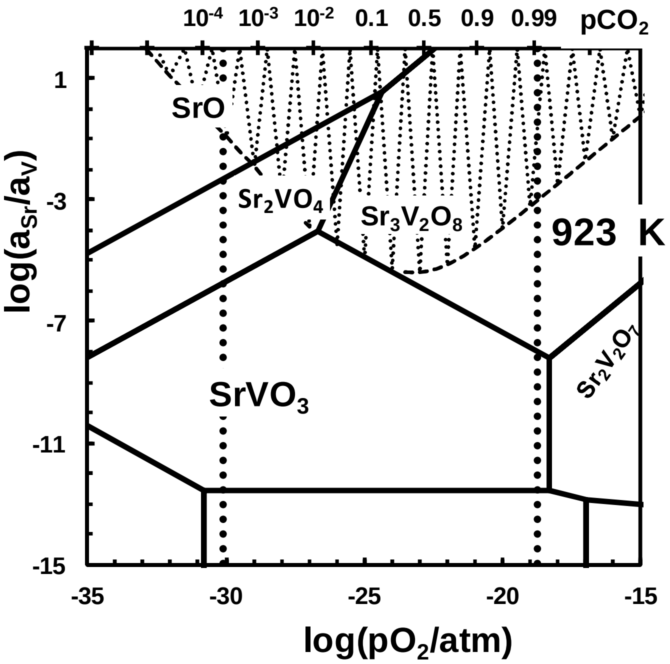

Fig 2.17. Redox equilibria for the Sr-V-O system at 1073K, and corresponding H_2/H_2O equilibrium. Vertical lines shows CO-rich conditions representative of CO_2 electrolysis (99% CO with η=-0.15V) and fuel cell conditions (90% CO_2 with η=0.1V (right)

In addition, the shaded area shows the conditions which may still lead to onset of carbonation ($SrCO_3$). Actually, these predictions indicate that the perovskite phase ($SrVO_3$) remains immune to carbonation at temperatures above 923 K, when only Sr-rich phases are prone to react with CO_2.

3. Redox transitions in strontium vanadates

This chapter focuses on the selected phase relationships in Sr-V-O system, including reversibility of redox transformation between V^{+4}-based $SrVO_{3-\delta}$ perovskite and V^{+5}-based strontium pyrovanadate ($Sr_2V_2O_7$) and orthovanadate ($Sr_3V_2O_8$), accompanying dimensional changes and variations of structural and electrical properties.

3.1 Crystal structure and microstructure of as-prepared materials

As prepared $SrVO_{3-\delta}$ ceramics were single phase with cubic perovskite structure (Fig 3.1A). The unit cell parameter shown in Table 3.1 was found to be close to previously reported values, which vary in the range 3.840-3.856 Å [Maekawa, 2004; Dougier, 1975A]. Sintered $SrVO_{3-\delta}$ ceramics were relatively porous with density ~80% of theoretical (Table 3.2) and grain size in the range 3-10 μm (Fig 3.2A).

Table 3.1
Unit cell parameters

Composition	Space group	Unit cell parameters	Unit cell volume(A)	Normalized volume[a] (A)
$SrVO_{3-\delta}$	Pm3m	a = 3.8498(3) A	57.06	57.06
$Sr_3V_2O_8$	R3m	a = 5.6194(3) A c = 20.1081(9) A	549.9	91.65
$Sr_2V_2O_7$	P1	a = 7.098 A α= 93.78º b = 12.980 A β = 90.88º c = 7.052 A γ = 99.45º	639.2	79.90

[a] per vanadium cation

All refection in the XRD pattern of as-prepared strontium pyrovanadate ceramics (Fig 3.1B) can be indexed on the basis of triclinic cell (space group P1) reported for α-$Sr_2V_2O_7$ single crystal [Huang, 1992]. The unit cell parameters (Table 3.1) were refined based on literature information, and allowed one to evaluate the relative density of pyrovanadate sintered ceramic (Table 3.2); this was ~89% of theoretical and grain size was in the range 8-55 μm (Fig 3.2B).

Though α-$Sr_2V_2O_7$ is often referred to as a high-temperature polymorph [Huang, 1992], a "low temperature" β-$Sr_2V_2O_7$ modification with tetragonal (space group $P4_1$) structured was reported however only in one work [Baglio, 1972] for single crystals prepared by a slow cooling of $Sr_2V_2O_7$-$NaVO_3$ mixture (7:50 weight ratio) from 1323 K.

Other authors [Huang, 1992] mentioned also that α → β phase transition occurs at ~918 K. Those authors pointed that heating of $2SrO:V_2O_5$ mixture below phase transition temperature produces β-$Sr_2V_2O_7$ while α-$Sr_2V_2O_7$ is formed at higher temperature. During this work, identical experiment was performed, but those observations were not confirmed: XRD pattern of $2SrO:V_2O_5$ mixture calcined in air at 853 K for 30 h with several intermediate regrinding still showed coexistence of α-$Sr_2V_2O_7$, $SrCO_3$ and some intermediate phases such as SrV_2O_6, with no indication of low temperature polymorph formation (Fig 3.3). Furthermore, no evidence of α → β transition on heating/cooling was observed by DSC and variable-temperature XRD for sintered and then powdered $Sr_2V_2O_7$ samples.

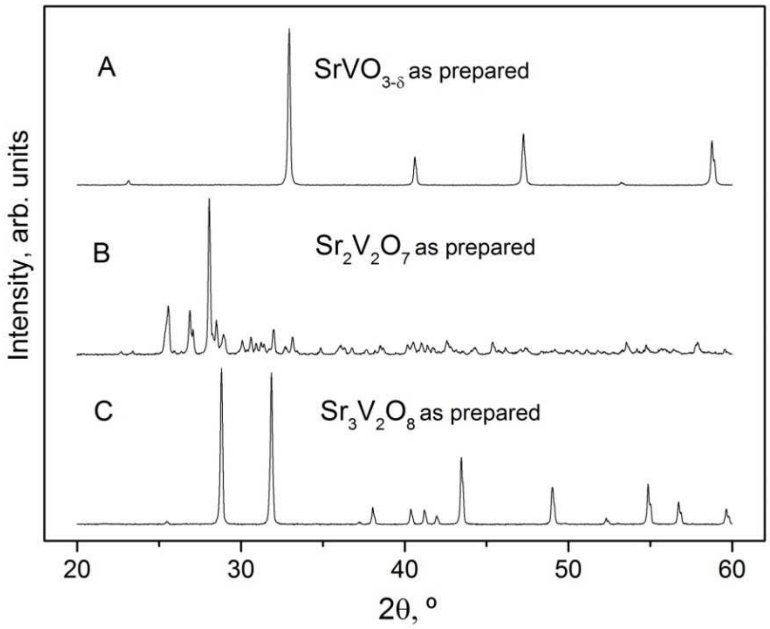

Fig 3.1. XRD patterns of as-prepared $SrVO_{3-\delta}$ **(A),** $Sr_2V_2O_7$ **(B)** and $Sr_3V_2O_8$ **(C)**.

XRD analysis of as-prepared strontium orthovanadate ($Sr_3V_2O_8$) samples showed formation of single-phase ceramics with rhombohedral lattice (space group R3m) (Fig. 3.1C) in agreement with the literature reports [Carrillo-Cabrera, 1993; Azdouz, 2010]. This compound is isostructural with orthophosphate $Sr_3(PO_4)_2$ and palmierite $PbK_2(SO_4)_2$ [Carrllo-Cabrera, 1993]; the calculated lattice parameters are listed in Table 1. The density of prepared ceramics was above 90% of theoretical (Table 3.2). Sintering at elevated temperature promoted however excessive grain growth (Fig 3.2C); these ceramic samples were quite brittle.

Table 3.2
Density and average thermal expansion coefficients

Composition	Density, g/cm^3	Relative density, %	Average TECs		
			Atmosphere	T, K	$(\alpha \times 10^6)\pm0.1$, K^{-1}
$SrVO_{3-\delta}$	4.33	80[a]	10% H_2-N_2	300-473/473-873/873-1223 300-1223	12.2/17.2/23.6 18.0
$Sr_3V_2O_8$	4.09	92	Air	373-873/873-1273 300-1273	12.8/16.9 14.3
$Sr_2V_2O_7$	3.61	89	Air	300-1023	15.0 ± 0.6

[a] theoretical density was calculated neglecting oxygen nonstoichiometry

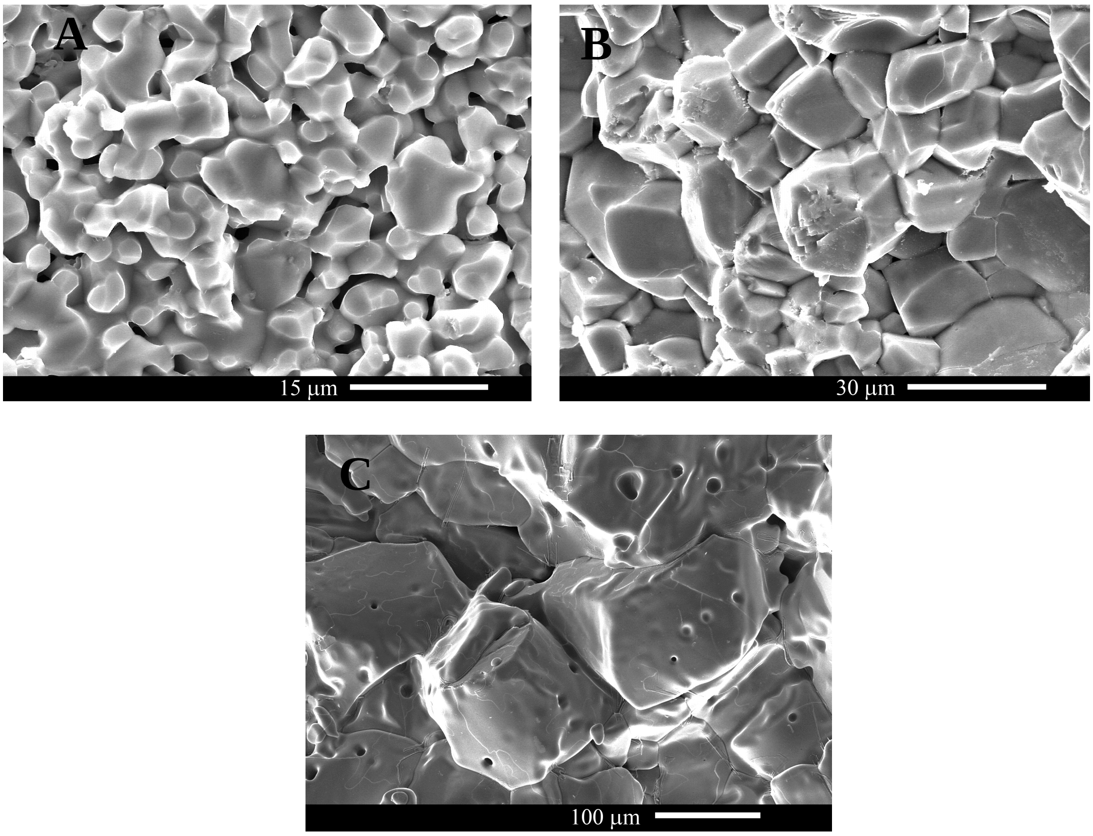

Fig.3.2. SEM micrographs of as-prepared fractured $SrVO_{3-\delta}$ **(A)**, $Sr_2V_2O_7$ **(B)** and $Sr_3V_2O_8$ **(C)** ceramics.

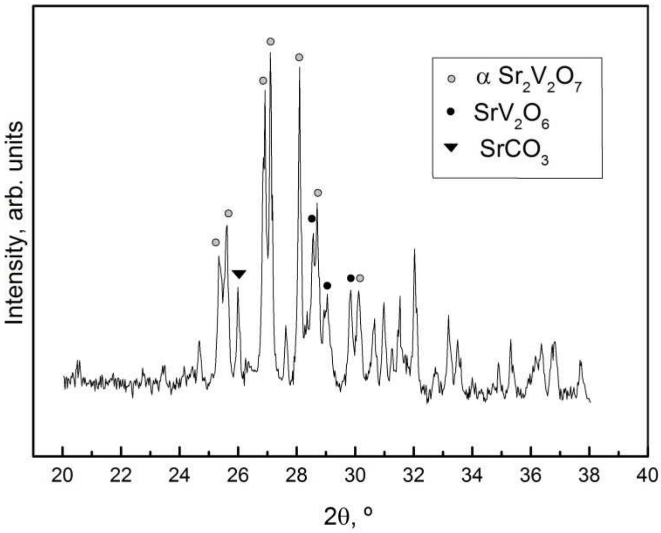

Fig 3.3. XRD patterns of $2SrO:V_2O_5$ mixture calcined in air at 853 K for 30 h.

3.2 Thermal expansion

Dilatometric curve of $SrVO_{3-\delta}$ ceramics in 10% H_2-N_2 atmosphere was found to exhibit a non-linear behaviour (Fig.3.4). Similar non-linearity is often observed for transition metal-based perovskites such as cobaltites and ferrites (e.g. Refs. [Yaremchenko, 2014; Lein, 2006]) and usually originates from the chemical contribution to thermochemical expansion. This chemical contribution is associated with the combined variations of oxygen nonstoichiometry and average oxidation state of transition metal cations induced by temperature or $p(O_2)$ changes. Indeed, the results of thermogravimetric studies also confirmed non-negligible variations of oxygen deficiency in $SrVO_{3-\delta}$ on heating/cooling (inset in Fig.3.4)

The average thermal expansion coefficient (TEC) of $SrVO_{3-\delta}$ at 300-1223 K was calculated to be equal to 18.0×10^{-6} K^{-1} (Table 3.2) and, in high-temperature range characteristic for SOFC operation, it reaches a value as high as 23.6×10^{-6} K^{-1}. These TEC values are substantially higher compared to those of common solid electrolytes such as stabilized zirconia, doped ceria and lanthanum gallate. This mismatch in thermal expansion impedes thermomechanical compatibility of strontium vanadate-based electrodes with solid electrolyte ceramics and needs to be adjusted via appropriate substitutions.

$Sr_3V_2O_8$ exhibits lower thermal expansion (Fig 3.4) with average TEC equal to 14.3×10^{-6} K^{-1} at 300-1273 K (Table 3.2). The obtained TEC values are in good agreement with the data reported previously by Simner et al. [Simner, 2000].

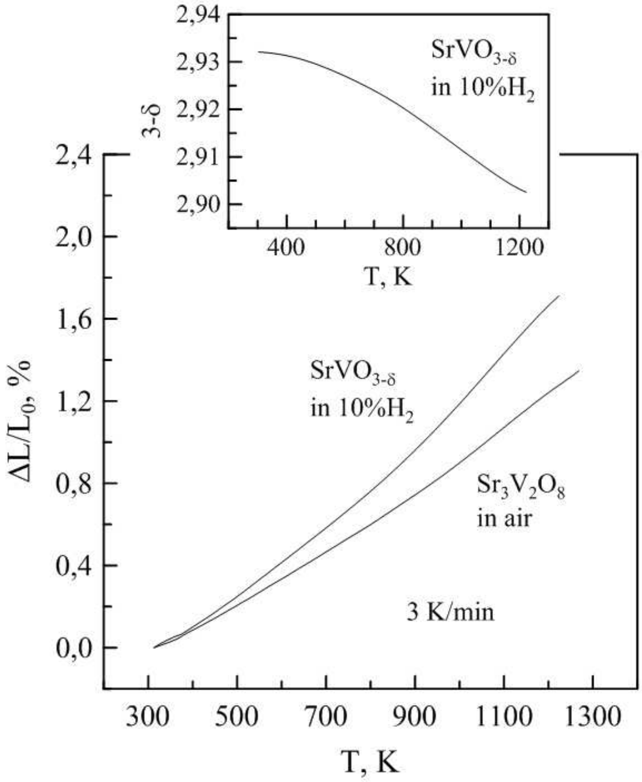

Fig. 3.4. Dilatometric curves of $SrVO_{3-\delta}$ ceramics in 10 % H_2-N_2 and $Sr_3V_2O_8$ ceramics in air. Inset shows variations of oxygen nonstoichiometry in $SrVO_{3-\delta}$ in 10 % H_2-N_2 atmosphere calculated from the thermogravimetric data.

Dilatometric behaviour of $Sr_2V_2O_7$ samples on heating in air was poorly reproducible. As example, Fig 3.5 shows the dilatometric curves for two ceramic samples in two consecutive runs in different temperature ranges. Still, there are several specific features. Firstly, all curves exhibit an anomaly (a change of slope o break) on heating at 673-773 K. The nature of this anomaly is not understood; as mentioned above, XRD and DSC results did not confirm the $\alpha \rightarrow \beta$ phase transition. Secondly, compared to the first run (heating and cooling in air), dilatometric curves in the second and subsequent runs typically show lower slope below 673 K and higher slope above 773 K. After keeping at room temperature for several days or annealing at low temperatures, the dilatometric curve again shows the first-run behaviour. Most likely, this phenomenon can be attributed to a slow lattice relaxation at lower temperature resulting in hysteresis of dimensional changes in heating/cooling cycles. This is partially confirmed by a tendency to expansion on cooling below ~323 K (Figure 3.5B). The TEC value on heating at 300-1023 K, averaged for several samples in several runs, corresponds to 15.0×10^{-6} K^{-1} (Table 3.2). The third feature relates to a deviation from the linear behaviour and even apparent shrinkage of $Sr_2V_2O_7$ samples on heating above ~ 1100 K. This behaviour can be attributed to deformation of ceramic samples under mechanical load in dilatometric equipment when temperature gets closer to the melting point.

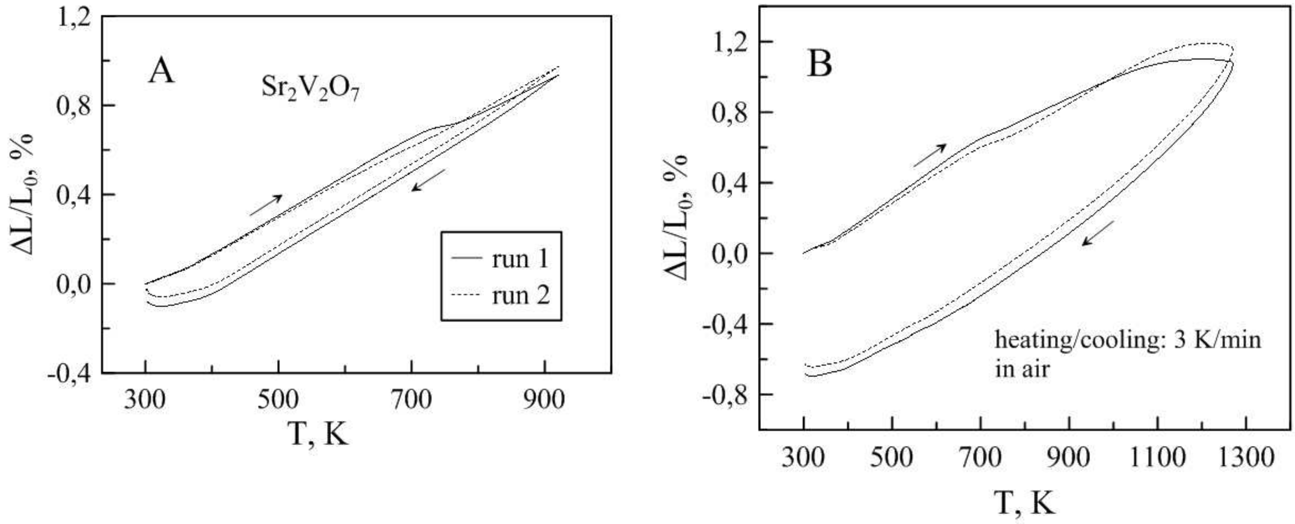

Fig 3.5. Dilatometric curves of $Sr_2V_2O_7$ ceramics in air in two subsequent runs in different temperature ranges.

3.3 Electrical conductivity

In agreement with literature reports [Yaremchenko, 2013; Cheng, 2005; Hui, 2001], electrical conductivity of perovskite type $SrVO_{3-\delta}$ exhibits metallic-like behaviour under reducing conditions in the studied temperature range (Fig 3.6A). The conductivity values reach 500-1300 S/cm at 873-1173 K. Note that the measured conductivity values are underestimated to some extent due to relatively high porosity of ceramic samples, already commented above. The electrical conductivity shows rather minor dependence on oxygen partial pressure slightly decreasing with reducing $p(O_2)$ (Fig 3.6B).

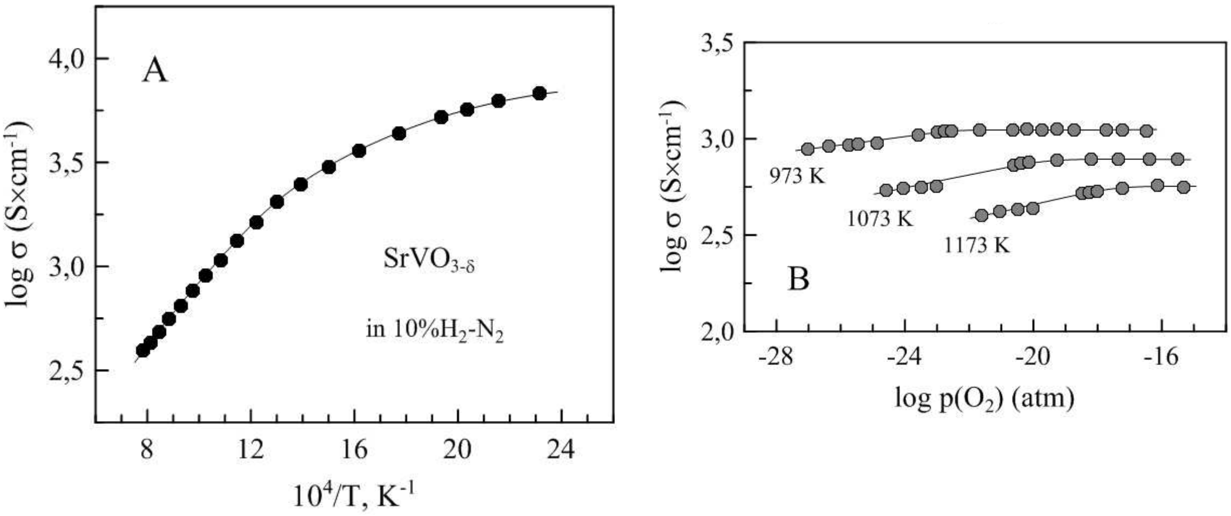

Fig.3.6. Electrical conductivity of $SrVO_{3-\delta}$ ceramics as function of temperature in 10%H_2 atmosphere **(A)** and as function of oxygen partial pressure at 973-1173 K **(B).**

Metallic conductivity in $SrVO_3$ perovskite is generally attributed to the presence of V^{+4} cations in $3d^1$ configuration forming broad conduction band [Dougier, 1975; Giannakopoulou, 1995; Palanisamy, 1975]. The behaviour of electrical conductivity can be explained by increasing oxygen deficiency and reduction of vanadium cations when shifting to lower $p(O_2)$:

$$2V^{+4} + O^{2-} \rightarrow 2V^{3+} + \frac{1}{2}O_2 \qquad \text{Eq. 3.1}$$

with electroneutrality condition

$$\left[V^{4+}\right] = 1 - 2\delta \qquad \text{Eq. 3.2}$$

This results in a lower concentration of tetravalent vanadium and increasing electron scattering on trivalent vanadium cation, and, therefore, minor decrease in conductivity.

Electrical conductivity of V^{+5}-based phases measured under oxidizing conditions is ~6-8 order of magnitude lower compared to that of $SrVO_{3-\delta}$ at 873-1273 K (Fig.3.7). The data on $Sr_2V_2O_7$ in air was found to be in good agreement with the results reported by Krasnenko et al. [Krasnenko, 1991]. Both $Sr_2V_2O_7$ and $Sr_3V_2O_8$ exhibit semiconducting behaviour. Strontium pyrovanadate shows higher conductivity than orthovandate at elevated temperatures, but also higher activation energy in the entire studied temperature range (Table 3.3).

Table 3.3
Activation energy for electrical conductivity

Composition	p(O_2), atm	T, K	E_A, kJ/mol
$Sr_2V_2O_7$	0.21	850-1200 / 1200-1290	88.9±0.3 / 155±13
	10^{-5}	850-1170 / 1170-1290	99±1 / 160±6
$Sr_3V_2O_8$	0.21	850-1170 / 1170-1290	32.2±0.3 / 80±3
	10^{-5}	850-1170 / 1170-1290	44.2±0.8 / 104±6

Note: The activation energy was calculated using Arrhenius model $\sigma = (A_0/T)\exp(-E_A/(RT))$.

It was suggested previously that $Sr_2V_2O_7$ and $Sr_3V_2O_8$ are predominantly ionic conductors [Krasnenko, 1984,1991; Leonidov 1992; Leonidova, 1996,]; the results of transference numbers determination by Tubandt (Faradaic efficiency) technique [Porotnikov,1989] and ^{90}Sr radioisotope diffusion studies [Leonidova, 1998] indicate that the major ionic charge carriers are Sr^{+2} cations. Reducing oxygen partial pressure from atmospheric to 5×10^{-5} atm decreases the total electrical conductivity (Fig 3.7), most likely, due to decreasing partial p-type electronic conduction, in agreement with literature data [Krasnenko, 1984]. The contribution of p-type electronic transport increase on heating as indicated by an increase of activation energy for the total conductivity above 1170 K (Figure 3.7 and Table 3.3).

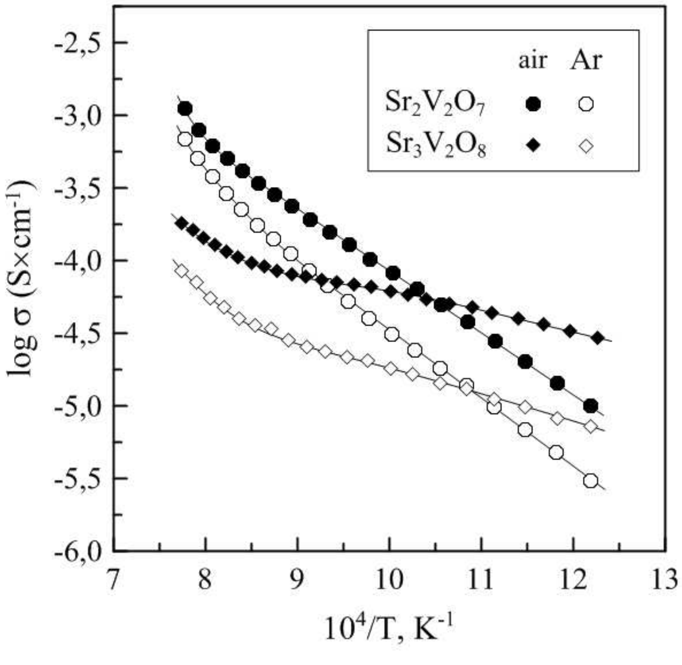

Fig.3.7. Temperature dependence of electrical conductivity of $Sr_2V_2O_7$ and $Sr_3V_2O_8$ ceramics in air and in Ar atmosphere (p(O_2) ~5×10^{-5} atm).

3.4 Redox transitions

3.4.1 Reduction of strontium orthovanadate

In addition to initial rhombohedral phase, the XRD pattern of $Sr_3V_2O_8$ reduced in flowing 10% H_2-N_2 mixture at 1173 K for 25 h showed only the traces of cubic perovskite phase (Fig. 3.8A). Very minor oxygen losses upon heating in the same atmosphere were demonstrated by thermogravimetric analysis (Fig. 3.8B), and the average oxidation state of vanadium cations after temperature increase up to 1273 K was still equal to ~4.98+. These results indicate quite good redox stability of orthovanadate lattice even under reducing conditions. In agreement with that, reduction at 1173 K resulted only in a minor increase on electrical conductivity (Fig. 3.8C) indicating partial transformation to the highly conducting $SrVO_{3-d}$ perovskite phase. After 30 h of reduction, electrical conductivity was still below 10^{-3} S/cm.

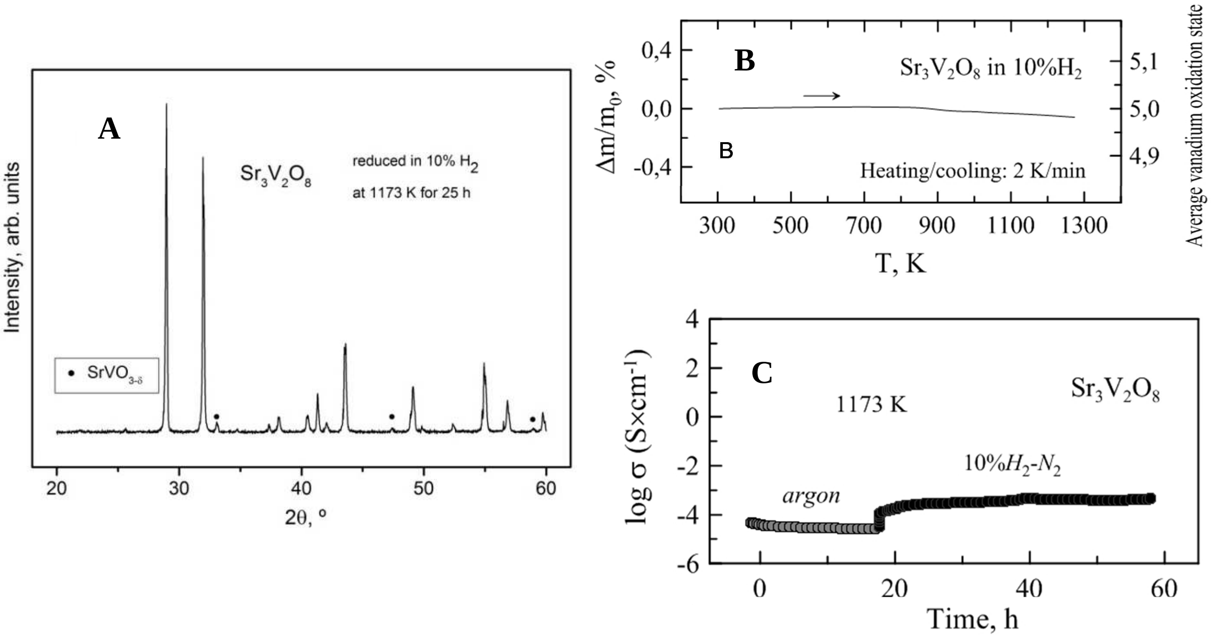

Fig.3.8. XRD pattern of $Sr_3V_2O_8$ reduced in 10%H_2 flow at 1173 K for 25 h **(A)**; thermogravimetric curves of powdered $Sr_3V_2O_8$ on heating in 10% H_2 flow (**B**); and variation of electrical conductivity of $Sr_3V_2O_8$ ceramics with time at 1173 K upon reduction in 10%H_2 **(C)** .

3.4.2 Reduction of strontium pyrovanadate

Reduction of $Sr_2V_2O_7$ in flowing 10%H_2-N_2 atmosphere at 1173 K for 25 h yielded a phase mixture comprising cubic perovskite as a major phase and $Sr_3V_2O_8$ as a secondary phase (Fig 3.9A). The presence of some amount of additional secondary phase, undetected by XRD, should be anticipated considering the mass balance.

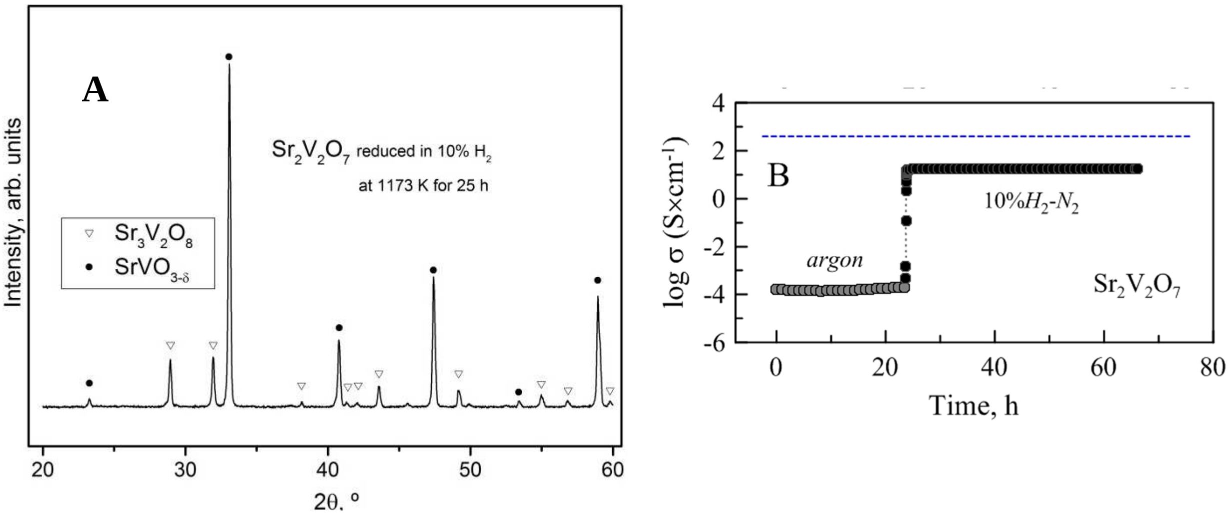

Fig.3.9. XRD pattern of $Sr_2V_2O_7$ reduced in 10% H_2 flow at 1173 K for 25 h **(A)** and variation of electrical conductivity of $Sr_2V_2O_7$ ceramic with time at 1173 K upon reduction in 10% H_2 flow **(B).** Dotted line corresponds to conductivity value of as-prepared $SrVO_{3-\delta}$ ceramics in 10% H_2 atmosphere at given temperature.

Thermogravimetric analysis shows that reduction of $Sr_2V_2O_7$ in 10%H_2-N_2 either on heating (Fig 3.10A) or isothermal treatment at 1173 K (Fig.3.10B) takes place in two steps. The first step occurs very fast in the course of isothermal reduction at 1173 K, and corresponds to temperature range 833-1023 K on constant heating at 2 K/min. The second step has slower kinetics and was not fully accomplished under applied experimental conditions. The boundary between those two steps is indicated by a break on the reduction curves corresponding to average vanadium oxidation state of ~ (4.375-4.390)+.

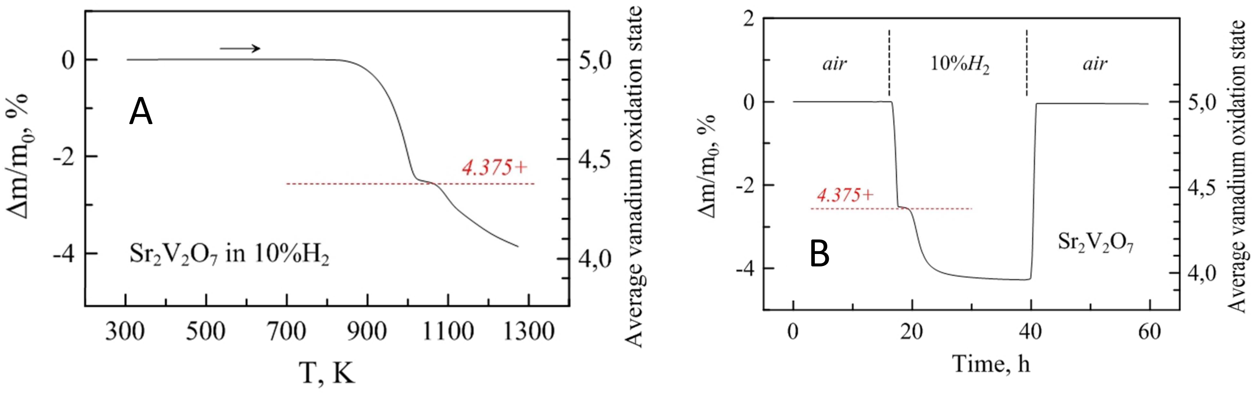

Fig 3.10. Thermogravimetric curves of powdered $Sr_2V_2O_7$ on heating in 10% H_2 flow **(A)** and relative weight change of powdered $Sr_2V_2O_7$ in one redox cycle at 1173 K **(B)**. Average oxidation state of vanadium cations was calculated assuming that all V is in 5+ state after equilibration with air.

To identify the path of transformations, several $Sr_2V_2O_7$ powdered samples were heated in 10%H_2-N_2 flow in TGA equipment to different temperatures with subsequent fast cooling and XRD analysis. XRD pattern of the sample heated to 1013 K showed the presence of only one phase – $Sr_3V_2O_8$ (Fig 3.11A). Very minor traces of additional phase identified as SrV_6O_{11} can be found in XRD pattern of the sample heated to 1043 K (Fig 3.11B). Heating to 1073 K resulted in appearance of perovskite phase and minor traces of V_2O_3 (Fig 3.11C).

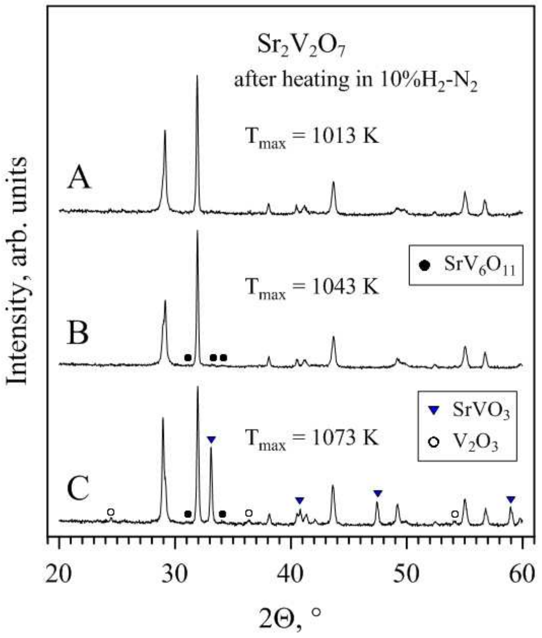

Fig. 3.11. XRD patterns of powdered $Sr_2V_2O_7$ samples heated in 10% H_2-N_2 flow in TGA equipment to T_{max} at 2 K/min and then immediately cooled to room temperature at 10 K/min.

In all cases, some broadening of the peak at 2Θ ~29.0 - 29.2º, corresponding to 015 reflection of $Sr_3V_2O_8$ phase, and variations of its intensity may be ascribed to inhomogeneous lattice parameter distribution across the sample in the course of dynamic phase transformation on heating.

Taking these XRD data into account, the major path of reduction reaction can be expressed as:

$$8Sr_2V_2O_7 \xrightarrow{-2.5O_2} 5Sr_3V_2O_8 + SrV_6O_{11} \xrightarrow{-xO_2} 8SrVO_{3-\delta} \qquad \text{Eq.3.3}$$

with a fast decomposition of pyrovanadate into orthovanadate and SrV_6O_{11} mixture and slow subsequent transformation into perovskite phase.

Assuming oxygen-stoichiometric compositions, the average oxidation state of vanadium cations in ($5Sr_3V_2O_8$ + SrV_6O_{11}) mixture equals to +4.375, thus being in agreement with thermogravimetric results. Formation of perovskite phase is kinetically stagnated at 1173-1273 K resulting in co-existing phases. Indeed, SrV_6O_{11} is a minority phase and often cannot be detected by XRD. These observations were already reported in literature [Li, 1994]. Re-oxidation of the phase mixture results in fast reversible formation of $Sr_2V_2O_7$ (Fig 3.10B) as confirmed by XRD.

Reduction of $Sr_2V_2O_7$ ceramics at 1173 K leads to sharp increase of electrical conductivity by 5 orders of magnitude (Fig 3.9B). The conductivity of reduced materials is however till about one order of magnitude lower compared to single-phase $SrVO_{3-\delta}$ and remains essentially unchanged for longer reduction time. This can be attributed to the presence of noticeable amount of insulating $Sr_3V_2O_8$ phase co-existing with highly-conducting perovskite. XRD pattern of ceramic sample crashed after the electrical conductivity measurement cycle was nearly identical to that of the powdered sampled reduced for 25 h at the same temperature (Fig 3.9A).

Heating of $Sr_2V_2O_7$ ceramics in reducing atmosphere results in a shrinkage (Fig. 3.16A), as can be expected from the XRD data for individual phases (Table 3.1). Similar to relative weight change (Fig 3.10A), samples shrinkage occurs in two steps, although the onset of each step is shifted to higher temperature due to slower reduction kinetics as expected for bulk ceramics. After subsequent cooling to room temperature, sample contraction corresponded to ~7% in volume, which is much smaller than the volume change for complete conversion $Sr_2V_2O_7$ to $SrVO_{3-\delta}$ (~29%) as given by differences I unit cell volume per vanadium cation (Table 3.1). Once more, contraction after thermochemical cycling in reducing atmosphere indicates that the fraction of perovskite phase is still relatively small (~24%), which is consistent with the XRD pattern of the sample showing a mixture of $Sr_3V_2O_8$, $SrVO_{3-\delta}$, SrV_6O_{11} and some additional phase identified as VO_2. We also should take into the account that a fraction of amorphous phase may also be present because the melting temperatures of oxidized vanadium-rich phases are relatively low [Brown, 1972; Fotiev, 1985]. Tests on dimensional changes during redox treatments showed also that these changes are not reversible (Fig 3.12), probably due to microstructural alterations. While reduction leads to a rather small contraction, in agreement with the dilatometric data, re-oxidation results in a noticeable expansion of ceramic compared to initial dimensions.

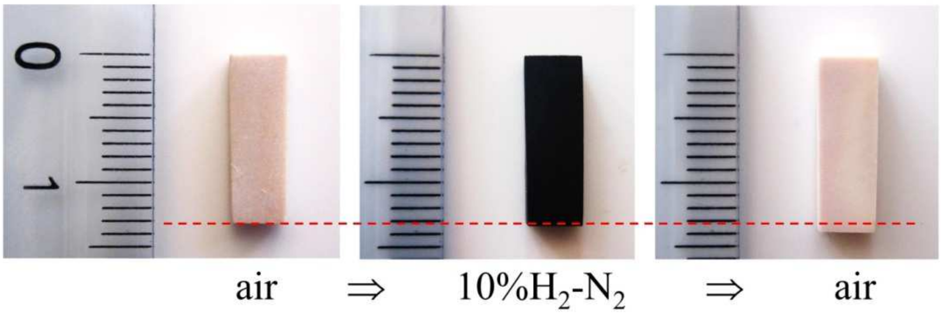

Fig 3.12. Image of bar-shaped $Sr_2V_2O_7$ ceramic samples illustrating irreversible length changes after redox treatments.

3.4.3 Oxidation of perovskite-type strontium vanadate

Thermogravimetric results (Fig 3.13A) suggest that oxidation of $SrVO_{3-\delta}$ on heating in air occurs in several step, in agreement with literature [Rey, 1990; Brown, 2005]. The first step starting at ~373 K is presumably associated with $V^{+3} \rightarrow V^{+4}$ oxidation and filling of oxygen vacancies, and is followed by a nearly plateau-like behaviour at 523 -653 K. Massive $V^{+4} \rightarrow V^{+5}$ oxidation at 673-1073 K results in a collapse of perovskite lattice and formation of strontium pyrovanadate phase, as confirmed by XRD analysis. (Fig 3.14B). The sample weight was constant on subsequent cooling. It was assumed, therefore, that all vanadium cations in oxidized sample are in 5+ oxidation state, thus making possible the calculations of oxygen nonstoichiometry in as-prepared $SrVO_{3-\delta}$ samples (see above).

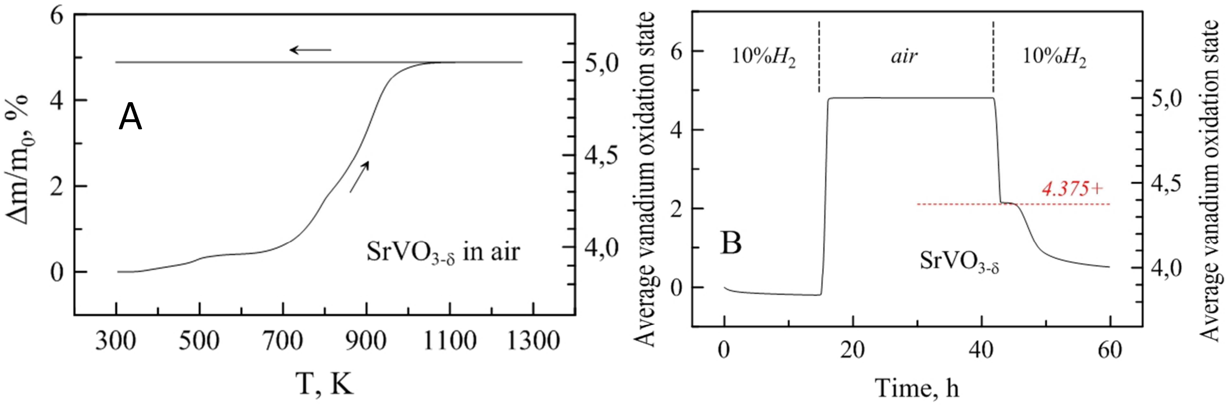

Fig.3.13. Thermogravimetric curves of powdered $SrVO_{3-δ}$ samples on heating in 10% H_2 flow **(A)** and in the course of isothermal treatment at 1173 K **(B)**

Thermogravimetric studies at 1173 K demonstrated very fast $SrVO_{3-δ}$ → $Sr_2V_2O_7$ transformation on oxidation (Fig 3.13B). The mechanism of reverse reduction of previously oxidized samples seems reasonably close to explained above (Eq. 3.3). XRD inspection confirmed that reduction in 10% H_2-N_2 flow for 25 h at 1173 K yielded a mixture of perovskite as a major phase with $Sr_3V_2O_8$ as secondary phase and traces of SrV_6O_{11} (Fig 3.14A).

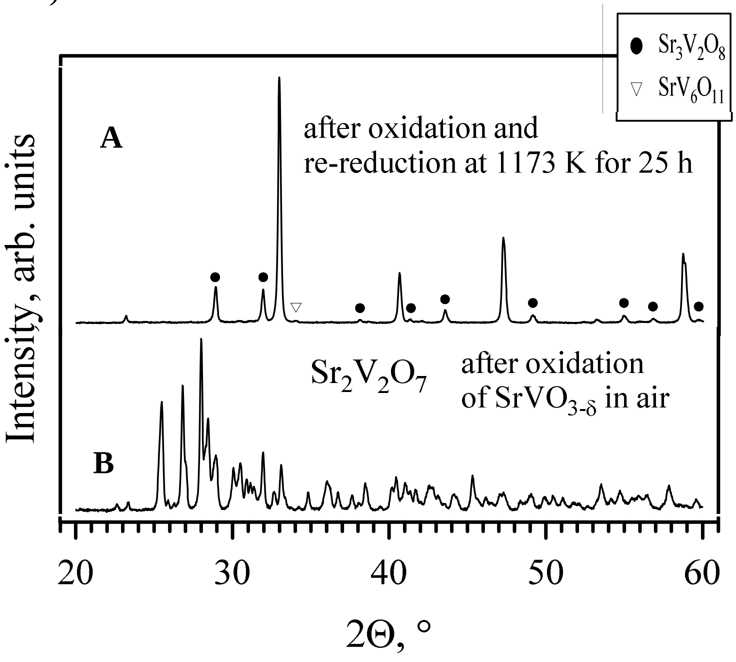

Fig 3.14. XRD patterns: after oxidation in air for 25 h at 1173 K and subsequent re-reduction in 10% H_2 flow at 1173 K for 25h **(A),** and $Sr_2V_2O_7$ obtained by oxidation of $SrVO_{3-δ}$ on heating in air to 1273 K **(B)**. Marked reflections are indexed according to JCPDS PDF #79-8160 and 81-1844.

The variations of electrical conductivity of $SrVO_{3-\delta}$ ceramics on oxidation-reduction cycle at 1173 K were in agreement with the phase changes, as expected. Oxidation results in ~6 orders of magnitude drop of conductivity due to transformation into strontium pyrovanadate phase (Fig. 3.15). The inverse reduction results in relatively fast increase of conductivity; however, the initial level observed for as-prepared $SrVO_{3-\delta}$ samples is not achieved even after 15 h, mainly due to a slow recovery of perovskite phase. XRD pattern of the ceramic sample after this experiment was almost identical to the one shown above (Fig 3.14A).

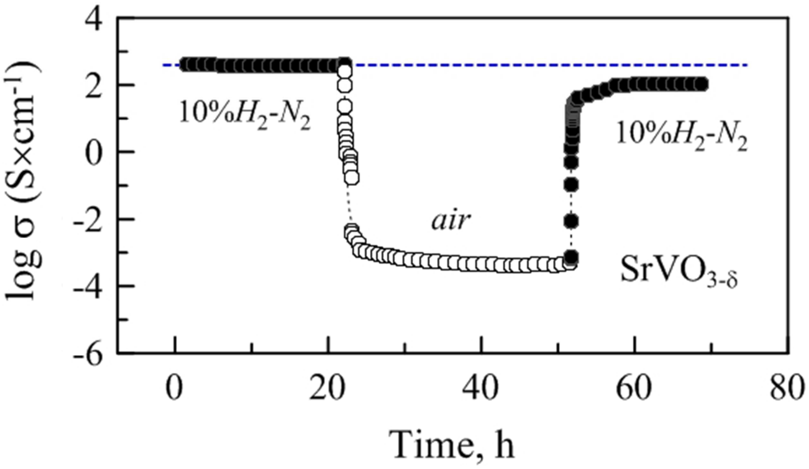

Fig.3.15. Variations of electrical conductivity of $SrVO_{3-\delta}$ ceramic samples with time at 1173 K upon oxidation in air and subsequent re-reduction in 10%H_2. Dotted line corresponds to conductivity value of as prepared $SrVO_{3-\delta}$ ceramics in 10% H_2 at given temperature.

Dilatometric measurements confirmed that oxidation of $SrVO_{3-\delta}$ ceramics on heating in air leads to significant volume expansion above 850 K (Fig 3.16A). Linear elongation of ceramic sample after heating/cooling cycle corresponded to ~9%. This is lower than expected 13.3% assuming complete conversion to $Sr_2V_2O_7$ and comparing unit cell volumes per vanadium cation (Table 3.1), but can be explained by noticeable porosity of $SrVO_{3-\delta}$ samples (Table 3.2) in combination with tendency of $Sr_2V_2O_7$ ceramics to deformation above ~1100 K (Fig 3.5B). The tests showed also that expansion on oxidation may be accompanied with appearance of cracks in ceramics samples (Fig. 3.16B). Inverse reduction did not result in reversible volume shrinkage, partly due to incomplete recovery of perovskite phase.

Finally, Figure 3.17 shows XRD patterns of $SrVO_{3-\delta}$ samples annealed at 1173 K in inert gas atmosphere with slightly different oxygen partial pressures. The results of phase analysis indicate that perovskite phase is not stable under these conditions, in agreement with some reports [Hui, 2001; Cheng, 2005]. The decomposition is slow at $p(O_2) = 5\times10^{-5}$ atm: only traces of $Sr_3V_2O_8$ and SrV_6O_{11} impurities were observed after annealing for 24 h (Fig. 3.17A). Treatment in slightly more oxidizing atmosphere with $p(O_2) = 10^{-4}$ atm and for longer time results however in a complete transformation into $Sr_3V_2O_8$ and SrV_6O_{11} mixture with some traces of $Sr_2V_2O_7$ (Fig 3.17B). These observations confirm that redox transformation between perovskite-type $SrVO_3$ and strontium pyrovanadate occurs through $Sr_3V_3O_8$ + SrV_6O_{11} intermediate.

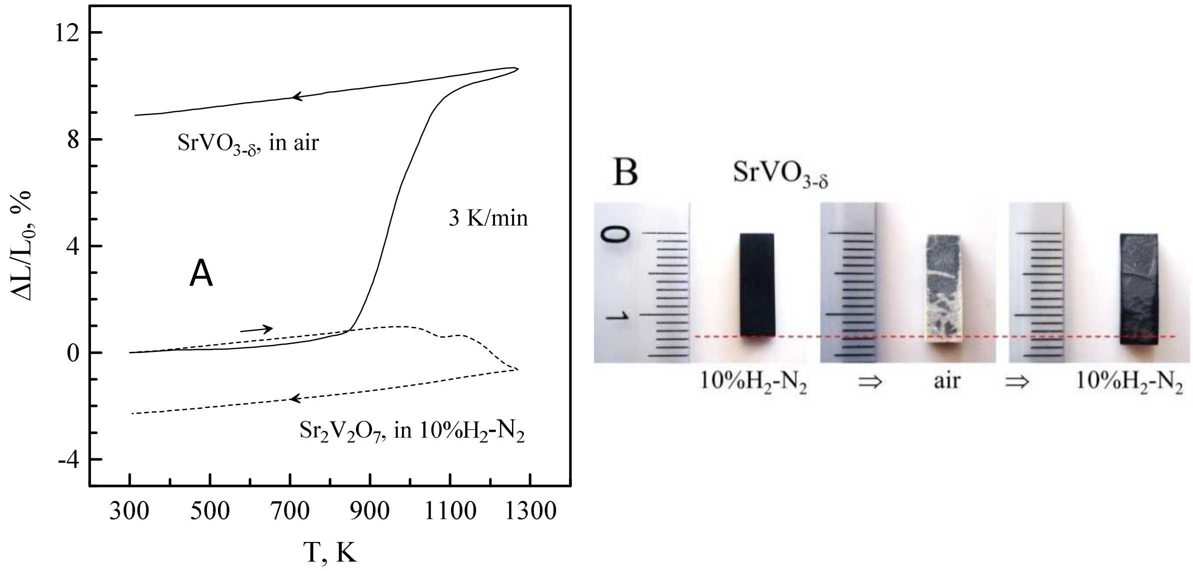

Fig. 3.16. Dilatometric curves on heating and subsequent cooling of $SrVO_{3-\delta}$ ceramic in air and $Sr_2V_2O_7$ ceramics in 10%H_2 **(A),** and images of bar-shaped $SrVO_{3-\delta}$ ceramic sample illustrating irreversible length changes after consecutive redox treatments **(B).** Each treatment included heating/cooling (5 K/min) in a given atmosphere with annealing at 1273 K for 1 h.

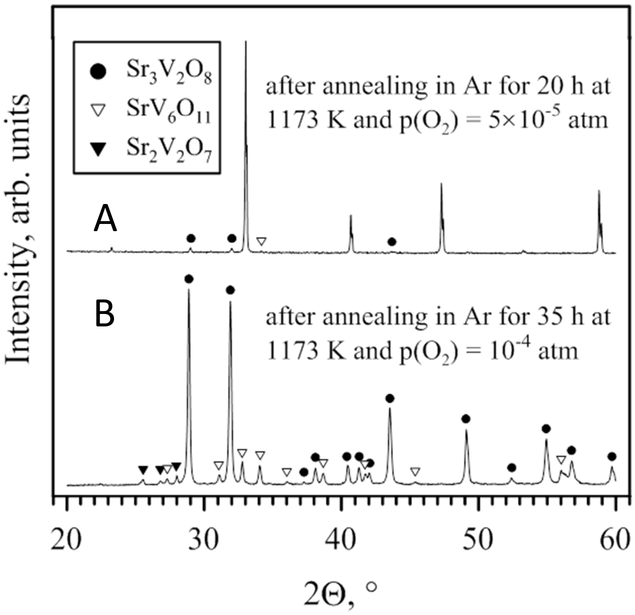

Fig.3.17. XRD patterns of $SrVO_{3-\delta}$ samples: after annealing in flowing Ar atmosphere with $p(O_2) = 5\times10^{-5}$ atm at 1173 K for 20h **(A)**; after annealing in flowing Ar atmosphere with $p(O_2) = 10^{-4}$ atm at 1173 K for 35 h **(B)**. Marked reflections are indexed according to JCPDS PDF # 81-1844 ($Sr_3V_2O_8$), 79-8160 (SrV_6O_{11}) and 81-0837 ($Sr_2V_2O_7$).

3.5 Final remarks and conclusions

Table 3.4 summarizes the obtained results on redox-induced transitions between strontium vanadates at elevated temperatures. Thus, the transformation of $Sr_2V_2O_7$ into $SrVO_{3-\delta}$ occurs via relatively stable intermediate, $Sr_3V_2O_8$, and is kinetically stagnated at temperatures ≤ 1273 K. Due to this, perovskite phase cannot be recovered after oxidation-reduction cycle at these temperatures, at least in a reasonable time span. Taking also into account significant volume changes in redox cycles and apparently irreversible microstructural changes, stabilization of perovskite phase up to high oxygen partial pressures is required for practical use of $SrVO_3$ in SOFC anodes.

Table 3.4

Phase compositions as result of thermal/redox treatments

Initial phase	Treatment	Product
$SrVO_{3-\delta}$	air, heating above 1073 K	$Sr_2V_2O_7$
	Ar, $p(O_2) = 5\times10^{-5}$ atm, 1173 K, 20 h	$SrVO_{3-\delta}$ + $Sr_3V_2O_8$ (traces) + SrV_6O_{11} (traces)
	Ar, $p(O_2) = 10^{-4}$ atm, 1173 K, 35 h	$Sr_3V_2O_8$ (major) + SrV_6O_{11} + $Sr_2V_2O_7$ (traces)
	10%H_2 → air (25 h) → 10%H_2 (25 h), 1173 K	$SrVO_{3-\delta}$ (major) + $Sr_3V_2O_8$ + SrV_6O_{11} (traces)
$Sr_2V_2O_7$	10%H_2, 1173 K, 25 h	$SrVO_{3-\delta}$ (major) + $Sr_3V_2O_8$
$Sr_3V_2O_8$	10%H_2, 1173 K, 25 h	$Sr_3V_2O_8$ (major) + $SrVO_3$ (traces)

Note: $p(O_2)$ in 10%H_2-N_2 atmosphere corresponded to ~ 10^{-19} atm at 1173 K.

The final conclusions of this chapter can be summarized as following:

i) Electrical conductivity and thermal expansion of $SrVO_{3-\delta}$, $Sr_3V_2O_8$ and $Sr_2V_2O_7$ were characterized under conditions corresponding to the phase stability domains;

ii) At 873-1273 K, metallic-like electronic conductivity in $SrVO_{3-\delta}$ is 6-8 orders of magnitude higher compared to semiconducting strontium orthovanadate and pyrovanadate;

iii) $Sr_3V_2O_8$ ceramics are relatively stable even under reducing conditions corresponding to 10%H_2-N_2 atmospheres, and undergoes very slow decomposition at temperatures $\leq$ 1273 K;

iv) Reduction-induced transformation of $Sr_2V_2O_7$ into $SrVO_{3-\delta}$ perovskite occurs in two steps through ($5Sr_3V_2O_8$+SrV_6O_{11}) intermediate. Due to relative stability of strontium orthovanadate, this process is kinetically stagnated at temperatures $\leq$ 1273 K yielding a mixture of co-existing phases;

v) As a result, perovskite phase and conductivity level cannot be recovered completely in a reasonable time span after oxidation-reduction cycle at these temperatures;

vi) Dilatometric studies confirmed that $SrVO_3 \leftrightarrow Sr_2V_2O_7$ redox transformation is accompanied with significant dimensional changes. These changes are irreversible, most likely, due to microstructural alterations. Their extent reasonably depends on a degree of phase transformation.

4. Effect of niobium substitution

It is demonstrated in the previous chapters that, in spite of some attractive advantages of perovskite-type strontium vanadate as anode material, there are a number of drawbacks hindering application of $SrVO_3$-based anodes in SOFC. This chapter is focused on the effect donor-type niobium doping into vanadium sublattice aiming to overcome these disadvantages. The work included detailed studies of redox behavior, stability limits, electrical conductivity and thermochemical expansion of Nb-substituted $SrVO_3$, as well as elaboration of the structural and defect chemistry guidelines for $Sr(V,Nb)O_3$-based system.

4.1 Phase composition, structure and microstructure

Fig 4.1 shows selected XRD patterns of the as-prepared $SrV_{1-x}Nb_xO_{3-\delta}$ ceramics. For x ≥ 0.10, the first sintering attempts after calcinations at 1173 K yielded ceramics samples containing $Sr_3V_2O_8$ and other phase impurities in addition to the target perovskite phase (Fig.4.1A). Therefore, an intermediate high-energy milling step was introduced to promote the homogenization of precursor powders and to facilitate the phase formation.

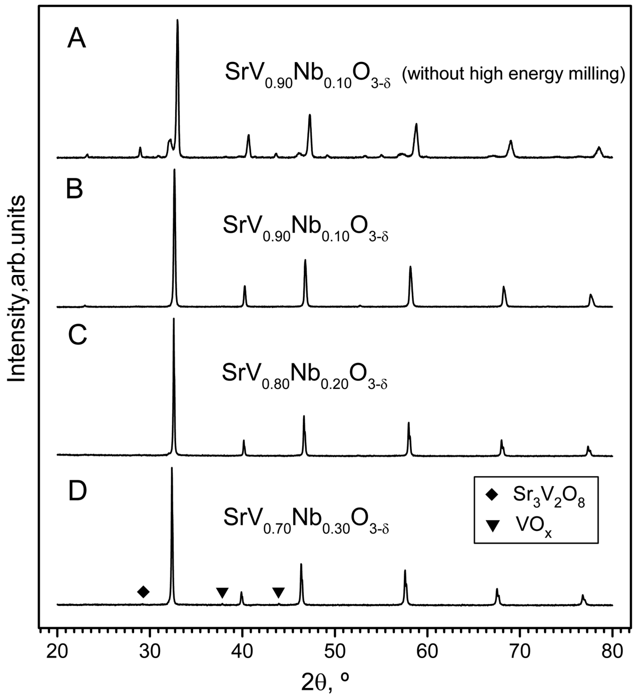

Fig.4.1. XRD patterns of as-sintered $SrV_{1-x}Nb_xO_{3-\delta}$ ceramics.

As-prepared compositions with x ≤ 0.20 were single-phase with cubic perovskite structure (space group $Pm\bar{3}m$) characteristic of parent $SrVO_{3-\delta}$ (Fig 4.1B and C). The presence of minor amounts of $Sr_3V_2O_8$ and $VO_{1+\delta}$ impurities was found in the XRD pattern of $SrV_{0.70}Nb_{0.30}O_{3-\delta}$ (Fig. 4.1D).

The substitution of higher-valence Nb^{+5} cations into the V^{+4} sublattice may be charge-compensated by the formation of V^{+3} cations, possibly in combination with a decrease in the residual fraction of pentavalent V^{+5}, and also decrease in the concentration of positively charged oxygen vacancies or the corresponding oxygen sub-stoichiometry, as follows:

$$[Nb_B^{\bullet}] + [\,B_B^{\bullet}] + 2[V_O^{\bullet\bullet}] = [B_B^{\prime}] \qquad \text{Eq. 4.1}$$

where symbol B is used for the parent B-site species (vanadium):

$$[\,B_B^{\bullet}] \equiv V^{+5}$$

$$[\,B_B^{\prime}] \equiv V^{+3}$$

$$[\,B_B^{\times}] \equiv V^{+4}$$

to avoid confusion with the usual notation of V for vacancies. Larger ionic radii of Nb^{+5} (r^{VI} = 0.64 A) and V^{+3} (r^{VI} = 0.64 A) cations compared to V^{+4} (r^{VI} = 0.58 A) explain a continuous increase of the unit cell parameter with x (Table 4.1). One should note that niobium cations may also undergo partial reduction to 4+ oxidation state under reducing conditions, as emphasized by oxygen nonstoichiometry changes in $Nb_2O_{5-\delta}$, reaching an oxygen deficiency δ close to 0.1 (i.e. $[Nb^{+4}]/[Nb] \leq 10\%$) in the latter oxide at 1173 K and $p(O_2) \sim 10^{-19}$ atm [Kofstad, 1968].

Table 4.1
Properties of as-prepared $SrV_{1-x}Nb_xO_{3-\delta}$ ceramics[a]

x	Unit cell parameter a, Å	Density, g cm^{-3}	Relative density, %
0	3.8498(3)	4.33	80
0.03	3.8642(4)	4.05	75
0.05	3.8672(4)	3.96	73
0.10	3.8827(3)	4.04	75
0.20	3.9015(3)	5.03	92
0.30	3.9284(5)	3.21	59

[a] Note: theoretical density was calculated neglecting possible oxygen nonstoichiometry

Fig.4.2(A-C) illustrates the microstructures of the prepared ceramic samples. The substitution of Nb suppresses to some extent the grain growth under identical processing/sintering conditions. The SEM/EDS elemental mapping confirmed a minor segregation of V-rich phase for the composition with x = 0.30 (Fig 4.2D). Sintered $SrV_{1-x}Nb_xO_{3-\delta}$ samples were quite porous; for most compositions, the density was ≤ 80%

of theoretical (Table 4.1). Although relatively high porosity results in underestimated values of electrical conductivity, at the same time it should also promote faster re-equilibration of the ceramic samples with the gas atmosphere on temperature and p(O_2) changes.

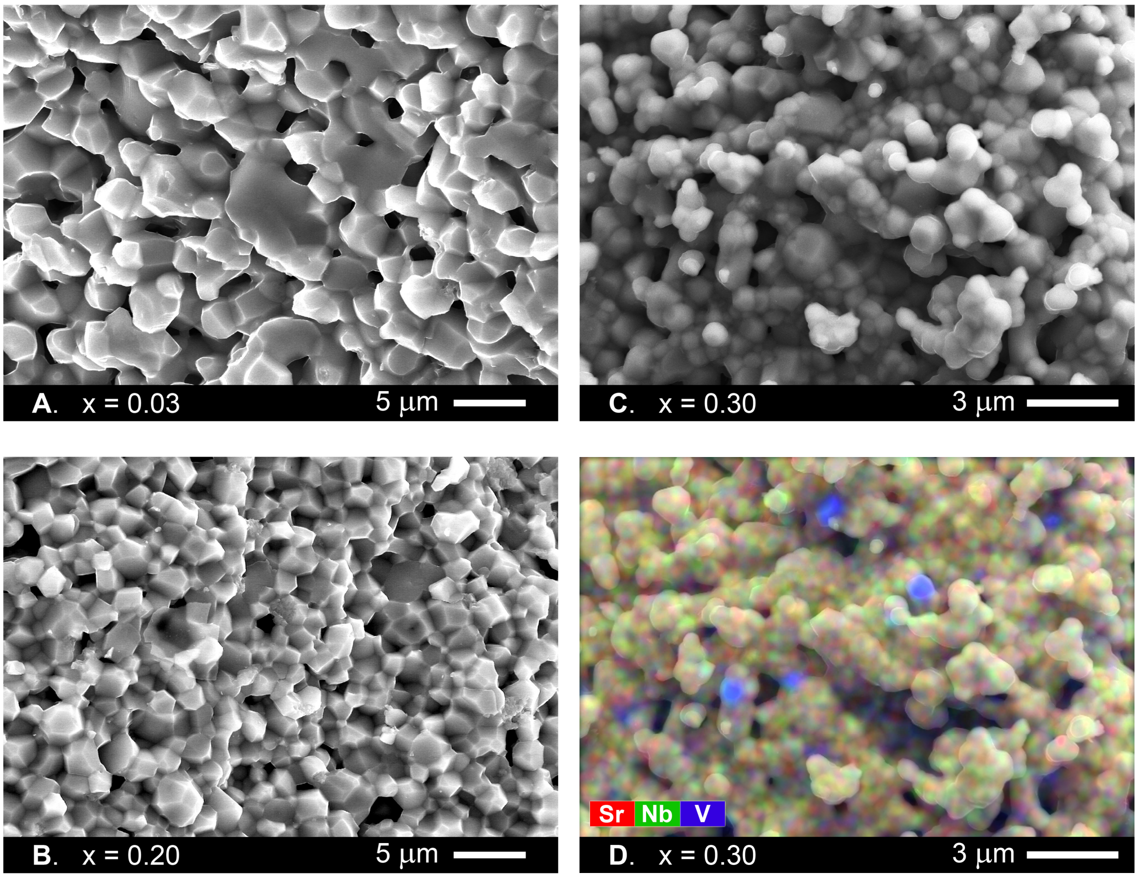

Fig 4.2. SEM micrographs **(A-C)** and SEM micrograph with overlaid EDS element mapping **(D)** of fractured cross-sections of as-prepared $SrV_{1-x}Nb_xO_{3-\delta}$ ceramics.

4.2 Thermochemical expansion under reducing conditions

Dilatometric curves of $SrV_{1-x}Nb_xO_{3-\delta}$ ceramics with $x \leq 0.10$ exhibit non-linear behavior under reducing conditions (Fig 4.3). As discussed in the previous chapter, similar behavior is characteristic for parent $SrVO_3$ and at least partly can be attributed to a chemical contribution to overall expansion.

Thermogravimetric studies demonstrated that all $SrV_{1-x}Nb_xO_{3-\delta}$ perovskites lose weight upon heating in 10%H_2-N_2 atmosphere (Fig 4.3A), corresponding to oxygen release from the lattice. Substitution by higher-valence niobium cations into vanadium sublattice progressively suppresses the weight losses and, therefore, variations of oxygen nonstoichiometry with temperature. In fact, the compositions with x = 0.20 and 0.30 start to lose lattice oxygen only above ~800 and 1000 K, respectively and possibly are oxygen stoichiometric at lower temperature. The weight change is almost negligible in the case of $SrV_{0.70}Nb_{0.30}O_{3-\delta}$, in correlation with essentially linear behavior of dilatometric curve (Fig4.3B).

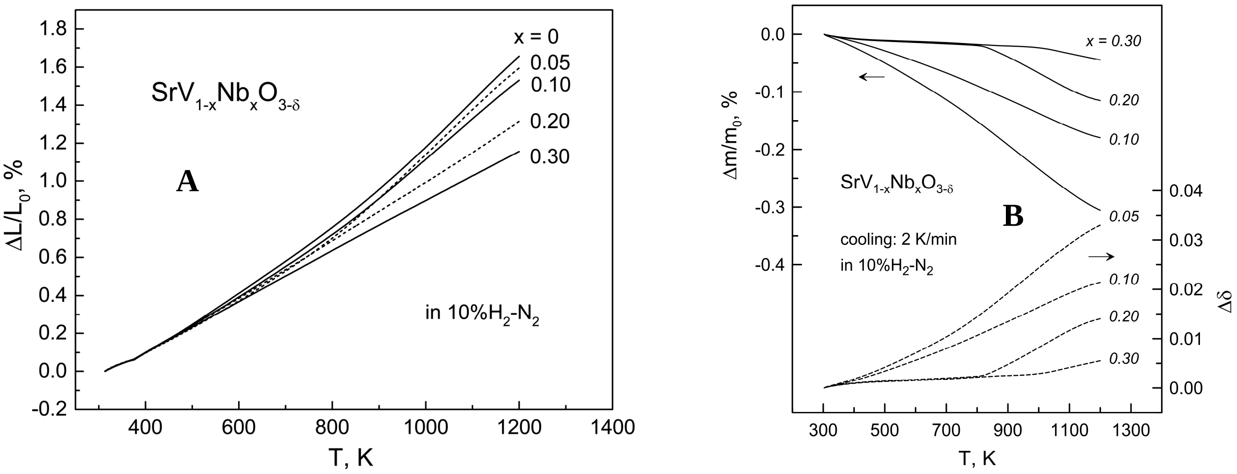

Fig.4.3. Dilatometric curves of $SrV_{1-x}Nb_xO_{3-\delta}$ ceramics **(A),** and thermogravimetric curves of powdered $SrV_{1-x}Nb_xO_{3-\delta}$ samples with corresponding relative changes in oxygen deficiency with temperature **(B)** in 10% H_2-N_2.

The average thermal expansion coefficients of $SrV_{1-x}Nb_xO_{3-\delta}$ ceramics continuously decrease with increasing Nb content (Table 4.2). The results indicate that this type of substitution suppresses both true thermal expansion and chemical contribution. The TEC value of $SrV_{0.70}Nb_{0.30}O_{3-\delta}$ approaches that of common solid electrolytes, thus ensuring improved thermomechanical compatibility with electrolyte materials.

Table 4.2
Average thermal expansion coefficients of $SrV_{1-x}Nb_xO_{3-\delta}$ ceramics and common solid electrolytes

x	Average TEC		
	Temperature range, K	$(\bar{\alpha}\times10^6) \pm 0.1$, K^{-1}	Atmosphere
0	373 – 773 / 773 – 1223	16.1 / 22.7	10% H_2-N_2
0.03	373 – 773 / 773 – 1223	14.8 / 23.0	10% H_2-N_2
0.05	373 – 773 / 773 – 1223	14.4 / 22.6	10% H_2-N_2
0.10	373 – 773 / 773 – 1223	15.2 / 20.5	10% H_2-N_2
0.20	373-1223	15.1	10% H_2-N_2
0.30	373-1223	13.3	10% H_2-N_2
*CGO[a]	373-1223	12.4	air
*LSGM[b]	373-1223	11.1	air
*8YSZ[c]	373-1223	10.5	air

[a] $Ce_{0.9}Gd_{0.1}O_{2-\delta}$ [b] $(La_{0.9}Sr_{0.1})_{0.98}Ga_{0.8}Mg_{0.2}O_{3-\delta}$ [c] $(ZrO_2)_{0.92}(Y_2O_3)_{0.08}$ *[Yaremchenko, 2014]

4.3 Electrical conductivity under reducing conditions

Electrical conductivity of $SrV_{1-x}Nb_xO_{3-\delta}$ ceramics was measured as a function of temperature in 10%H_2-N_2 atmosphere (Fig 4.4). As mentioned above, the experimental values of conductivity should be underestimated due to porosity of the samples; the true values are expected to be ~1.1-2.0 times higher, depending on porosity (Fig.4.4B), and can be corrected by reasonable models such as homogeneous distribution of spherical pores $\sigma_0 = \sigma\ (1+0.5\varepsilon)/(1-\varepsilon)$ [Mizusaki, 1996].

For all studied materials, the electrical conductivity exhibits metallic-like behavior decreasing on heating in the studied temperature range. Substitution with niobium results in a gradual decrease of conductivity. This seems quite reasonable since metallic-type electronic conductivity in $SrVO_3$ perovskite is generally attributed to V^{+4} cations in $3d^1$ configuration forming a broad conduction band [Dougier, 1975], as mentioned in the previous chapter. Thus, a decrease in electronic conductivity may be ascribed to decreasing concentration of V^{4+} and electron scattering caused by the combined effects of Nb^{+5}, V^{+3} and possibly even a residual fraction of V^{+5} in B-site positions; this should account for the strong dependence of conductivity on the fraction of Nb (inset of Fig 4.4). Still, electronic conductivity for most compositions remains acceptable for fuel electrode applications (> 100 S cm^{-1} at 873-1223 K, except for x = 0.30).

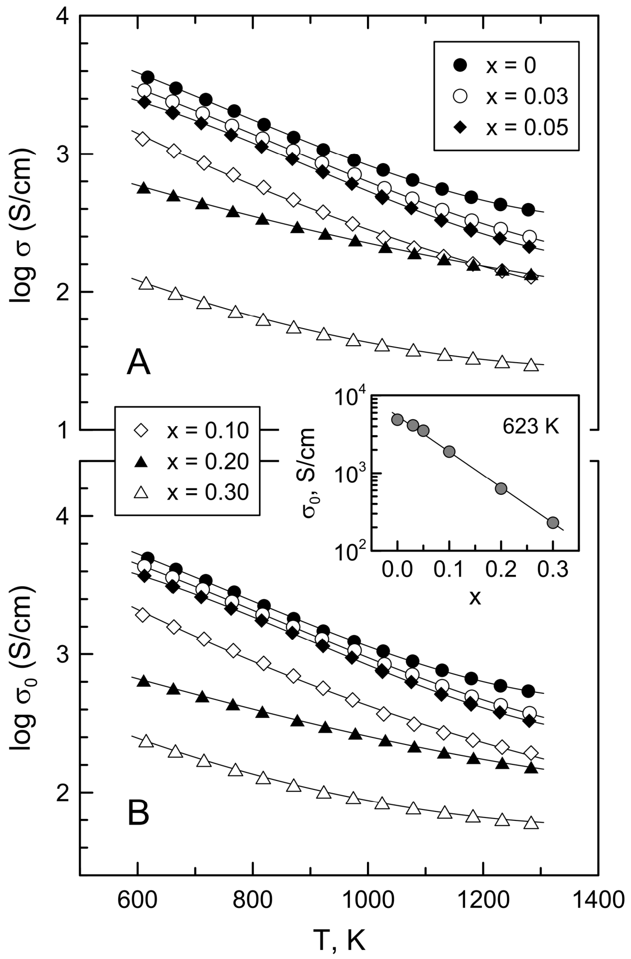

Fig 4.4. Temperature dependence of electrical conductivity of $SrV_{1-x}Nb_xO_{3-\delta}$ ceramics in 10%H_2-N_2 atmosphere: **(A)** experimental values (σ), and **(B)** values corrected for porosity (ε) using the model for materials with homogeneous distribution of spherical pores $\sigma_0 = \sigma(1+0.5\varepsilon)/(1-\varepsilon)$. Inset shows the dependence of electrical conductivity on Nb content at 623 K.

The dependence of electrical conductivity of $SrV_{1-x}Nb_xO_{3-\delta}$ on $p(O_2)$ is relatively weak under reducing conditions, within the phase stability domain (Fig.4.5). Such behavior of electronic transport is rather favorable for fuel electrode applications ensuring uniformity of electrical properties across electrode layers under polarization or under variation of fuel gas composition. A slight increase of conductivity with increasing $p(O_2)$ for compositions with $x \leq 0.10$ can be attributed to a slight variation of oxygen deficiency in the perovskite lattice and the corresponding decrease in the fraction of species responsible for electron scattering. The dependence of conductivity on $p(O_2)$ is negligible for $SrV_{0.70}Nb_{0.30}O_{3-\delta}$ and $SrV_{0.80}Nb_{0.20}O_{3-\delta}$; this is consistent with previous discussion on oxygen deficiency variations (Fig.4.3B), implying that the concentration of V^{+3} remains nearly unchanged in these cases (more details in next section).

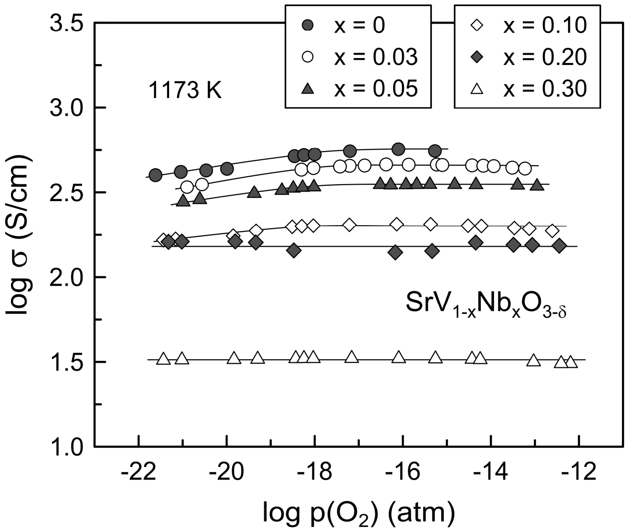

Fig 4.5. Oxygen partial pressure dependence of electrical conductivity of $SrV_{1-x}Nb_xO_{3-\delta}$ ceramics at 1173 K.

4.4 Defect chemistry guidelines

The impact of Nb addition in $Sr(V,Nb)O_3$ may be interpreted by the expected effects on defect chemistry:

$$SrO + (1-x)BO_2 + 0.5xNb_2O_5 \xrightarrow{-0.25xO_2} Sr_{Sr}^{\times} + (1-2x)B_B^{\times} + xB'_B + xNb_B^{\bullet} + 3O_O^{\times} \qquad \text{Eq. 4.2}$$

This must be combined with changes in oxygen stoichiometry upon varying the thermochemical conditions (Fig 4.3B), and the corresponding reduction to trivalent V^{+3}, as described by:

$$4B_B^{\times} + 2O_O^{\times} \overset{k_{red}}{\Leftrightarrow} 4B'_B + 2V_O^{\bullet\bullet} + O_2 \qquad \text{Eq. 4.3}$$

Changes in defect chemistry in a generic sample with composition $SrV_{1-x}Nb_xO_{3-\delta}$ may then be described on combining the lattice conservation condition:

$$[B_B^{\times}] + [B_B^{\bullet}] + [B'_B] + [Nb_B^{\bullet}] = 1 \qquad \text{Eq. 4.4}$$

with the mass action constant of the redox reaction (Eq.(4.3)) and electroneutrality (Eq.(4.1)), this yields:

$$[\mathrm{B}_\mathrm{B}^{\times}]=\frac{1+2\delta}{1+2\left(\dfrac{k_{red}}{\mathrm{p(O_2)}}\right)^{1/4}\left(\dfrac{3-\delta}{\delta}\right)^{1/2}} \qquad \text{Eq. 4.5}$$

$$[\mathrm{B}_\mathrm{B}^{\prime}]=\frac{(1+2\delta)\left(\dfrac{k_{red}}{\mathrm{p(O_2)}}\right)^{1/4}\left(\dfrac{3-\delta}{\delta}\right)^{1/2}}{1+2\left(\dfrac{k_{red}}{\mathrm{p(O_2)}}\right)^{1/4}\left(\dfrac{3-\delta}{\delta}\right)^{1/2}} \qquad \text{Eq. 4.6}$$

$$[\mathrm{B}_\mathrm{B}^{\bullet}]=\frac{(1+2\delta)\left(\dfrac{k_{red}}{\mathrm{p(O_2)}}\right)^{1/4}\left(\dfrac{3-\delta}{\delta}\right)^{1/2}}{1+2\left(\dfrac{k_{red}}{\mathrm{p(O_2)}}\right)^{1/4}\left(\dfrac{3-\delta}{\delta}\right)^{1/2}}-x-2\delta \qquad \text{Eq. 4.7}$$

In addition, one should take into account possible disproportionation of B-site species, as follows:

$$2\mathrm{B}_\mathrm{B}^{\times}\overset{k_d}{\Leftrightarrow}\mathrm{B}_\mathrm{B}^{\bullet}+\mathrm{B}_\mathrm{B}^{\prime} \qquad \text{Eq. 4.8}$$

On combining the corresponding mass action constant $k_d=[\mathrm{B}_\mathrm{B}^{\bullet}][\mathrm{B}_\mathrm{B}^{\prime}]/[\mathrm{B}_\mathrm{B}^{\times}]^2$ with Eqs.(4.5-4.7) one obtains:

$$(1-2x-2\delta)\left\{\left(\frac{k_{red}}{\mathrm{p(O_2)}}\right)^{1/2}\frac{3-\delta}{\delta}\right\}-(x+2\delta)\left\{\left(\frac{k_{red}}{\mathrm{p(O_2)}}\right)^{1/2}\frac{3-\delta}{\delta}\right\}^{1/2}-k_d(1+2\delta)=0 \qquad \text{Eq. 4.9}$$

Eq.(4.9) reduces to a classic quadratic equation ($ay^2+by+c=0$), with $y=\left\{\left[(k_{red}/\mathrm{p(O_2)})^{1/2}(3-\delta)/\delta\right]\right\}^{1/2}$, which allows easy defect chemistry simulations for the effects of composition and changes in redox conditions, even if one does not have information on the mass action constant of the oxidation reaction. Still, there is great uncertainty about the disproportionation reaction and the corresponding level of oxidation to pentavalent V^{5+}. Oxidizing conditions give rise to secondary phases with prevailing pentavalent V^{5+}, namely $Sr_2V_2O_7$ or $Sr_3V_2O_8$ (see previous Chapter), suggesting that stability of the perovskite structure is critically affected by oxidation to pentavalent vanadium, and that the energetics of incorporation of V^{5+} in the perovskite lattice is unfavorable. Thus, one may consider a plausible condition when the mass action constant of reaction (eq. 4.8) is very low ($k_d << 1$), allowing one to neglect the contribution of $[B_B^{\bullet}]$ to charge neutrality, which corresponds to values of k_d in the order of 10^{-3} or lower, as illustrated in Fig.4.6. Otherwise, the concentrations of V^{3+} and V^{5+} and their contribution to electron scattering should increase with the mass action constant of disproportionation. The limiting condition for negligible fraction of pentavalent vanadium ions is readily obtained for a simplified neutrality condition $[Nb_B^{\bullet}] \approx [B'_B] - [B_B^{\bullet}] - 2[V_O^{\bullet\bullet}]$, which can be combined with Eqs.(4.4-4.5) to yield:

$$k_{red} = p(O_2)\left(\frac{\delta}{3-\delta}\right)^2\left(\frac{x+2\delta}{1-2x-2\delta}\right)^4 \qquad \text{Eq. 4.10}$$

The impact of additions of Nb^{5+} is simulated in Fig.4.7, with significant increase in trivalent V^{3+}, decrease in oxygen stoichiometry and mainly suppression of pentavalent V^{5+}. Note that the corresponding changes in tetravalent V^{4+} are relatively small, thus confirming that decrease in conductivity by at least one order of magnitude (Fig.4.4) should be ascribed to electron scattering rather than decrease in concentration of carriers. The combined effects of Nb additions on concentrations of trivalent V^{3+} and pentavalent V^{5+} (Fig.4.7) also indicate that this species does not affect significantly the electronic conductivity.

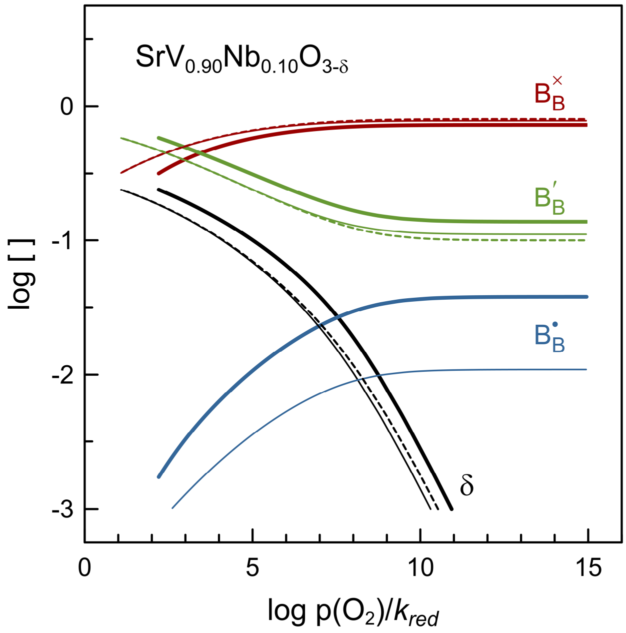

Fig 4.6. Simulated Kroger-Vink diagrams for $SrV_{0.90}Nb_{0.10}O_{3-\delta}$ computed for different values of the mass action constant of disproportionation reaction k_d =10^{-2} (thick lines) and 2×10^{-3} (thin lines). The limiting solutions for negligible disproportionation (and negligible concentration of pentavalent V^{5+}) are shown dashed.

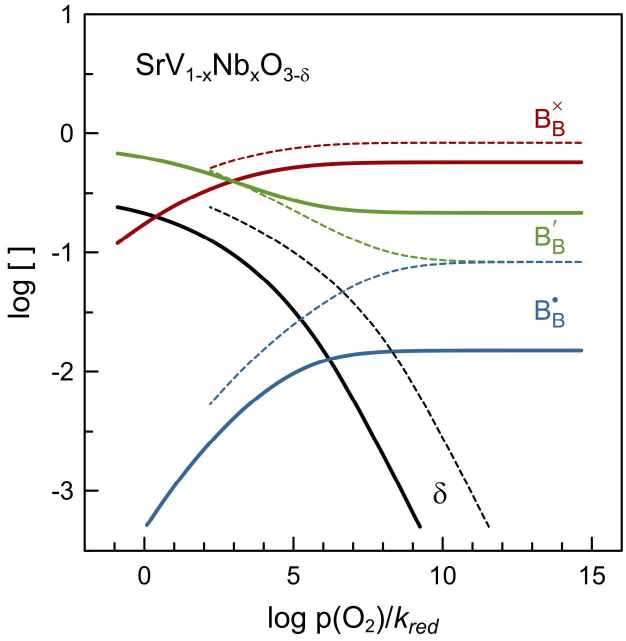

Fig 4.7. Simulated Kroger-Vink diagrams for $SrV_{0.80}Nb_{0.20}O_{3-\delta}$ (solid lines) and $SrVO_{3-\delta}$ (dashed lines) computed on assuming k_d = 10^{-2}.

4.5 Stability boundary of perovskite phase

The upper p(O_2)-stability boundaries of the cubic perovskite phase of $SrV_{1-x}Nb_xO_{3-\delta}$ at 1173 K were determined from the sudden break of log σ – log p(O_2) dependencies as illustrated in figure 4.8. Electrical conductivity was measured by a step-wise increase of oxygen partial pressure and equilibration at each p(O_2) until an abrupt drop in conductivity values was observed. This reduction was attributed to the onset of decomposition of the cubic perovskite phase and segregation of strontium orthovanadate with lower conductivity (as discussed in the previous Chapter). The presence of this insulating phase was confirmed by post-mortem XRD analysis (Fig 4.9). Thus, the p(O_2) value between the last two data points was considered as an approximate phase stability limit for a given composition.

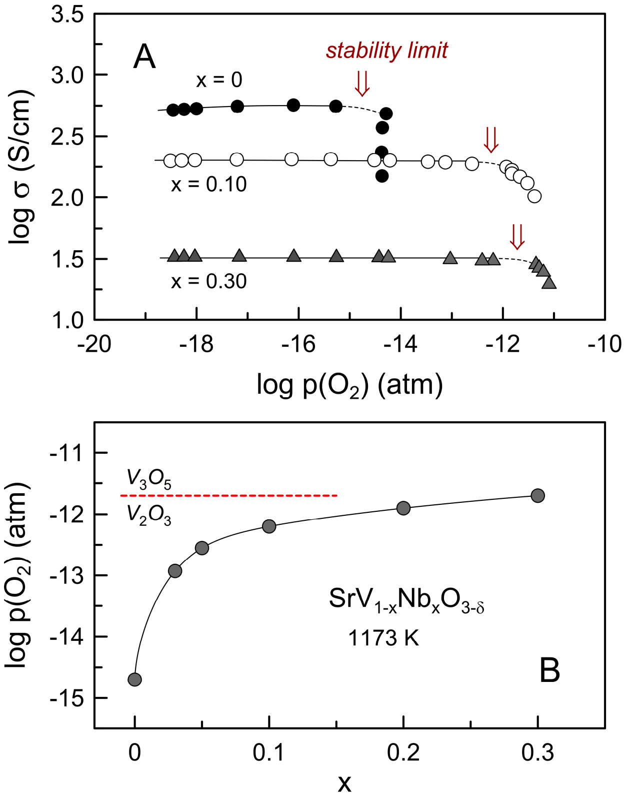

Fig 4.8. Determination of approximate stability limits of $SrV_{1-x}Nb_xO_{3-\delta}$ perovskites from *log σ - log p(O_2)* dependencies **(A)**, and approximate high-p(O_2) stability boundary of perovskite phase for Sr(V,Nb)$O_{3-\delta}$ system at 1173 K **(B).** Dotted horizontal line in (**B**) marks the phase boundary between V_2O_3 and V_3O_5 at this temperature [Okinaka, 1971].

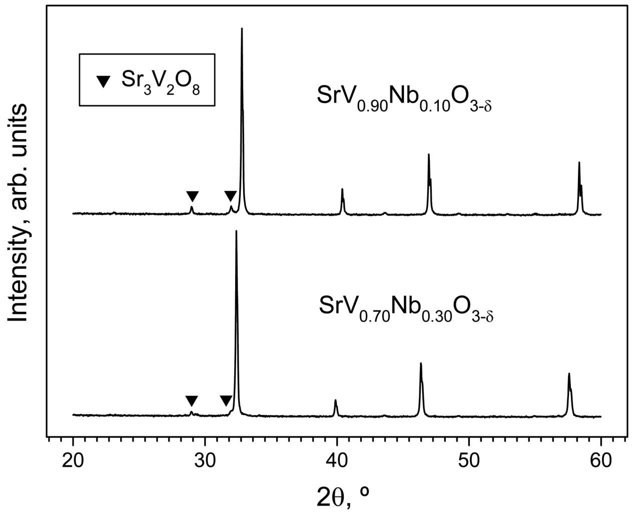

Fig 4.9. XRD patterns of $SrV_{1-x}Nb_xO_{3-\delta}$ ceramics after phase stability boundary determination (see Fig.4.8A). Marked reflections are indexed according to JCPDS PDF # 81-1844.

Substitution by niobium results in a gradual increase of perovskite lattice stability, shifting the upper $p(O_2)$ phase boundary from 2 ~ 10^{-15} atm for $SrVO_{3-\delta}$ to 2 ~10^{-12} atm for $SrV_{0.70}Nb_{0.30}O_{3-\delta}$ (Fig 4.8). Still, the decomposition of even latter composition occurs at much lower oxygen partial pressure than that desired for practical applications.

The effect of Nb on stability may be understood if one considers the point defect model to predict changes in the tolerance factor, based on Shannon ionic radii, [Shannon, 1976], with the average ionic radius of B-site species, i.e:

$$\tau = \frac{r_{O^{2-}} + r_{Sr^{2+}}}{\sqrt{2}\left(r_{O^{2-}} + [B_B^{\times}]r_{V^{4+}} + [B_B^{\bullet}]r_{V^{5+}} + [B_B']r_{V^{3+}} + [Nb_B^{\bullet}]r_{Nb^{5+}}\right)} \qquad \text{Eq. 4.11}$$

Representative simulations could be computed to examine the evolution from reducing to oxidizing conditions, as demonstrated in Fig.4.10 for $SrV_{1-x}Nb_xO_{3-\delta}$. These simulations suggest that parents $SrVO_{3-\delta}$ evolves from a favorable tolerance factor ($\tau = 1$) under reducing conditions to less favorable structural and defect chemistry changes under oxidizing conditions ($\tau > 1$). The predicted increase in the tolerance factor and the corresponding limited redox stability of $SrVO_{3-\delta}$ may be ascribed to the onset of a fraction of V^{+5}, by disproportionation (eq. 4.8). In addition, V^{+5} tends to accept the preferential tetrahedral coordination, because the radii ratio $r_V^{+5} : r_O^{-2} \approx 0.254$ is close to the ideal value (r_C: $r_A \approx 0.225$) expected for 4-fold coordination. Indeed, pentavalent V^{5+} usually assumes tetrahedral coordination in oxide compounds, as found for the orthovanadate phase $Sr_3V_2O_8$ (space group $R\bar{3}m$) [Durif, 1959]; this is the preferential reaction product observed after oxidative decomposition of $SrV_{1-x}Nb_xO_{3-\delta}$ samples, as confirmed by XRD analysis. Addition of Nb lowers the tolerance factor, by increasing the concentrations of larger B-site cations suppressing the onset of pentavalent V^{+5} and also approaching the ideal value in an oxidizing atmosphere.

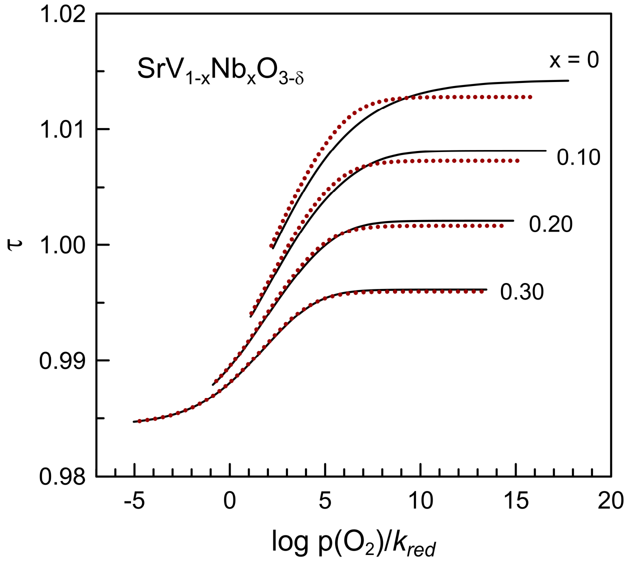

Fig.4.10. Predictions of tolerance factor of $SrV_{1-x}Nb_xO_{3-\delta}$ and its dependence on redox changes based on defect concentrations (Eq.(4.11)). Solid lines were computed on assuming negligible disproportionation ($k_d \approx 0$), and dotted lines were computed for $k_d \approx 0.04$.

4.6 Oxidative decomposition in air and under inert atmosphere

Figure 4.11 shows the relaxation of electrical conductivity of $SrV_{0.80}Nb_{0.20}O_{3-\delta}$ ceramics upon reducing → oxidizing → reducing and reducing → inert → reducing cycling at 1173 K. After changing the atmosphere from reducing to oxidizing, the conductivity dropped rapidly by more than 4 orders of magnitude in a few hours and then slowly continued to decrease. Obviously, this is associated with the onset of insulating phases, such as $Sr_2V_2O_7$ and $Sr_3V_2O_8$, as revealed by X-ray diffraction. Switching back to a reducing atmosphere resulted in a reverse reduction of the sample and fast restoration of the conductivity level. In fact, electrical conductivity at the end of redox cycling was even slightly higher compared to the initial value. Post-mortem XRD analysis showed the presence of two secondary phases - $Sr_3V_2O_8$ and Nb-lean secondary perovskite - in addition to the main perovskite phase (Fig.4.12). XRD peaks of this secondary perovskite are clearly displaced to higher angles, showing that its unit cell parameter is closer to that of undoped $SrVO_{3-\delta}$, which possesses superior electrical conductivity. Thus, the enhanced conductivity of the secondary perovskite explains the unexpected final gain in conductivity after partial oxidative decomposition. Cross-sectional SEM analysis demonstrated the presence of cracks (Fig 4.13A) and significant microstructural changes close to the surface (Fig.4.13(B and C), as compared to Fig.4.2B), whereas the microstructure in the middle of the sample remained mostly unchanged. Furthermore, SEM/EDS analysis of near-surface areas confirmed phase separation, with Nb-enriched and Nb-depleted grains (Fig.4.13D)

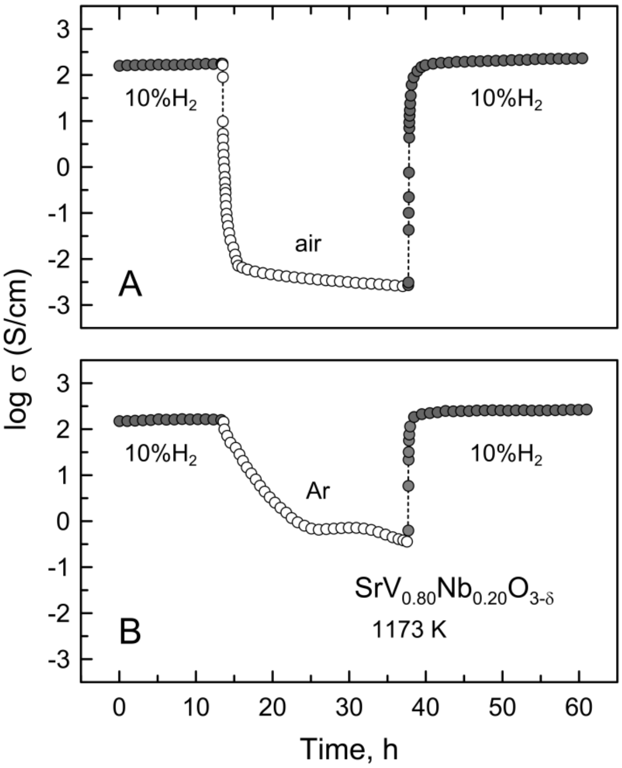

Fig 4.11. Relaxation of electrical conductivity of $SrV_{0.80}Nb_{0.20}O_{3-\delta}$ ceramics in **(A)** $10\%H_2 \rightarrow air \rightarrow 10\%H_2$ and **(B)** $10\%H_2 \rightarrow Ar \rightarrow 10\%H_2$ redox cycles at 1173 K.

Thermogravimetry of powdered ceramic samples shows even faster oxidative decomposition in air (Fig.4.14), as expected by magnifying the area for oxygen exchange. Post-mortem X-ray diffraction analysis (Fig 4.12B) showed co-segregation of $Sr_3V_2O_8$ and $Sr_{1-x}NbO_3$, whereas reflections of the major perovskite phase are shifted to slightly higher angles; this shrinkage of the unit cells corresponds to residual Nb-lean compositions $SrV_{0.80+y}Nb_{0.20-y}O_{3-\delta}$, as shown in Fig.4.15.

Real time electrical conductivity relaxation of $SrV_{0.80}Nb_{0.20}O_{3-\delta}$ during the reducing → inert → reducing cycles shows a slower evolution from 10%H_2-N_2 to an argon atmosphere (Fig 4.11B), partly due to slower stabilization of oxygen partial pressure in the gas phase. The conductivity decreased with nearly constant rate in first 10 h, after changing from reducing to inert atmosphere, followed by much slower degradation after stabilization of $p(O_2)$ in gas flow. Note also that the overall drop of conductivity after 24 h of oxidation in Ar was ~ 2 orders of magnitude less compared to oxidation in air. Inverse reduction results in rapid recovery and even slight increase of conductivity level, as demostrated previously for changes induced by the reducing → oxidizing → reducing cycle. However, post-mortem SEM analysis after reducing → inert → reducing cycling did not reveal any noticeable microstructural changes, and only negligible traces of $Sr_3V_2O_8$ phase were detected in corresponding XRD pattern (Fig.4.12C).

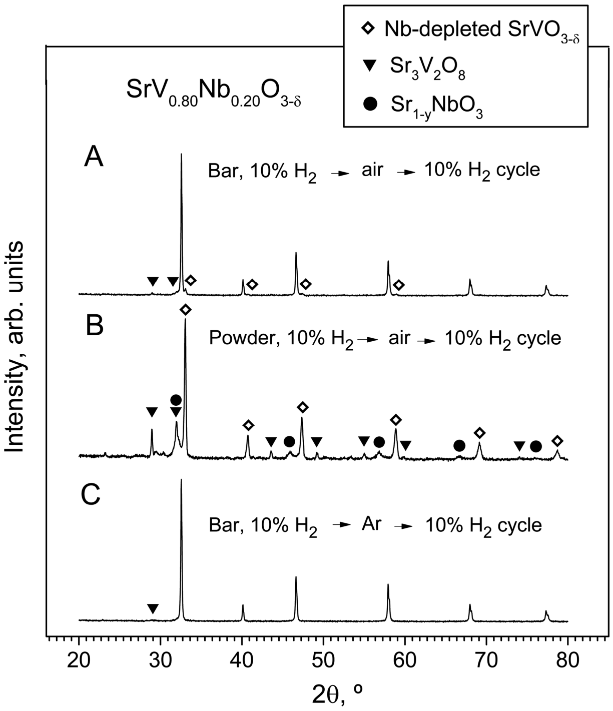

Fig 4.12. XRD patterns of $SrV_{0.80}Nb_{0.20}O_{3-\delta}$ samples after redox cycling at 1173 K. Patterns **(A)** and **(C)** were obtained after conductivity relaxation studies, performed with bulk ceramic samples (Fig.4.11), and pattern **(B)** was obtained after thermogravimetric studies of crushed samples (see Fig.4.14).

These results demonstrate that oxidative decomposition of $SrV(Nb)O_{3-\delta}$ is kinetically limited under inert atmosphere, thus making possible the fabrication of $SrVO_3$-based electrodes in these conditions. Prospects for metastable tolerance to inert atmospheres are even more obvious after relatively long-term (20 h) exposition to inert atmosphere at 1173 K (Fig 4.16). Only minor traces of $Sr_3V_2O_8$ phase can be detected in XRD patterns, almost at background level. In addition, changes in lattice parameter are relatively small and indicate that the composition of the perovskite phase remains nearly unchanged (Fig.4.15).

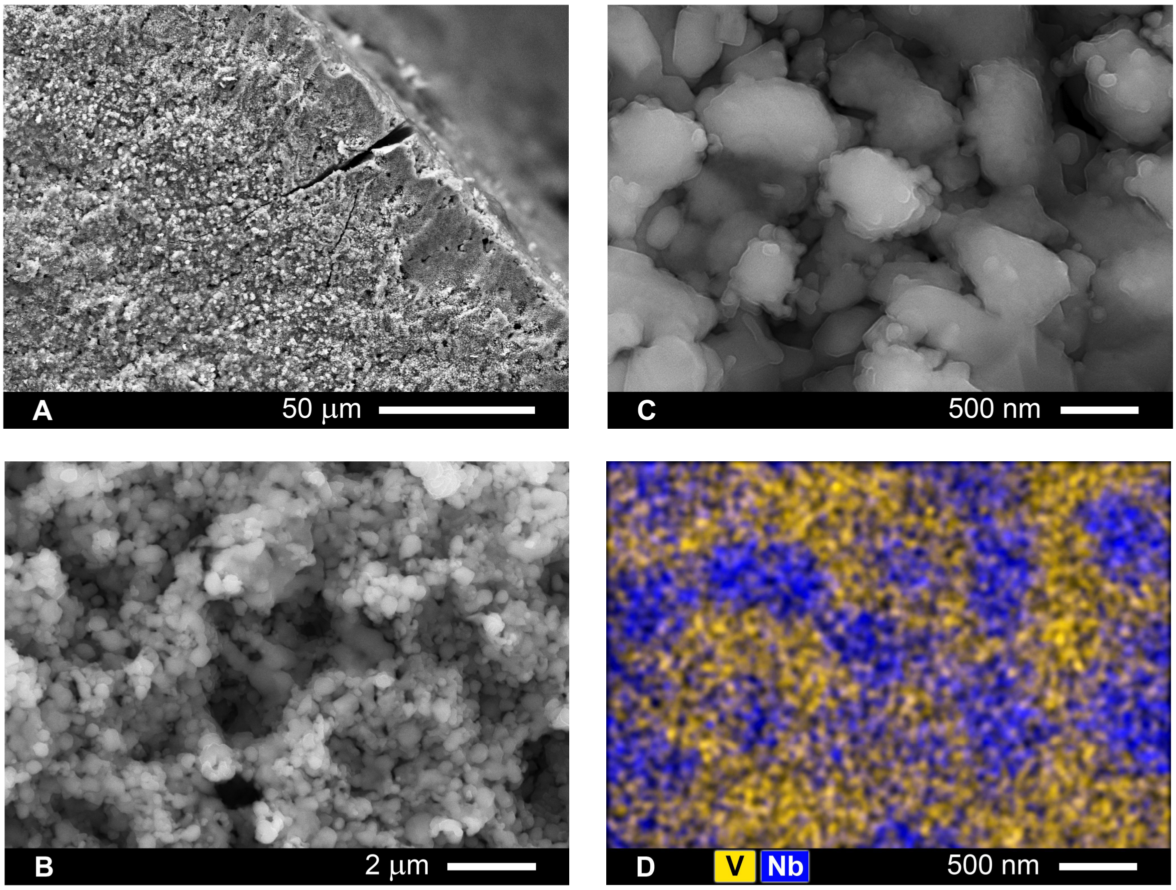

Fig 4.13. (A-C) SEM micrographs of fractured cross-section of $SrV_{0.80}Nb_{0.20}O_{3-\delta}$ ceramic samples after conductivity relaxation measurements in $10\%H_2 \rightarrow air \rightarrow 10\%H_2$ redox cycle at 1173 K, and **(D)** EDS elemental mapping corresponding to micrograph (C).

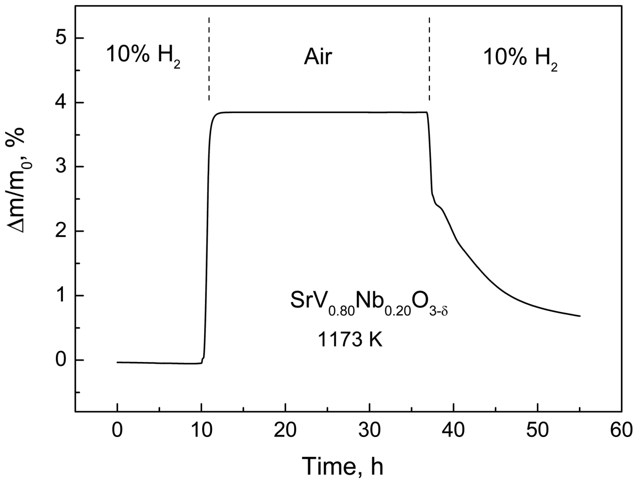

Fig 4.14. Relative weight change of powdered $SrV_{0.80}Nb_{0.20}O_{3-\delta}$ sample in $10\%H_2\rightarrow$air$\rightarrow10\%H_2$ redox cycle at 1173 K.

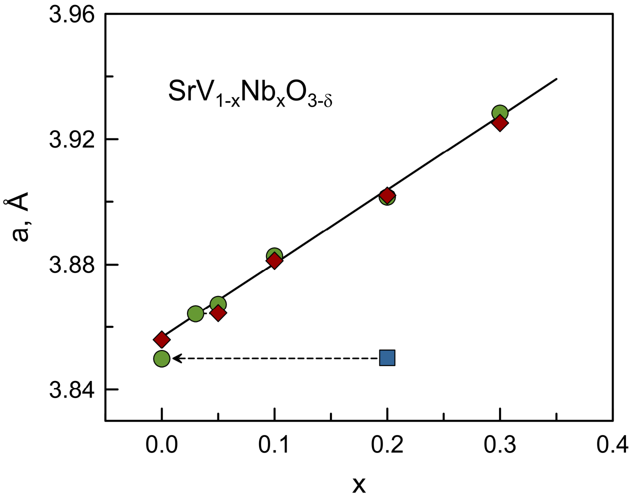

Fig 4.15. Lattice parameter values obtained for the as-prepared $SrV_{1-x}Nb_xO_{3-\delta}$ samples **(circles)** and for the corresponding residual Nb-lean perovskites $SrV_{1-x+y}Nb_{x-y}O_{3-\delta}$ after exposing powdered samples to the reducing → inert → reducing cycle **(diamonds)** or reducing → oxidizing → reducing cycle **(square)**. Dotted lines show the expected changes in composition.

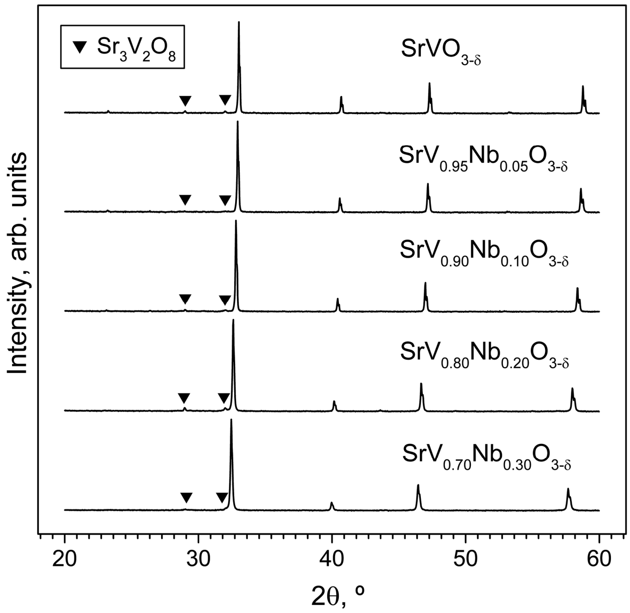

Fig.4.16. XRD patterns of powdered $SrV_{1-x}Nb_xO_{3-\delta}$ ceramic samples after thermal treatment in Ar flow ($pO_2 = 10^{-5}$ atm) at 1173 K for 20 h.

4.7 Conclusions

The conclusions of this chapter can be summarized as following:

i) $SrV_{1-x}Nb_xO_{3-\delta}$ (x = 0-0.30) ceramics were prepared by solid-state synthesis under reducing conditions and sintered at 1773 K in 10%H_2-N_2 flow. XRD and SEM/EDS studies showed that the single-phase cubic perovskite range is up to $x \approx 0.25$;

ii) $SrV_{1-x}Nb_xO_{3-\delta}$ ceramics exhibit metallic-like electrical conductivity, which is nearly $p(O_2)$-independent and decreases with niobium substitution; this still exceeds 100 S/cm at temperatures below 1273 K for compositions with $x \leq 0.20$;

iii) Substitution with niobium extends the stability domain of cubic perovskite phase shifting the high-$p(O_2)$ stability boundary from ~ 2×10^{-15} atm for undoped $SrVO_{3-\delta}$ to ~ 2×10^{-12} atm for x = 0.30;

iv) Substitution with niobium also suppresses partly the thermochemical expansion characteristic for parent $SrVO_{3-\delta}$, by lowering changes in oxygen deficiency and concentration of partially reduced V^{3+} cations occurring under reducing conditions;

v) Defect chemistry modeling provides useful guidelines to understand the role of Nb additions on redox and oxygen stoichiometry changes, and their impact on properties and stability;

vi) $SrV_{1-x}Nb_xO_{3-\delta}$ perovskites undergo oxidative decomposition in air without complete reversibility, even after relatively short redox cycles at temperatures below 1273 K. Still, decomposition is kinetically stagnated under inert gas conditions suggesting reversible or nearly reversible behavior in short-term redox cycling between reducing and inert atmospheres.

5. Perovskite-type $Sr_{1-x}Ln_xV_{1-y}Nb_yO_{3-\delta}$ system: Impact of donor-type co-substitutions

It was demonstrated in the previous Chapter that partial donor-type substitution of vanadium by niobium results in extension of perovskite phase stability domain, although the effect is limited. Excessive doping into the vanadium sublattice was found to result in a drop of electrical conductivity and segregation of phase impurities.

In this Chapter, the doping strategy included moderate substitution by rare-earth cations (La and Y) into strontium sublattice with minor co-substitution by niobium into vanadium sublattice.

Earlier, Meng et al. [Meng, 1990] reported the formation of single-phase $Sr_{2/3}Y_{1/3}VO_{3-\delta}$. More recent studies demonstrated however that solid solubility of yttrium cations is strontium sublattice of $SrVO_{3-\delta}$ is limited to ~ 25% of A sites [Yaremchenko, 2013]. Although $Sr_{1-x}La_xVO_{3-\delta}$ system was studied in more details, especially for La-rich side, the reports on solid solution formation ranges are not completely consistent; the available data are summarized in Table 5.1. The discrepancy in literature reports is caused apparently by different preparation techniques and generally reflects some difficulties in preparation of single-phase strontium-rich compositions without phase impurities such as $Sr_3V_2O_8$. Taking into account the literature data and estimated tolerance factors (Fig. 5.1), the concentration of rare-earth cations in this work has been fixed to 20% of strontium sites, with the Nb content varying between 0 and 10 at.% in vanadium sublattice.

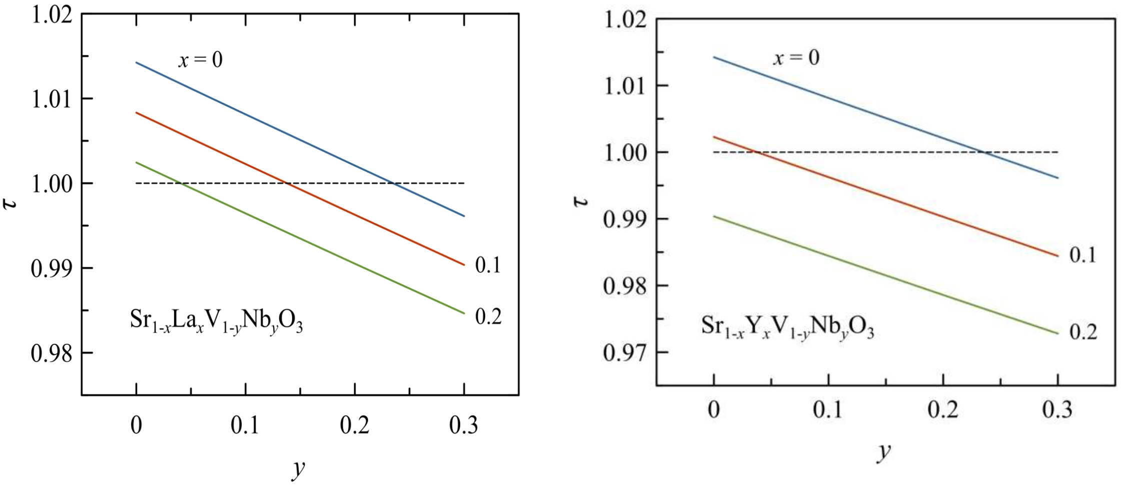

Fig 5.1. Calculated Goldschmidt tolerance factors for $Sr_{1-x}Ln_xV_{1-y}Nb_yO_3$ system: **(A)** Ln = La and **(B)** Ln = Y.

Table 5.1

Literature data on solid solution formation ranges in pseudo-binary $Sr_{1-x}La_xVO_{3-\delta}$ system

Reported compositional range	Crystal lattice	Ref.
$0.6 \leq x \leq 1.0$	hexagonal (rhombohedral)	[Dougier, 1970]
$x < 0.6$ $0.60 \leq x < 0.77$ $0.77 \leq x < 1.0$	multiphase rhombohedral $LaCoO_3$-type orthorhombic $GdFeO_3$-type	[Dougier, 1975 B]
$x < 0.8$ $0.8 \leq x \leq 1.0$	cubic tetragonal	[Shin-ike, 1976]
$0.1 \leq x < 0.7$	cubic perovskite *	[Mahajan, 1992]
$0.7 \leq x \leq 1.0$	tetragonal perovskite	
$0.5 \leq x \leq 0.8$	cubic perovskite	[Skopenko, 1993]
$0.5 \leq x \leq 0.7$	rhombohedral	[Inaba, 1995]
$0.8 \leq x \leq 1.0$	pseudotetragonal	
$x = 0.7, 0.8$	cubic perovskite	[Hui, 2001]
$x = 0.3, 0.5, 0.7$	cubic perovskite **	[Cheng, 2005; Fung, 2013]
$x < 0.5$ $x = 0.5$ $0.6 \leq x \leq 0.8$ $0.9 \leq x \leq 1.0$	multiphase cubic perovskite *** multiphase orthorhombic perovskite	[Ge, 2009]

* phase purity or lattice symmetry is not certain for some samples.

** broadened XRD peaks; phase purity is not certain.

*** phase purity is not certain.

5.1 Phase composition, structure and microstructure

XRD analysis of as prepared $Sr_{1-x}Ln_xV_{1-y}Nb_yO_{3-\delta}$ (Ln = La or Y) ceramics confirmed formation of single-phase materials with cubic perovskite structure. Unit cell parameters calculated from the XRD data are listed in Table 5.2

Table 5.2
Density and lattice parameters of as-prepared $Sr_{1-x}Ln_xV_{1-y}Nb_yO_{3-\delta}$ ceramics

Composition	Lattice parameter *a*, Å	Density, g/cm^3	Relative density*, %
$SrVO_{3-\delta}$	3.8498(3)	4.33	80
$Sr_{0.8}La_{0.2}VO_{3-\delta}$	3.8704(1)	4.17	74
$Sr_{0.8}La_{0.2}V_{0.95}Nb_{0.05}O_{3-\delta}$	3.8884(2)	4.11	73
$Sr_{0.8}La_{0.2}V_{0.90}Nb_{0.10}O_{3-\delta}$	3.8942(2)	3.97	70
$Sr_{0.8}Y_{0.2}VO_{3-\delta}$	3.8613(1)	4.25	79
$Sr_{0.8}Y_{0.2}V_{0.95}Nb_{0.05}O_{3-\delta}$	3.8708(1)	3.56	66
$Sr_{0.8}Y_{0.2}V_{0.90}Nb_{0.10}O_{3-\delta}$	3.8739(1)	3.71	68

* Theoretical density was calculated neglecting oxygen nonstoichiometry

Moderate substitutions of strontium by smaller lanthanum and yttrium cations result in an expansion of the perovskite lattice. This can be understood considering defect chemistry of substituted strontium vanadate, as partly explained in the previous Chapter. Donor doping in either sublattice must be charge-compensated, and this occurs via partial reduction of variable-valence vanadium cations in $\mathrm{Sr}^{2+}\mathrm{V}^{4+}\mathrm{O}_3^{2-}$ lattice:

$$(1-x)\mathrm{SrO}+(1-y)\mathrm{VO}_2+0.5x\mathrm{Ln}_2\mathrm{O}_3+0.5y\mathrm{Nb}_2\mathrm{O}_5 \xrightarrow{-0.25(x+y)\mathrm{O}_2} \mathrm{Sr}^{2+}_{1-x}\mathrm{Ln}^{3+}_{x}\mathrm{V}^{4+}_{1-x-2y}\mathrm{V}^{3+}_{x+y}\mathrm{Nb}^{5+}_{y}\mathrm{O}^{2-}_{3} \qquad \text{Eq. 5.1}$$

Larger ionic radii of V^{3+} (r^{VI} = 0.64 Å) and Nb^{5+} (r^{VI} = 0.64 Å) cations compared to V^{4+} (r^{VI} = 0.58 Å) explain a continuous increase of unit cell parameter with substitution (Table 5.2) occurring for both $Sr_{1-x}Y_xV_{1-y}Nb_yO_{3\pm\delta}$ and $Sr_{1-x}La_xV_{1-y}Nb_yO_{3\pm\delta}$, in spite of decreasing average size of lanthanide species in A-site positions relative to Sr^{2+}. The tendency is in agreement with the data reported for $Sr_{1-x}La_xVO_{3-\delta}$ system [Shin-ike, 1976; Mahajan, 1992].

The micrsotructures of as prepared ceramic materials are illustrated in Figure 5.2. All samples were quite porous, with relative density between 66 and 80% of theorteical (Table 5.2). The substitution, especially in vanadium sublattice, was also found to suppress the grain grotwh: the grain size decreased from 3-10 μm for the parent material to 0.5-3 μm for $Sr_{0.80}La_{0.20}V_{0.90}Nb_{0.10}O_{3-\delta}$. Both effects are suitable to ensure microstructural stability of porous electrocatalysts at relatively high operation temperatures.

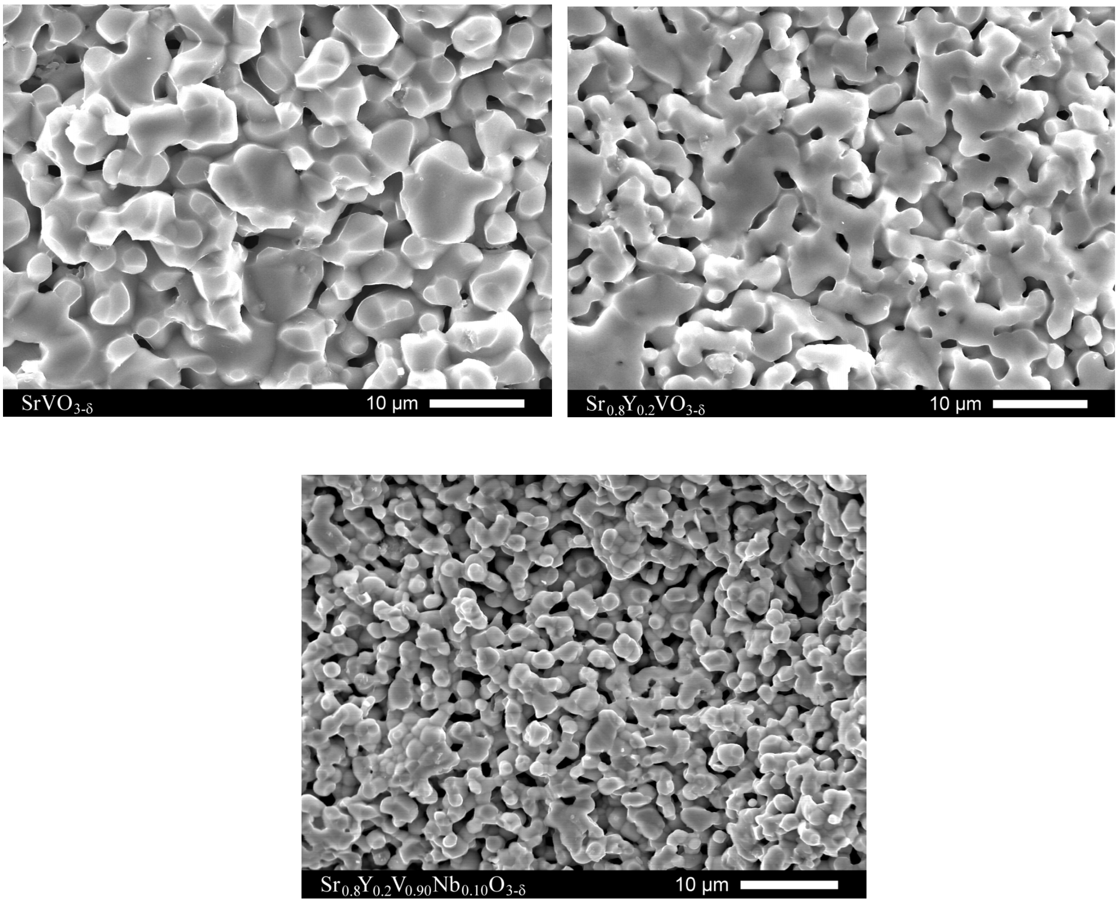

Fig.5.2. SEM micrographs of fractured as-prepared $Sr_{1-x}Y_xV_{1-y}Nb_yO_{3-\delta}$ ceramics.

5.2 Electrical conductivity and defect chemistry

As for parent material, $Sr_{1-x}Ln_xV_{1-y}Nb_yO_{3-\delta}$ ceramics possess metallic-like conductivity (σ) decreasing on heating (Fig. 5.3A). Substitution of strontium by rare-earth cations and simultaneous incorporation of niobium cations into vanadium sublattice results in a gradual reduction of electronic transport. Lanthanum-containing materials exhibit a slightly higher (~1.2-1.5 times) conductivity compared to yttrium-substituted counterparts.

Still, for all compositions, the measured values of electrical conductivity exceed 100 S/cm at temperatures ≤ 1223 K being sufficiently high for electrode applications.

$Sr_{1-x}Ln_xV_{1-y}Nb_yO_{3-\delta}$ ceramics exhibit relatively weak $p(O_2)$-dependence of electrical conductivity under reducing conditions (Fig.5.3B). The conductivity of Y-substituted vanadates decreases slightly with reducing $p(O_2)$ below 10^{-18}-10^{-17} atm, whereas La-doped counterparts show negligible σ-$p(O_2)$ dependence in the studied range.

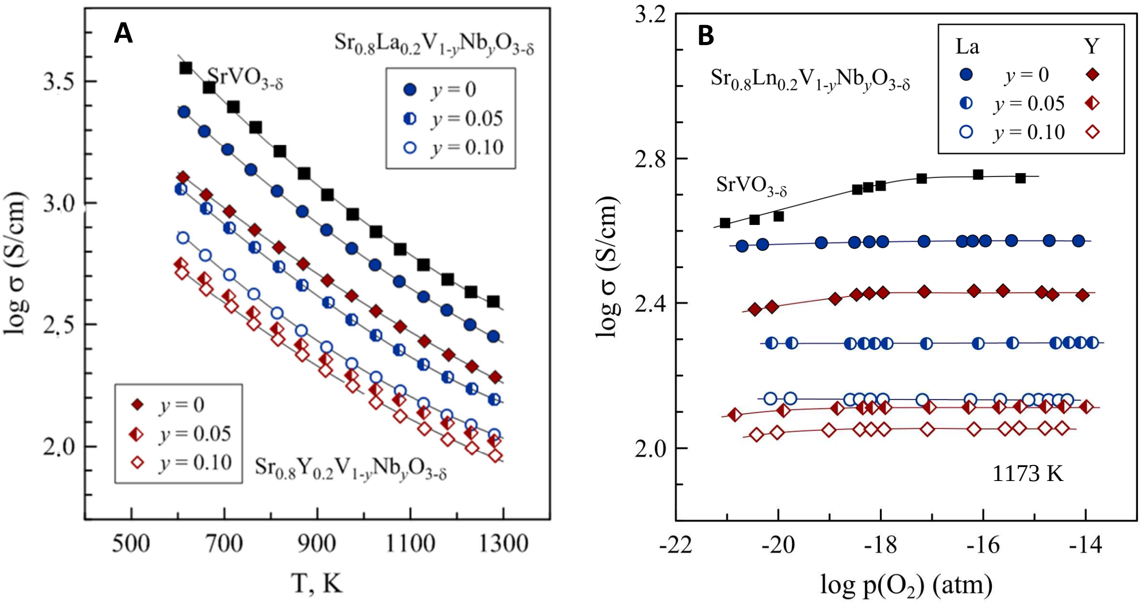

Fig 5.3. Electrical conductivity of $Sr_{1-x}Ln_xV_{1-y}Nb_yO_{3-\delta}$ ceramics as function of temperature in 10%H_2-N_2 atmosphere **(A)** and as function of oxygen partial pressure at 1173 K **(B)**.

The effects of donor-type substitutions on electrical properties of strontium vanadate can be interpreted considering the oxygen nonstoichiometry and defect chemistry of $Sr_{1-x}Ln_xV_{1-y}Nb_yO_{3-\delta}$ perovskites. Thermogravimetric studies demonstrated that all studied compositions exhibit weight losses on heating attributed to oxygen release from the crystal lattice and reduction of vanadium cations. (Fig.5.4)

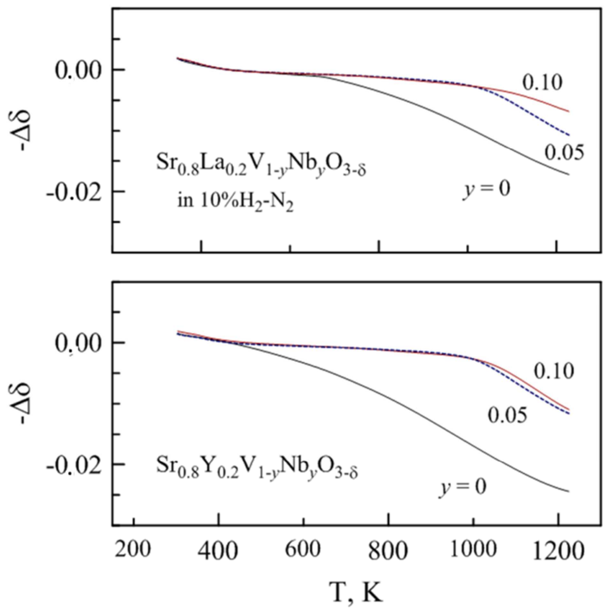

Fig 5.4. Relative changes of oxygen nonstoichiometry in $Sr_{1-x}Ln_xV_{1-y}Nb_yO_{3-\delta}$ ceramics under 10%H_2-N_2 atmosphere (cooling, 2°C/min).

The onset of oxygen losses corresponds to ~600 K for $Sr_{0.8}La_{0.2}VO_{3-\delta}$ and ~950-1000 K for $Sr_{1-x}Ln_xV_{1-y}Nb_yO_{3-\delta}$, whereas $Sr_{0.8}Y_{0.2}VO_{3-\delta}$ exhibits variable oxygen content in the entire studied temperature range, suggesting that crystal lattice of Y-substituted $SrVO_{3-\delta}$ is oxygen deficient even at low temperature, while other materials tend to oxygen stoichiometry on cooling. Partly, this was confirmed by the thermogravimetric data on the oxidation of substituted vanadates in air (see below).

Oxygen nonstoichiometry changes upon varying thermochemical conditions and corresponding reduction to V^{+3}, as was described by equation 4.3. Neglecting the fractions of Nb^{4+} and residual V^{5+} (which are not expected to have a prevailing effect on overall charge neutrality), the electroneutrality condition for $Sr_{1-x}Ln_xV_{1-y}Nb_yO_{3-\delta}$ can be expressed by:

$$[Ln^{\bullet}_{Sr}]+[Nb^{\bullet}_{B}]+2[V^{\bullet\bullet}_{O}]=[B'_{B}] \qquad \text{Eq. 5.2}$$

Combining with the lattice conservation condition:

$$[B^{\times}_{B}]+[B'_{B}]+[Nb^{\bullet}_{B}]=1 \qquad \text{Eq.5.3}$$

one may obtain expressions for the equilibrium constant of redox reaction Eq.(4.3):

$$K_{\mathrm{red}} = \mathrm{p(O_2)} \left(\frac{\delta}{3-\delta} \right)^2 \left(\frac{x+y+2\delta}{1-x-2y-2\delta} \right)^4 \qquad \text{Eq.5.4}$$

and for the concentrations of V^{4+} and V^{3+} cations:

$$[\mathrm{B_B^{\times}}] = (x+y+2\delta) \left(\frac{\mathrm{p(O_2)}}{K_{\mathrm{red}}} \right)^{1/4} \left(\frac{\delta}{3\text{-}\delta} \right)^{1/2} \qquad \text{Eq.5.5}$$

$$[\mathrm{B_B'}] = (1-x-2y-2\delta) \left(\frac{K_{\mathrm{red}}}{\mathrm{p(O_2)}} \right)^{1/4} \left(\frac{3\text{-}\delta}{\delta} \right)^{1/2} \qquad \text{Eq.5.6}$$

The impact of donor-type doping on concentrations of defects is simulated in Fig.5.5. Substitution of strontium by lanthanide and co-substitution of vanadium by niobium results in significant increase of V^{3+} fraction and suppression of oxygen deficiency. As mentioned above, metallic-type electronic conductivity in $SrVO_3$ perovskite is generally attributed to V^{4+} cations in $3d^1$ configuration forming broad conduction band. Thus, decrease of electrical conductivity with doping can be ascribed to a gradual decrease in concentration of carriers, $[V^{4+}]$, combined with electron scattering on Nb^{5+} and V^{3+} defects in vanadium sublattice. At the same time, equilibrium constant of redox reaction Eq.4.3 may be affected by the nature of substituting cation resulting in a shift of *defect concentration – p(O$_2$)* dependencies to more oxidizing or reducing conditions (Fig.5.6). This can reasonably explain some difference in T- and $p(O_2)$-dependencies of conductivity of La- and Y-substituted materials in the studied range of conditions (Fig.5.3B).

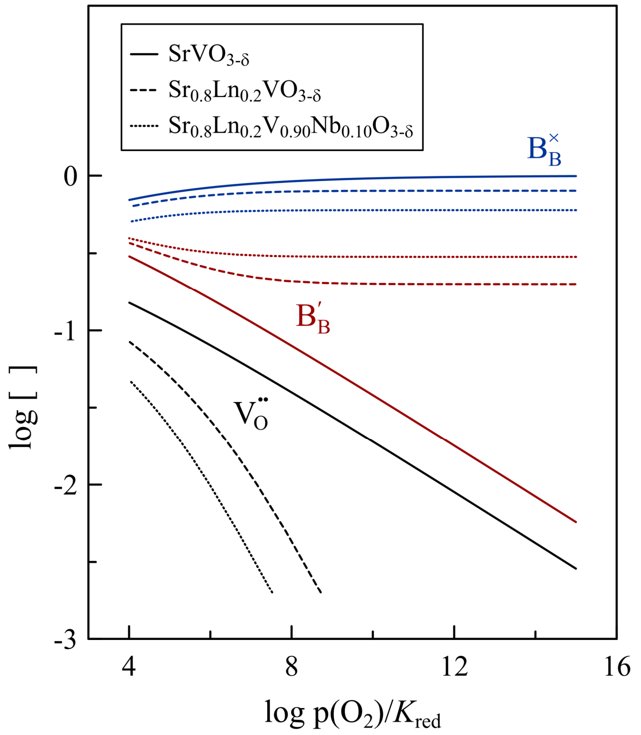

Fig. 5.5. Simulated Kröger-Vink diagrams of $SrVO_{3-\delta}$, $Sr_{0.8}Ln_{0.2}VO_{3-\delta}$ and $Sr_{0.8}Ln_{0.2}V_{0.90}Nb_{0.10}O_{3-\delta}$.

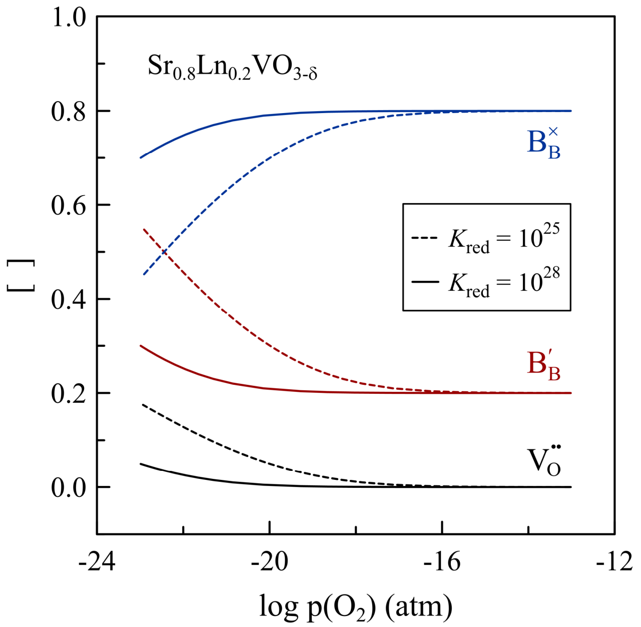

Fig 5.6. Simulated Kröger-Vink diagrams of $Sr_{0.8}Ln_{0.2}VO_{3-\delta}$ computed for different values of the equilibrium constant K_{red}.

5.3 Stability limits of perovskite phase

As for parents $SrVO_{3-\delta}$, substituted $Sr_{0.80}Ln_{0.20}V_{1-y}Nb_yO_{3-\delta}$ perovskites were found to be unstable in air. Thermogravimetric analysis of powdered samples demonstrated that the samples start to uptake oxygen on heating above ~473-573 K (Fig 5.7). Massive oxidation occurs at 673-873 K and is complete on heating to 1073 K. Post-mortem XRD analysis showed that oxidized $Sr_{0.80}Ln_{0.20}VO_{3-\delta}$ samples consisted of $Sr_2V_2O_7$ phase in combination with either $LaVO_4$ or YVO_4 (Fig 5.8). A number of additional reflections (probably originating from the phases of Sr-Nb-O system and/or other compounds) can be identified in the XRD patterns of oxidized co-substituted $Sr_{0.80}Ln_{0.20}VO_{3-\delta}$ vanadates.

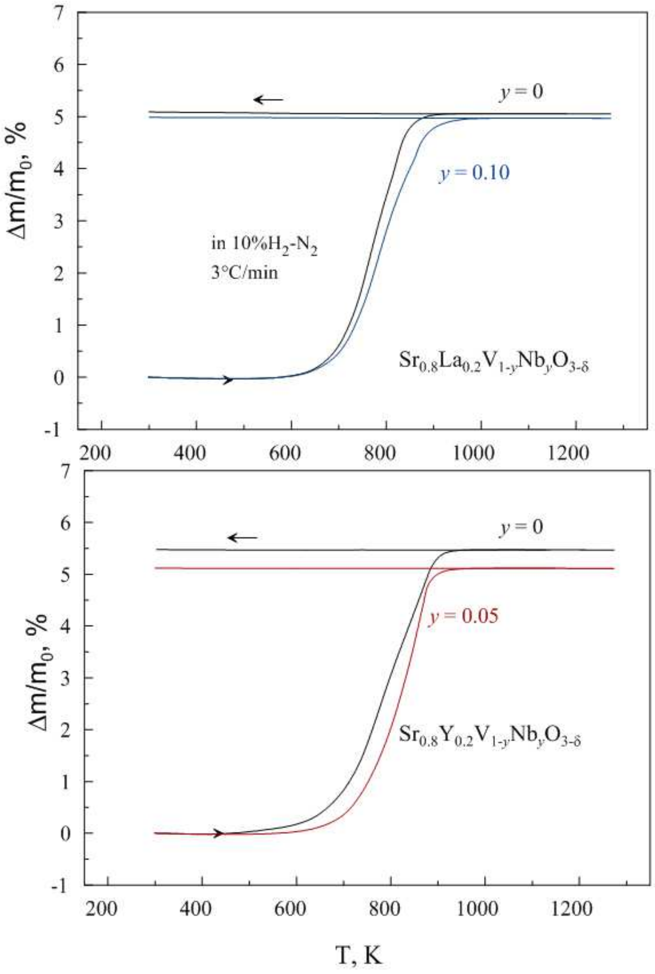

Fig 5.7. Relative weight gain on oxidation of powdered $Sr_{0.8}Ln_{0.2}V_{1-y}Nb_yO_{3-\delta}$ ceramic samples in one heating/cooling cycle in air.

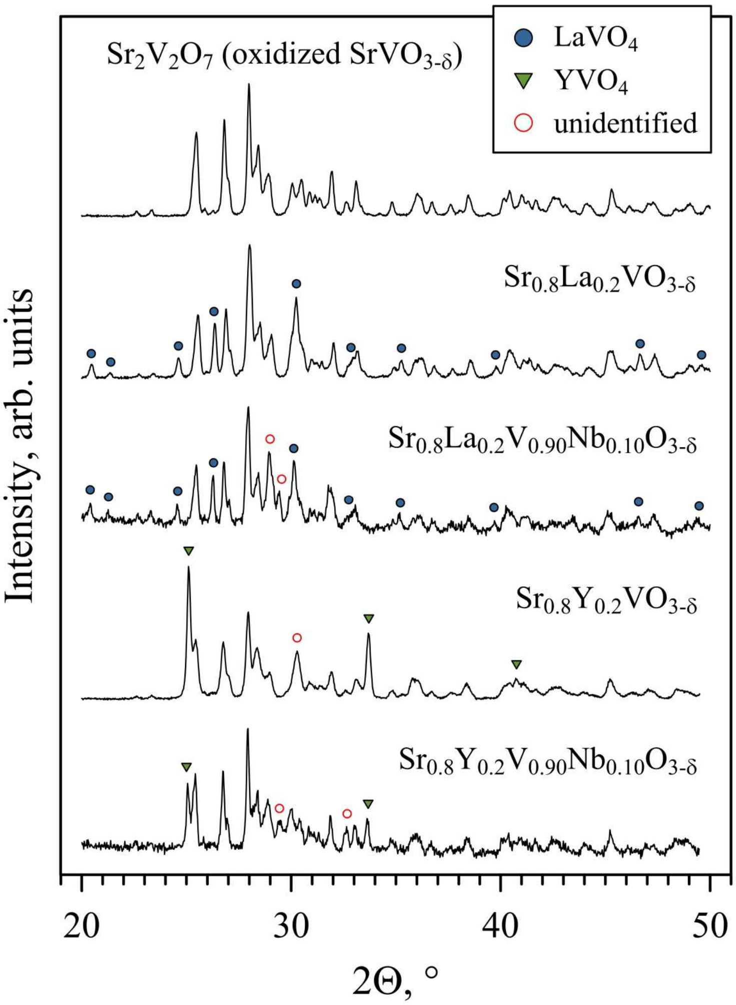

Fig 5.8. XRD patterns of $Sr_{1-x}Ln_xV_{1-y}Nb_yO_{3-\delta}$ oxidized in air in one heating/cooling cycle (2°C/min, T_{max} = 1000°C). Most intense reflections of $LaVO_4$ (JCPDS PDF # 75-3158), YVO_4 (JCPDS PDF # 82-1968) and unidentified phase(s) are marked with symbols. Unmarked intense reflections belong to $Sr_2V_2O_7$ phase (JCPDS PDF # 81-0737).

As expected, the oxidation is accompanied with significant dimensional changes as confirmed by dilatometry (Fig 5.9 and Table 5.3). Significant expansion at 773-973 K originating mainly from $SrVO_3 \rightarrow Sr_2V_2O_7$ phase transformation is followed sometimes with some contraction at temperatures close to 1273 K due to deformation of samples under non-zero mechanical load in dilatometric equipment, possibly caused by formation of intermediate phase with low melting point (e.g. $Sr(VO_3)_2$) (Brown, 1972).

Table 5.3
Dimensional changes of $Sr_{0.8}La_{0.2}V_{0.90}Nb_{0.10}O_{3-\delta}$ ceramics after dilatometric studies at different temperature

Sample 1 (T_{max} = 1273 K)	Sample 2 (T_{max} = 1023 K)
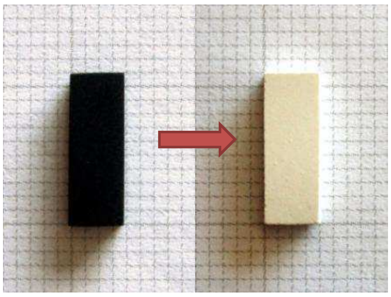	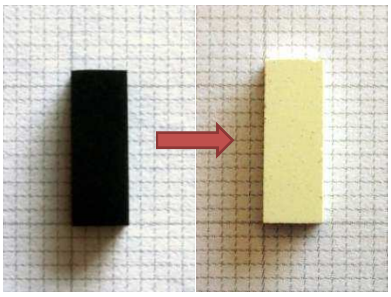

after experiment:

	ΔL, %	ΔS, %	ΔV, %	Density, g/cm^3
Sample 1	-1.2	8.7	7.4	3.10
Sample 2	5.6	12.2	18.5	2.94

Note: L, S and V are the bar-shaped sample length, cross-section area and volume.

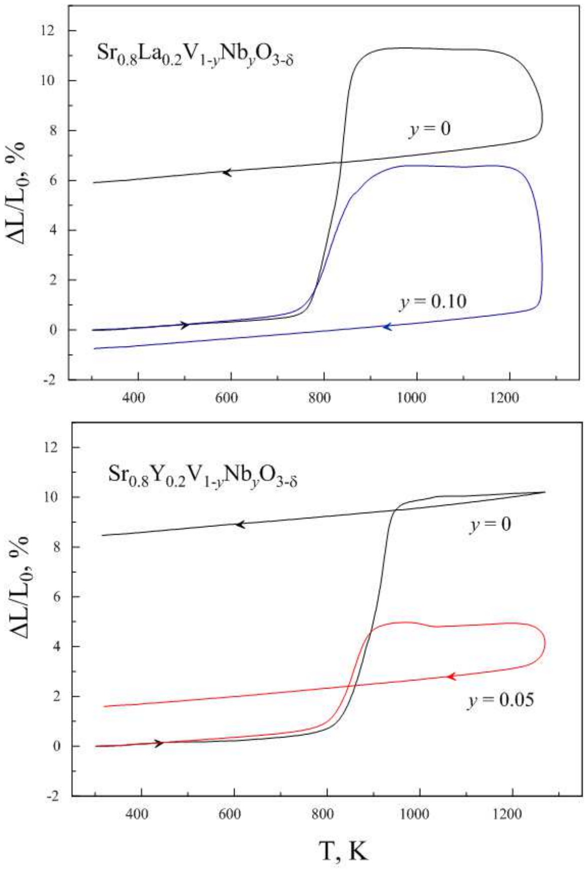

Fig 5.9. Relative length change of $Sr_{0.8}Ln_{0.2}V_{1-y}Nb_yO_{3-\delta}$ ceramic samples on oxidation in one heating/cooling cycle (3°C/min) in air.

Assuming $Sr_2V_2O_7$ and $LnVO_4$ to be the only products of $Sr_{0.8}Ln_{0.2}VO_{3-\delta}$ oxidation (i.e. all vanadium is in the 5+ oxidation state), one may roughly estimate the room-temperature oxygen non-stoichiometry in the original perovskite from the TGA data (Fig 5.7). The estimated values of δ correspond to ~0.02 and ~0.04 for $Sr_{0.8}La_{0.2}VO_{3-\delta}$ and $Sr_{0.8}Y_{0.2}VO_{3-\delta}$, respectively. This is generally in agreement with the observed $\Delta\delta$-T trends under reducing conditions, as discussed above. For other compositions, such estimations were impossible due to uncertainty with the phase composition of the oxidation products.

As for Nb-substituted vanadates, approximate upper-$p(O_2)$ phase stability boundaries of perovskite phase at 1173 K were determined from the *log σ - log p(O₂)* dependencies, as illustrated in Fig 5.10 for $Sr_{0.8}Ln_{0.2}V_{1-y}Nb_yO_{3-\delta}$ ceramics. Electrical conductivity was measured isothermally on step-wise increase of oxygen partial pressure and equilibration at each $p(O_2)$ until a drop in conductivity values was observed. This drop was attributed to the onset of decomposition of cubic perovskite phase and segregation of strontium orthovanadate $Sr_3V_2O_8$. The presence of oxidation products, including $Sr_3V_2O_8$ and SrV_6O_{11} phases, was confirmed by post-mortem XRD analysis. The $p(O_2)$ value corresponding to a loss of conductivity was considered as an approximate phase stability limit for a given composition. In the case of $Sr_{0.8}La_{0.2}VO_{3-\delta}$, the stability limit was found to fall in a $p(O_2)$ range between ~10^{-10} and ~10^{-5} atm (where it was not possible to maintain a constant $p(O_2)$ in H_2-H_2O-N_2 flow). This was confirmed by repeating the experiment for three different samples.

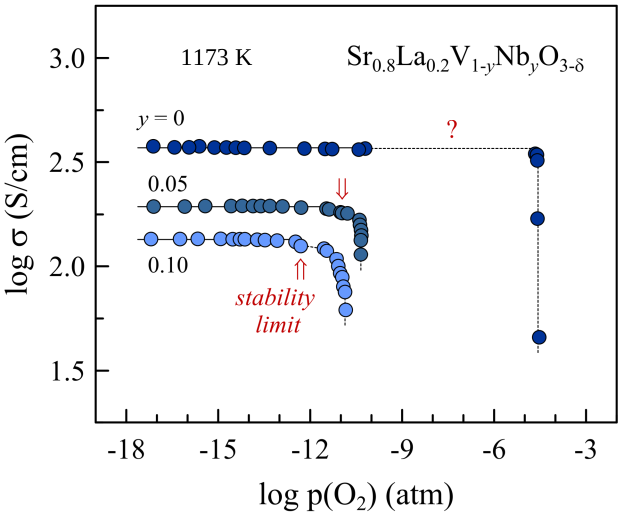

Fig 5.10. Determination of approximate phase stability limits of $Sr_{0.8}La_{0.2}V_{1-y}Nb_yO_{3-\delta}$ perovskites at 1173 K from the *log σ - log p(O₂)* dependencies.

As expected, donor-type substitutions were found to expand the phase stability domain of perovskite phase. The stability boundary shifts to higher oxygen partial pressure in the sequence $SrVO_3$ ($\tau = 1.014$) < $Sr_{0.8}Y_{0.2}VO_3$ ($\tau = 0.990$) < $Sr_{0.8}La_{0.2}VO_3$ ($\tau = 1.002$) (Fig 5.11). Surprisingly, co-substitution by Nb into vanadium sublattice does not result in further improvement of stability in the case of La-substituted vanadates, but instead in early destabilization of perovskite phase on moving towards inert or oxidizing conditions.. In fact, upper $p(O_2)$ stability boundary of $Sr_{0.8}Ln_{0.2}V_{0.90}Nb_{0.10}O_{3-\delta}$ is similar to that of Ln-free $SrV_{0.80}Nb_{0.20}O_{3-\delta}$. To some extend, these observations are consistent with decrease in tolerance factor with increasing additions of Nb, for constant lanthanide content. However, changes in tolerance factor would imply even greater changes in stability limit with increasing content of Nb for compositions $Sr_{0.8}Y_{0.2}V_{1-y}Nb_yO_{3-\delta}$, which is not observed. Thus, one may only assume that stability boundary is determined by a complex interplay between structural parameters, donor dopant concentration and fraction of V^{+3} cations.

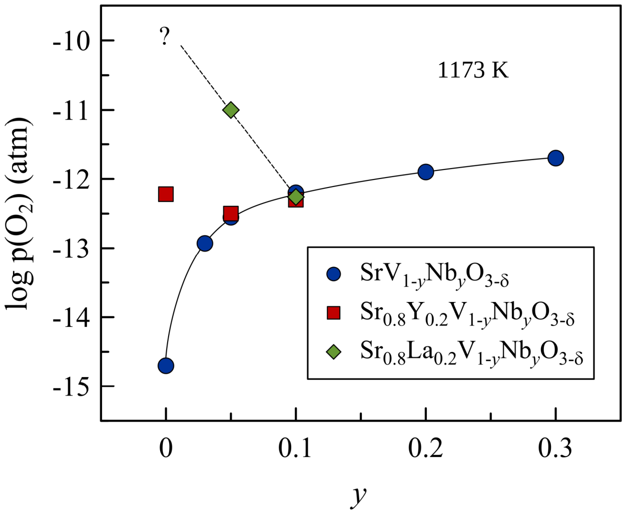

Fig 5.11. Approximate upper-$p(O_2)$ stability limits of perovskite phase. Cubic perovskite phase exists below the stability boundary; perovskite phase decomposition occurs at oxygen partial pressures above the stability limit. The data on $SrV_{1-y}Nb_yO_{3-\delta}$ system (from the previous Chapter) are shown for comparison.

5.4 Metastability under inert atmosphere

Figure 5.12 shows the relaxation of electrical conductivity of $Sr_{0.8}La_{0.2}V_{1-y}Nb_yO_{3-\delta}$ ceramics upon reducing → inert → reducing atmosphere cycling at 1173 K. Changing from reducing to inert atmosphere results in slow decrease of conductivity associated with the partial decomposition and segregation of insulating $Sr_3V_2O_8$ phase. After 24 h in inert gas flow, electrical conductivity dropped by one order of magnitude in the case of $Sr_{0.8}La_{0.2}VO_{3-\delta}$, but less than threefold in the case of Nb- co-substituted vanadate. Note also that the conductivity degradation rate was significantly slower compared to $SrV_{0.80}Nb_{0.20}O_{3-\delta}$ ceramics under identical conditions (see Chapter 4). Changing back to reducing atmosphere results in a nearly instant recovery of conductivity level. In the case of $Sr_{0.8}La_{0.2}V_{0.90}Nb_{0.10}O_{3-\delta}$ sample, the conductivity in the end of experiment was even ~15% higher compared to initial value.

Although a microstructural inspection did not reveal any visible alterations after the experiments (Fig 5.13), post-mortem XRD confirmed the presence of traces of the oxidized $Sr_3V_2O_8$ phase (Fig 5.14A and B). The thermogravimetric data obtained in an equal redox cycle (Fig. 5.15) also showed that oxidation is not completely reversible, and the sample actually does not return to the initial state. Partial oxidation (probably, limited to the surface) and re-reduction may be expected to follow the approximate sequence:

$Sr_{0.8}La_{0.0}V_{1-y}Nb_yO_{3-\delta}$ → $Sr_3V_2O_8$ (*major phase*) → dopant-depleted $SrVO_{3-\delta}$ (+*impurities*)

with comparatively slow second step, as it was demonstrated in Chapter 3. This explains the traces of $Sr_3V_2O_8$ after re-reduction, and also slightly higher final conductivity of Nb-containing sample (due to superior conductivity of dopant-depleted $SrVO_{3-\delta}$).

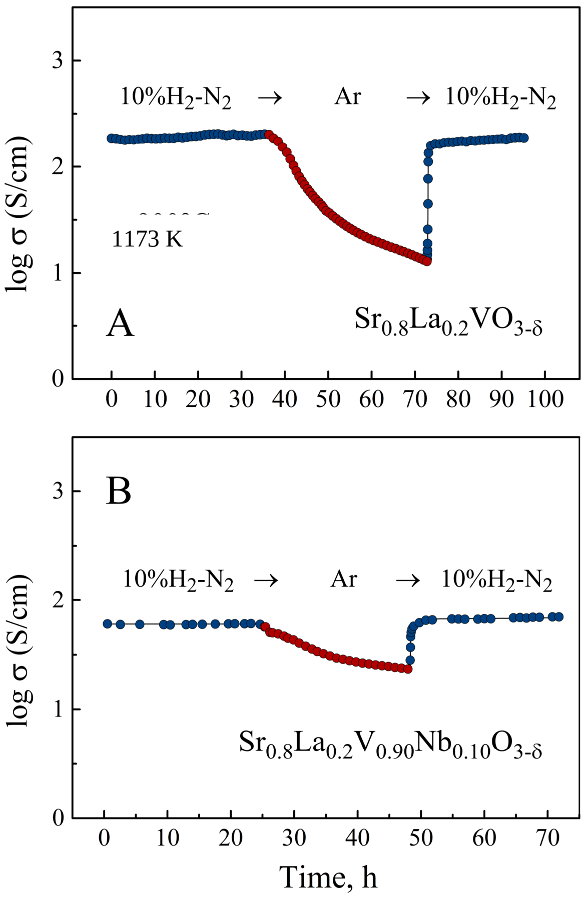

Fig 5.12. Relaxation of electrical conductivity of $Sr_{0.8}La_{0.2}V_{1-y}Nb_yO_{3-\delta}$ ceramics in one 10% H_2 → Ar → 10%H_2 redox cycle at 1173 K.

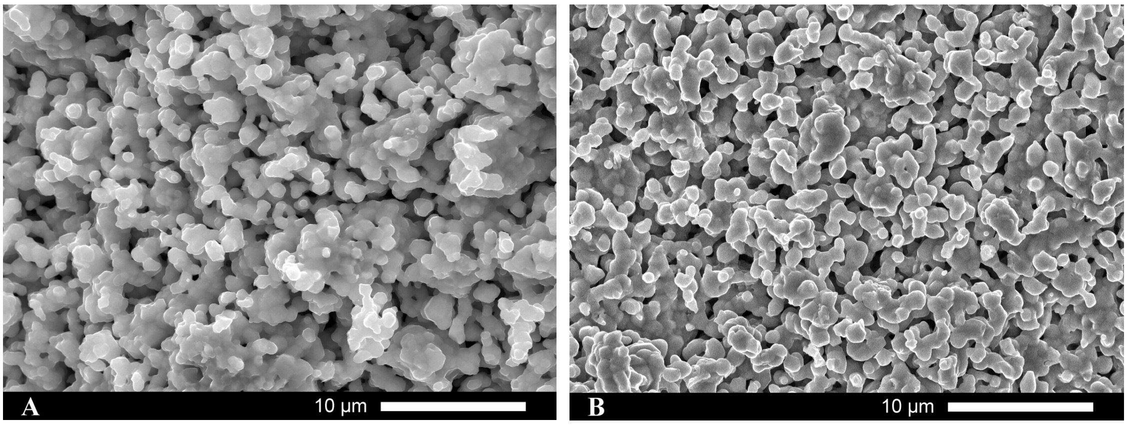

Fig 5.13. SEM micrographs of fractured $Sr_{0.8}La_{0.2}V_{0.90}Nb_{0.10}O_{3-\delta}$ ceramics: **(A)** as-prepared and **(B)** after conductivity relaxation studies in one 10% H_2 → Ar → 10%H_2 redox cycle at 1173 K

Sluggish kinetics of oxidation under inert gas conditions was confirmed further by the tests in argon atmosphere. XRD patterns of $Sr_{0.80}La_{0.20}VO_{3-\delta}$ powdered samples calcined at $p(O_2)$ ~5×10^{-5} atm for 20 h at 1173 K showed traces of oxidation products (mainly $Sr_3V_2O_8$) in addition to the original perovskite phase (Fig 5.14C and D).

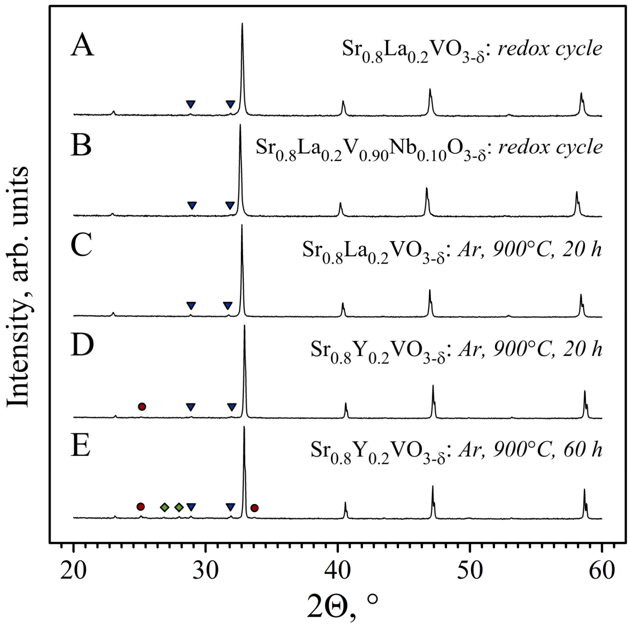

Fig 5.14. XRD patterns of powdered $Sr_{0.8}Ln_{0.2}V_{1-y}Nb_yO_{3-d}$ ceramics: **(A-B)** after conductivity relaxation studies in one 10% H_2 → Ar → 10%H_2 redox cycle at 1173 K; **(C-E)** after thermal treatment in Ar flow at 1173 K for 20 h **(C-D)** and 60 h **(E)**. Phase impurities: triangles – $Sr_3V_2O_8$ (JCPDS PDF # 81-1844); circles – YVO_4 (JCPDS PDF # 82-1968); diamonds – $Sr_2V_2O_7$ (JCPDS PDF # 81-0737).

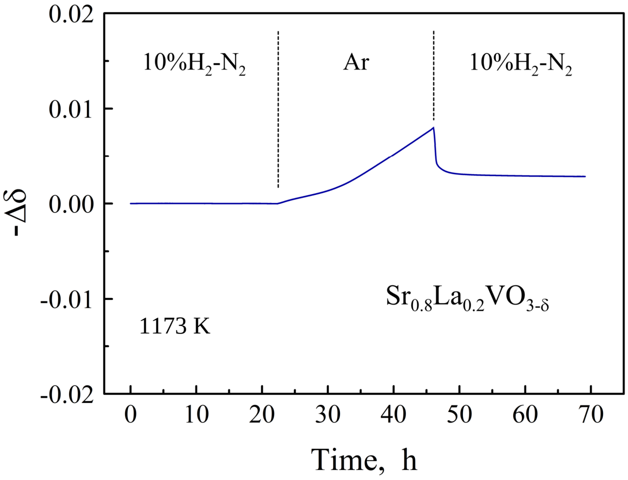

Fig 5.15. Relative changes of oxygen content in powdered $Sr_{0.8}La_{0.2}VO_{3-\delta}$ sample in one 10%H_2 → Ar → 10%H_2 cycle at 1173 K.

Increasing the calcination time up to 60 h resulted in a rather negligible increase in the oxidation products fraction (Fig 5.14E)

The oxygen uptake by powdered $Sr_{0.8}La_{0.2}V_{0.90}Nb_{0.10}O_{3-\delta}$ samples in one heating/cooling cycle up to 1473 K in Ar flow was below 0.005 oxygen atoms per formula unit; several examples of thermogravimetric curves are presented in Fig. 5.16. This oxygen uptake can be assigned to both oxygen nonstochiometry changes in the perovskite phase and minor segregation of oxidation product ($Sr_3V_2O_8$ in XRD patterns, on the background level) and was accompanied with only minor perovskite lattice constant (Fig. 5.17) and dimensional (Fig 5.18) changes.

Summarizing, these results demonstrate that oxidative decomposition of $Sr_{0.8}Ln_{0.2}V_{1-y}Nb_yO_{3-\delta}$ vanadates is kinetically limited in an inert atmosphere ensuring nearly reversible behavior in short cycles between reducing and inert conditions. This makes it possible to fabricate solid electrolyte cells with $SrVO_3$-based porous electrodes in inert environment without critical degradation of electrode material.

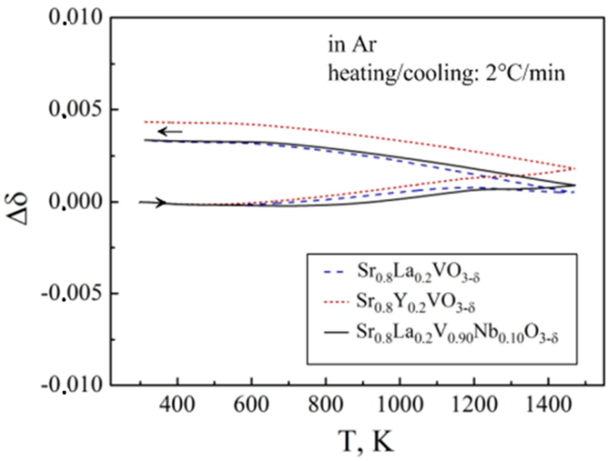

Fig 5.16. Relative changes of oxygen content in powdered $Sr_{0.8}Ln_{0.2}V_{1-y}Nb_yO_{3-\delta}$ samples on heating and subsequent cooling in argon flow.

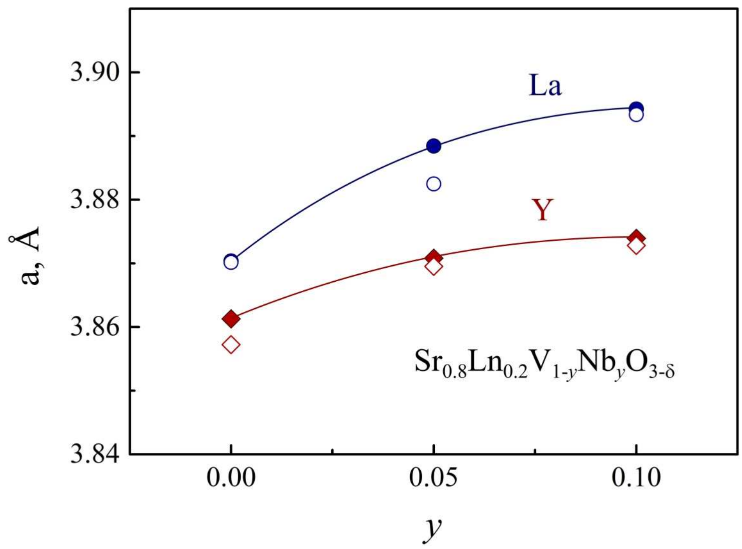

Fig 5.17. Comparison of the lattice parameters of perovskite-type $Sr_{0.8}Ln_{0.2}V_{1-y}Nb_yO_{3-\delta}$: as-prepared (closed symbols) and after heating-cooling cycle (T_{max} = 1473 K) in argon flow (open symbols).

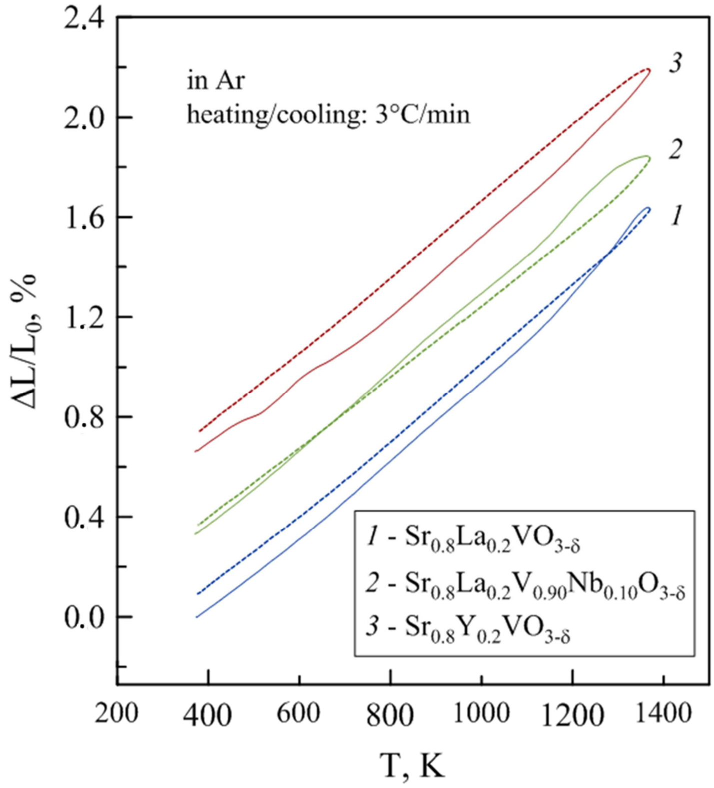

Fig 5.18. Dilatometric curves of $Sr_{0.8}Ln_{0.2}V_{1-y}Nb_yO_{3-\delta}$ ceramics on heating (solid lines) and subsequent cooling (dotted lines) in argon flow. The curves are shifted with respect to each other along Y axis for clarity.

5.5 Thermomechanical compatibility with solid electrolytes

As discussed in Chapter 3, parent $SrVO_{3-\delta}$ ceramics exhibit excessive thermal expansion coefficient under reducing conditions (Table 5.4) and non–linear behaviour of dilatometric curve on heating (Fig 5.19), attributed to chemical contribution to overall expansion. The chemical expansion in $SrVO_{3-\delta}$-based materials originates mainly from oxygen losses from the lattice on heating accompanied with $V^{4+} \rightarrow V^{3+}$ reduction and increase of average size of B-site cations; this is characteristic for many other perovskite-like and fluorite-type oxides containing variable-valence cations.

Substitutions by rare-earth cations into strontium sublattice and co-substitutions of vanadium with niobium reduce oxygen nonstoichiometry variations with temperatures (Fig.5.3) and, consequently, suppress the chemical contribution. The average TEC values of $Sr_{0.8}Ln_{0.2}V_{0.90}Nb_{0.10}O_{3-\delta}$ decrease down to 14.9×10^{-6} K^{-1} (Table 5.4), and $\Delta L/L_0$-T dependencies show essentially linear behavior (Fig.5.19), in correlation with the thermogravimetric data. Although thermal expansion coefficients of substituted vanadates are still higher compared to that of solid electrolytes (Table 4.2), it is expected to be further dumped by solid electrolyte component of composite electrodes, thus ensuring the thermomechanical stability of porous electrode layers.

Table 5.4

Average linear thermal expansion coefficients of $Sr_{1-x}Ln_xV_{1-y}Nb_yO_{3-\delta}$ ceramics in 10%H_2-N_2 atmosphere

Composition	Temperature range, K	TEC ($\bar{\alpha}\times10^6$) ± 0.1, K^{-1}	ρ*
$SrVO_{3-\delta}$	373-773 / 773-1223 / 373-1223	16.1 / 22.7 / 18.0	0.9995 / 0.9993 / 0.9956
$Sr_{0.8}La_{0.2}VO_{3-\delta}$	373-773 / 773-1273 / 373-1273	14.0 / 17.2 / 15.6	0.9995 / 0.9997 / 0.9988
$Sr_{0.8}La_{0.2}V_{0.95}Nb_{0.05}O_{3-\delta}$	373-1273	15.3	0.99986
$Sr_{0.8}La_{0.2}V_{0.90}Nb_{0.10}O_{3-\delta}$	373-1273	14.9	0.99991
$Sr_{0.8}Y_{0.2}VO_{3-\delta}$	373-773 / 773-1273 / 373-1273	14.4 / 18.2 / 16.1	0.9997 / 0.9995 / 0.9984
$Sr_{0.8}Y_{0.2}V_{0.95}Nb_{0.05}O_{3-\delta}$	373-1273	15.1	0.99989
$Sr_{0.8}Y_{0.2}V_{0.90}Nb_{0.10}O_{3-\delta}$	373-1273	14.9	0.99991

* ρ is the correlation coefficient of a linear $\Delta L/L_0$ - T dependence.

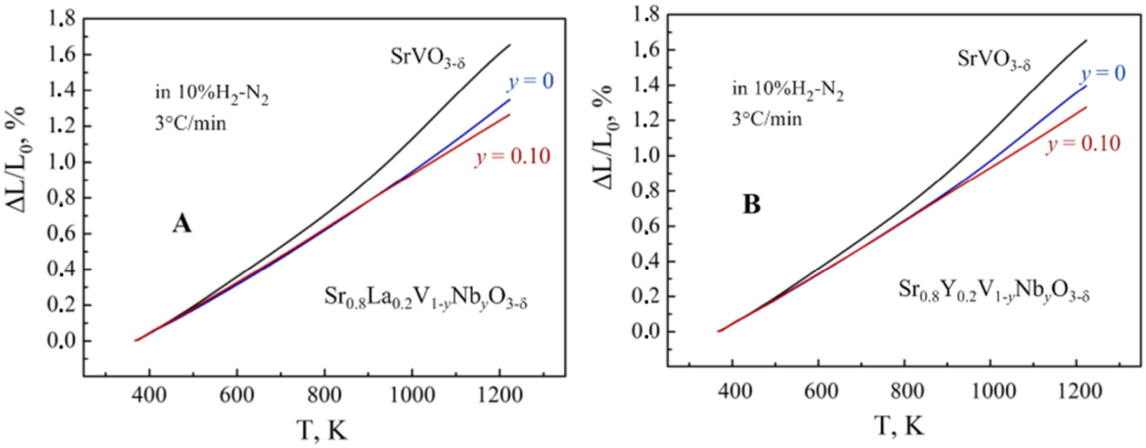

Fig 5.19. Dilatometric curves of **(A)** $Sr_{1-x}La_xV_{1-y}Nb_yO_{3-\delta}$ and **(B)** $Sr_{1-x}Y_xV_{1-y}Nb_yO_{3-\delta}$ ceramics in 10%H_2-N_2 atmosphere.

5.6 Conclusions

This chapter can be summarized as following:

i) Single-phase $Sr_{0.8}Ln_{0.2}V_{1-y}Nb_yO_{3-\delta}$ (Ln = La or Y, y = 0-0.10) ceramics with cubic perovskite structure can be synthesized by solid-state route under reducing conditions at 1773 K in 10%H_2-N_2 atmosphere.

ii) $Sr_{0.8}Ln_{0.2}V_{1-y}Nb_yO_{3-\delta}$ ceramics exhibit metallic-like electrical conductivity. The conductivity is nearly p(O_2)-independent in the studied oxygen partial pressure range and decreases with donor-type substitutions. For the studied compositional range, electrical conductivity exceeds 100 S/cm at temperatures ≤ 1223 K being sufficiently high for SOFC electrode applications.

iii) Partial substitutions of strontium by rare-earth metal cations expand the phase stability domain to more oxidizing conditions. At 1173 K, the upper-p(O_2) stability boundary was found to shift from $\sim 10^{-15}$ atm for the parent strontium vanadate to $\sim 6\times 10^{-13}$ atm for $Sr_{0.8}Y_{0.2}VO_{3-\delta}$, whereas oxidative decomposition of $Sr_{0.8}La_{0.2}VO_{3-\delta}$ occurs in the p(O_2) range between 10^{-10} and 10^{-5} atm.

iv) Co-substitution by niobium into vanadium sublattice has rather minor (Y-containing series) or even negative (La-containing series) effect on the perovskite phase stability boundary, but results in slower kinetics of oxidative decomposition under inert atmosphere.

v) Sluggish oxidation kinetics under inert gas environment, demonstrated by electrical, thermogravimetric and dilatometric studies, results in nearly reversible behavior of substituted vanadates after exposure to inert atmosphere, thus enabling the fabrication of solid-electrolyte cells with $SrVO_{3-\delta}$-based anodes under these conditions.

vi) An additional benefit of donor-type substitution is suppressed chemical expansion on thermocycling and, consequently, better thermomechanical compatibility of $Sr_{0.8}Ln_{0.2}V_{1-y}Nb_yO_{3-\delta}$ ceramics with solid electrolytes.

6. $SrVO_3$-$SrTiO_3$ solid solutions

Summarizing the work reported in the previous Chapters on the properties of $SrVO_3$-based materials, relevant for solid oxide fuel cell anodes applications, and on the effect of donor-type substitutions in either B or both sublattices, one may conclude that substituted materials do exhibit improved stability in combination with acceptable electrical properties, but the phase stability domain is still limited to reducing conditions.

Inspection of literature (Refs.[Marina, 2008; Brandon, 2011] and subsection 1.4.2.5.2) showed that $SrTiO_3$-based perovskites represent another group of ceramic oxide materials with a number of relevant properties attractive for SOFC anode applications. These include remarkable thermodynamic and dimensional stability in a wide range of T-$p(O_2)$ conditions and, similar to $SrVO_3$, sulfur tolerance and resistance to carbon depositions. At the same time, strontium titanate-based ceramics typically show electrical conductivity $\leq$ 10 S/cm under prospective operation conditions of fuel electrodes, implying significant current collection limitations with impact on electrode performance.

This chapter is focused on $SrVO_3$-$SrTiO_3$ pseudobinary system aiming to find a compromise between high electrical conductivity of vanadate and high stability of titanate lattice. Different synthetic procedures are also addressed in order to develop suitable approaches for electrode fabrication.

6.1. $Sr(V,Ti)O_3$ series prepared under reducing conditions

6.1.1 Phase composition, structure and microstructure

XRD analysis confirmed solid solubility for the entire range of compositions in the $SrVO_3$-$SrTiO_3$ system under reducing conditions. As prepared $SrV_{1-x}Ti_xO_{3-\delta}$ ceramics were phase-pure with cubic perovskite-type structure (space group *Pm*3*m*), as found for both $SrVO_3$ and $SrTiO_3$ parent compounds.

Substitution of vanadium by titanium cations results in an expansion of the perovskite lattice, according to Vegard law (Fig 6.1), due to larger ionic radii of Ti^{+4} (r^{VI} = 0.605 Å) cations compared to V^{+4} (r^{VI} = 0.580 Å) [Shannon, 1976]. Sintered $SrV_{1-x}Ti_xO_{3-\delta}$ samples were comparatively porous, with density below 75% of theoretical (Table 6.1), even though they were sintered at 1773 K (the highest temperature of available controlled-atmosphere furnace).

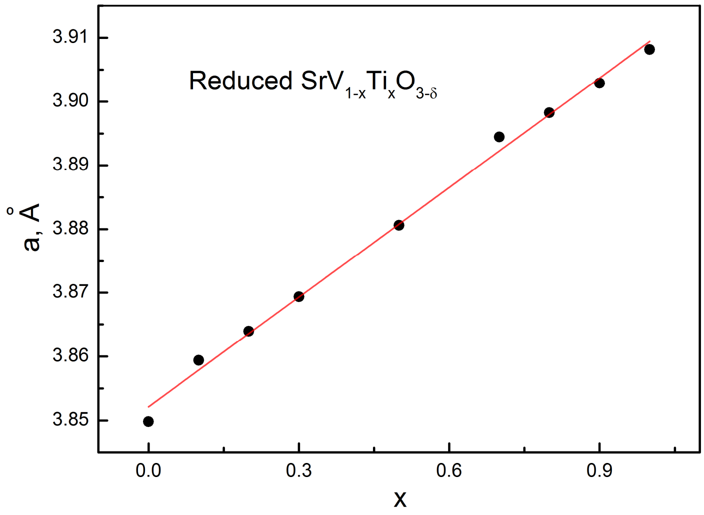

Fig 6.1. Lattice parameters of $SrV_{1-x}Ti_xO_{3-\delta}$ solid solutions synthesized under reducing conditions.

Table 6.1
Density of as-prepared reduced $SrV_{1-x}Ti_xO_{3-\delta}$ ceramics

Composition	Density, g/cm^3	Relative density*, %
$SrVO_{3-\delta}$	4.33	80
$SrV_{0.9}Ti_{0.1}O_{3-\delta}$	3.71	69
$SrV_{0.8}Ti_{0.2}O_{3-\delta}$	3.66	68
$SrV_{0.7}Ti_{0.3}O_{3-\delta}$	3.46	65
$SrV_{0.5}Ti_{0.5}O_{3-\delta}$	3.75	72
$SrV_{0.3}Ti_{0.7}O_{3-\delta}$	3.41	65
$SrV_{0.2}Ti_{0.8}O_{3-\delta}$	3.27	63
$SrV_{0.1}Ti_{0.9}O_{3-\delta}$	2.96	57

* Theoretical density was calculated neglecting oxygen nonstoichiometry

Fig. 6.2 illustrates the SEM micrographs of selected ceramic samples. All prepared materials possessed similar microstructures with a minor variation of grain size and non-negligible fraction of pores, in agreement with the density calculations. As mentioned in previous Chapters, non-negligible porosity should result in underestimated electrical conductivity values, but also promotes faster re-equilibration of the samples after a temperature or/and p(O_2) change.

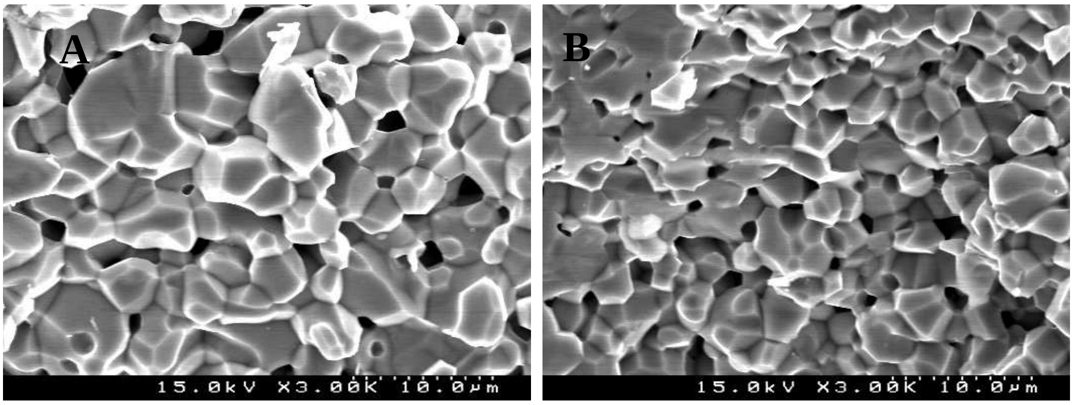

Fig 6.2 SEM micrographs of fractured cross-sections for **(A)** $SrV_{0.7}Ti_{0.3}O_{3-\delta}$ and **(B)** $SrV_{0.5}Ti_{0.5}O_{3-\delta}$ ceramics.

6.1.2 Thermochemical expansion under reducing conditions

The effects of substitution by titanium were found to be very similar to those provided by donor-type substitutions. The compositions with $x \leq 0.50$ were found to exhibit non-linear dilatometric behavior (Fig.6.3A). As for parent $SrVO_{3-\delta}$, this can be attributed, at least partly, to variations of oxygen nonstoichiometry with temperature (Fig.6.4) and corresponding chemical contribution to dimensional changes.

Dilatometric studies demonstrated that thermal expansion in strontium vanadate-titanate series under reducing conditions decreases gradually with increasing titanium content (Fig.6.3A). On one hand, substitution by titanium increasingly suppresses δ variations on thermal cycling (Fig.6.4), mostly due to decrease of total vanadium content. On the other hand, undoped $SrTiO_3$ ceramics have a quite moderate thermal expansion coefficient, ~ 11 ppm/K [Mori, 2011]. Thus, thermochemical expansion in $SrV_{1-x}Ti_xO_{3-\delta}$ system decreases with x due to reduction in both true thermal expansion and chemical contributions, and average TEC values for Ti-rich compositions approach that of conventional solid electrolyte ceramics (Fig.6.3B).

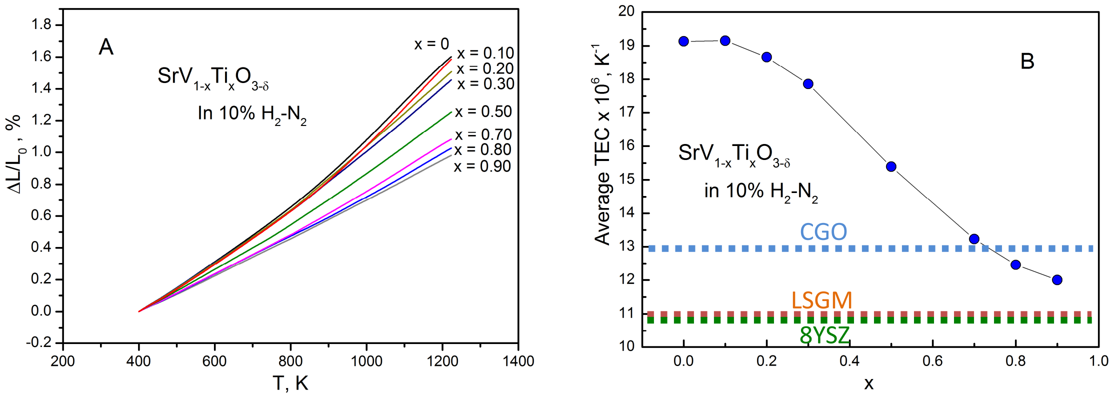

Fig 6.3. Dilatometric curves **(A)** and average thermal expansion coefficients (423-1223 K) **(B)** of SrV$_{1-x}$Ti$_x$O$_{3-\delta}$ ceramics in 10% H$_2$-N$_2$ atmosphere. The data on CGO, LSGM and 8YSZ solid electrolytes [Yaremchenko, 2014] are shown for comparison.

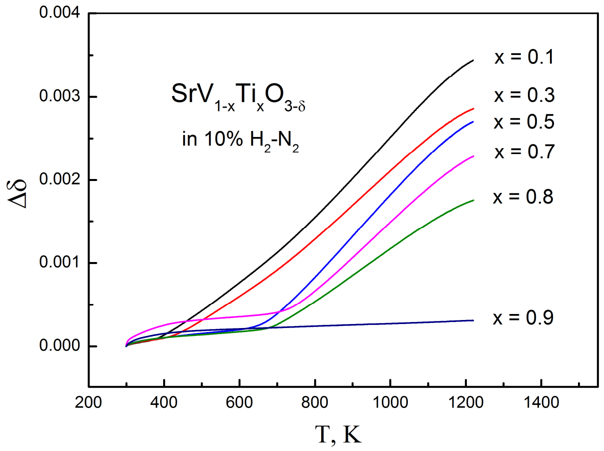

Fig 6.4. Relative changes of oxygen deficiency in SrV$_{1-x}$Ti$_x$O$_{3-\delta}$ on heating in 10% H$_2$-N$_2$ atmosphere.

6.1.3 Electrical conductivity

The conductivity of reduced SrV$_{1-x}$Ti$_x$O$_{3-\delta}$ ceramics was found to vary significantly with titanium content, changing by 3.5 orders of magnitude in high-temperature range, and shows a transition from metallic behavior for V-rich compositions to semiconducting behavior for Ti-rich ceramics (Fig.6.5A). Increasing titanium content decreases the fraction of V^{4+} responsible for electronic conduction in vanadates, and reasonably suppresses the conductivity. The intermediate composition with 50 at.% of titanium in B sublattice still shows reasonable level of electrical conductivity, ~20 S/cm at 1173 K. At lower vanadium contents, x ≥ 0.7, electrical transport is likely to occur via polaron-hopping mechanism involving V^{4+}/V^{3+} and Ti^{4+}/Ti^{3+} pairs, and shows temperature-activated behavior. As reduction from tetravalent to trivalent state is likely to occur under sufficiently reducing conditions (see Fig.2.17/Chapter II), the V^{4+}/V^{3+} couple is still expected to contribute to electronic transport even at small concentrations, as demonstrated by continuous decrease of electronic transport with *x* for Ti-rich side of the system.

As for donor-substituted vanadates, solid solutions in $SrVO_3$-$SrTiO_3$ system demonstrate very weak dependence of electrical conductivity on oxygen partial pressure (Fig.6.5B). The behavior of compositions with moderate substitution level, x = 0.1-0.2, resembles that of undoped $SrVO_{3-\delta}$: the conductivity decreases slightly with reducing $p(O_2)$ due to minor variations of oxygen nonstoichiometry and V^{3+} fractions (eq. 3.1). On the contrary, semiconducting Ti-rich ceramics show n-type behavior, characteristic for undoped and acceptor-doped $SrTiO_3$ [Chan, 1981; Eror, 1982]. Electrical conductivity increases with reducing $p(O_2)$, and the slope of $\sigma - p(O_2)$ dependencies also increases with decreasing V content and conductivity level.

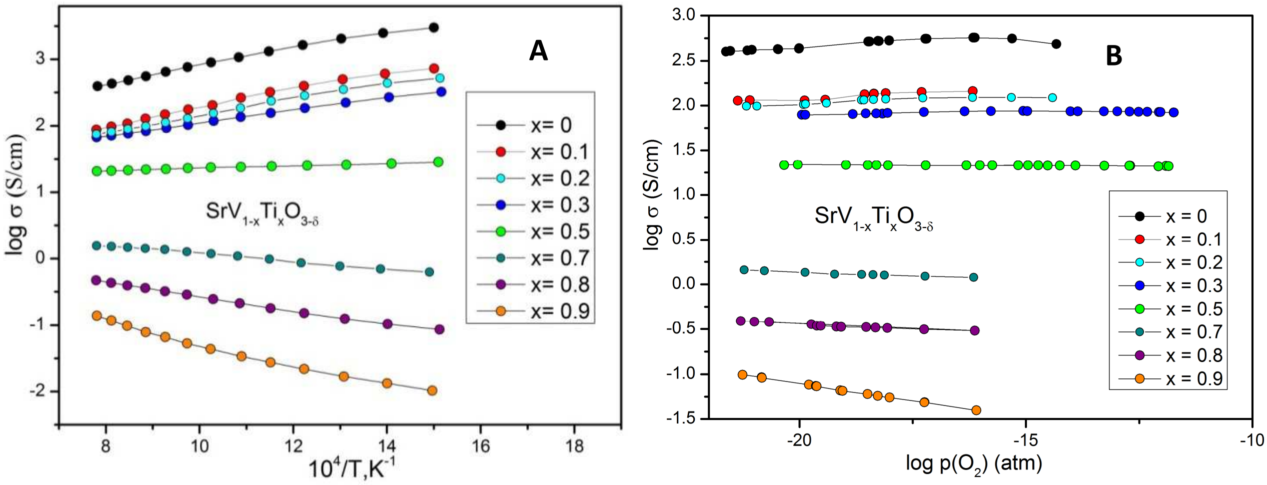

Fig 6.5. Electrical conductivity of $SrV_{1-x}Ti_xO_{3-\delta}$ ceramics as function of temperature 10% H_2-N_2 atmosphere **(A)** and as function of oxygen partial pressure at 1173 K **(B)**.

6.1.4 Stability of perovskite phase

Fig.6.6(A-B) compares thermogravimetric and dilatometric curves of Ti-rich $SrV_{1-x}Ti_xO_{3-\delta}$ in one heating/cooling cycle in air with that of undoped strontium vanadate. Decreasing vanadium content reasonably results in a lower oxygen uptake associated with $V^{3+} \rightarrow V^{4+} \rightarrow V^{5+}$ oxidation and decomposition of perovskite phase. Related dimensional changes are also reduced and become negligible for Ti-rich samples. Still, even for compositions with highest titanium content, oxidation in air results in a phase separation and segregation of minor amounts V^{5+}-based impurity phases, $Sr_2V_2O_7$ and $Sr_3V_2O_8$, in addition to main $SrTiO_3$-based cubic perovskite, as demonstrated by XRD (Fig.6.6C). In fact, oxygen uptake is nearly proportional to the vanadium fraction in $SrV_{1-x}Ti_xO_{3-\delta}$ (Fig.6.6A), which is also consistent with affinity of V^{5+} to 4-fold coordination (see discussion in subsection 4.5).

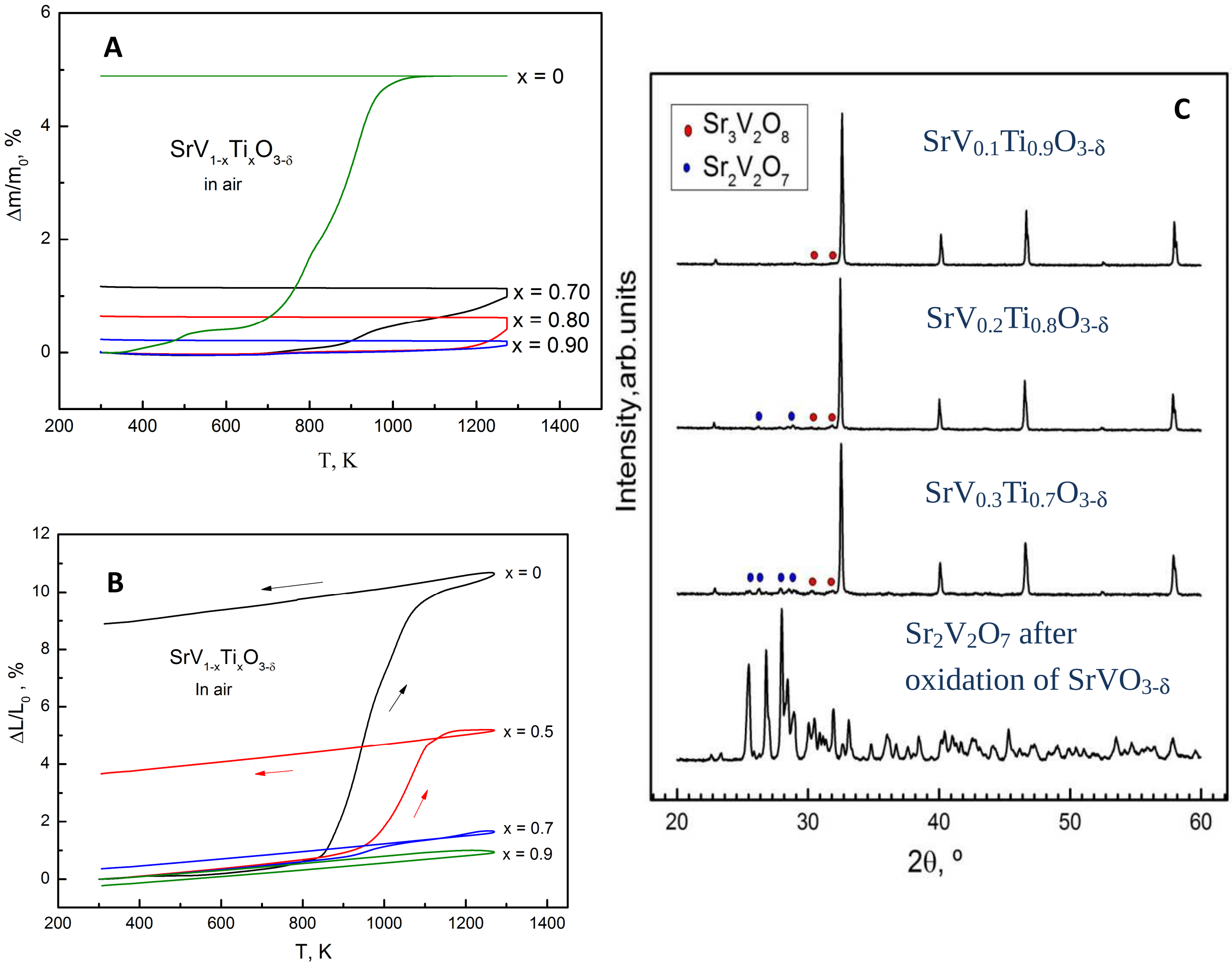

Fig 6.6. Thermogravimetric **(A)** and dilatometric curves **(B)** of $SrV_{1-x}Ti_xO_{3-\delta}$ ceramic samples recorded in one heating/cooling cycle in air, and XRD patterns collected after this cycle **(C)**. The TGA cycle included isothermal dwell for 5 h at 1273 K.

The approximate upper-p(O_2) stability boundaries of perovskite-type $SrV_{1-x}Ti_xO_{3-\delta}$ solid solutions at 1173 were determined from the *conductivity vs p(O_2)* data collected increasing p(O_2) in a stepwise manner with equilibration at each step (Fig.6.7A). Once again, a drop of conductivity was attributed to decomposition of original perovskite phase with segregation of insulating $Sr_3V_2O_8$ confirmed by XRD analysis after experiment (Fig.6.7B). Still, substitution of only 10 at.% of vanadium by titanium was found to shift the stability limit of perovskite phase to higher oxygen partial pressure by 2 orders of magnitude. For compositions with ≥30 %Ti in B sublattice phase decomposition occurred in $p(O_2)$ range between approximately 10^{-11} and 10^{-5} atm and could not be determined precisely because the buffer ability of reducing gases is lost in the transition to inert conditions.

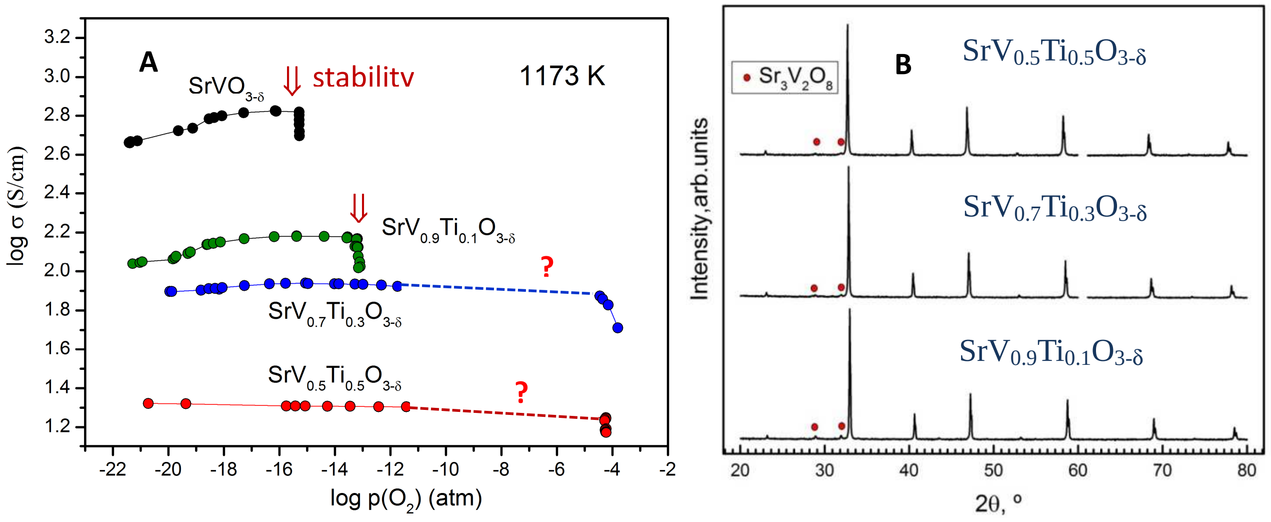

Fig 6.7. Determination of approximate upper-$p(O_2)$ stability limits of $SrV_{1-x}Ti_xO_{3-\delta}$ perovskites from the *log σ – log p(O₂)* data **(A)**, and XRD patterns recorded after these experiments **(B)**. Marked reflections are indexed according to JCPDS #81-1844.

Still, all compositions in $SrVO_3$-$SrTiO_3$ system were found to undergo phase separation under inert gas atmosphere at elevated temperatures. Fig.6.8 shows XRD patterns of selected $SrV_{1-x}Ti_xO_{3-\delta}$ samples calcined in Ar flow with $p(O_2) \sim 10^{-5}$ at for 20 h at 1173 K. Similar to donor-substituted vanadates, $Sr(V,Ti)O_{3-\delta}$ solid solutions showed sluggish kinetics of oxidation under these conditions. The degree of phase separation and amount of oxidation product reasonably decreased with increasing titanium content (Fig.6.8 and Table 6.2), and only minor traces of $Sr_3V_2O_8$ phase were observed in $SrV_{0.1}Ti_{0.9}O_3$ samples after the calcination procedure.

Table 6.2

Fraction of $Sr_3V_2O_8$ phase in $SrV_{1-x}Ti_xO_{3-\delta}$ samples after annealing in Ar flow at 1173 K, determined by semi-quantification of XRD data

Sample	$p(O_2)$, atm	Time, h	$Sr_3V_2O_8$, vol.%
$SrV_{0.9}Ti_{0.1}O_{3-\delta}$	10^{-5}	20	8.1
$SrV_{0.5}Ti_{0.5}O_{3-\delta}$	10^{-5}	20	2.2
$SrV_{0.1}Ti_{0.9}O_{3-\delta}$	10^{-5}	20	1.6

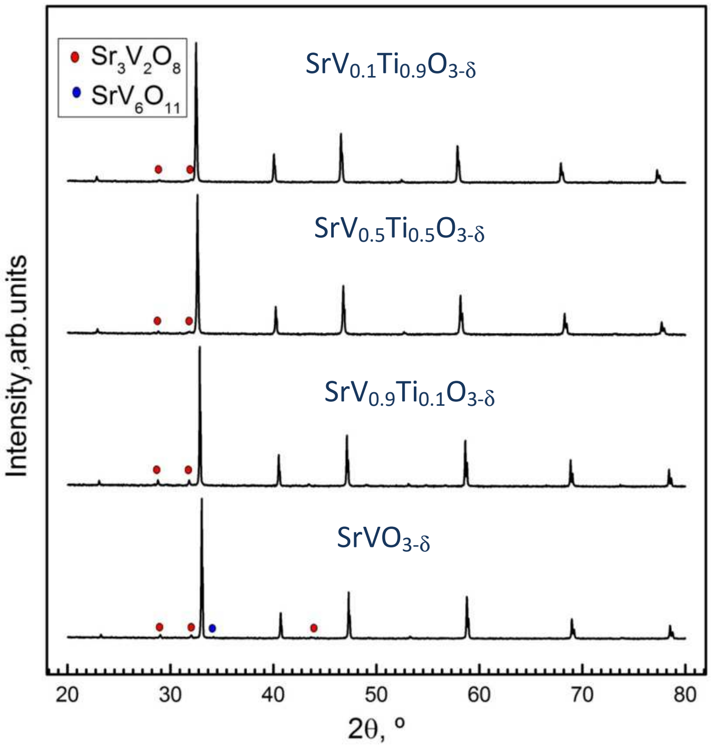

Fig 6.8. XRD patterns of powdered $SrV_{1-x}Ti_xO_{3-\delta}$ ceramic samples after thermal treatment in Ar flow ($p(O_2) \sim 10^{-5}$ atm) at 1173 K for 20 h.

The redox behavior of Ti-substituted strontium vanadate on cycling between reducing and oxidizing or inert conditions was, again, similar to that of donor-substituted vanadates. Fig.6.9A compares relaxation of electrical conductivity of $SrV_{0.5}Ti_{0.5}O_{3-\delta}$ ceramics in two different redox cycles at 1173 K. Oxidation in air results in a fast drop of conductivity by 3 orders of magnitude caused by segregation of insulating $Sr_2V_2O_7$ and $Sr_3V_2O_8$ phases. Nevertheless, switching back to reducing atmosphere resulted in a reverse reduction of the sample and nearly instant restoration of the conductivity level (Fig 6.9A). Thermogravimetric data collected in the identical cycle (Fig.6.9B) indicate, however, that re-reduction in fact proceeds slower and is a two-step process, similar to parent $SrVO_{3-\delta}$ (see Chapter 3). The initial state of the sample was not restored by the end of the cycle (Fig.6.9B). Post-mortem XRD analysis confirmed the presence of oxygen-rich $Sr_3V_2O_8$ and also onset of a secondary perovskite phase (Fig.6.10 (top)). SEM/EDS analysis of ceramic sample after conductivity relaxation experiment also demonstrated irreversible microstructural changes and separation into V- and Ti-rich phases (Fig.6.11A vs 6.11(C-D)). Thus, the apparent restoration of conductivity level after re-reduction must be attributed to the phase separation with formation a mixture of highly-conductivity Ti-depleted $SrVO_{3-\delta}$ and low-conductive V-depleted $SrTiO_3$ phases.

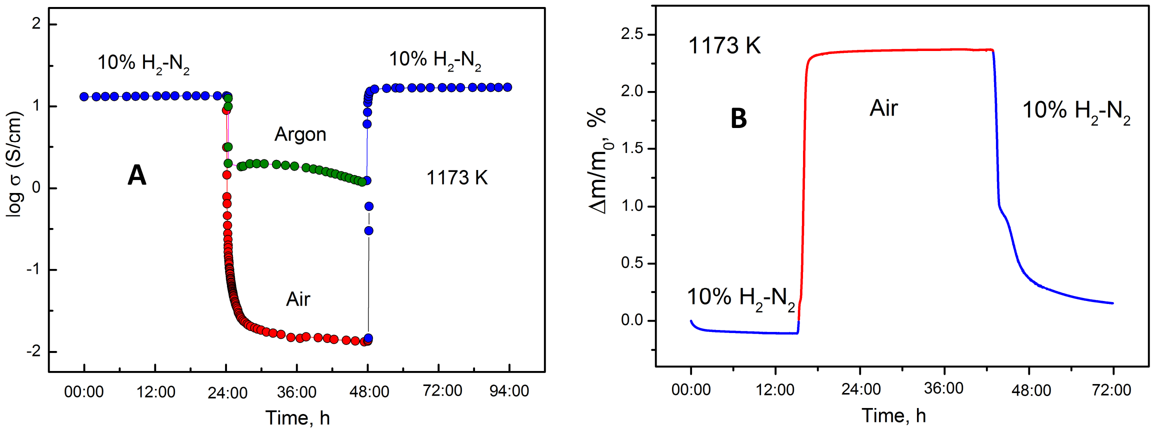

Fig 6.9. Relaxation of electrical conductivity of $SrV_{0.5}Ti_{0.5}O_{3-\delta}$ samples in reducing→air→reducing and reducing→inert→reducing redox cycles at 1173 K **(A)**, and relative weight change of powdered $SrV_{0.5}Ti_{0.5}O_{3-\delta}$ sample in identical reducing→air→reducing cycle **(B)**.

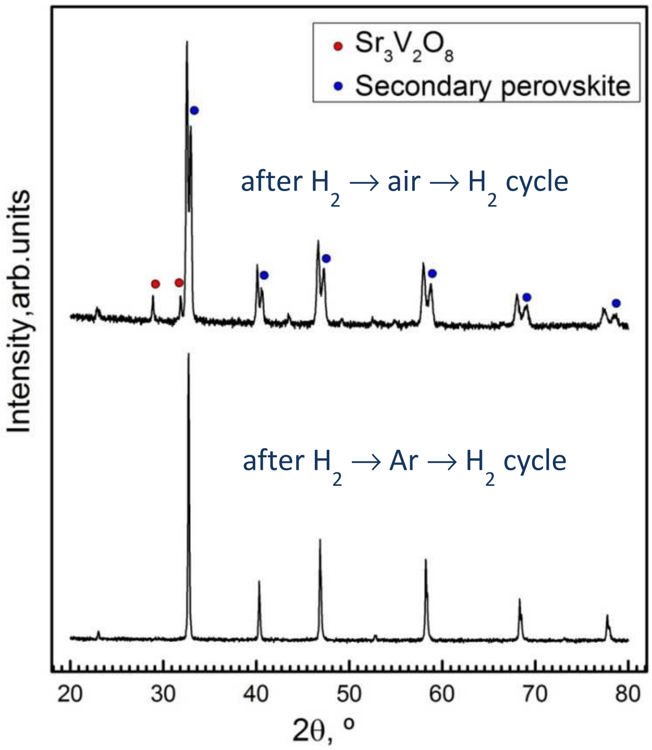

Fig 6.10. XRD patterns of $SrV_{0.50}Ti_{0.50}O_{3-\delta}$ samples after redox cycling at 1173 K.

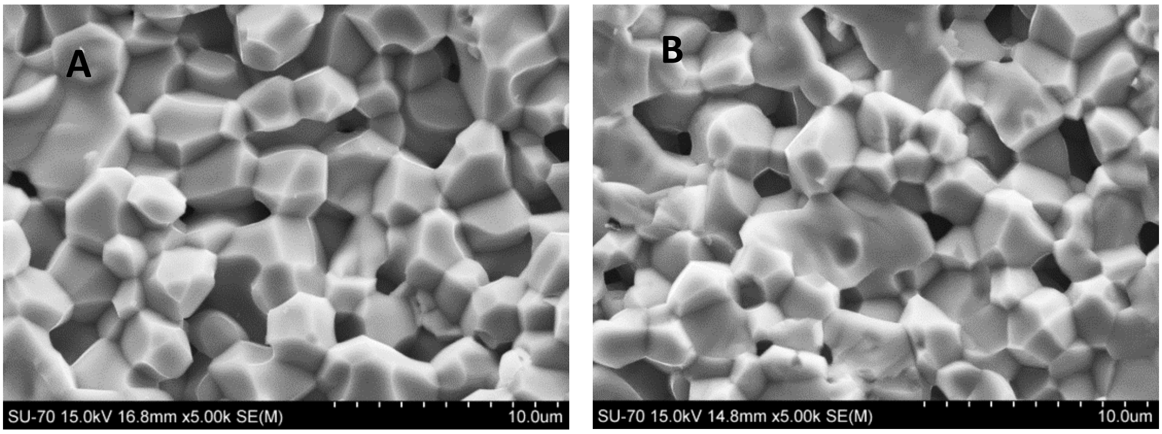
A
SU-70 15.0kV 16.8mm x5.00k SE(M)
10.0um
B
SU-70 15.0kV 14.8mm x5.00k SE(M)
10.0um

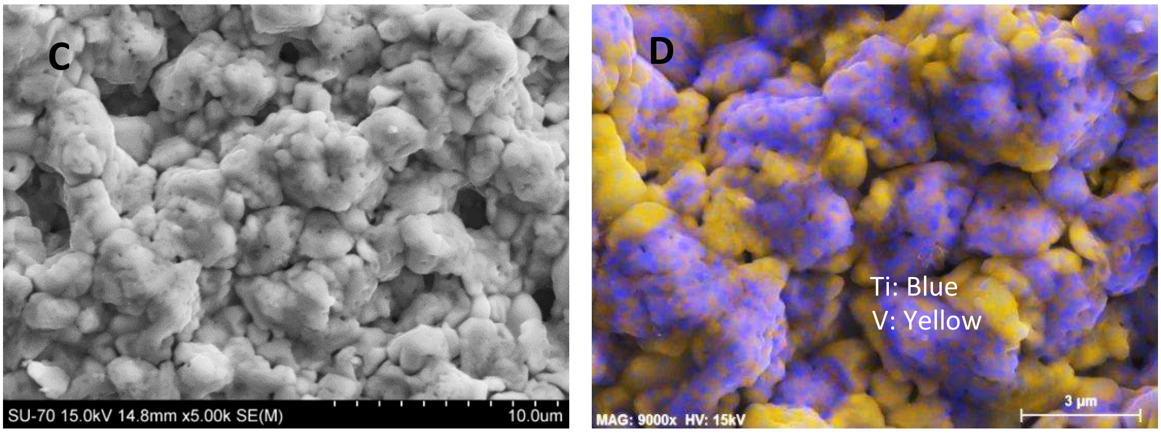

Fig 6.11. SEM micrographs of fractured $SrV_{0.50}Ti_{0.50}O_{3-\delta}$ ceramic samples: as-prepared **(A)**; after reducing → inert → reducing redox cycle **(B)**; after reducing → air → reducing redox cycle **(C)**; and **(D)** EDS elemental mapping corresponding to micrograph (C).

Oxidation in inert gas flow resulted in a smaller drop of conductivity and comparatively slower degradation (Fig.6.9A), probably limited to the surface of the grains. Again, inverse reduction results in rapid recovery of conductivity level. In this case, however, neither secondary phases were observed in XRD patterns after the experiment (Fig.6.10 (bottom)), nor noticeable microstructural changes could be revealed by post-mortem SEM inspection (Fig.6.11B). Once again, these observations confirm that oxidative decomposition is kinetically limited on thermal treatment under inert gas atmosphere.

6.2. Sr(V,Ti)O_3 series prepared under oxidizing conditions

Although substitution by titanium extends the stability domain of $SrVO_3$–based perovskite phase, reduced $SrV_{1-x}Ti_xO_{3-\delta}$ solid solutions still undergo phase separation and irreversible microstructural and phase composition changes on exposure to air or even inert atmospheres at elevated temperatures. Thus, processing of $SrV_{1-x}Ti_xO_{3-\delta}$ anode layers would imply additional difficulties related to processing under reducing atmospheres. On the other hand, multiphase products of redox cycling demonstrated comparatively high level of electrical conductivity, in the range required for anode applications.

The second half of this Chapter was focused therefore on the alternative approach of direct processing of anode materials of the $SrV_{1-x}Ti_xO_{3-\delta}$ series under oxidizing conditions, as well as formation of multiphase ceramics starting from oxidized components.

6.2.1 Phase composition, structure and microstructure

Preparation of oxidized materials with nominal cation composition $SrV_{1-x}Ti_xO_3$ (x = 0.7-0.9) was performed by two different routes, as illustrate in Fig.2.2. In first route, the precursor powders were calcined in air with step-wise increase of temperature (Table 2.2) and multiple intermediate regrinding until no further changes could be observed by XRD analysis. In second route, the precursor powders underwent a limited number of calcination steps. Then, ceramic samples for both series of samples were sintered in air at 1273-1373 K. Hereafter, the first series is based on Ti-rich compositions referred to as “SVT_ox_P” or as “single-phase perovskite”, and the second series – as “SVT_ox_MP” or “multiphase” compositions.

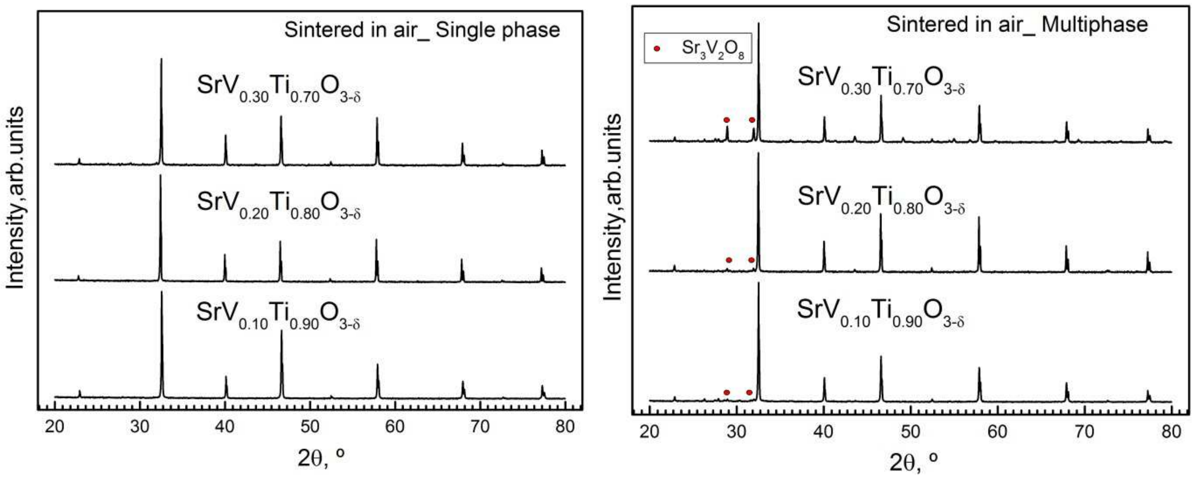

Fig 6.12. XRD patterns of $SrV_{1-x}Ti_xO_3$ samples sintered in air. $Sr_3V_2O_8$ impurity is marked according to JCPDS PDF #81-1844.

XRD results showed that repeated calcinations at elevated temperatures make it possible to obtain oxidized phase-pure $SrV_{1-x}Ti_xO_3$ solid solutions with cubic perovskite-type structure (Fig.6.12, left), although minor amounts of impurities undetectable by XRD or minor losses of vanadium oxide in the course of calcinations cannot be excluded completely. The solid solution range was limited to $x \sim 0.7$, as compositions with higher vanadium content ($x \leq 0.6$) contained significant amount of secondary phases even after prolonged calcinations.

As follows from the explanation of series abbreviation, the second series of $SrV_{1-x}Ti_xO_3$ ceramics comprised secondary phases in addition to main $SrTiO_3$-based cubic perovskite component. The main secondary phase was $Sr_3V_2O_8$, and its fraction increased with decreasing *x* (Fig.6.12, right).

Fig.6.13 compares the microstructures of as-prepared ceramic materials. Multiphase ceramics showed heterogeneous grain size distribution with different type of grains shape. SEM/EDS elemental mapping confirmed the presence of two phases, Ti-rich and V-rich, in agreement with XRD results. Multiphase ceramics also had lower density (higher porosity) (Table 6.3) caused by lower temperatures of processing/sintering in order to maintain multiphase composition and to avoid liquid phase formation (Fig.2.1).

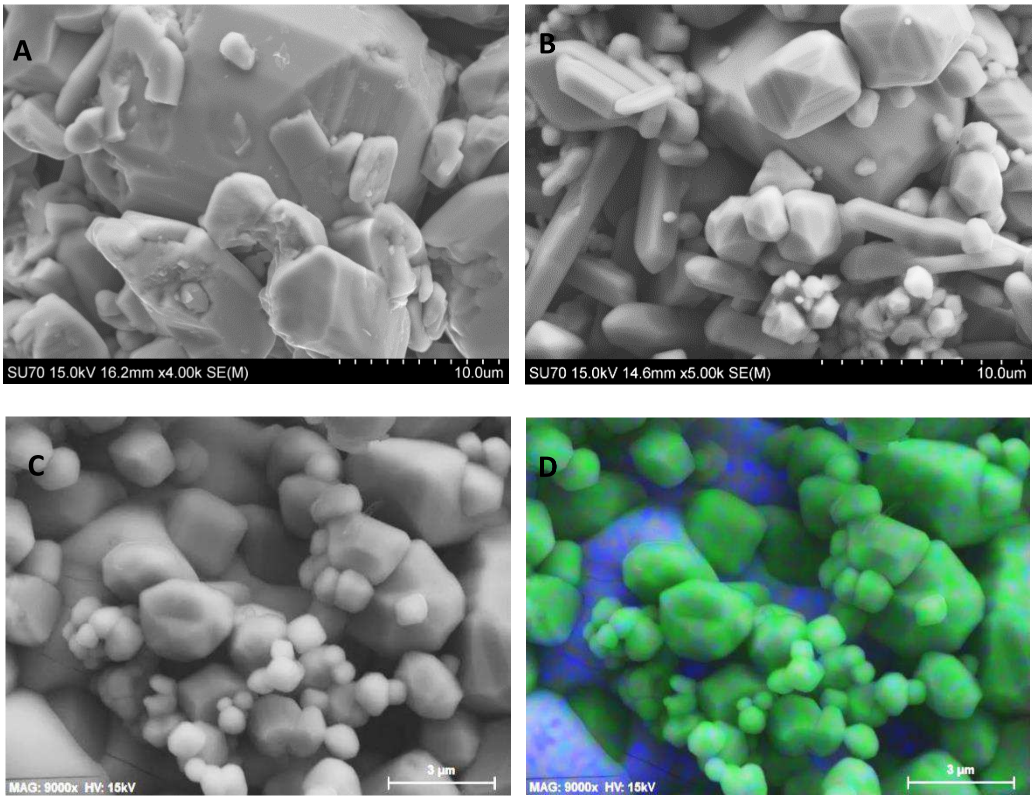
A
SU70 15.0kV 16.2mm x4.00k SE(M)
10.0um
B
SU70 15.0kV 14.6mm x5.00k SE(M)
10.0um
C
MAG: 9000x HV: 15kV
3 µm
D
MAG: 9000x HV: 15kV
3 µm

Fig 6.13. SEM micrographs: **(A)** single-phase $SrV_{0.3}Ti_{0.7}O_{3-\delta}$; **(B-C)** multiphase $SrV_{0.3}Ti_{0.7}O_{3-\delta}$; and **(D)** micrograph C with overlaid EDS elemental mapping (Ti: green; V: blue).

Table 6.3

Properties of the as-prepared $SrV_{1-x}Ti_xO_3$ ceramics sintered in air

	Single-phase		Multiphase
Composition	Unit cell parameter *a*, Å	Density, g/cm^3	Density, g/cm^3
$SrV_{0.1}Ti_{0.9}O_{3\pm\delta}$	3.9071(2)	3.20	2.31
$SrV_{0.2}Ti_{0.8}O_{3\pm\delta}$	3.9048(5)	3.30	2.37
$SrV_{0.3}Ti_{0.7}O_{3\pm\delta}$	3.9041(4)	3.29	2.81

6.2.2 Thermal expansion

Dilatometric studies of oxidized single-phase $SrV_{0.3}Ti_{0.7}O_3$ ceramics showed very minor difference in thermal expansion on heating in air or in 10%H_2-N_2 atmosphere between room temperature and 1273 K (Fig 6.14). The values of average thermal expansion coefficients (TECs) in this temperature range were similar, (11.4-11.5)×10^{-6} K^{-1}, in both atmospheres. This indicates that reduction of oxidized single-phase $SrV_{1-x}Ti_xO_3$ proceeds without noticeable dimensional changes.

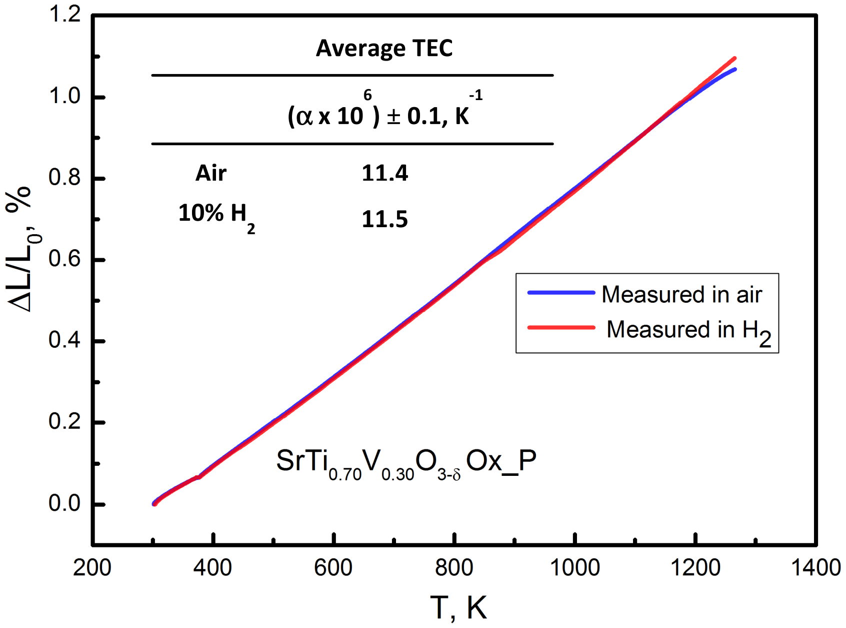

Fig 6.14. Dilatometric curves of oxidized single-phase $SrV_{0.3}Ti_{0.7}O_3$ ceramics obtained on heating in oxidizing and reducing atmospheres. Inset Table lists corresponding average TECs at 373-1273 K.

6.2.3 Electrical conductivity and redox behavior

All oxidized $SrV_{1-x}Ti_xO_3$ ceramics, single-phase and multiphase, showed semiconducting behavior in air with comparatively low electrical conductivity (Fig.6.15) comparable to undoped $SrTiO_3$ [Chan, 1981], $Sr_2V_2O_7$ and $Sr_3V_2O_8$ (Fig.3.7). The materials showed comparable levels of conductivity without monotonous compositional dependence and with a minimum at intermediate V contents.

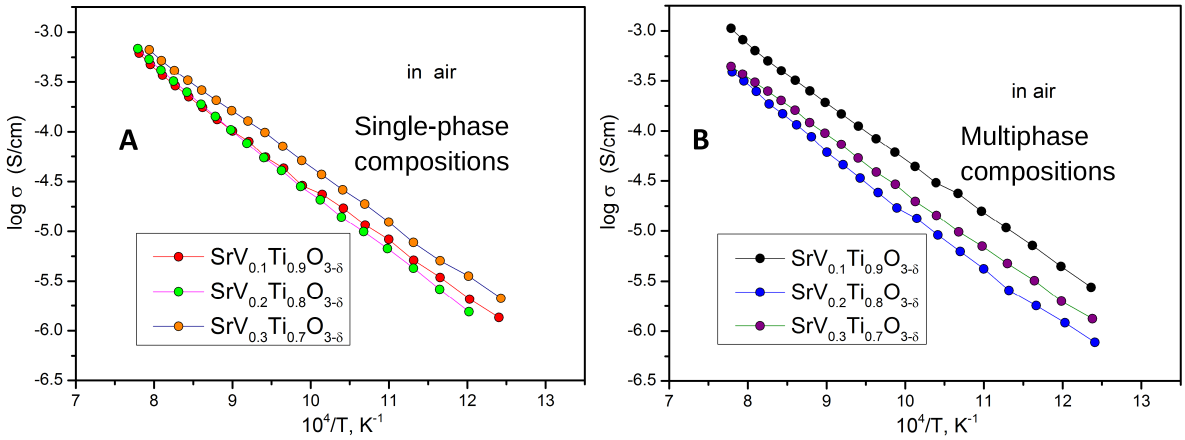

Fig 6.15. Temperature dependence of electrical conductivity of $SrV_{1-x}Ti_xO_3$ ceramics in air: **(A)** single-phase perovskites, and **(B)** multiphase compositions.

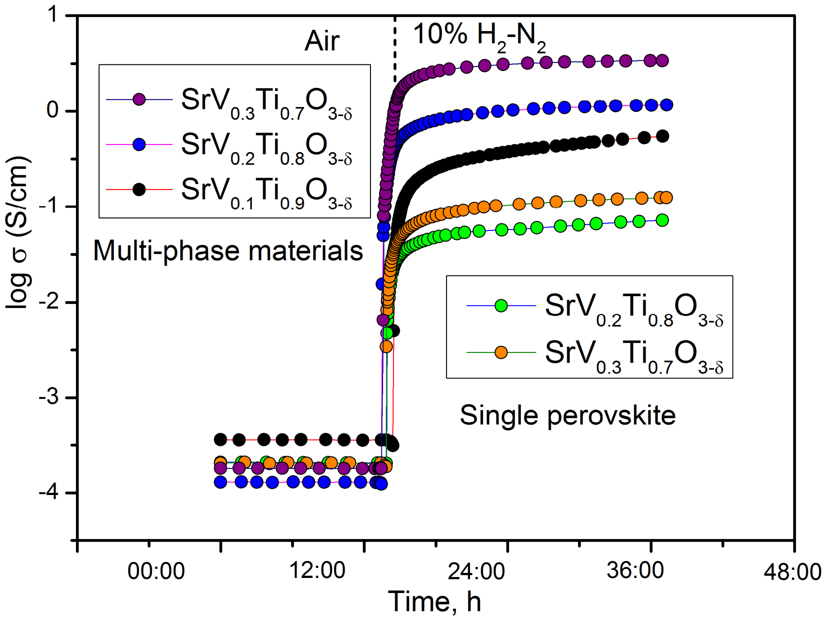

Fig 6.16. Variations of electrical conductivity of $SrV_{1-x}Ti_xO_3$ ceramics with time on reduction in 10% H_2-N_2 flow at 1173 K.

Fig.6.16 shows relaxation of electrical conductivity of oxidized $SrV_{1-x}Ti_xO_3$ on in-situ reduction at 1173 K. Switching from oxidizing to reducing atmosphere results in nearly instant increase of electrical conductivity by 2.5-4.0 orders of magnitude. This initial sharp gain is followed by further slower augmentation of conductivity reflecting, most likely, an initial stage of fast surface reduction followed by slower reduction of grains interior.

The mechanisms behind the conductivity are slightly different for single-phase perovskite and for multiphase ceramics. In the first case, increase of conductivity is caused by increase of oxygen nonstoichiometry and reduction of transition metal cations, $V^{5+}\rightarrow V^{4+}$, followed by partial $V^{4+}\rightarrow V^{3+}$ and, in lesser degree, $Ti^{4+}\rightarrow Ti^{3+}$ reduction. The latter pairs are responsible for n-type electronic transport, as discussed above for reduced $SrV_{1-x}Ti_xO_3$ solid solutions. Note that, after 24 h of reduction, conductivity in these single-phase ceramics correlates with vanadium content, but still is significantly lower compared to reduced $SrV_{1-x}Ti_xO_3$ counterparts sintered at high temperatures (Fig.6.5).

In the case of multiphase samples, the increase of electrical conductivity on reduction originates mainly from the transformation of oxidized V-rich components, $Sr_2V_2O_7$ and $Sr_3V_2O_8$, into perovskite-type $SrVO_{3-\delta}$ with superior conductivity. As demonstrated in Chapter 3, this transformation is slow below 1273 K, and, after 24 h of reduction, ceramic samples still comprised significant fraction of $Sr_3V_2O_8$, in addition to major $SrTiO_3$-based and secondary $SrVO_3$-based perovskites (Fig.6.17A). Nevertheless, this approach resulted in formation of composite material with highly conductive strontium vanadate component well distributed in dimensionally stable strontium titanate matrix (Fig.6.17B). This resulted in comparatively high electrical conductivity which showed direct correlation with the fraction of $SrVO_3$-based component and significantly exceeded that of single-phase counterparts with nominally identical cation compositions (Fig.6.16). Noteworthy, the difference in conductivity gain upon reduction of single-phase and multiphase materials showed also direct correlation with oxygen losses recorded by TGA on heating and subsequent isothermal treatment in 10%H_2-N_2 atmosphere at 1273 K. This seems to suggest slow kinetics of reduction of oxidized $SrV_{1-x}Ti_xO_3$ characteristic for other donor-doped strontium titanates [Yaremchenko, 2016; Neagu, 2010].

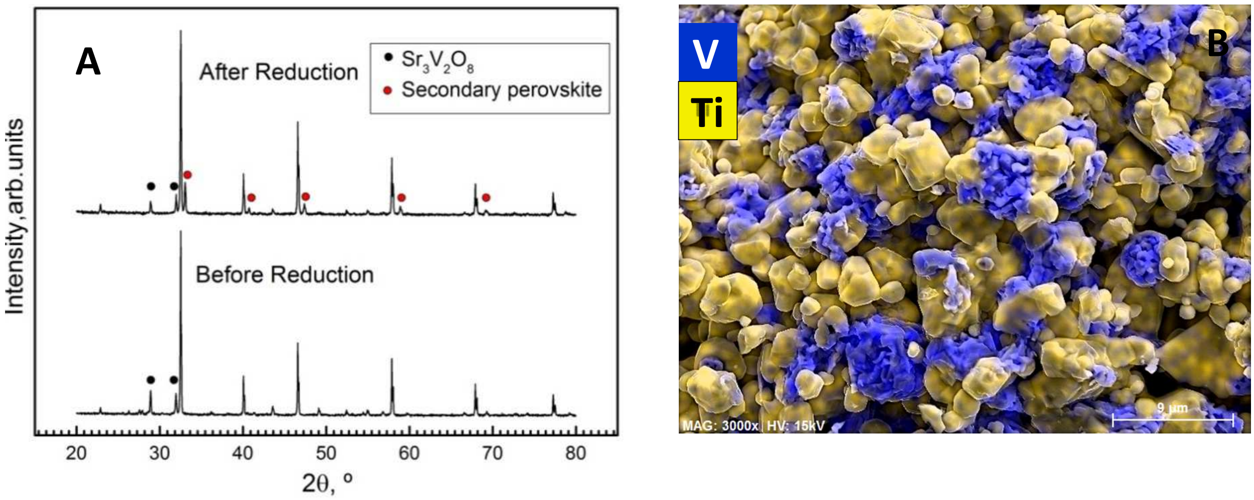

Fig 6.17. (A) XRD patterns of multiphase $SrV_{0.3}Ti_{0.7}O_3$ ceramics before and after reduction (marked reflections are indexed according to JCPDS PDF #81-1844), and **(B)** SEM micrograph with EDS elemental mapping of the sample after reduction.

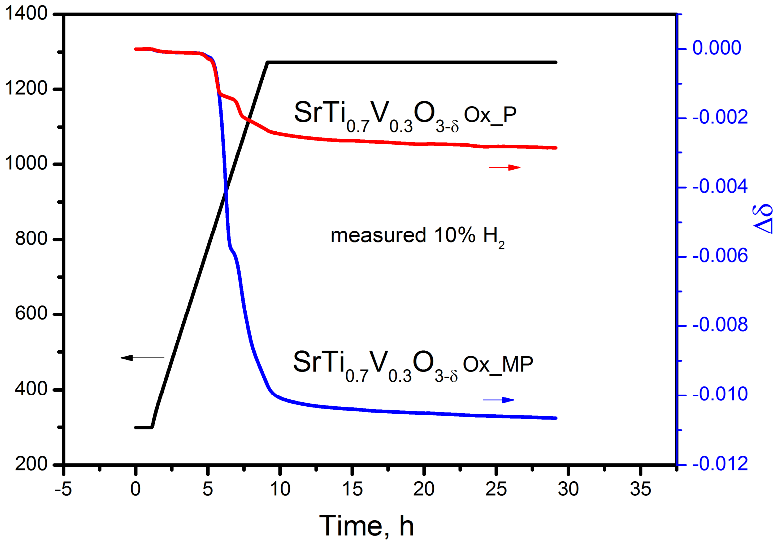

Fig 6.18. Relative changes of oxygen content per formula unit of powdered samples with nominal $SrV_{0.3}Ti_{0.7}O_3$ composition on heating and isothermal treatment under reducing atmosphere at 1273 K.

6.3 Conclusions

i) $SrVO_3$ and $SrTiO_3$ form entire range of solid solutions with cubic perovskite-type structure under reducing conditions.

ii) Substitution by titanium cations into vanadium sublattice suppresses gradually oxygen deficiency variations and thermochemical expansion of $Sr(V,Ti)O_3$ ceramics, thus improving the thermomechanical compatibility with solid electrolytes.

iii) This type of substitution results also in a gradual decrease of electrical conductivity of perovskite-type $SrV_{1-x}Ti_xO_{3-\delta}$ solid solutions under reducing conditions. Still, the compositions with 50 or less at.% of titanium in vanadium sublattice demonstrate the level of conductivity acceptable for SOFC electrode applications ($\sigma > 20$ S/cm at temperatures below 1273 K)

iv) As for donor doping, substitution of vanadium by titanium results in a gradual shift of upper-$p(O_2)$ stability boundary of perovskite phase to higher oxygen partial pressures. For compositions with 30 and more at.% of titanium in B sublattice, oxidative decomposition occurs in the $p(O_2)$ range between 10^{-11} and 10^{-5} atm at 1173 K. This means that SOFC anodes based on perovskite-type $SrV_{1-x}Ti_xO_{3-\delta}$ still must be sintered either under reducing conditions or in inert gas atmosphere where oxidative decomposition is kinetically stagnated.

v) The solubility of vanadium cations in B sublattice of $SrTiO_3$ under oxidizing conditions is limited to ~30 at.%. The electrical conductivity of single-phase V-substituted $SrTiO_3$ remains comparatively low after reduction at 1173 K.

vi) An attractive approach is the fabrication of composite anodes starting from oxidized multiphase mixture with total nominal cation composition $SrV_{1-x}Ti_xO_{3-\delta}$ and moderate fraction of V-based phase (e.g. $x \sim 0.7$). Transformation of strontium orthovanadate on reduction into highly-conductive perovskite-type strontium vanadate phase finely distributed in the stable $SrTiO_3$-based matrix results in substantial increase of electrical conductivity. This approach opens a window for further optimization based on precise microstructural control and thermal pre-history under oxidizing conditions.

7. Preliminary screening of electrode performance

Based on the results discussed in Chapters 4-6, $SrV_{0.5}Ti_{0.5}O_{3-\delta}$ and $Sr_{0.8}La_{0.2}VO_{3-\delta}$ were considered as single-phase compositions with a best combination of electrical properties and phase stability. These two vanadates synthesized under reducing conditions and one multiphase material with nominal cation composition $SrV_{0.3}Ti_{0.7}O_3$ (marked below as $SrV_{0.3}Ti_{0.7}O_3$_MP) prepared in air were selected for preliminary electrochemical testing as anode materials. This Chapter includes evaluation of chemical compatibility of selected materials with solid electrolytes, electrode preparation procedures, and preliminary screening of electrochemical performance of electrode layers.

7.1 Chemical compatibility between electrodes and electrolytes

Reactivity between electrode and electrolyte, in the course of high temperature bonding of cell components or under operation conditions, can results in formation of undesired phases with poor transport properties at the electrode/electrolyte interface, with negative effect on mass transport, electrode polarization and long-term stability. Keeping this in mind, selected perovskite-type vanadates were tested for chemical compatibility with 8YSZ and CGO solid electrolytes.

A small amount of powdered vanadate was mixed with equal amount (50:50 wt.%) of solid electrolyte powders, grounded, pressed into pellet and fired under reducing atmosphere at 1473 K. XRD patterns, collected after calcination, are shown in Figs.7.1 and 7.2.

Both substituted materials, $Sr_{0.8}La_{0.2}VO_{3-\delta}$ and $SrV_{0.5}Ti_{0.5}O_{3-\delta}$, as well as undoped strontium vanadate were found to react with 8YSZ under applied conditions with formation of $Sr_3Zr_2O_7$ phase. The amount of reactivity product was comparable in all cases. $Sr_3Zr_2O_7$ and other Ruddlesden-Popper phases of $Sr_{n+1}Zr_nO_{3n+1}$ are known to show very low electrical conductivity, ~ 10^{-5} S/cm at 1273 K [Poulsen, 1992] and therefore can be expected to have an adverse effect on the electrode performance.

The situation was somewhat different in the case of CGO as a solid electrolyte. Undoped $SrVO_{3-\delta}$ reacted with CGO with formation of $Sr_3V_2O_8$ as a by-product. $SrV_{0.5}Ti_{0.5}O_{3-\delta}$ also tends to react with CGO under used conditions; impurity peaks in XRD pattern were assigned to Ruddlesden-Popper $Sr_3Ti_2O_7$ phase. At the same time, $Sr_{0.8}La_{0.2}VO_{3-\delta}$ showed better stability in contact with CGO solid electrolytes compared to other tested vanadates: only minor impurity peaks, almost on the background level, were observed in XRD pattern after the compatibility test. Although mechanisms of reaction with CGO are not obvious at the moment, it seems that decreasing strontium content is vanadate phase by substitution in A sublattice is favorable for improved chemical stability with respect to ceria; this is confirmed by the suppressed reactivity of $Sr_{0.8}La_{0.2}VO_{3-\delta}$ and is also supported by thermodynamic predictions of the dependence of unwanted reaction product $Sr_3V_2O_8$ on activity ratio a_{Sr}:a_V (see Chapter II, fig.2.16) and dependence of $Sr_3Ti_2O_7$ on activity ratio a_{Sr}:a_{Ti} [Monteiro, 2012].

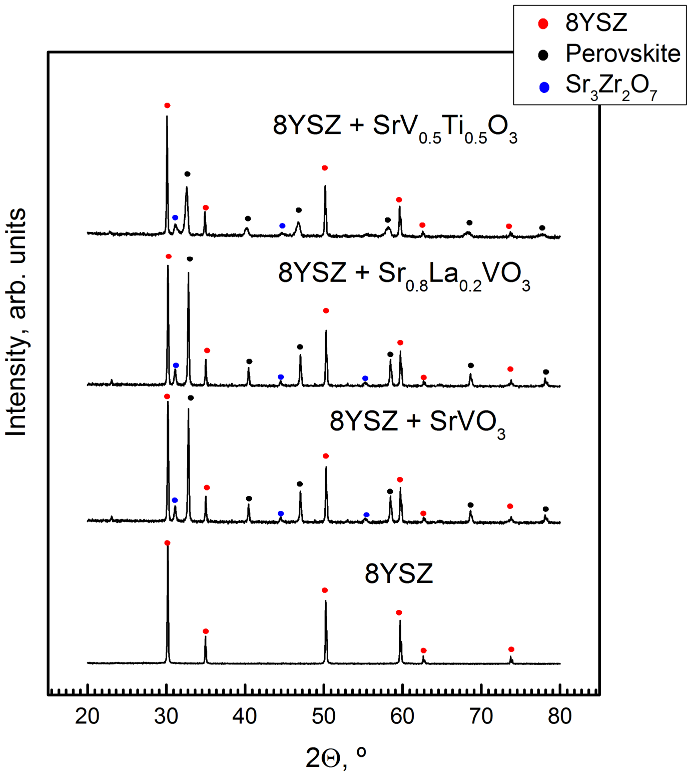

Fig 7.1. XRD patterns of vanadate – 8YSZ mixtures (50:50 wt.%) calcined in 10%H_2-N_2 flow at 1473 K for 10 h. The pattern of 8YSZ is shown for comparison.

Nevertheless, high-temperature reactivity between strontium vanadate-based materials and two most common solid electrolytes indicates that it is necessary to minimize the electrode firing temperature to suppress the reactivity between components.

7.2 Electrodes prepared by screen printing

7.2.1 Microstructural characterization

$SrV_{0.5}Ti_{0.5}O_{3-\delta}$ and $SrV_{0.3}Ti_{0.7}O_3$_MP electrode layers were applied on commercial 8YSZ substrates (Kerafol, thickness 200 μm) by screen printing, as described in Chapter 2, and sintered under reducing atmosphere and in air, respectively. Fig.7.3 shows polished cross-sections of electrodes sintered at different temperatures.

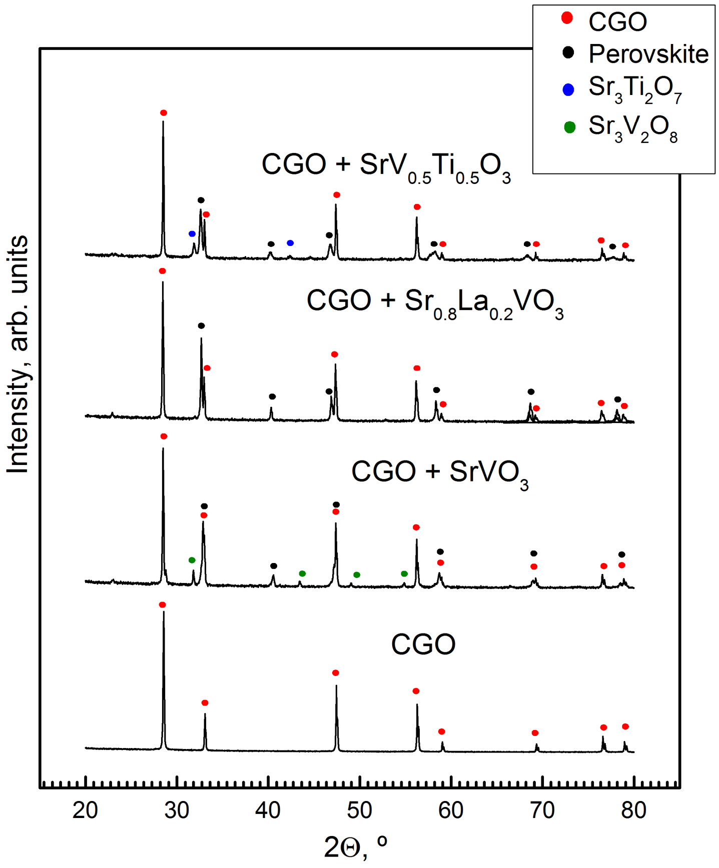

Fig 7.2. XRD patterns vanadate – CGO mixtures (50:50 wt.%) calcined in 10%H_2-N_2 flow at 1473 K for 10 h. The pattern of CGO is shown for comparison.

In all cases, electrode layers appear to be well bonded to dense 8YSZ electrolyte, with no evidence of exfoliation. In the case of $SrV_{0.5}Ti_{0.5}O_{3-\delta}$, synthesized at high temperatures and ball-milled before electrode deposition, variation of firing temperature between 1423 and 1573 K has a rather minor effect on the electrode microstructure: porosity and particle size remains very similar (Fig.7.3(A-D)). This is in agreement with a rather poor sinterability of $SrVO_{3-\delta}$-based ceramics even at temperatures as high as 1773 K, as demonstrated in the previous Chapters.

On the contrary, sintering of $SrV_{0.3}Ti_{0.7}O_3$_MP electrode layers under oxidizing atmosphere even at 1423 K led to noticeable crystallite growth of both major phases, $SrTiO_3$-based and $Sr_3V_2O_8$ (Fig.7.3E and G). Further increase of firing temperature to 1473 K resulted in excessive grain growth and electrode layer densification, promoted most likely by trace amounts of low-melting-point phases of Sr-V-O system, such as $Sr_2V_2O_7$ (Fig.2.1).

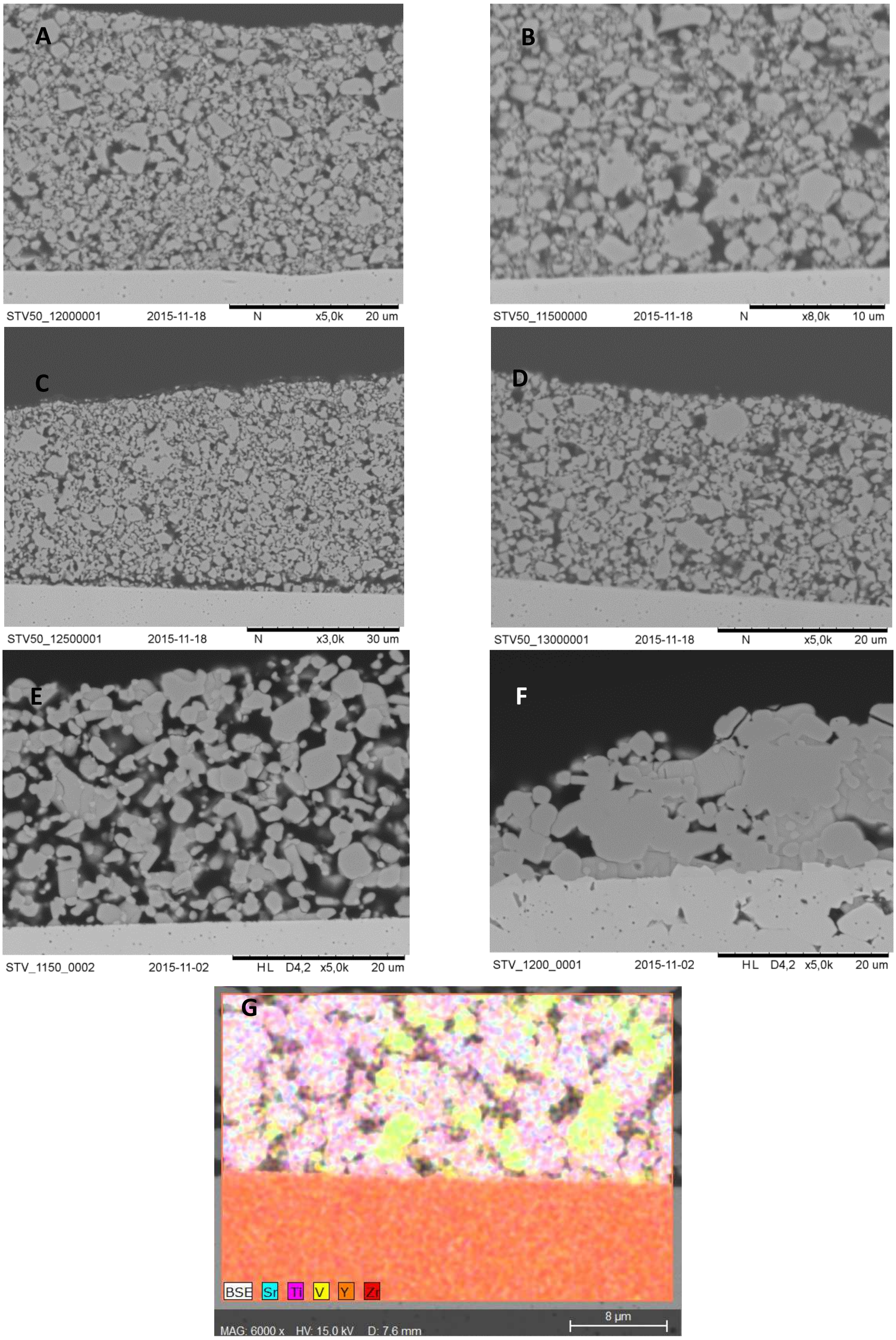
A
STV50_12000001 2015-11-18 N x5,0k 20 um
B
STV50_11500000 2015-11-18 N x8,0k 10 um
C
STV50_12500001 2015-11-18 N x3,0k 30 um
D
STV50_13000001 2015-11-18 N x5,0k 20 um
E
STV_1150_0002 2015-11-02 HL D4,2 x5,0k 20 um
F
STV_1200_0001 2015-11-02 HL D4,2 x5,0k 20 um
G
BSE Sr Ti V Y Zr
8 µm
MAG: 6000 x HV: 15.0 kV D: 7.6 mm

Fig 7.3. SEM micrographs of anode layers prepared by screen printing onto 8YSZ solid electrolyte. **(A,B,C and D):** $SrV_{0.5}Ti_{0.5}O_3$ electrode layer sintered under reducing atmosphere at 1423, 1473, 1523 and 1573 K, respectively; **(E and F):** $SrV_{0.3}Ti_{0.7}O_3$_MP electrode layer sintered in air at 1423 and 1473 K, respectively; **(G)** EDS elemental mapping corresponding to micrograph E.

7.2.2 Electrochemical tests of screen-printed electrodes

Preliminary characterization of electrochemical activity of electrode layers was performed by electrochemical impedance spectroscopy (EIS) using 2-electrode cells with symmetrical cell configuration, as explained in subsection 2.1.6.3.1. Impedance spectra given below are for comparative illustration. Ohmic (R_{Ohm}) and total polarization (R_p) resistances were estimated from the values corresponding to interception of semicircles with real axis. Detailed analysis of different contributions to the impedance spectra was considered out of scope of this preliminary electrochemical assessment.

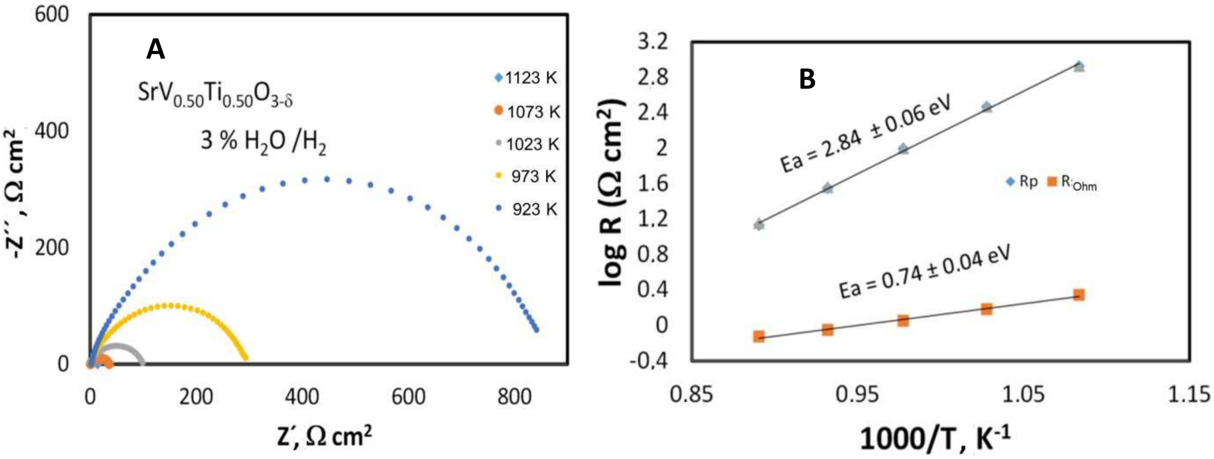

Fig 7.4. (A) Impedance spectra of symmetrical cell with $SrV_{0.5}Ti_{0.5}O_3$ electrode layers (T_{sint} = 1448 K) collected in 3% H_2O-H_2 atmosphere, and **(B)** temperature dependence of Ohmic and polarization resistances.

Figure 7.4A shows impedance spectra of symmetrical cell with $SrV_{0.5}Ti_{0.5}O_{3-\delta}$ electrodes sintered at 1448 K, collected in 3%H_2O-H_2 fuel atmosphere at 923-1123 K. Temperature dependences of ohmic resistance of the cell and specific electrode polarization resistance are presented in Fig.7.4B. Under the studied conditions, the cell had reasonably low ohmic resistance. At the same time, $SrV_{0.5}Ti_{0.5}O_{3-\delta}$ electrodes exhibited quite high polarization resistance, even at relatively high temperatures (e.g. 35 and 98 Ohm×cm^2 at 1073 and 1023 K, respectively). This poor performance can be explained, at least partly, by the low concentration of ionic defects in $SrV_{0.5}Ti_{0.5}O_{3-\delta}$, as revealed by poor tolerance to oxygen stoichiometry changes (see Chapter VI), and corresponding poor catalytic activity for hydrogen oxidation.

Therefore, as a next step, $SrV_{0.5}Ti_{0.5}O_{3-\delta}$ electrodes were functionalized via infiltration of CGO and Ni in order to introduce an ionically-conducting secondary phase and to improve electrocatalytic activity. Infiltration was performed as described in subsection 2.1.6.2 and was repeated three times. The results of EIS characterization of the cell with infiltrated electrode are shown in Fig.7.5, and the values of ohmic and polarization resistances of the cell before and after electrode modification are compared in Table 7.1.

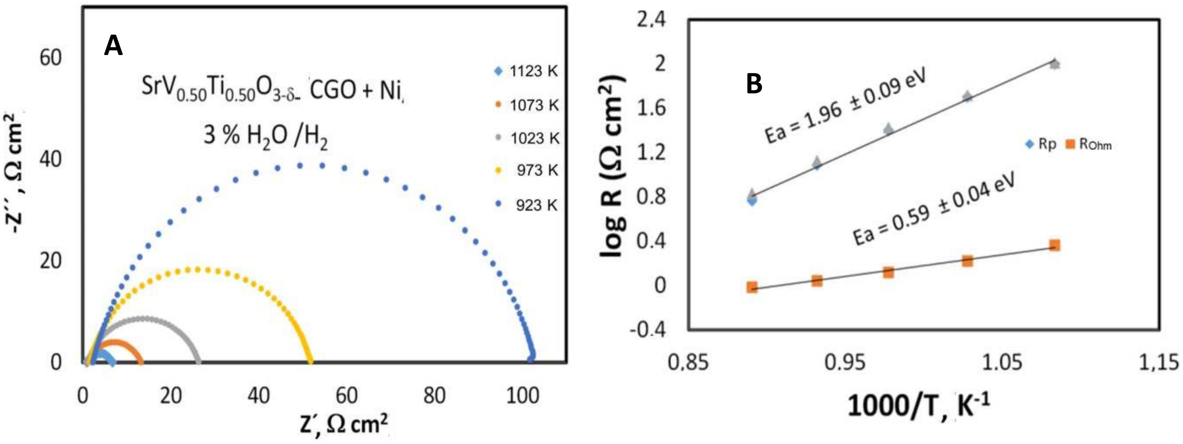

Fig 7.5. (A) Impedance spectra of symmetrical cell with $SrV_{0.5}Ti_{0.5}O_3$+CGO+Ni electrode layers collected in 3% H_2O-H_2 atmosphere, and **(B)** temperature dependence of Ohmic and polarization resistances.

Modification of electrode made it possible to decrease polarization resistance of the electrode, by 2.4 times at 1123 K to 8.4 times at 923 K. Still, polarization resistance remained excessively high, 12.2 Ohm×cm^2 at 1073 K. Although electrode performance probably could be further improved to some extent by introducing higher fraction of CGO, it seems that the main factor responsible for poor electrode performance is limited mass transfer at the electrode/electrolyte interface caused by reactivity between electrode and electrolyte in the course of electrode sintering.

Table 7.1
Comparison of ohmic and electrode polarization resistance of symmetrical cells with $SrV_{0.5}Ti_{0.5}O_{3-\delta}$ electrodes sintered at 1448 K, before and after modification.

T, K	as-prepared electrode		infiltrated with CGO and Ni	
	R_{Ohm}, Ohm cm^2	R_p, Ohm cm^2	R_{Ohm}, Ohm cm^2	R_p, Ohm cm^2
1123	0.75	13.6	0.96	5.8
1073	0.88	35.3	1.1	12.2
1023	1.1	98.5	1.3	25.1
973	1.5	293	1.7	50.2
923	2.2	840	2.3	99.5

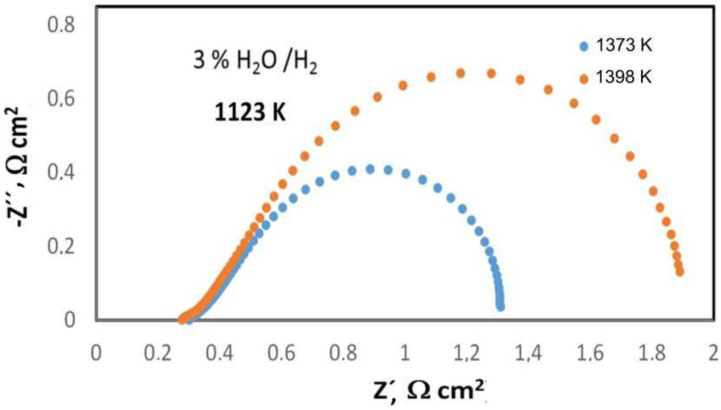

Fig 7.6. Impedance spectra of symmetrical cells with $SrV_{0.3}Ti_{0.7}O_3$_MP electrode layers collected in 3% H_2O-H_2 atmosphere at 1123 K. Electrode layers were sintered at 1373 and 1398 K.

Similar experiments were carried out in symmetrical cell configuration with $SrV_{0.30}Ti_{0.70}O_3$_MP electrodes fired in air and reduced in-situ in the fuel atmosphere at 1123 K. Fig.7.6 compares impedance spectra of the cells with electrodes sintered at two different temperatures. These electrode were found to exhibit significantly lower ohmic and polarization resistance compared to the similar cells with $SrV_{0.5}Ti_{0.5}O_{3-\delta}$ electrodes. Partly, this can be attributed to a lower temperature of electrode firing. However, it seems that more important factors are multiphase composition and lower overall fraction of vanadium. $SrTiO_3$-based electrodes exhibit better chemical compatibility with respect to 8YSZ solid electrolyte [Bochentyn, 2013], if compared to results discussed in subsection 7.1. Furthermore, for multiphase electrode, only part of electrode/electrolyte interface corresponds to the direct contact between 8YSZ and V-containing phase. Lower reactivity between components results in a lower ohmic resistance and substantially better electrochemical performance of electrode.

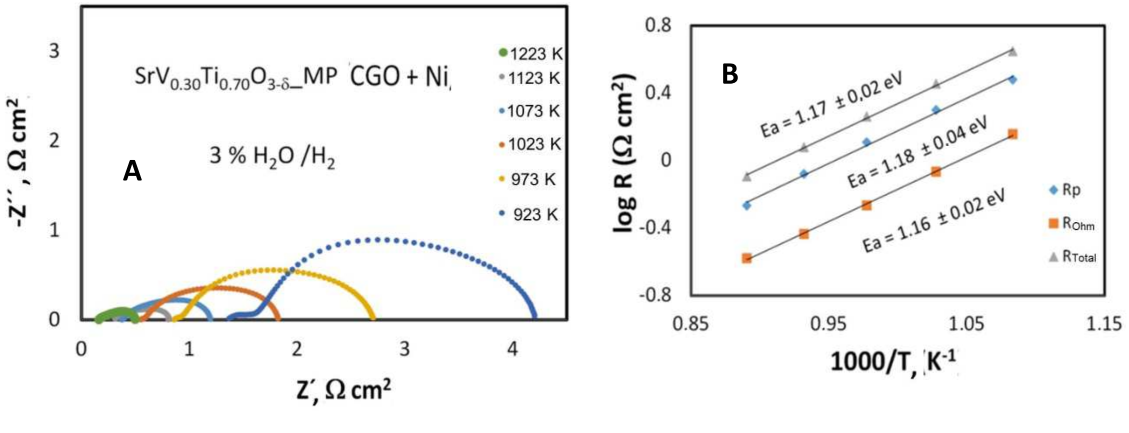

Fig 7.7. (A) Impedance spectra of symmetrical cell with $SrV_{0.3}Ti_{0.7}O_3$_MP+CGO+Ni electrode layers collected in 3% H_2O-H_2 atmosphere, and **(B)** temperature dependence of different contributions.

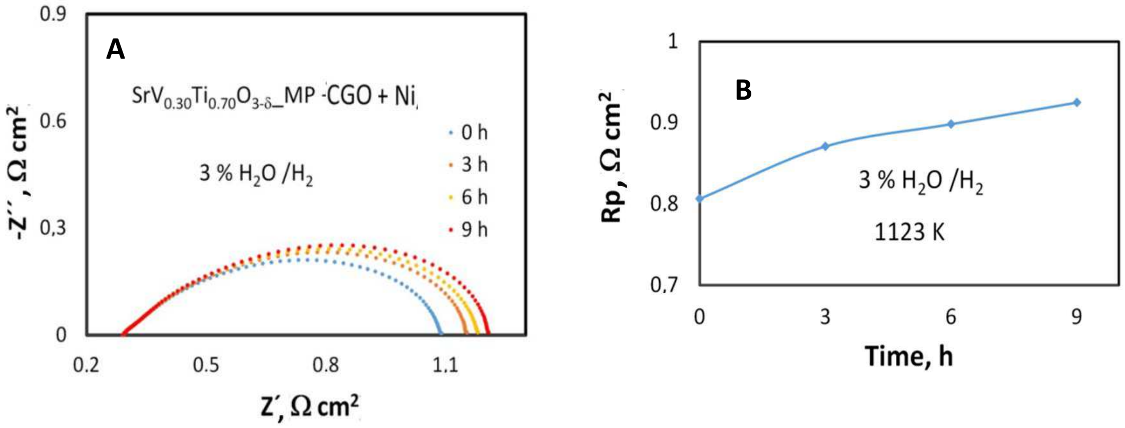

Fig 7.8. **(A)** Impedance spectra of symmetrical cells with $SrV_{0.3}Ti_{0.7}O_3$_MP electrode layers collected in 3% H_2O-H_2 atmosphere at 1123 K with 3 h intervals, and **(B)** drift of polarization resistance with time.

Increasing the firing temperature from 1373 K to 1398 K results in somewhat higher polarization resistance (Fig.7.6), most likely, due to densification of electrode and decrease of active surface area (Fig.7.3(E and F)), probably also accompanied with increased reactivity between electrode and electrolyte.

$SrV_{0.30}Ti_{0.70}O_3$_MP electrodes were infiltration with CGO and Ni, and corresponding results of electrochemical measurements are shown in Fig.7.7. Such modification made it possible to decrease polarization resistance twice, from 1.0 to 0.49 Ohm cm^2 at 1123 K in 3%H_2O-H_2 fuel. Thus, these electrodes demonstrate competitive electrochemical performance if compared to other ceramic anodes reported in literature (see Table 1.2).

Fig.7.8 demonstrates the results of short-term durability test for another cell with the same electrodes. This cell showed slightly higher electrode polarization resistance at 1123 K, and R_p tended to increase slowly with time suggesting time-dependent degradation of electrode microstructure or electrode/electrolyte interface. Thus, further optimization of electrode composition and processing conditions are required for better microstructural control and to reach improved and stable performance.

7.3 Electrode layers prepared by brush painting

7.3.1 Microstructural characterization

In this subsection, electrode inks were applied on the flat surfaces of sintered 8YSZ pellets (thickness 1.0-1.5 mm) using a brush. The tested electrode materials included $SrV_{0.5}Ti_{0.5}O_{3-\delta}$, $Sr_{0.8}La_{0.2}VO_{3-\delta}$, and also composites made by intimate mixing of these vanadates with commercial 8YSZ and CGO powders (50:50 wt.%). Fig.7.9 illustrates microstructures of electrode layers fired at different temperatures in 10%H_2-N_2 atmosphere. All prepared electrodes show quite similar morphology and porosity, apparently due to the same reasons as discussed above for screen-printed $SrV_{0.5}Ti_{0.5}O_{3-\delta}$ electrodes.

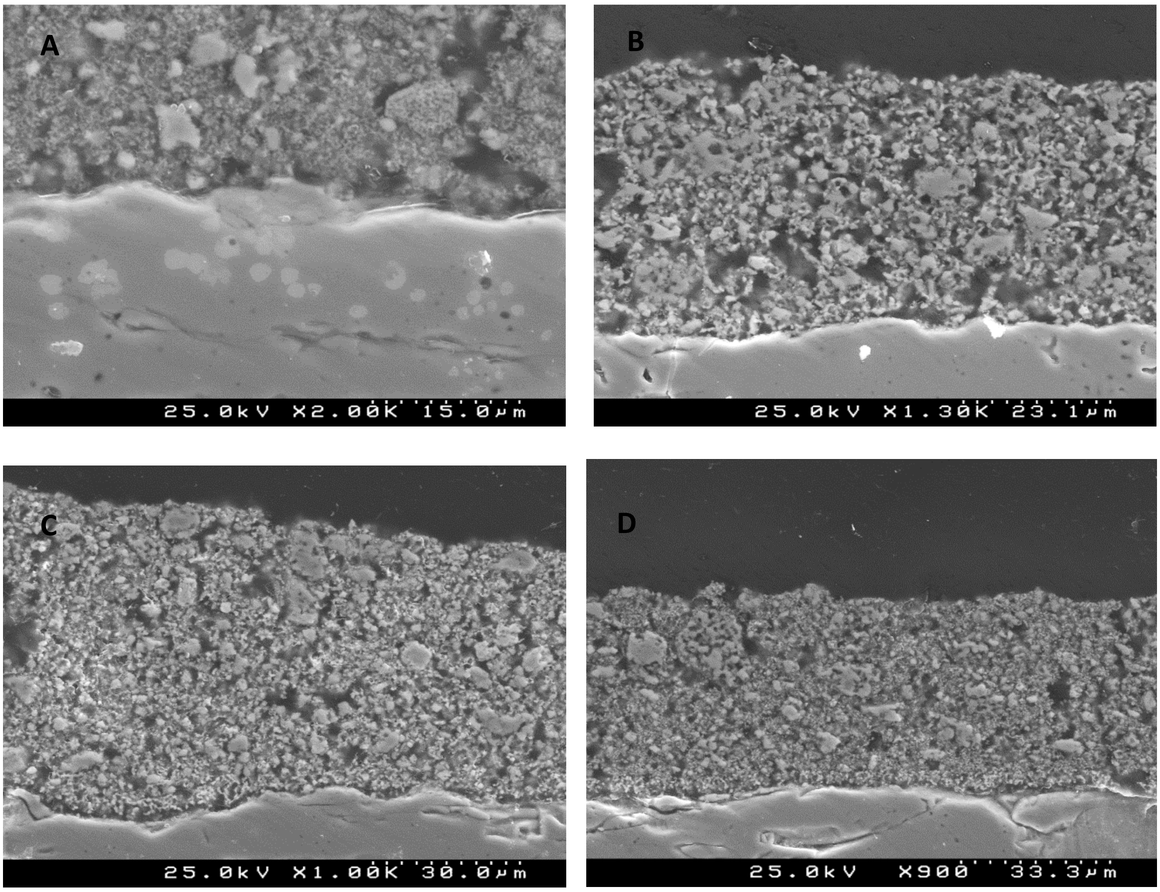

Fig 7.9. SEM micrographs (polished cross-sections) of electrodes layers applied by brush-painting onto 8YSZ electrolyte: **(A)** $Sr_{0.8}La_{0.2}VO_{3-\delta}$+8YSZ (50:50 wt.%) sintered at 1523 K; **(B)** $Sr_{0.8}La_{0.2}VO_{3-\delta}$+CGO (50:50 wt.%) sintered at 1523 K; **(C)** $Sr_{0.8}La_{0.2}VO_{3-\delta}$+(50:50 wt.%) sintered at 1473 K; and **(D)** $Sr_{0.8}La_{0.2}VO_{3-\delta}$+CGO (50:50 wt.%) sintered at 1423 K, with Ni infiltration.

7.3.2 CGO buffer layer

Taking into account non-negligible reactivity between vanadates and 8YSZ at temperatures around 1473 K, and also a lower reactivity between vanadates and CGO under identical conditions, at least in the case of $Sr_{0.8}La_{0.2}VO_{3-\delta}$, the next step of electrode deposition included also application of a thin intermediate CGO layer between 8YSZ electrolyte and vanadate-based electrode in order to minimize reactivity. CGO layer (few microns) was painted on the surface of 8YSZ pellet and fired at 1673 K for 2 h prior to electrode deposition and firing.

7.3.3 Electrochemical characterization of prepared electrodes

The results of preliminary screening of symmetrical cells with different $SrV_{0.5}Ti_{0.5}O_{3-\delta}$-and $Sr_{0.8}La_{0.2}VO_{3-\delta}$-based electrode layers at 1123 K in 3%H_2O-10%H_2-N_2 atmosphere are summarized in Table 7.2. Analysis of obtained polarization resistance values make it possible to draw a number of conclusions which are to be the basis for further detailed work.

Comparison of the results for several cells with plain $SrV_{0.5}Ti_{0.5}O_{3-\delta}$ electrodes sintered at 1473 K shows non-negligible scattering of obtained R_p values. This comparatively poor reproducibility suggests the necessity to optimize the ink preparation and electrode application procedures. Variation of firing temperature between 1423 and 1523 K had no pronounced effect on the electrode performance, but this can be caused by the same reproducibility issues.

Plain $Sr_{0.8}La_{0.2}VO_{3-\delta}$ electrode layer apparently exhibited even worse electrochemical activity compared to $SrV_{0.5}Ti_{0.5}O_{3-\delta}$ electrodes; this is still to be reproduced.

Addition of 20-50 wt.% of ionic conductor, either CGO or 8YSZ, o $SrV_{0.5}Ti_{0.5}O_{3-\delta}$-based electrode resulted in a strong deterioration of electrode performance: polarization resistance increased by 4-6 times. This obviously should be assigned to the reactivity between two components during the electrode sintering.

Surprisingly, addition of intermediate CGO buffer layer between composite electrode made either of $SrV_{0.5}Ti_{0.5}O_{3-\delta}$ or $Sr_{0.8}La_{0.2}VO_{3-\delta}$, with 50 wt.% fraction of CGO, resulted in significant improvement of electrode performance compared to the plain vanadate layers and, in particular, compared to same composite electrodes without buffer layer. This is still to be explained.

Finally, surface modification via infiltration of nickel as catalyst led to further reduction of electrode polarization for both plain vanadate layers and composite electrodes with CGO buffer layer. Note that the fraction of nickel in the electrodes corresponded roughly to 1-3 wt.%. For now, the best electrode performance, with R_p = 0.6 Ohm cm^2 at

1123 K, was obtained for $Sr_{0.8}La_{0.2}VO_{3-\delta}$+CGO (50:50 wt.%) electrode with CGO buffer layer and surface modification with Ni catalyst.

These preliminary observations certainly open the door for further improvement of preparation, architecture and electrochemical activity of $SrVO_3$-based electrodes.

Table 7.2

Summary of preliminary screening experiments for brush-painted electrodes

Cell	Electrode	CGO buffer layer	Second component / wt. fraction	Infiltration	Sintering T, K	R_p, Ohm×cm^2 (1123 K)
1	SVT [a]	-	-	-	1473	10.1
2	SVT	-	-	Ni	1473	6.8
3	SVT	-	-	-	1423	15.8
4	SVT	-	-	-	1473	19.2
5	SVT	-	-	-	1473	26.5
6	SVT	-	-	Ni	1473	5
7	SVT	-	-	-	1523	13.5
8	SVT+Pt [b]	-	-	-	1523	4.6
9	SVT	-	CGO / 50%	-	1473	103.4
10	SVT	-	CGO / 50%	Ni	1473	142
11	SVT	-	8YSZ / 50%	-	1473	82
12	SVT	-	CGO / 20%	-	1473	117
13	SVT	+	CGO / 50%	-	1473	8.7
14	SVT	+	CGO / 50%	Ni	1473	2.3
15	SVT	+	CGO / 50%	CGO	1473	16.3
16	SVT	+	CGO / 50%	CGO+Ni	1473	5.5
17	SLV [a]	-	-	-	1523	146.5
18	SLV	+	CGO / 50%	-	1473	7.6
19	SLV	+	CGO / 50%	Ni	1473	0.6
20	SLV	+	CGO / 50%	-	1150	8.2
21	SLV	+	CGO / 50%	Ni	1423	2
22	SLV	+	CGO / 50%	-	1523	6.3
23	SLV	+	CGO / 50%	Ni	1523	1.2

[a] SVT and SLV stand for $SrV_{0.5}Ti_{0.5}O_{3-\delta}$ and $Sr_{0.8}La_{0.2}VO_{3-\delta}$, respectively;

[b] SVT+Pt indicate $SrV_{0.5}Ti_{0.5}O_{3-\delta}$ with thin Pt layer painted on the top.

7.4 Preliminary conclusions on electrode behavior

i) Similar to other Sr-rich materials, $SrVO_3$-based perovskites react with 8YSZ solid electrolyte at elevated temperatures (1473 K) with formation of insulating strontium zirconate phase which may be expected to deteriorate the performance of anodes. Therefore, a decrease of the electrode firing temperature is necessary to minimize reactivity.

ii) Although $SrVO_3$ and its derivatives also tend to react with CGO10 solid electrolyte under the same conditions, the reactivity may be suppressed by partial substitution of Sr.

iii) Preliminary electrochemical tests indicated that single-phase $SrVO_3$-based anode layers applied onto 8YSZ solid electrolyte exhibit rather poor electrocatalytic activity towards hydrogen oxidation, partly due to low oxygen-ionic contribution to the total electrical conductivity. Introducing a fraction of solid electrolyte (CGO10) into electrode layers makes it possible to decrease the polarization resistance. The electrochemical activity of $SrVO_3$-based composite anodes can be further improved by surface modification via infiltration of Ni catalyst.

iv) The results of preliminary electrochemical screening emphasize the role of CGO10 buffer layer between $SrVO_3$-based anodes and 8YSZ electrolyte, suppressing the deteriorating effect of reactivity between cell components on the electrochemical performance.

v) These results confirm also that the fabrication of composite $SrVO_3$-$SrTiO_3$ anodes starting from the oxidized components via in-situ reduction is indeed a promising approach leading to better electrochemical performance compared to the electrodes based on single-phase $SrV_{1-y}Ti_yO_3$ components under similar conditions.

8. Final remarks and future work

8.1 Main conclusions

$SrVO_3$-based oxide materials have been studied as prospective ceramic components for solid oxide fuel cell anodes, with the aim to design alternative anode components to replace state-of-the-art Ni-based cermets in hydrocarbon-fueled SOFCs; this was stimulated by expectations of ability to prevent carbon deposition and unique sulfur tolerance or even ability to process H_2S as a fuel rather than a critical contaminant.

Still, key drawbacks were also identified at a very early stage of development of this project, with emphasis on limited redox stability, implying undue processing difficulties, risks of reactivity with other cell materials, and poor tolerance to redox cycling. Excessive thermochemical expansion also raised immediate concerns about compatibility with other cell materials, and risks of thermochemical shock. These limitations were addressed by selective composition changes guided by structural criteria, such as correlations between the tolerance factor of the perovskite structure combined with additional guidelines provided by thermodynamic modeling and defect chemistry.

Experimental methods were also adjusted to those challenges. Detailed characterization included phase and structural analysis, microstructural studies, electrical measurements as function of temperature and oxygen partial pressure, assessment of phase stability limits and redox behavior on cycling between reducing and oxidizing conditions, evaluation of thermochemical expansion and dimensional changes of redox cycling, and preliminary electrochemical tests.

The main results can be summarized as follows:

i) Perovskite-type $SrVO_{3-\delta}$ possesses high metallic conductivity under reducing conditions, but also excessive thermal expansion and limited phase stability. Under oxidizing atmosphere, it undergoes a transformation into insulating $Sr_2V_2O_7$ phase. This is accompanied by excessive dimensional and microstructural changes and is not completely reversible at temperatures below 1273 K.

ii) Two substitutional approaches were employed in order to expand the phase stability domain of $SrVO_3$. The first approach was donor-type substitution by higher-valence cations into one or both sublattices in order to oppose the oxidation of vanadium cations at higher $p(O_2)$ and to adjust the tolerance factor. Second approach represented substitution of vanadium by titanium, since isostructural $SrTiO_3$ exhibits remarkable phase stability and dimensional stability in a wide range of $p(O_2)$-T conditions and also a moderate thermal expansion.

iii) Moderate substitutions by rare-earth cations (La, Y) into Sr sublattice, by niobium cations into V sublattice, and co-substitutions were found to result in a gradual shift of upper-p(O_2) stability boundary of perovskite phase towards higher oxygen pressures, simultaneously suppressing oxygen nonstoichiometry and thermochemical expansion, and also decreasing to some extent electrical conductivity. The impacts of substitutions were interpreted in terms of expected effects on defect chemistry and structural stability (tolerance factor).

iv) $SrVO_3$ and $SrTiO_3$ were found to form an entire range of solid solutions under reducing conditions. The effects of substitution by titanium were found to be similar to those provided by donor-type doping. Increasing titanium content in $SrV_{1-x}Ti_xO_3$ solid solutions extended perovskite phase stability domain to higher p(O_2) and resulted in a gradual decrease of oxygen deficiency, thermochemical expansion and electrical conductivity.

v) For all studied materials, the decomposition of cubic perovskite phase still occurs at oxygen partial pressures below 10^{-5} atm. At the same time, donor- and titanium-substituted strontium vanadates demonstrate sluggish oxidation kinetics under inert gas atmosphere. This results in a reversible behavior in relatively short-term redox cycles between reducing and inert atmospheres, and also makes it possible to consider fabrication of vanadate-based fuel electrodes under inert gas conditions.

vi) Another promising approach is the fabrication of $SrVO_3$- and $SrTiO_3$-based composites starting from oxidized phases with thermal pre-treatment in air. In-situ reduction at 1123-1173 K produces a composite anode material with substantial level of electrical conductivity, where highly-conducting $SrVO_3$ phase is finely distributed in the stable $SrTiO_3$-based matrix.

vii) Preliminary screening of electrochemical performance of $SrVO_3$-based electrodes yielded guidelines for further optimization of electrode fabrication, architecture and electrocatalytic activity. The roles of buffer interlayer, ionically-conducting secondary phase, catalytic functionalization, and also a necessity to reduce the electrode fabrication temperature were emphasized.

8.2 Future work

Though this work represents real progress towards the initial objectives, one must also recognize that those were somewhat excessive expectations and, thus, further work will be needed for conclusive confirmation for prospective use of $SrVO_3$-based anodes in hydrocarbon-fueled SOFC. Thus, one proposes the following directions for continuation of this work:

a) Extended thermodynamic analysis of interaction of $SrVO_3$-based electrodes with sulfur-based impurities present in fossil fuels (e.g. H_2S, SO_2…) and corresponding risks of degradation by onset of reaction products (Sr, $SrSO_4$…);

b) Optimization of fabrication procedures and new architectures of $SrVO_3$-based anodes, which might minimize risks of reactivity with other cell materials and overcome incompatibilities based on differences in thermochemical or redox behavior

c) Detailed study of electrochemical behavior in contacts with hydrogen and methane fuels with variable degrees of conversion;

d) Experimental assessment of stability of $SrVO_3$-based anodes in fuels with different level of contamination;

e) Electrochemical testing of complete single fuel cells under realistic conditions of real hydrocarbon fuels.

References

Abudula, A.; Ihara, M.; Komiyama, H.; Yamada. K.; Solid State Ionics 86-88 **(1996**) 1203

Advancing the Science of Climate Change, NRC, National Research Council, The National Academies Press, Washington, Dc, USA **(2010)**

Aguilar. L, PhD Dissertation, Georgia Institute of Technology **(2004A)**

Aguilar. L, Zha, Cheng, Z., Winnick, J., Liu, M. J. Power Sources, 135 **(2004C)** 17-24

Aguilar. L, Zha, S., Li, S., Winnick, J., Liu, M. Solid State Lett, 7 **(2004B)** A324

Alif, A., Radenahmad, N., Cheok, Q., Shams, S., Kim, J.H., Azad, A.K., Renewable and Sustainable Energy Reviews 60 **(2016)** 822-835

Atkinson, A., Solid State Ionics, 95 **(1997)** 249-258

Atkinson, A.; Barnett, S.; Gorte, R. J.; Irvine, J. T.S.; McEvoy, A.J.; Mogensen, M. Nature Mater. 3 **(2004)** 17.

Azdouz, M., Manoun, B., Essehli, R. Azrour, M. Bih, L., Benmokhtar S., Hou, A.A., Lazor, P. J.Alloy. Comp. 498 **(2010**) 42-51

Baglio, J.A., Dann, J.N. J. Solid State Chem. 4. **(1972)** 87-93

Bebelis, S.; Neophytides, S. Kotsionopoulos, N.; Triantafyllopoulos, N. Colomer, M.T.; Jurado, J.; Solid State Ionics 177 **(2006)** 2087-2091

Bochentyn, B., Karcwewski, J., Gazda, M., Jasinki, P., Jusz, B., Phys. Status Solidi A 210 **(2013)** 538-545

Boukamp, B.A. Nature Materials 2 **(2003)** 294

Brandom, N.P, Skinner, S., Steel, B.C.H, Annu.Rev.Mater. Res. 33 **(2003)** 183

Brandon H. Smith, William C. Holler, Michael D Gross., Solid State Ionics, 192 **(2011)** 383-386

Brown Jr, J.J J. Am.Ceram.Soc 55 **(1972)** 500-503

Caillot, T.; Gelin, P.; Dailly, J.; Gauthier, G.; Cayron, C.; Laurencin, J.; Catal Today 128 **(2007)** 264-268

Canales-Vazquez, J., Tao, S.W., Irvine, J.T.S. Solid State Ionics, 159 **(2003)** 159-165

Carrillo-Cabrera, W., Von Schnering, H.G., Krist. Z. 205 **(1993)** 271-276

Castellano, R.; “Alternative energy Technologies”. Chapter 4 Pag. 68 **(2012)**

Chan, R.K., Sharma, R.K., Smyth, D.M., J. Electroche. Soc., 128 **(1981)** 1762-1769

Chen, T.; Wang, W.; Miao, H.; Tingshuai, Li; Cheng, Xu J.Power Sources 196 **(2011)** 2461-2468

Cheng, Z., Zha, S. Aguilar, L., Liu, M. Solid State Ionics 176 **(2005)** 1921-1928

Dees, D.; Balachandrdan, U.; Doris, S.; Heiberger, J.; McPheeter, C.; Picciolo, J. Electrochemical Society Proceedings of the First International Symposium on solid Oxide Fuel Cells,89-11, **(1999)** 317

Deng Z.Q, Niu H.J., Kuang X.J. Allix M., Claridge J.B. Rosseinsky M.J., Chem Mater 20, **(2008)** 6911-6

Dimitrios K. Niakolas. Applied Catalysis A: General 486 **(2014)** 123-142

Dougier, P., Casalot, A., J. Solid State Chem. 2 **(1970)** 396-403

Dougier, P., Fan, J.C.C., Goodenough, J.B. J.Solid State Chem. 14 **(1975A)** 247-259

Dougier, P., Hagenmuller, P., J. Solid State Chem. 15 **(1975B)** 158-166

Dr. Pieter Tans, NOAA/ESRL (www.esrl.noaa.gov/gmd/ccgg/trends/) (retrieved on Sept. **2015**)

Durif, A., Acta Crystallogr., 12 **(1959)** 420

Eror, N.G., Balachandran, U., J.Am. Ceram. Soc. 65 **(1982)** 426-431

Fergus, J.W., Solid State Ionics, 117 **(2006)** 1529-1541

Fotiev. A.A., Trunov, V.K., Zhuravlev, VD. Nauka, Moscow. **1985**

Frade, J.R., Kharton, V.V., Yaremchenko, A.A., Naumovich, E., J. Power Sources 130 **(2004)** 77-84

Fuel Cell Efficiency, World Energy Council, **(2007);** www.worldenergy.org

Fung, K.Z., Tsai, S.Y., Liu, C.Y., ECS Trans. 57 **(2013)** 1423-1428

Ge, X.M., Chan, S.H., J. Electrochem. Soc. 156 **(2009)** B386

Giannakopoulou, V., Odier, P., Bassat, J.M., Loup, J.P. Solid State Commun. 93 **(1995)** 579-583

Godickemeir, M. and Gaucker, L.J. J.Electrochem. Soc. 145(2) **(1998)** 414-420

Goodenough J.B and Huang, K. Proceddings of the Fuel Cells 97 review meeting **(1997)**

Gorte R.J.; Kim, H.; vohs, J.M.; J. Power Sources 106 **(2002)** 10

Guer, T.M., Chem. Rev., 113 **(2013)** 6179-6206

He. H.; Hill, J.M.; Appl.Catal A Gen., 317 **(2007)** 284-292

Holstein. W, J.Catal, 152 **(1995)** 42-51

Holtappels, P., Poulsen, F.W., Mogensen, M. Solid State Ionics, 135 **(2000)** 675-679

Huang, J., Sleight, A.W. Mater. Res. Bull. 27 (**1992**) 581-590

Huang, K..;Lee,H.Y.; Goodenough, J.B J Electrochem soc. 145 **(1998)** 3220

Huang, Y. H., Dass, R. I., Denyszyn, J.C., Goodenough, J.B. Journal of the Electrochemical Society. 153 **(2006A)** A1266-A1272

Huang, Y.H., Dass, R.I., Xing Z.L., Goodenough, J.B. Science, 312 **(2006B)** 254-257

Huang. X.J., Weppner. W. Journal of the Chemical Society-Faraday Trasactions, 92 **(1996)** 2173-2178

Hui, S., Petric, A. Solid State Ionics 143 **(2001)** 275-283

Hui, S.Q., Petric, A. Journal of the Electrochemical Society, 149 **(2002A)** J1-J10

Hui, S.Q., Petric, A. Journal of the European Ceramic Society, 22 **(2002B)** 1673-1681

Inaba, F., Arima, T., Ishikawa, T., Katsufuji, T., Tokura, Y. Phys. Rev.B 52 **(1995)** R2221-R2224

Intergovernmental Panel on Climate Change (IPCC) Fourth Assessment Report, Chapter 1 **(2007)**

Irvine. J.T.S. St Andrews presentation: Impedance Spectroscopy **(2010)**

Irvine. J.T.S. West. Advanced Materials 2 (3) **(1990)** 132-138

Ishihara, T., Matsuda, H., Takita, Y., J. Electrochem. Soc., 116 **(1994)** 3801-3803

Jensen, S.H., Larsen, P.H., Mogensen, M., International Journal of Hydrogen Energy, 32 **(2007)** 3253

Jiang, S. P., Liu, L., Khuong, P.O.B., Ping, W.B., Li, H., Pu, H. Journal of Power Sources, 176 **(2008)** 82-89

Jiang, S.P., Chan, S.H., Journal of Materials Science, 39 **(2004)** 4405-4439

Jiang, S.P., Chen, X.J., Chan, S.H., Kwok, J.T. Journal of the Electrochemical Society, 153 **(2006A)** A850-A856

Jiang, S.P., Chen, X.J., Chan, S.H., Kwok, J.T., Khor, K. Solid State Ionics 177 **(2006B)** 149-157

Jiang, S.P., Liu, L., Khuong, P.O.B., Ping, W.B., Li, H., Pu, H. Journal of Power Sources, 176 **(2008)** 82-89

Jiang, S.P.; Wang, W. Solid State Ionics 152 **(2005A)** 1398

Jiang, S.P.; Wang, W. Solid State Ionics 176 **(2005B)** 1185

Jiang, S.P.; Wang, W. Solid State Ionics 176 **(2005C)** 1351

Jorgensen, M.J.; Holtappels, P.; Appel, C.C. J Appl electrochem. 30 **(2000)** 411

Kaiser, A; Bradley, J.L; Slater, P.R; Irvine, J.T.S Solid State Ionics 135 **(2000)** 519-524

Karczewlski, J., Riegel, B., Gazda, M., Jasinki, P., Jusz, B. Journal of Electroceramics, 24 **(2010)** 326-330

Kelaidopoulou, A., Siddle, A., Dicks, A.L., Kaiser, A., Irvine, J.T.S. Fuel Cells, 1 **(2001A)** 219-225

Kelaidopoulou, A., Siddle, A., Dicks, A.L., Kaiser, A., Irvine, J.T.S. Fuel Cells, 1 **(2001B)** 226-232

Kharton, V.V., Kovalevsky, A.V., Viskup, A.P., Shaula, A.L., Figueiredo, F.M., Naumovich, E.N., Marques, F.M.B. Solid state Ionics, 160 **(2003)** 247-258

Kharton, V.V., Marques, FMB., Atkinson, A., Solid State Ionics, **174 (2004)** 135-149

Kharton, V.V., Shuangbao, L., Kovalevsky, A.V., Naumovich, E.N Solid State Ionics 96 **(1997)** 141-151

Kim, H.; Liu, C.; Worrell, W.L.; Vohs, J.M.; Gorte, R.J.; J.Electrochem. Soc 149 **(2002)** A247-A250

Kofstad, P. J. Less-Common Met., 14 **(1968)** 153

Korobitsyn, M.A., Hirs, G.G “Analysis of Cogeneration Alternatives”; ASME paper 95-CTP-11 **(1995)**

Kramer, S.A., Tuller H.L., Solid State Ionics. 82, **(1995)** 15-23

Krasnenko, T.I., Petrov, V.S., Judrina, L.V., Andrianova, L.V., Fotiev, A.A. Inorg Mater. 27 **(1991)** 1271-1273.

Krasnenko, T.I., Syrneva, O.N., Fotiev, A.A. Inorg. Mater, 20 **(1984)** 412-415

Krasnenko, T.I., Tugova, N.P., Slodobin, B.V., Fotiev, A.A., Syrneva, O.N Kiyaeva, G.A. Deposited Doc. VINITI. No 2866-83 **(1983)**

Kromp, A.; Dierickx, S.; Leonide, A.; Weber, A.; Ivers-Tiffee, E ECS Transactions, 41(33) **(2012)** 161-169

Kuharuangrong S. J.Power Sources 171, **(2007),** 506-510

Kuo, J. H.; Anderson, H.U.; Sparlin, D.M. J Solid State Chem. 87 **(1990)** 55

Laguna-Becero, M.A., Hanifi, A.R., Monzón, H., cunningham, J., Etsell, T.H., Sarkar, P.P., J. Mater. Chem. A, 2 **(2014)** 9764-9770

Lahl, N. Solid Oxide Fuel Cells VI, Electrochemical Society Proceedings Vol. 99-19, pp. 1057-1066 **1999**.

Lashtabeg, A., Canales-Vazquez, J., Irvine, J.T.S., Bradley, J.L. Chemistry of Materials, 21 **(2009)** 3549-3561

Lein, H.L., Wiik, K., Grande, T. Solid State Ionics 177 **(2006)** 1795-1798

Leonidov, L.A., Leonidova, O.N., Fotiev, A.A.. Sov Electrochem. 28 **(1992)** 1241-1247

Leonidova, O.N Fotiev, A.A., Leonidov, L.A., Russ.J. Electrochem 32 **(1996)** 478-481

Leonidova, O.N., Leonidov, L.A., Dontsov, G.I., Zhukovskaya, A.S. Phys. Solid State 40 **(1998)** 200-203

Lewis A. Owen, Professor Kevin T Pickering “An introduction to Global Environment Issues”. Chapter 7   Pag. 263 **(2006)**

Li, H.Zh., Liu, L.M., Reis, K.P., Jacobson, A.J. J.Alloy Comp. 203 **(1994)** 181-187

Li, T.S.; Wang, G Electrochem Solid-State Lett., 14 **(2011)** B35-B37

Li, T.S.; Wang, W.G.; Chen, T.; Miao, H.; Xu, C J.Power Sources 195 **(2010)** 7025-7032

Liu, X.; Su, Z.; Liu, J.; Pei, L.; Liu, W.; He, L. J.Alloys Com. 21 **(2000)** 305,

Liu. J.; Barnett, S.A.; Solid State Ionics 158 **(2003)** 11-16

Liu. J.; Barnett, S.A.; Solid State ionics 158 **(2011)** 11

Loehman, R. “Development of Reliable Methods for Sealing Solid Oxide Fuel Cell Stacks,” SECA Core Technology Program Review, January 27-28, **2005.**

Lu, X.C., Zhu, J.H. Solid State Ionics, 178 **(2007)** 1467-1475

Macias, J., Yaremchenko, A.A., Frade, J.R J. Alloys Compd., 601 **(2014)** 186

Maekawa, T. Kurosaki, K., Yamanaka, S. J. Alloy. Comp. 426 **(2006)** 46-50

Maekawa, T., Kurosaki, K., Yamanaka, S. Journal of Alloys and Compounds 426 **(2006)** 46-50

Mahajan, A.V., Johnston, D.C., Torgeson, D.R., Borsa, F. Phys. Rev. B 46 **(1992)** 10973-10985

Marina, O.A., Canfield, N.L., Stevenson, J.W. Solid State Ioncis, 149 **(2002)** 21-28

Marina, O.A., Canfield, N.L., Stevenson, J.W. Solid State Ionics, 149 **(2002)** 21-28

Marrero-Lopez, D., Pena-Martinez, J., Ruiz-Morales, J.C., Gabas, M., Nunez, P., Aranda, M.A.G., Ramos-Barrado, J.R. Solid State Ionics, 180 **(2010)** 1672-1682

Marrero-Lopez, D., Pena-Martinez, J., Ruiz-Morales, J.C., Martin-Sedeno, M.C., Nunez, P. Journal of Solid State Chemistry, 182 **(2009)** 1027-1034

Mastrandrea, M., Schneider, S., Science, 304 **(2004)** 571

Matsuzaki, Y.,Yasuda, I., Solid State Ionics 132 **(2000)** 261-269

Meibuhr, S.G. Electrochim. Acta, 11 **(1966)** , 1301

Meng, J., Ren, Y.F., He, P., Chin. J. Chem., 8 **(1990)** 289-294

Michibata, H., Itoh, K., Hagiwara, A., Kawada, T., Mizusaki, J. Electrochemistry 79 **(2011)** 246-248

Mingyang Gong, Xingbo Liu, Jason Trembly, Christopher Johnson, Journal of Power Sources 168 **(2007)** 289-298

Minh, N. Q; Takahashi, T. "Science and Technology of Ceramic Fuel Cells", Elsevier, Amsterdam **(1995)**

Mizusaki, J., Tsuchiya, S., Waragai, K., Tagawa, H., Arai, Y., Kuwayama, Y. J. Am. Ceram. Soc., 79 **(1996)** 109

Mogensen, D.; Grunwaldt, J.D.; Hendrdiksen, P.V.; Dam-Johansen, K.; Nielsen, J.U. J.Power Sources 196 **(2011)** 25-38

Monteiro, J.F., MSc thesis, University of Aveiro **(2009).**

Mori, K., Miyamoto, H., Takenobu, K., Kishizaba, H. and Sakaki, Y. Proceeding of the sixth European Solid Oxide Fuel Cell Forum, 28 June to 2 July **(2004)** Lucerne, Switzerland vol 3 pp 1208-1213

Mori, M., Wang, Z., Serizawa, N., Itoh, T., Journal of Fuel Cell Science and Technology, **(2011),** Vol. 8, 051010.

Mori, M.; Itoh, H.; Mori, N.; Abe, T.; Yamamoto, O.;Takeda, Y.; Imanishi, N. In Badwal, S.P.S.; Bannister, M.J.; Hannink, R.H. J. Science and Technology of Zirconia V. Lancaster, PA: Technomic Publishing Co., **1993**, 776-785

Muhammad Shirjeel Khan, Seung-Bok Lee, Rak-Hiun song, Jong-Won Lee, Tak-Hyoung Lim, Seok-Joo Park Ceramic International, 42 **(2016)** 35-48

Mukundan, R., Brosha, E., Garzon, F. Solid STate Lett. 7 **(2004)** A5

Muller. A.C., Weber, A. and Ivers-tiffee. E. Proceeding of the sixth European Solid Oxide Fuel Cell Forum, 28 June to 2 July **(2004)** Lucerne, Switzerland vol 3 pp 1231-1238

Neagu, D., Irvine, J.T.S. Chemistry of Materials, 22 **(2010)** 5042-5053

Nernst. W DRP 104872 **(1897)**

Nernst. W US Patent 685730 **(1889)**

Nernst. W, Z. Elektrochem.. 6 **(1899)** 41

Okinaka, H., Kosuge, K., Kachi, S., Trans.JIM; 12 **(1971)** 44

Ormerod, R.M., Chem. Soc.Rev. 32 **(2003)** 17

Palanisamy, T., Gopalakrishan, J. Sastri, M.V.C., Anorg, Z. Allg. Chem. 415 **(1975)** 275-284

Parfitt, D., Chroneos, A., Atrancona, A., Kilner, J.A. Journal of Materials Chemistry, 21 **(2011)** 2183

Park, S.D.; Vohs, J.M.; Gorte, R.J.; Nature 404 **(2000)** 265

Porat, O. Heremans C. Tuller H.L., J. Am. Ceram. Soc **(1997C)** 80, 2278-84

Porat, O., Heremans, C., Tuller, H.L. Solid State Ionics, 80 **(1997A)** 2278-2284

Porat, O., Heremans, C., Tuller, H.L. Solid State Ionics, 94 **(1997B)** 75-83

Porotnikov, N.V., Krasnenko, T.I., Fotiev, A.A., Neorg, Zh., Khim 34 **(1989)** 2650-2653

Poulsen, F.W., Van der Puil, N., Solid State Ionics, 53-56 **(1992)** 777-783

Primdahl, S., Hansen, J.R., Grahl-Madsen, L., Larsen, P.H. Journal of the Electrochemical Society, 148 **(2001**) A74-A81

Pudmich, G., Boukamp, B.A., Gonzalez-Cuenca, M., Jungen, W., Zipprich, W., Tietz, F. Solid State Ionics, 135 **(2000)** 433-438

Recent Trends in Fuel Cell Science and Technology **(2007)**

Reich, C.M., Kaiser, A., Irvine, J.T.S., Fuel Cells, 1 **(2001)** 249-255

Rey, M.J., Dehaudt, Ph., Joubert, J.C., Lambert-Andron, B., Cyrot, M., Cyrot-Lackmann, F. J.Solid State Chem.86 **(1990)** 101-108

Ringuedé, A., Bronine, D., Frade, J.R., Electrochiica Acta, 48 **(2002)** 437-442

Rodriguez-Carvajal. J. Physica B 192 **(1993)** 55

Ruiz-Morales, J.C., Canales-Vazquez, J., Savaniu, C., Marrero-Lopez, D., Nunez, P., Zhou, W.Z., Irvine, J.T.S. Physical Chemistry Chemical Physics, 9 **(2007)** 1821-1830

Samokhvalov, A., Tatarchuk, B.J., Phys. Chem. Chem. Phys., 13 **(2011)** 3197-3209

Sasaki, K.; Haga, K.; Yoshizumi, T.; Minematsu, D.; Yuki, E.; Liu, R.; Uryu, C.; Oshima, T.; Ogura, T.; Shiratori, Y.; Ito, K.; Koyama, M.; Yokomoto. K.; J.Power Sources 196 **(2011)** 9130-9140

Sauvet, A.L.; Fouletier, J.; electrochim. Acta 47 **(2001)** 987

Sfeir.J. J.Power Sources 118 **(2003)** , 276

Shannon, R.D., Acta Crystallogr., Sect. A: Cryst. Phys., Diffr., Theor. Gen. Crystallogr., 32 **(1976)** 751

Shao,Z.; Haile, S.M Nature 431 **(2004)** 170

Shin-ike, T., Sakai, T., Adachi, G., Shiokawa, J. Mater.Res.Bull, 11 **(1976)** 249-254

Shri Prakash, B.; Senthil Kumar, S.; Aruna, S.T.; Energy Rev., 36 **(2014)** 149-179

Simner, S.P., Hardy, J.S., Stevenson, J.W., Armstrong, T.R 128 **(2000)** 53-63

Skarmoutsos, D.; Tsoga, A.; Naoumidis, A.; Nikolopoulos, P.; Solid State Ionics 135 **(2000)** 439-444

Skopenko, V.V., Nedilko, S.A., Lishko, T.P., Drozd, V.A., Dokl.Akad,Nauk Ukr.SSR. **(1993)** 150-152

Skorodumova, N.V., Simak, S.I., Lundqvist, B.I., Abrikosov, I.A., Johansson, B. Phys. Rev. Lett. 89 **(2002).**

Slater, P.R., Irvine, J.T.S. Solid State Ionics, 120 **(1999A)** 125-134

Slater, P.R., Irvine, J.T.S. Solid State Ionics, 124 **(1999B)** 61-72

Slater, P.R; Irvine, J.T.S Solid State Ionics 124, **(1999)** 61-72

Solomon, S., Dahe, Q., Manning, M., Intergovernmental Panel on Climate Change (IPCC), in Climate Change. Univ. Press, New York **(2007)** 996

Spacil,H.S., U.S Patent 3-558-360-30 Oct. 1964; modified on 2-11-1967 and 31-3-**1970**

Steele B.C.H. Solid State Ionics 129**, (2000)**, 95-110

Steele, B.C.H Ceramic International, 19 **(1993)** 269

Steele, B.C.H, Heinzel. A, Nature 414 **(2001)** 345

Subramanian M.A., Aravamudan G. Rao G.V.S. a review Prog Solid State Chem **(1983)** 15, 55-143

Sun, C., Stimming, U., Journal of Power Sources, 171 **(2007)** 247-260

Sun, C.W., Sun, J., Xiao, G.L., Zhang, H.R., Qiu, X.P., Li, H., Chen, L.Q., J. Phys. Chem. B 110 **(2006)** 13445

Sun, L.P., Li, Q., Zhao, H., Huo, L.H., Grenier, J.C., Journal of Power Sources, 183 **(2008)** 43-48

Takeda, Y.; Kano, R.; Noda, M.; Tomida, Y.; Yamamoto, O.J. Electrochem. Soc. 134 **(1987)** 2656

Tao, S.W., Irvine, J.T.S. Journal of Materials Chemistry, 12 **(2002)** 2356-2360

Tao, S.W., Irvine, J.T.S. Nature Materials, 2 **(2003)** 320-323

Tao, S.W., Irvine, J.T.S. Solid State Ionics 154 **(2002B)** 659-667

Tao, S.W., Irvine, J.T.S., Kilner, J.A. Advanced Materials, 17 **(2005)** 1734

Tatsuya Takeguchi, Yukimune Kani, Tatsuya Yano, Ryuji Kukuchi, Koichi Eguchi, Keigo Tsujimoto, Yoshitaka Uchida, Akira Ueno, Koiji Omoshiki, Masanobu Aizawa. Journal of Power Sources, 112 **(2002)** 588-595

Vernoux, P., Djurado, E., Guillodo, M. Journal of the American Ceramic Society, 84 **(2001)** 2289-2295

Vernoux, P., Guillodo, M., Fouletier, J., Hammou, A. Solid State Ionics, 135 **(2000)** 425-431

Vozdecky, P., Roosen, A., Ma, Q.L., Tietz, F., Buchkremer, H.P. Journal of Materials Science 46 **(2011)** 3493-3499

Wang, X.P.; Jiang, S.P.; J Solid State Electrochem. 8 **(2004)** 914

West, A.R., Solid State Chemistry and its Applications, Wiley **(1988)**

Yahiro, H., Eguchi, K., Arai, H., Solid State Ionics, 36 **(1989)** 71-75

Yamamoto, O.; Arati, Y.; Takeda, Y.; Imanishi, N.; Mizutoni,Y.; Kawai, M.; Nakamura, Y.; Solid state Ionics 79 **(1995)** 137.

Yamamoto, O.; Electrochem. Acta 45 **(2000)** 2423-2435

Yaremchenko, A.A., Brinkmann, B., Janssen, R., Frade, J.R. Solid State Ionics 247-248 **(2013)** 86-93

Yaremchenko, A.A., Mikhalev, S.M., Kravchenko, E.S., Frade. J.R. J.Eur. Ceram. Soc. 34 **(2014)** 703-715

Yaremchenko, A.A., Naumovich, E.N., Patricio. S.G., Merkulov, O.V., Patrakeev, M.V., Frade, J.R., Inorg. Chem, 55 **(2016)** 4836-4849

Yaremchenko, A.A.; Kharton, V.V.; Bannikov, D.O.; Znosak, D.V.; Frade, J.R.; Cherepanov, V.A. Solid State Ionics 180 **(2009)** 878-885

Yashiro, K., Kobayashil, T., Han, L.Q., Kaimal, A., Nigara, Y., Kawada, T., Mizusaki, J., Kawamura, K. Solid Oxide Fuel Cells Vii **(2001)**

Yokokawa, H., Sakai, N., Kawada, T. Dokiya, M. J. Sol. State Chem., 94 **(1991)** 106-120

Yokokawa, H.; Sakai, N.; Kawada, T.; Dokiya, M. Solid Sate Ionics 40-41 **(1990)** 398

Yoshioka, H., Mieda, H., Funahashi, T., Mineshige, A., Yazaw, T., Mori, R., J. Eur. Cerami. Soc., 34 **(2014)** 373-379

Zhang, Z.L.; Verykios, X.E.; Catal Today 21 **(1994)** 589

Zha, S. W., Cheng, Z., Liu, M.L. Electrochemical and Solid State Letters 8 **(2005)** A406-A408